

# **ACOUSTIC TRANSDUCTION – MATERIALS AND DEVICES**

**Period 1 January 1998 to 31 December 1998**

**Annual Report**

**VOLUME I**

**OFFICE OF NAVAL RESEARCH  
Contract No: N00014-96-1-1173**

**APPROVED FOR PUBLIC RELEASE –  
DISTRIBUTION UNLIMITED**

**Reproduction in whole or in part is permitted for any  
purpose of the United States Government**

**Kenji Uchino**

**PENNSSTATE**



**THE MATERIALS RESEARCH LABORATORY  
UNIVERSITY PARK, PA**

**Reproduced From  
Best Available Copy**

**19990427 041**

# REPORT DOCUMENTATION PAGE

Form Approved  
OMB No. 0704-0188

Public reporting burden for this collection of information is estimated to average 1 hour per response, including the time for reviewing instructions, searching existing data sources, gathering and maintaining the data needed, and completing and reviewing the collection of information. Send comments regarding this burden estimate or any other aspect of this collection of information, including suggestions for reducing this burden, to Washington Headquarters Services, Directorate for Information Operations and Reports, 1215 Jefferson Davis Highway, Suite 1204, Arlington, VA 22202-4302, and to the Office of Management and Budget, Paperwork Reduction Project (0704-0188), Washington, DC 20503

1. AGENCY USE ONLY (Leave blank)		2. REPORT DATE 04/05/99	3. REPORT TYPE AND DATES COVERED ANNUAL REPORT 01/01/98-12/31/98	
4. TITLE AND SUBTITLE ACOUSTIC TRANSDUCTION -- MATERIALS AND DEVICES			5. FUNDING NUMBERS ONR CONTRACT NO: N00014-96-1-11173	
6. AUTHOR(S) KENJI UCHINO				
7. PERFORMING ORGANIZATION NAME(S) AND ADDRESS(ES) Materials Research Laboratory The Pennsylvania State University University Park PA 16802			8. PERFORMING ORGANIZATION REPORT NUMBER	
9. SPONSORING/MONITORING AGENCY NAME(S) AND ADDRESS(ES) Office of Naval Research      Office of Naval Research ONR 321SS                          Regional Office Chicago Ballston Centre Tower One      536 S Clark Str., RM 208 800 N Quincy Street              Chicago IL 60605-1588 Arlington VA 22217-5660			10. SPONSORING/MONITORING AGENCY REPORT NUMBER	
11. SUPPLEMENTARY NOTES				
12a. DISTRIBUTION / AVAILABILITY STATEMENT			12b. DISTRIBUTION CODE	
13. ABSTRACT (Maximum 200 words)				
14. SUBJECT TERMS			15. NUMBER OF PAGES	
			16. PRICE CODE	
17. SECURITY CLASSIFICATION OF REPORT	18. SECURITY CLASSIFICATION OF THIS PAGE	19. SECURITY CLASSIFICATION OF ABSTRACT	20. LIMITATION OF ABSTRACT	

## ABSTRACT

This report documents work performed over the period 1 January 1998 to 31 December 1998 on a MURI under the Office of Naval Research Contract N00014-96-1-1173. The topic "Acoustic Transduction Materials and Devices" brings together groups in the Materials Research Laboratory (MRL), the Applied Research Laboratory (ARL), and the Center for Acoustics and Vibrations (CAV) at Penn State.

Research on the program is adequately represented in the 80 technical appendices.

Outstanding accomplishments include:

Exploration of several new relaxor ferroelectric perovskite solid solution with morphotropic phase boundaries. New evidence of the onset of nonlinearity in soft donor doped PZTs at surprisingly low (1V/cm) fields. Confirmation of the relaxor phase induced by electron irradiation in PVDF:TrFE copolymers, and a processing method which permits very high (4%) electrostrictive strain in the transverse direction, vital for the practical use in actuator systems. In composite transducer, "first fruits" of the cooperative program are cymbal arrays which form most effective acoustic projectors, and a new "dog bone" design which permits deeper submergence for the cymbal. Agile transducers, the 3-D acoustic intensity probe and high force high strain torsional and step and repeat systems continue to make excellent progress. In actuator studies true acoustic emission is proving to be an excellent tool in reliability studies and a new design of small-scale (mini) piezoelectric motor shows outstanding performance. Thick thin film studies and are now "gearing up" for the development of the mini tonpilz arrays. New combinations of ultrasonic and resonance methods appear to offer unique capability for complete characterization of ferroelectric piezoelectric materials.

The mode of presentation of the report emphasizes the outstanding progress made in published research. It is important to also document that the slower and more painstaking development of practical transducer systems in the cymbal and mini tonpilz arrays is progressing very favorably.

## TABLE OF CONTENTS

APPENDICES LISTING .....	2
ABSTRACT .....	9
INTRODUCTION .....	10
1.0 GENERAL SUMMARY PAPERS .....	11
2.0 MATERIALS STUDIES .....	11
2.1 Polycrystal Perovskite Ceramics .....	11
2.2 Relaxor Ferroelectric Single Crystal Systems .....	12
2.3 New High Strain Polymer Materials .....	12
3.0 TRANSDUCER STUDIES .....	13
3.1 Composite Structures .....	13
3.2 Frequency Agile Transducers .....	13
3.3 3-D Acoustic Intensity Probes .....	13
4.0 ACTUATOR STUDIES .....	14
4.1 Materials : Designs : Reliability .....	14
4.2 Photostrictive Actuators .....	14
4.3 Torsional and High Force Actuators.....	14
5.0 MODELING and CHARACTERIZATION .....	14
5.1 Finite Element and Other Methods.....	14
5.2 Relaxor Ferroelectrics .....	15
5.3 Thin and Thick Thin Films .....	15
5.4 Domain Studies .....	16
5.5 Electrostriction .....	16
6.0 GRADUATE STUDENTS IN THE PROGRAM .....	17
7.0 HONORS and AWARDS .....	17
8.0 PAPERS PUBLISHED IN REFEREED JOURNALS .....	17
9.0 PAPERS SUBMITTED FOR PUBLICATION.....	21
10.0 PAPERS APPEARING IN NON REFERRED PROCEEDINGS .....	25
11.0 INVITED PAPERS PRESENTATIONS AT NATIONAL AND INTERNATIONAL MEETINGS .....	26
12.0 INVITED PAPERS PRESENTED AT UNIVERSITY, INDUSTRY, AND GOVERNMENT LABORATORIES .....	29
13.0 CONTRIBUTED PAPERS AT NATIONAL AND INTERNATIONAL MEETINGS .....	31
14.0 BOOKS (AND SECTIONS THERE OF) .....	36



## APPENDICES

### VOLUME I

#### GENERAL SUMMARY PAPERS

1. Cross, L.E., "Recent Developments in Piezoelectric Ferroelectric Materials and Composites," Proceedings of the 4<sup>th</sup> European Conference on Smart Structures and Materials in Conjunction with the 2<sup>nd</sup> International Conference on Micromechanics, Intelligent Materials and Robotics, Harrogate, UK (6-8 July 1998).
2. Newnham R.E., "Functional Composites for Sensors and Actuators," Chapter in *The Era of Materials*, edited by S. Majumdar, R. Tressler, and E. Miller, 259-275, Pennsylvania Academy of Science (1998).
3. Uchino, K., "Piezoelectric Ultrasonic Motors: Overview," *Smart Mater. Struct.* **7**, 273-285 (1998).
4. Newnham, R.E., "Phase Transformations in Smart Materials," *Acta Cryst.* **A54**, 729-737 (1998).

#### 2.0 MATERIALS STUDIES

##### 2.1 Polycrystal Perovskite Ceramics

5. Liu, S.F., I.R. Abothu, S. Komarneni, P. Poosanaas, D.S. Paik, Y. Ito, and K. Uchino, "PLZT Ceramics from Conventional and Microwave Hydrothermal Powders," Proceedings in Asian Meeting on Ferroelectrics (AMF2), Singapore (December 8-11, 1998).
6. Abothu, I.R., P. Poosanaas, S. Komarneni, Y. Ito, and K. Uchino, "Nanocomposite Versus Monophasic Sol-Gel Processing of PLZT Ceramics," Proceedings in Asian Meeting on Ferroelectrics (AMF2), Singapore (December 8-11, 1998).
7. Kim, J.S., Y.H. Chen, and K. Uchino, "Dielectric and Piezoelectric Properties of Fe<sub>2</sub>O<sub>3</sub>-Doped 0.57PSN-0.43PT Ceramics," *J. Korean Phys. Soc.* **32** [2], S1248-1250 (1998).
8. Alberta, E.F. and A.S. Bhalla, "Electrical Property Diagram and Morphotropic Phase Boundary in the Pb(In<sub>1/2</sub>Ta<sub>1/2</sub>)O<sub>3</sub>-PbTiO<sub>3</sub> Solid Solution System," *Ferroelectric Letters* (1998). [accepted]
9. Meng, J.F., Z-Y. Cheng, B.K. Rai, R.S. Katiyar, E. Alberta, R. Guo, and A.S. Bhalla, "Photoluminescence in PbMg<sub>1/3</sub>Nb<sub>2/3</sub>O<sub>3</sub>-PbIn<sub>1/2</sub>Nb<sub>1/2</sub>O<sub>3</sub> Systems," *J. Mater. Res.* **13** (7), 1861 (1998).
10. Alberta, E.F. and A.S. Bhalla, "Investigation of the Lead Indium Niobate-Lead Magnesium Niobate Solid Solution," *Materials Letters* (1998). [accepted]
11. Alberta, E.F., A.S. Bhalla, and T. Takenaka, "Large Hydrostatic Piezoelectric Constant and Temperature Dependence of the Piezoelectric Properties of Bi(NiTi)<sub>1/2</sub>O<sub>3</sub>:PbTiO<sub>3</sub> Ceramics," *Ferroelectrics Letters* (1998). [accepted]
12. Zhang, Q.M. and J. Zhao, "Electromechanical Properties of Lead Zirconate Titanate Piezoceramics Under the Influence of Mechanical Stress, IEEE Trans. UFFFC (accepted).
13. Kugel, V.D. and L.E. Cross, "Behavior of soft Piezoelectric Ceramics under High Sinusoidal Electric Fields," *J. Appl. Phys.* **84** (5), 2815-2830 (1998).

## VOLUME II

### 2.0 MATERIALS STUDIES

#### 2.1 *Polycrystal Perovskite Ceramics* (continued)

14. Du, X-H., Q.M. Wang, U. Belegundu, and K. Uchino, "Piezoelectric Property Enhancement in Polycrystalline Lead Zirconate Titanate by Changing Cutting Angle," J. Ceram. Soc. Jpn. (1999). [accepted]
15. Mueller, V. and Q.M. Zhang, "Nonlinearity and Scaling Behavior in Donor Doped Lead Zirconate Titanate Piezoceramic," Appl. Phys. Lett. **72**, 2692 (1998).
16. Uchino, K and H. Aburatani, "Field Induced Acoustic Emission in Ferroelectric Ceramics," Proc. IEEE Ultrasonic Symp., Sendai, Japan (October 1998). [in press]
17. Newnham, R.E. and S. Trolier-McKinstry, "Size Effects in Ferroics" Integrated Ferroelectrics **20**, 1-13, Gordon & Breach Science Publishers (March 1998).

#### 2.2 *Relaxor Ferroelectric Single Crystal Systems*

18. Uchino, K., "High Electromechanical Coupling Piezoelectrics: Relaxor and Normal Ferroelectric Solid Solutions," Solid State Ionics **108**, 43-52 (1998).
19. Wada, S. S.E. Park, L.E. Cross, and T.R. Shrout, "Domain Configuration and Ferroelectric Related Properties of Relaxor Based Single Crystals," J. Korean Phys. Soc. **32**, S1290-S1293 (1998).
20. Belegundu, U., X. H. Du, and K. Uchino, "In-Situ Observation of Domain Orientation in  $\text{Pb}(\text{Zn}_{1/3}\text{Nb}_{2/3})\text{O}_3$ - $\text{PbTiO}_3$  Single Crystals," Proc. 5<sup>th</sup> Intl. Symp. Ferroic Domains and Mesoscopic Structures, University Park, PA (April 1998).
21. Du, X.H., J. Zheng, U. Belegundu, and K. Uchino, "Crystal Orientation Dependence of Piezoelectric Properties of Lead Zirconate Titanate Near the Morphotropic Phase Boundary," J. Appl. Phys. Ltrs. **72** (19), 2421-2423 (1998).
22. Rehrig, P.W., S.-E. Park, S. Trolier-McKinstry, G.L. Messing, B. Jones, and T.R. Shrout, "Piezoelectric Properties of Zirconium-Doped Barium Titanate Single Crystals Grown by Templated Grain Growth," submitted to J. Appl. Phys.
23. Du, X., Q.M. Wang, U. Belegundu, A. Bhalla, and K. Uchino, "Crystal Orientation Dependence of Piezoelectric Properties of Single Crystal Barium Titanate," Mat. Ltr. (1999) [accepted].
24. Guo, R., H.T. Evans, Jr., and A.S. Bhalla, "Crystal Structure Analysis and Polarization Mechanisms of Ferroelectric Tetragonal Tungsten Bronze Lead Barium Niobate," Ferroelectrics **206/207**, 123-132 (1998).

#### 2.3 *New High Strain Polymer Materials*

25. Zhao, X., V. Bharti, Q.M. Zhang, T. Ramotowski, F. Tito, and R. Ting, "Electromechanical Properties of Electrostrictive P(VDF-TrFE) Copolymer," Appl. Phys. Ltrs. **73**, 2054 (1998).
26. Bharti, V., G. Shanthi, H. Xu, Q.M. Zhang, and K. Liang, "Evolution of Transitional Behavior and Structure of Electron Irradiated Poly(vinylidene fluoride-trifluoroethylene) Copolymer Films," Appl. Phys. Ltrs. [accepted].
27. Cheng, Z.-Y., V. Bharti, T.B. Xu, S. Wang, and Q.M. Zhang, "Transverse Strain Responses in Electrostrictive Poly (vinylidene fluoride-trifluoroethylene) Films and Development of a Dilatometer for the Measurement," J. Appl. Phys. [accepted]

## VOLUME III

### 2.0 MATERIALS STUDIES

#### 2.3 *New High Strain Polymer Materials* (continued)

28. Bharti, V., X.Z. Zhao, Q.M. Zhang, T. Ramotowaski, F. Tito, and R. Ting, "Ultrahigh Field Induced Strain and Polarized Response in Electron Irradiated Poly(vinylidene fluoride-trifluoroethylene) Copolymer," *Mat. Res. Innovat.* **2**, 57-63 (1998).
29. Su, J., P. Moses, and Q.M. Zhang, "A Bimorph Based Dilatometer for Field Induced Strain Measurement in Soft and Thin Free Standing Polymer Films," *Rev. Sci. Instruments* **69** (6), 2480 (1998).

### 3.0 TRANSDUCER STUDIES

#### 3.1 *Composite Structures*

30. Hughes, W.J., "Transducers, Underwater Acoustic," *Encyclopedia of Applied Physics*, Vol. 22, 67 (1998).
31. Tressler, J.F., W.J. Hughes, W. Cao, K. Uchino, and R.E. Newnham, "Capped Ceramic Underwater Sound Projector."
32. Zhang, J., W.J. Hughes, A.C. Hladky-Hennion, and R.E. Newnham, "Concave Cymbal Transducers."
33. Wang, Q.M., X.-H. Du, B. Xu, and L.E. Cross, "Theoretical Analysis of the Sensor Effect of Cantilever Piezoelectric Benders," *J. Appl. Phys.* **85** (3), 1702-1712 (1998).
34. Fernandez, J.F., A. Dogan, J.T. Fielding, K. Uchino, and R.E. Newnham, "Tailoring the Performance of Ceramic-Metal Piezocomposite Actuators, 'Cymbals'," *Sensors and Actuator A65*, 228-237 (1998).
35. Wang, Q.M. and L.E. Cross, "A Piezoelectric Pseudoshear Multilayer Actuator," *Appl. Phys. Ltrs.* **72** (18), 2238 (1998).
36. Geng, X. and Q.M. Zhang, "Resonance Modes and Losses in 1-3 Composites for Ultrasonic Transducer Applications," *J. Appl. Phys.* **85** (3), 1342 (1999).

#### 3.2 *Frequency Agile Transducers*

37. Hebert, C.A. and G. A. Lesieutre, "Flexural Piezoelectric Transducers with Frequency Agility Obtained Via Membrane Loads," *J. Intel. Mat. Sys. & Str.* (1998). [accepted].
38. Davis, C.L. and G.A. Lesieutre, "An Actively Tuned Solid State Vibration Absorber Using Capacitive Shunting of Piezoelectric Stiffness," *J. Sound & Vibration* (1998). [accepted]
39. Bernard, J., G.A. Lesieutre, and G.H. Koopmann, "Active Broadband Force Isolation using a Flexural Piezoelectric Inertial Actuator," *J. Sound & Vibration* (1999). [submitted]

## VOLUME IV

### 3.0 TRANSDUCER STUDIES

#### 3.3 3-D Acoustic Intensity Probes (continued)

40. Lauchle, G.C. and A.R. Jones, "Unsteady Lift Force on a Towed Sphere," *J. Fluids and Structures* **112** (1998).
41. Lauchle, G.C., A.R. Jones, J.J. Dreyer, and J. Wang, "Flow-Induced Lift Forces on a Towed Sphere," *Proc. Of ASME Noise Control and Acoustics Division ASME 1998, NCA-28*, 103-111 (1998).
42. Brungart, T.A. G.C. Lauchle, S. Deutsch, and E. Riggs, "Outer-Flow Effects on Turbulent Boundary Layer Wall Pressure Fluctuations," *J. Acoust. Soc. Am.* **105** (4) (April 1999).
43. Brungart, T.A., G.C. Lauchle, and R.K. Ramanujam, "Installation Effects of Fan Acoustic and Aerodynamic Performance," *Noise Control Eng. J.* **47** (January/February 1999).

### 4.0 ACTUATOR STUDIES

#### 4.1 Materials : Designs : Reliability

44. Uchino, K., "New Trend in Ceramic Actuators," *Proc. 6<sup>th</sup> Intl. Aerospace Symp. '98*, Nagoya, Japan, p. S1-2, 1-10 (July 14-15, 1998).
45. Uchino, K., "Materials Issues in Design and Performance of Piezoelectric Actuators: An Overview," *Acta. Mater.* **46** (11), 3745-3753 (1998).
46. Yao, K., W. Zhu, K. Uchino, Z. Zhang, and L.C. Lim, "Design and Fabrication of a High Performance Multilayer Piezoelectric Actuator with Bending Deformation."
47. Aburatani, H. and K. Uchino, "Acoustic Emission in Damaged Ferroelectric Lead Zirconate Titanate Ceramics," *Jpn. J. Appl. Phys.* **37**, L553-L555 (1998).
48. Atherton, P.D. and K. Uchino, "New Developments in Piezo Motors and Mechanisms," *Proc. 6<sup>th</sup> Intl. Conf. On New Actuators (Actuator 98)*, Bremen, Germany, p. 164-169 (June 17-19, 1998).
49. Uchino, K. and B. Koc, "Compact Piezoelectric Ultrasonic Motors," *2<sup>nd</sup> Asian Meeting on Ferroelectrics (AMF-2)*, Singapore (December 7-11, 1998).
50. Koc, B., Y. Xu, and K. Uchino, "Ceramic/Metal Composite Piezoelectric Motors," *IEEE Ultrasonic Symposium*, Sendai, Japan (October 1998).
51. Koc, B., Y. Xu, and K. Uchino, "Roto-Linear Ultrasonic Motors," *Proc. 6<sup>th</sup> Intl. Conf. On New Actuators (Actuator 98)*, Bremen, Germany, p. 349-352 (June 17-19, 1998).
52. Koc, B., A. Dogan, Y. Xu, R.E. Newnham, and K. Uchino, "An Ultrasonic Motor Using a Metal-Ceramic Composite Actuator Generating Torsional Displacement," *Jpn. J. Appl. Phys.* **37**, 5659-5662 (1998).

#### 4.2 Photostrictive Actuators

53. Poosanaas, P. and K. Uchino, "Photostrictive Effect in Lanthanum-Modified Lead Zirconate Titanate Ceramics Near The Morphotropic Phase Boundary," *J. Mat. Chem. & Phys.* (October 1998). [submitted]
54. Uchino, K. and P. Poosanaas, "Photostriction in PLZT and Its Applications," *Proc. CIMTEC '98*, Florence, Italy (June 14-19, 1998).

## VOLUME V

### 4.0 ACTUATOR STUDIES

#### 4.3 *Torsional and High Force Actuators* (continued)

55. Glazounov, A.E., Q.M. Zhang, and C. Kim, "Torsional Actuator Based on Mechanically Amplified Shear Piezoelectric Response," *Sensors and Actuators* (1998). [submitted]
56. Frank, J., G.H. Koopmann, W. Chen, and G.A. Lesieutre, "Design and Performance of a High Force Piezoelectric Inchworm Motor."

### 5.0 MODELING and CHARACTERIZATION

#### 5.1 *Finite Element and Other Methods*

57. Qi, W. and W. Cao, "Finite Element and Experimental Study of Composite and 1-D Array Transducers," *SPIE* **3341** (1998).
58. Wang, H., W. Jiang, and W. Cao, "Characterization of Lead Zirconate Titanate Piezoceramic Using High Frequency Ultrasonic Spectroscopy," *J. Appl. Phys.* (1998). [accepted]
59. Zhu, S.N., B. Jiang, and W. Cao, "Characterization of Piezoelectric Materials Using Ultrasonic and Resonant Techniques," *Proceedings of SPIE Imaging '98*, **3341**, 154-162 (1998).
60. Cao, W., "Virtual Design of Medical Transducers," *Proceedings of SPIE Imaging '98*, **3341**, 56-63 (1998).
61. Cao, W., "Elastic Property Characterization in Thin Samples of Sub-Wavelength in Thickness," *Ferroelectrics* **206/207**, 355-363 (1998).
62. Cao, W., S.N. Zhu, and B. Jiang, "Analysis of Shear Modes in A Piezoelectric Resonator," *J. Appl. Phys.* **83**, 4415-4420 (1998).

#### 5.2 *Relaxor Ferroelectrics*

63. Giniewicz, J.R., A.S. Bhalla, and L.E. Cross, "Variable Structural Ordering in Lead Scandium Tantalate-Lead Titanate Materials," *Ferroelectrics* **211**, 281-297 (1998).
64. Pan, X., W.D. Kaplan, M. Rühle, and R.E. Newnham, "Quantitative Comparison of Transmission Electron Microscopy Techniques for the Study of Localized Ordering on a Nanoscale," *J. Am. Ceram. Soc.* **81** (3), 597-605 (1998).
65. Zhao, J., A.E. Glazounov, and Q.M. Zhang, "Change in Electromechanical Properties of 0.9PMN:0.1PT Relaxor Ferroelectric Induced by Uniaxial Compressive Stress Directed Perpendicular to the Electric Field," *Appl. Phys. Ltrs.* **74**, 436 (1999).
66. Zhao, J., V. Mueller, and Q.M. Zhang, "The Influence of the External Stress on the Electromechanical Response of Electrostrictive  $0.9\text{Pb}(\text{Mg}_{1/3}\text{Nb}_{2/3})\text{O}_3$ - $0.1\text{PbTiO}_3$  in the dc Electrical Field Biased State," *J. Mat. Res.* **14**, 3 (1999).

## VOLUME VI

### 5.0 MODELING and CHARACTERIZATION

#### 5.3 *Thin and Thick Thin Films*

67. Maria, J.P., W. Hackenberger, and S. Trolier-McKinstry, "Phase Development and Electrical Property Analysis of Pulsed Laser Deposited  $\text{Pb}(\text{Mg}_{1/3}\text{Nb}_{2/3})\text{O}_3$ - $\text{PbTiO}_3$  (70/30) Epitaxial Films," *J. Appl. Phys.* **84** (9), 5147-5154 (1998).
68. Shepard, J.F., Jr., P.J. Moses, and S. Trolier-McKinstry, "The Wafer Flexure Technique for the Determination of the Transverse Piezoelectric Coefficient ( $d_{31}$ ) of PZT Thin Films," *Sensors and Actuators A* **71**, 133-138 (1998).
69. Zavala, G. J.H. Fendler, and S. Trolier-McKinstry, "Stress Dependent Piezoelectric Properties of Ferroelectric Lead Zirconate Titanate Thin Films by Atomic Force Microscopy," *J. Korean Phys. Soc.* **32**, S1464-S467 (1998).
70. Wasa, K., Y. Haneda, T. Satoh, H. Adachi, I. Kanno, K. Setsune, D.G. Schlom, S. Trolier-McKinstry, C.-B. Eom, "Continuous Single Crystal  $\text{PbTiO}_3$  Thin Films Epitaxially Grown on Miscut (001)  $\text{SrTiO}_3$ ," *J. Korean Phys. Soc.* **32**, S1344-S1348 (1998).
71. Xu, B., Y. Ye, L.E. Cross, J.J. Bernstein, and R. Miller, "Dielectric Hysteresis from Transverse Electric Fields in Lead Zirconate Titanate Thin Films," *Appl. Phys. Ltrs.* (1998). [submitted]
72. Xu, B., N.G. Pai, Q.-M. Wang, and L.E. Cross, "Antiferroelectric Thin and Thick Films for High Strain Microactuators," *Integrated Ferroelectrics* **22**, 545-557 (1998).

#### 5.4 *Domain Studies*

73. Erhart, J. and W. Cao, "Effective Material Properties in Twinned Ferroelectric Crystals," *J. Appl. Phys.* (1999). [submitted]
74. Belegundu, U., M. Pastor, X.H. Du, L.E. Cross, and K. Uchino, "Domain Formation in  $0.90\text{Pb}(\text{Zn}_{1/3}\text{Nb}_{2/3})\text{O}_3$ - $0.10\text{PbTiO}_3$  Single Crystals under Electric Field along [111] Direction," *IEEE '98, Sendai, Japan* (1998).
75. Zhu, S.N. and W. Cao, "Pyroelectric and Piezoelectric Imaging of Ferroelectric Domains in  $\text{LiTaO}_3$  by Scanning Electron Microscopy," *Phys. Status Solidi* (1998). [submitted]
76. Hatch, D.M. and W. Cao., "Determination of Domain and Domain Wall Formation at Ferroic Transitions," *Ferroelectric* (1998). [submitted]
77. Mueller, V. and Q.M. Zhang, "Threshold of Irreversible Domain Wall Motion in Soft PZT-Piezoceramic. *Ferroelectrics* **206/207**, 113-122 (1998).
78. Aburatani, H., J.P. Witham, and K. Uchino, "A Fractal Analysis on Domain Related Electric Field Induced Acoustic Emission in Ferroelectric Ceramics," *Jpn. J. Appl. Phys.* **37**, 602-605 (1998).

### 5.5 Electrostriction

79. Newnham, R.E., V. Sundar, R. Yimnirun, J. Su, and Q.M. Zhang, "Electrostriction in Dielectric Materials," in *Advances in Dielectric Ceramic Materials*, eds. K. Nair and A. Bhalla. Ceramic Trans. **88**, 154-39 (1998).
80. Sundar, V., R. Yimnirun, B.G. Aitken, and R.E. Newnham, "Structure Property Relationships in the Electrostriction Response of Low Dielectric Permittivity Silicate Glasses," Mat. Res. Bull. **33**, 1307-1314 (1998).

## ABSTRACT

This report documents work performed over the period 1 January 1998 to 31 December 1998 on a MURI under the Office of Naval Research Contract N00014-96-1-1173. The topic "Acoustic Transduction Materials and Devices" brings together groups in the Materials Research Laboratory (MRL), the Applied Research Laboratory (ARL), and the Center for Acoustics and Vibrations (CAV) at Penn State.

Research on the program is adequately represented in the 80 technical appendices.

Outstanding accomplishments include:

Exploration of several new relaxor ferroelectric perovskite solid solution with morphotropic phase boundaries. New evidence of the onset of nonlinearity in soft donor doped PZTs at surprisingly low (1V/cm) fields. Confirmation of the relaxor phase induced by electron irradiation in PVDF:TrFE copolymers, and a processing method which permits very high (4%) electrostrictive strain in the transverse direction, vital for the practical use in actuator systems. In composite transducer, "first fruits" of the cooperative program are cymbal arrays which form most effective acoustic projectors, and a new "dog bone" design which permits deeper submergence for the cymbal. Agile transducers, the 3-D acoustic intensity probe and high force high strain torsional and step and repeat systems continue to make excellent progress. In actuator studies true acoustic emission is proving to be an excellent tool in reliability studies and a new design of small-scale (mini) piezoelectric motor shows outstanding performance. Thick thin film studies and are now "gearing up" for the development of the mini tonpilz arrays. New combinations of ultrasonic and resonance methods appear to offer unique capability for complete characterization of ferroelectric piezoelectric materials.

The mode of presentation of the report emphasizes the outstanding progress made in published research. It is important to also document that the slower and more painstaking development of practical transducer systems in the cymbal and mini tonpilz arrays is progressing very favorably.



## INTRODUCTION

This report describes the research performed over the period of 1 January 1998 to 31 December 1998 on an MURI under Office of Naval Research contract N00014-96-1-1173 on the topic "Acoustic Transduction: Materials and Devices." The program began 31 July 1996 and brings together activities in the Materials Research Laboratory (MRL), the Applied Research Laboratory (ARL), and the Center for Acoustic Vibration (CAV) at Penn State. Principal Investigator on the program is Professor Kenji Uchino, Professor of Electrical Engineering at Penn State, and the Program Officer in ONR is Dr. Jan Lindberg.

The overarching program objective is the development of acoustic transduction materials and devices of direct relevance to US Navy needs and with application in commercial sector products. The initial focus was upon high performance sensors and high authority high strain actuators for transducing functions. New materials and improved material systems are being developed on the program, and these carry the need for new device structures, improved drive and control strategies and developing emphasis upon performance and reliability under a wide range of operating conditions.

Responsibility for the program elements are assigned as follows:

MATERIAL STUDIES	A.S. Bhalla
COMPOSITE SYSTEMS	R.E. Newnham
DEVICE STRUCTURES	T.R. Shrout
MODELLING	W. Cao
DEVICE FABRICATION and TESTING	W.J. Hughes
AIR ACOUSTICS and STEP and REPEAT SYSTEMS	G. Lesieutre

Following long established precedent, the report will draw upon published results in the form of appendices which will be interconnected by a very brief narrative summary to highlight the major achievements of the past year's work. For convenience the studies are presented under:

- 1.0 GENERAL SUMMARY PAPERS
- 2.0 MATERIALS STUDIES
  - 2.1 Polycrystal Perovskite Ceramics
  - 2.2 Relaxor Ferroelectric Single Crystal Systems
  - 2.3 New High Strain Polymer Materials
- 3.0 TRANSDUCER STUDIES
  - 3.1 Composite Structures
  - 3.2 Frequency Agile Transducers
  - 3.3 3-D Acoustic Intensity Probes
- 4.0 ACTUATOR STUDIES
  - 4.1 Materials : Designs : Reliability
  - 4.2 Photostrictive Actuators
  - 4.3 New Torsional Amplifier/Actuators
  - 4.4 High Force Amplifiers and Inchworms

## 5.0 MODELING and CHARACTERIZATION

- 5.1 Finite Element and Other Methods
- 5.2 Relaxor Ferroelectrics
- 5.3 Thin and Thick Thin Films
- 5.4 Domain Studies
- 5.5 Electrostriction

## 1.0 GENERAL SUMMARY PAPERS

These papers provide introductory reviews of several of the major topics in the program. The revolutionary change which has been brought about by the new high coupling high strain single crystal perovskite structure ferroelectrics is briefly introduced and the first probable area of application indicated (1). Functional composites introduce the fascinating arena of 'smart' materials and structures and points up some of the analogues to biological systems (2). Resonant piezoelectric motor structures are nicely reviewed, bringing out the salient characteristics of current designs and some of the reliability issues which are receiving much attention (3). The role of solid state phase transformations in all current solid state actuators is properly underlined with examples from piezoelectric, magnetostrictive and shape memory systems (4).

## 2.0 MATERIALS STUDIES

### 2.1 *Polycrystal Perovskite Ceramics*

Papers in this group fall neatly under three categories: Low temperature preparative routes, new polycrystal relaxor solid solutions, and more basic studies of lead zirconate:titanate "commercial" ceramics. In preparation studies PLZT is used as the vehicle to explore hydrothermal and microwave hydrothermal (5) and nanocomposite (6) powder synthesis below 150°C. From these initial studies the final densified sintered product appears to be improved by the nanocomposite method.  $\text{Fe}_2\text{O}_3$  acceptor doping was used in the  $\text{PbSc}_{1/2}\text{Nb}_{1/2}\text{O}_3\text{:PbTiO}_3$  0.57:0.43 composition (7) to improve mechanical quality factor ( $Q_m \cong 297$ ). Lead indium tantalate:lead titanate (8) lead indium niobate:lead titanate (9), and lead magnesium niobate:lead indium niobate (10) are fabricated in phase pure perovskite form and shown to have interesting morphotropic phase boundaries (MPBs) and dielectric, piezoelectric and electrostrictive properties. For the  $\text{Bi}(\text{Ni}_{1/2}\text{Ti}_{1/2})\text{O}_3\text{PbTiO}_3$  solid solution MPB occurs at compositions near 0.4  $\text{PbTiO}_3$  (11), where the poled ceramic shows unusually high hydrostatic piezoelectricity with  $d_h \sim 111$  pC/n and a  $d_{hgh} \cong 1055 \times 10^{-15}$  m<sup>2</sup>/N.

Studies of both soft and hard commercial PZTs have explored the effect of high uniaxial longitudinal and transverse stress (12), the soft PZTs show easy stress depoling, but this may be substantially alleviated by a suitable DC bias field. In the hard PZTs, the local defect fields in well aged samples delay depoling and enhance recovery from transient stresses, but behaviors are now time dependent. The behavior of soft PZT under high sinusoidal AC field drive is discussed in (13). It is suggested that internal stress may contribute substantially to the nonlinearity observed.

Effective  $d_{33}$  and  $k_{33}$  in PZT for directions tilted with respect to the poling direction are explored in (14). Tetragonal phase compositions show only monotonic decay of both  $d_{33}$  and  $k_{33}$  with tilt angle, but in the rhombohedral phase effective  $d_{33}$  has a maximum value at a

tilt angle  $\sim 45^\circ$  with respect to the poling direction. Threshold fields for nonlinearity in soft PZTs are explored in (15) and found to occur at fields  $E_{t1} \cong 100$  V/cm and  $E_{t2} \cong 1$  Volt/cm. Both are characterized by scaling behavior

$$x = x_0 A \left[ \frac{(E + E_c)}{E_c} \right]^\phi$$

where  $x$  is the dielectric or piezoelectric constant. True acoustic emission, as distinct from earlier vibro-acoustic behaviors is studies in (16) and shown to exhibit the expected Kaiser effect.

The Laboratory has major ongoing studies on size effects in ferroelectrics, just the tip of this iceberg is exhibited in (17).

## 2.2 Relaxor Ferroelectric Single Crystal Systems

Paper (18) gives some of the history of the development of the high strain high coupling relaxor MPB single crystals, and a possible explanation for their unique properties. The unusual poling behavior in the rhombohedral phase compositions of PZN:PT is underscored in (19) and the absence of observable wall motion after poling in the 001 oriented field is discussed. For crystals with composition PZN:PT 0.9:0.1 very close to the MPB (20), polarizing microscope studies delineate the tetragonal:rhombohedral phase change and the co-existence of both phases down to  $-100^\circ\text{C}$ . The importance of intrinsic single domain properties in these systems is highlighted by calculations from the phenomenological model for PZT (21) which show strong enhancement to effective  $d_{33}$  for orientations tilted away from the polar axis in the rhombohedral domains at compositions close to the MPB. Templated grain growth is used in (22) to develop "poorman's" single crystals of  $\text{Ba}(\text{Zr}_x\text{Ti}_{1-x})\text{O}_3$  which show most interesting high piezoelectric constants. This looks to be a most interesting route for further studies. For  $\text{BaTiO}_3$  single crystals (23) agreement between measured and calculated permittivity and effective piezoelectric  $d_{33}$  again confirm the dominant intrinsic contribution of the domain itself to these properties. Important evidence of the atomistic origin of the fluctuations in the relaxor tungsten bronze lead barium niobate can be adduced from the very large anisotropic thermal coefficients for the  $\text{Pb}^{2+}$  and  $\text{Ba}^{2+}$  cations on the A2 site in this crystal structure (24).

## 2.3 High Strain Polymer Electrostrictors

The group of papers (25-29) by Q. Zhang and co-workers confirm that in PVDF:TrFE copolymers in the composition range 50:50 to 65:35 VDF:TrFE high energy electron irradiation can convert the polymer from a conventional to a relaxor ferroelectric. Relaxor response is confirmed by dielectric dispersion with Vogel:Fulcher type response, but more importantly very high strain (4%) electrostriction and strong field induced piezoelectricity  $k_{33} \sim 33\%$  are also induced. With suitable treatment high strain high coupling

behavior can be induced for both longitudinal and transverse effects. A new bimorph based measuring device (29) is introduced which permits characterization over a wide strain range with minimal constraint of the soft polymer

### 3.0 TRANSDUCER STUDIES

#### 3.1 *Composite Structures*

Boundary conditions on underwater transducers are spelled out in an effective introduction (30). Application of the cymbal flextensional transducer in an array for shallow water sound projection is discussed in (31) and response comparable to the more widely used tonpilz transducer demonstrated. To increase pressure tolerance a concave cymbal which mimics the Navy "dog bone" design has been explored (32). Pressures up to 6 MPa are tolerated while maintaining high hydrostatic response. Sensing response of a simple cantilever mounted piezoelectric bimorph bender is discussed in (33). Detailed discussion of the cymbal is given in (34) including consideration of the parameters which control performance and which can be controlled to minimize thermal displacements. A new type of pseudo-shear multilayer actuator is considered in (35) which permits very large angular and linear displacements at low frequency and modest drive field. A more detailed analysis of the resonant modes in 1-3 type polymer ceramic composites is given in (36) which underscores the unexpected importance of the quality factor of the ceramic in these composites.

#### 3.2 *Frequency Agile Transducers*

The basic principle of a compressive axial or radial loading to improve the coupling coefficient and change the resonant frequency of a bending mode beam or disk shaped transducer is confirmed in (37). Changes up to 36% in frequency and 38% in coupling coefficient were demonstrated. The potential importance and applicability of a tunable piezoelectric vibration absorber is discussed in (38) and demonstrated for a capacitatively tuned piezoelectric element. In comparison to passive damping a maximum 20 dB improvement in vibration reduction across the tuning range is accomplished. Active broadband force isolation using a flexural piezoelectric inertial actuator is discussed in (39). From model studies an actuator providing minimum 0.03 N/V between 25 and 400 Hz was designed and built. The system under control provided 6 dB reduction in vibration to a rigid base at frequencies between 20 and 90 Hz.

#### 3.3 *3-D Acoustic Intensity Probes*

The papers (40-41) discuss flow induced lift forces on a towed sphere. For the range of flow conditions studied the unsteady lift forces are proportional to the product of an area and the dynamic pressure of the flow. Computed spectra were found to agree very well with measured effects. In paper (42) outer flow effects on turbulent boundary layer wall pressure fluctuations were studied in a moving wall wind tunnel facility developed for the work. Experimental data suggest that even over the range of frequencies dominated by outer-flow turbulence structure wall pressure fluctuations are insensitive to the details of the outer flow.

In an elegant study of noise from the fan in an upright vacuum cleaner it was demonstrated (43) that as much as 25 dB reduction in blade rate and harmonic noise could be

obtained at little extra cost by eliminating same flow obstructions, which also gives much improved motor cooling.

#### 4.0 ACTUATOR STUDIES

##### 4.1 *Materials : Designs : Motor Systems*

Current trends in ceramic actuators are enumerated in (44) where the driving applications are identified in precise positioning, miniature motors, and adaptive mechanical damping. Materials issues are nicely covered in (45) which identified ceramic problems, coupling to the device structure, and drive control as important inter-related issues. A new type of multilayer bending mode actuator is discussed in (46) using a transverse flexural mode to generate higher displacement, and blocking force at higher frequency. In (47) proper acoustic emission is shown to be a useful indicator of damage in poled piezoelectric actuators.

Papers (48-52) deal primary with piezoelectric motors. Paper (48) summarizes current motor developments and actuator needs. The more compact motors using both standing and traveling wave techniques are summarized in (49). A very interesting "windmill" design from the Penn State Group is summarized in (50). More details of the design are given in (51). Rotary characteristics of this motor are 1.2 mNm starting torque in both forward and reverse directions at a drive voltage level of 20 volts rms. Further development using a ball bearing support for an 11 mm diameter "windmill" type motor is discussed in (52). Maximum torque for this motor is 1.36 mNm at 480 rpm.

##### 4.2 *Photostrictive Actuation*

Photostriction which is the superposition of photovoltaic and piezoelectric responses in piezoelectric ceramics are of interest for special actuator devices. The phenomenon in PLZT as a function of composition at Zr:Ti ratios close to the MPB are discussed in (53) for WO<sub>3</sub> modified PLZT ceramics. More detail of the types of device structure envisioned are covered in (54) which explores photo driven relays and walking devices.

##### 4.3 *Torsional and High Force Actuators*

An interesting type of tubular actuator constructed from longitudinally poled PZT segments is discussed in (55). The design is one of the very few which provide amplified motion without loss of torque and looks most promising for compact actuation and in resonance for small compact motor structures.

The inchworm is one of the few piezoelectrically driven systems which can develop large displacement under submicron positioning control. The design described in (56) uses multilayer actuators for both displacement and clamping, resulting in high actuating force (150 N), and large holding force (350 N) but also retaining all the other advantages of the inchworm concept.

#### 5.0 MODELING and CHARACTERIZATION STUDIES

##### 5.1 *Finite Element and Modeling Methods*

Combined finite element and experimental methods have been used to calculate and observe the beam patterns generated by 1-D transducer arrays (57). For the study reported in

(58) high frequency ultrasonic spectroscopy in water has been used to characterize the phase velocity and attenuation in soft PZT-5H (59) in the frequency range 20-60 MHz. Resonant frequency techniques are frequently difficult to apply to piezoceramics because of sample to sample variability. In (60) it is shown that a combination of ultrasonic and longitudinal resonance methods can be used to give a complete characterization of crystals in 4 mm and 3 mm symmetry. The possibilities of computer simulated design of transducing structures is discussed in (61) and shown to offer efficient and economical methods to check out design parameters before more expansive fabrications are attempted. Traditionally ultrasound methods have only been used for the precise measurement of elastic parameters in solids where linear dimensions are large compared to wavelength  $\lambda$  for the frequency used. In a new approach (61) it is demonstrated that ultrasonic methods can be applied for precise measurement on samples as thin as 5% of  $\lambda$ . In (62) it is shown that two types of shear motion may be associated with the same shear strain and formulae for calculating  $k_{15}$  from resonance and antiresonance frequencies are given for each type.

### 5.2 *Relaxor Ferroelectrics*

Order:disorder and its effect upon relaxor behavior has been explored for the Sc:Ta cations in the PST:PT solid solutions over the composition range to 0.075 lead titanate (63). Highly ordered annealed samples in this composition range exhibit near normal first order ferroelectric transition in contrast to the classical relaxor behavior in the disordered composition. In (64) high resolution transmission electron microscopy (HRTEM) combined with image processing is shown to be a suitable technique to provide quantitative measurement of local ordering in PMN type systems. The effects of uniaxial compressive stress applied perpendicular to the probing electric field in PMN:PT is shown to induce strong symmetry breaking between  $d_{32}$  and  $d_{31}$  in the field biased condition at temperatures around  $T_m$  (65) from which it is possible to deduce the size of the polar micro regions. The influence of uniaxial elastic stress applied along the field direction of PMN:PT 0.9:0.1 is studied in (66) and shown to reduce both dielectric constant and polarization levels, however induction of the macro-polar state under high DC field can result in enhanced hydrostatic piezoelectric response.

### 5.3 *Thin and Thick Thin Films*

Pulsed laser techniques were used in (67) to deposit single crystal PMN:PT films on  $\text{SrRuO}_3$  conductive oxide films on  $\text{LaAlO}_3$  single crystal substrates. High temperature and high oxygen/ozone pressures were however needed to produce stoichiometric perovskite structure films where dielectric permittivity and remanent polarization were similar to bulk compositions. In (68) a new flexure technique is discussed which permits determination of the transverse piezoelectric coefficient  $d_{31}$  for PZT and similar piezoelectric ferroelectric thin films. Atomic force microscopy was used in (69) to explore the stress dependence of piezoelectric response on a nanometer scale and to further confirm the minor role played by ferroelastic domain wall motion in these responses. Continuous  $\text{PbTiO}_3$  films were grown on  $\text{SrTiO}_3$  1.7° canted substrates by rf magnetron sputtering (70) and shown to have extremely flat surfaces on an atomic scale. PZT thick thin films grown over a  $\text{ZrO}_2$  films on silicon

substrates by sol-gel methods (71) are shown to exhibit excellent symmetrical ferroelectric hysteresis under transverse field generated by interdigitated surface electrodes. These structures have interesting application in diaphragm type pressure sensors. Both square and slanted loop double hysteresis can be controlled in antiferroelectric PSnZT films by suitable trivalent doping (72) and form interesting high strain digital actuators.

#### 5.4 Domain Studies

A new treatment of domain structures in finite size crystals suggests that all variants are not equally represented and that a particular set may be favored under some boundary conditions (73). For two domain twin sets global symmetry and material properties are derived and the numerical results presented for  $\text{LiNbO}_3$  and  $\text{BaTiO}_3$ . Domain switching in 0.9 PZN: 0.1PT has been observed for 111 oriented E fields. The structures are compared in (74) with those observed at constant temperature and varying PT content. Domain contrast in SEM on polished  $\text{LiTaO}_3$  surfaces without metal coating is observed in (75) and attributed to pyroelectric and piezoelectric effects. A general procedure to model and predict domain wall formation for the  $\text{Pm } \bar{3}m - I4/mmm$  structural phase transition is given in (76) using a group theoretical approach and Landau-Ginsburg continuum theory. The dependence of wall profile on different Landau expansion coefficients in the free energy is demonstrated. Two different thresholds for nonlinear behavior under 100 Hz AC fields are demonstrated in soft PZTs (77) and attributed to the depinning of walls rather than anharmonicity of the wall energy. Domain related true acoustic emission is observed in Ferroelectric Ceramics (78). The fractal dimension differs for domain wall and true piezoelectric deformation.

#### 5.5 Electrostriction

Electrostriction is the basic electromechanical coupling in all insulators. Polarization related coefficients  $Q_{ijkl}$  are shown to range from  $\sim 10^{-3} \text{ m}^4/\text{C}^2$  in relaxor ferroelectrics to  $\sim 10^3 \text{ m}^4/\text{C}^2$  in some soft polymers (79) and have become accessible for the first time, to precise measurement by ultradilatometry and AC compressometer techniques.

Electrostriction in alkali alumino silicate glasses, and in pure silica have been measured (80) to explore the role played by alkali ions and by the silicate framework structure. The dispersion in the response of the alkali alumino silicate is also reflected in the frequency dependence of  $Q_{11}$  for those glasses.



## 6.0 GRADUATE STUDENTS IN THE PROGRAM

Student	Advisor	Student	Advisor
E. Alberta	A.S. Bhalla	C. Hebert (Graduated Aug. 1998)	G.A. Lesieutre
J. Bernard	G.A. Lesieutre	J.A. McConnell	G.C. Lauchle
J. Wang	G.C. Lauchle	K.J. Bastyr (MS, Fall 1998)	G.C. Lauchle
K. Kang	G.C. Lauchle	K. Majahan (MSEE, Fall 1998)	R. Tutwiler
S. Madhavan	R. Tutwiler	R. Dave	R. Tutwiler
P. Bednarchik	W.J. Hughes	D. VanTol	W.J. Hughes
L. Wang	R.J. Davis	J.D. Zhong	R.E. Newnham
B. Yi	Q. Zhang	Y.H. Chen	K. Uchino
B. Koc	K. Uchino		

## 7.0 HONORS and AWARDS

### R.E. Newnham

Alcoa Corporation Award, Pittsburgh, 1998  
 Alumni Achievement Award Ceramics:Penn State, 1998  
 Kriedl Lecture, New Mexico, MRS  
 Maddin Lecture, University of Pennsylvania  
 National Academy of Engineering Lecture, 1998

### A.S. Bhalla

Trustee of Am Ceram. Soc., 1999  
 Editor, Ferroelectrics Review, 1998

### G. Lauchle

Elected to Board of Directors of Institute of Noise Control Engineers, 1998  
 Appointed Chair Propagation and Sources Technical Committee of Institute of Noise Control Engineers, 1998

### Ruyan Guo

Elected Secretary of Electronics Division of ACerS, 1998

## 8.0 PAPERS PUBLISHED IN REFEREED JOURNALS

1. Meng, J.F., Z-Y. Cheng, B.K. Rai, R.S. Katiyar, E. Alberta, R. Guo, and A.S. Bhalla, "Photoluminescence in  $\text{PbMg}_{1/3}\text{Nb}_{2/3}\text{O}_3$ - $\text{PbIn}_{1/2}\text{Nb}_{1/2}\text{O}_3$  Systems," J. Mater. Res., **13** (7), 1861-1864 (1998)
2. Alberta, E.F. and A.S. Bhalla, "High Strain and Low Mechanical Quality Factor Piezoelectric  $\text{Pb}[(\text{Sc}_{1/2}\text{Nb}_{1/2})_{0.575}\text{Ti}_{0.425}\text{O}_3]$ ," Materials Letters **35**, 199-201 (1998).
3. Guo, R., H.T. Evans, Jr., and A.S. Bhalla, "Crystal Structure Analysis and Polarization Mechanisms of Ferroelectric Tetragonal Tungsten Bronze Lead Barium Niobate," Ferroelectrics **206-207**, 123-132 (1998).
4. Giniewicz, J.R., A.S. Bhalla, and L.E. Cross, "Variable Structural Ordering in Lead Scandium Tantalate-Lead Titanate Materials." Ferroelectrics **211**, 281-297 (1998).
5. Kugel, V.D. and L.E. Cross, "Behavior of Soft Piezoelectric Ceramics under High Sinusoidal Electric Fields," Journal of Applied Physics **84** (5), 2815-2830 (1998).



6. Kundu, T.K., M. Mukherjee, D. Chakravorty, and L.E. Cross, "Dielectric Behavior of Nanocomposites of Lead Sulphide and Ferroelectric Glass Ceramics," *Journal of Applied Physics* **83** (8), 4380-4384 (1998).
7. Levy, M., R.M. Osgood, Jr., R. Liu, L.E. Cross, G.S. Cargill III, A. Kumar, and H. Bakhru, "Fabrication of Single-Crystal Lithium Niobate Films by Crystal Ion Slicing," *Applied Physics Letters* **73** (16), 2293-2295 (1998).
8. Wang, Q.M. and L.E. Cross, "A Piezoelectric Pseudoshear Multilayer Actuator," *Applied Physics Letters* **72** (18), 2238-2240 (1998).
9. Wang, Q. and L.E. Cross, "Determination of Young's Modulus of the Reduced Layer of a Piezoelectric Rainbow Actuator," *Journal of Applied Physics* **83** (10), 5358-5363 (1998).
10. Wang, Q.M. and L.E. Cross, "Tip Deflection and Blocking Force of Soft PZT-Based Cantilever RAINBOW Actuators," *J. Am. Ceram. Soc.* **82** (10), 103-110 (1998).
11. Wang, Q.M., X.-H. Du, B. Xu, and L.E. Cross, "Theoretical Analysis of the Sensor Effect of Cantilever Piezoelectric Benders," *J. of Appl. Physics* **85** (3), 1702-1712 (1998).
12. Xu, B., P. Moses, N.G. Pai, and L.E. Cross, "Charge Release of Lanthanum-Doped Lead Zirconate Titanate Stannate Antiferroelectric Thin Films," *Applied Physics Letters* **72** (5), 593-595 (1998).
13. Xu, B., N.G. Pai, and L.E. Cross, "Lanthanum Doped Lead Zirconate Titanate Stannate Antiferroelectric Thin Films from Acetic Acid-based Sol-Gel Method," *Materials Letters* **34**, 157-160 (1998).
14. Xu, B., N.G. Pai, Q.-M. Wang, and L.E. Cross, "Antiferroelectric Thin And Thick Films for High-Strain Microactuators," *Integrated Ferroelectrics* **22**, 545-557 (1998).
15. Aburatani, H. and K. Uchino, "A Study of Acoustic Emission in Piezoelectric Multilayer Ceramic Actuator," *Jpn. J. Appl. Phys.* **37** (Pt. 1, No. 1), 204-209 (1998).
16. Aburatani, H., J. P. Witham, and K. Uchino, "A Fractal Analysis on Domain Related Electric Field Induced Acoustic Emission in Ferroelectric Ceramics," *Jpn. J. Appl. Phys.* **37** (Pt. 1, No. 2), 602-605 (1998).
17. Kim, J. S. and K. Uchino, "Piezoelectric Ultrasonic Motors," *Bull. Korean Inst. Electrical and Electronic Mater. Eng.*, **11** [2], 149-152 (1998).
18. Yoon, S. J. and K. Uchino, "High Power Characteristics of  $\text{Pb}(\text{Y}_{2/3}\text{W}_{1/3})\text{O}_3$ - $\text{Pb}(\text{Zr,Ti})\text{O}_3$  Ceramics," *J. Korean Inst. Electrical and Electronic Mater. Eng.* **11** [5], 394-399 (1998).
19. Kim, J. S., Y. H. Chen, and K. Uchino, "Dielectric and Piezoelectric Properties of  $\text{Fe}_2\text{O}_3$ -Doped 0.57PSN-0.43PT Ceramics," *J. Korean Phys. Soc.* **32** [2], S1248-1250 (1998).
20. Du, X. H., J. Zheng, U. Belegundu, and K. Uchino, "Crystal Orientation Dependence of Piezoelectric Properties of Lead Zirconate Titanate Near the Morphotropic Phase Boundary," *J. Appl. Phys. Letters* **72** (19), 2421-2423 (1998).
21. Uchino, K., J. Zheng, A. Joshi, Y. H. Chen, S. Yoshikawa, S. Hirose, S. Takahashi, and J. W. D. de Vries, "High Power Characterization of Piezoelectric Materials," *J. Electroceramics* **2**, 33-40 (1998).
22. Uchino, K., "High Electromechanical Coupling Piezoelectrics: Relaxor and Normal Ferroelectric Solid Solutions," *Solid State Ionics* **108**, 43-52 (1998).

23. Uchino, K., "Piezoelectric Ultrasonic Motors: Overview," *Smart Mater. Struct.* **7**, 273-285 (1998).
24. Poosanaas, P., A. Dogan, S. Thakoor, and K. Uchino, "Influence of Sample Thickness on the Performance of Photostrictive Ceramics," *J. Appl. Phys.* **84** [3], 1508-1512 (1998).
25. Fernandez, J.F., A. Dogan, J.T. Fielding, K. Uchino, and R.E. Newnham, "Tailoring the Performance of Ceramic-Metal Piezocomposite Actuators, 'Cymbals'," *Sensors and Actuators A* **65**, 228-237 (1998).
26. Uchino, K., "Materials Issues in Design and Performance of Piezoelectric Actuators: An Overview," *Acta Mater.* **46** [11], 3745-3753 (1998).
27. Koc, B., A. Dogan, Y. Xu, R.E. Newnham, and K. Uchino, "An Ultrasonic Motor Using a Metal-Ceramic Composite Actuator Generating Torsional Displacement," *Jpn. J. Appl. Phys.* **37**, 5659-5662 (1998).
28. Uchino, K., "Piezoelectric Devices for Medical Ultrasonic Scanning," *J. Advanced Medicine* **5**, 38-40 (1998).
29. Kim, J.S. and K. Uchino, "Piezoelectric Actuators and Ultrasonic Motors," *Bull. Korean Inst. Electr. and Electron. Mater. Engr.* **11** (2), 149-152 (1998).
30. Aburatani, H. and K. Uchino, "Acoustic Emission in Damaged Ferroelectric Lead Zirconate Titanate Ceramics," *Jpn. J. Appl. Phys.* **37**, L553-L555 (1998).
31. Kugel, V.D., B. Xu, Q.M. Zhang, and L.E. Cross, "Bimorph-Based Piezoelectric Air Acoustic Transducer: Model. Sensors and Actuators," *A69*, 234 (1998).
32. Mueller, V. and Q.M. Zhang, "Threshold of Irreversible Domain Wall Motion in Soft PZT-Piezoceramic," *Ferroelectrics* **206/207**, 113 (1998).
33. Su, J., P. Moses, and Q.M. Zhang, "A Piezoelectric Bimorph Based Dilatometer for Field Induced Strain Measurement in Soft and Thin Free Standing Polymer Films," *Rev. Sci. Instruments* **69**, 2480 (1998).
34. Mueller, V. and Q.M. Zhang, "Nonlinearity and Scaling Behavior in Donor Doped Lead Zirconate Titanate Piezoceramic," *Appl. Phys. Lett.* **72**, 2692 (1998).
35. Zhao, X., V. Bharti, Q.M. Zhang, T. Ramotowski, F. Tito, and R. Ting, "Electromechanical Properties of Electrostrictive P(VDF-TrFE) Copolymer," *Appl. Phys. Lett.* **73**, 2054 (1998).
36. Bharti, V., X. Zhao, Q.M. Zhang, T. Ramotowski, F. Tito, and R. Ting, "The Field Induced Strain and Polarization Response in Electron Irradiated Poly(vinylidene Fluoride -trifluoroethylene) Copolymer," *J. Mater. Res. Innovations* **2** (2), 57-63(1998).
37. Zhao, J., A.E. Glazounov, and Q.M. Zhang, "Change in Electromechanical Properties of 0.9PMN-0.1PT Relaxor Ferroelectric Induced by Uniaxial Compressive Stress Directed Perpendicular to the Electric Field. *Appl. Phys. Lett.* **74**, 436 (1999).
38. Geng, X. and Q.M. Zhang, "Resonance Modes and Losses in 1-3 Composites for Ultrasonic Transducer Applications," *J. Appl. Phys.* **85**, 1342 (1999).
39. Cao, W., S.N. Zhu, and B. Jiang, "Analysis of Shear Modes in a Piezoelectric Resonator," *J. Appl. Phys.* **83**, 4415-4420 (1998).
40. Cao, W., "Elastic Property Characterization in Thin Samples of Sub-Wavelength in Thickness," *Ferroelectrics* **206**, 355-363 (1998).

41. Shepard Jr., J.F., F. Chu, I. Kanno, and S. Trolier-McKinstry, "Characterization and Aging Response of the  $d_{31}$  Piezoelectric Coefficient of Lead Zirconate Titanate Thin Films," to appear in J. Appl. Phys. **85** (9) (1999).
42. Maria, J.P., W. Hackenberger, S. Trolier-McKinstry, "Phase Development and Electrical Property Analysis of Pulsed Laser Deposited  $\text{Pb}(\text{Mg}_{1/3}\text{Nb}_{2/3})\text{O}_3\text{-PbTiO}_3$  (70/30) Epitaxial Films," J. Appl. Phys. **84** (9) 5147-5154 (1998).
43. Shepard, Jr., J.F., P.J. Moses, and S. Trolier-McKinstry, "The Wafer Flexure Technique for the Determination of the Transverse Piezoelectric Coefficient ( $d_{31}$ ) of PZT Thin Films," Sens. Actuators A **71**, 133-138 (1998).
44. Wasa, K., Y. Haneda, T. Satoh, H. Adachi, I. Kanno, K. Setsune, D. G. Schlom, S. Trolier-McKinstry, and C. B. Eom, "Continuous Single Crystal  $\text{PbTiO}_3$  Thin Films Epitaxially Grown on Miscal (001)  $\text{SrTiO}_3$ ," J. Korean Phys. Soc. **32**, S1344-S1348 part 4, Supplement (1998).
45. Zavala, G., J.H. Fendler, and S. Trolier-McKinstry, "Stress Dependent Piezoelectric Properties of Ferroelectric Lead Zirconate Titanate Thin Films by Atomic Force Microscopy," J. Korean Phys. Soc. **32**, S1464-S1367 part 4, Supplement (1998).
46. Maria, J.P., S. Trolier-McKinstry, D.G. Schlom, M.E. Hawley, and G.W. Brown, "The Influence of Energetic Bombardment on the Structure and Properties of Epitaxial  $\text{SrRuO}_3$  Thin Films Grown by Pulsed Laser Deposition," J. Appl. Phys. **83** (8) 4373-4379 (1998).
47. Cross, L.E. and S. Trolier-McKinstry, "Ferroelectrics," 276-289 in *Era of Materials*, edited by S. K. Mujumdar, R. E. Tressler, and E. W. Miller, The Pennsylvania Academy of Science, Easton, PA (1998).
48. Newnham, R.E., "Functional Composites for Sensors and Actuators," Chapter in *The Era of Materials*, edited by S. Majumdar, R. Tressler, and E. Miller, 259-275, Pennsylvania Academy of Science (1998).
49. Newnham, R.E. and S. Trolier-McKinstry, "Size Effects in Ferroics, Integrated Ferroelectrics," Integrated Ferroelectrics **20**: 1-13 Gordon and Breach Science Publishers (March 1998).
50. Pan, X., D. Kaplan, M. Rühle, and R.E. Newnham, "A Quantitative Comparison of TEM Techniques for the Study of Localized Ordering on a Nano-Scale," J. Am. Ceram. Soc. **81** (3), 597-605 (March 1998).
51. Hladky-Hennion, A.C., A. Dogan, and R.E. Newnham, "Finite Element Modeling of Transduction Materials with Application to Cymbal Actuators and Sensors, Proceedings 1998 Actuators Meeting.
52. McNeal, M.P., S.-J. Jang, and R.E. Newnham, "The Effect of Grain and Particle Size on the Microwave Properties of Barium Titanate," J. Appl. Phys. **83** (6) (1998).
53. Tressler, J.F., S. Alkoy, A. Dogan, and R.E. Newnham, "Functional Composites for Sensors, Actuators, and Transducers," Proceedings of the 6<sup>th</sup> Intl. Symp. on Ceramic Materials & Components for Engines, 79-84, Arita, Japan (October 1998).
54. McCauley, D., R.E. Newnham, and C.A. Randall, "Intrinsic Size Effects in a Barium Titanate Glass-Ceramic," J. Am. Ceram. Soc. **81** (4), 979-87 (1998).
55. Fernandez, J.F., A. Dogan, J.T. Fielding, K. Uchino, and R.E. Newnham, "Tailoring the Performance of Ceramic-Metal Piezocomposite Actuators, 'Cymbals'," Sensors and Actuators A Physics **65**, 228-237 (1998).

56. Newnham, R.E., "Composite Sensors and Actuators" in *Mathematics of Multiscale Materials*, edited by G. Milton, K. Golden, G. Grimmett, R.D. James, G.W. Milton, and P.N. Sen, Springer-Verlag, NY, pp. 209-211 (1998).
57. Tressler, J.F., W. Cao, K. Uchino, and R.E. Newnham, "Finite Element Analysis of the Cymbal-Type Transducer," IEEE Trans. UFFC **45**, 1363-1369 (1998).
58. Sundar, V., R. Yimnirun, B.G. Aitken, and R.E. Newnham, "Structure Property Relationships in the Electrostriction Response of Low Dielectric Permittivity Silicate Glasses," Mat. Res. Bull. **33**, 1307-1314 (1998).
59. Newnham, R.E., "Phase Transformations in Smart Materials," Acta Cryst. A **54**, 729 (1998).
60. Lauchle, G.C., A.R. Jones, J.J. Dreyer, and J. Wang, "Flow-Induced Lift Forces on a Towed Sphere," Proc. Of the ASME Noise Control and Acoustics Division ASME 1998, NCA-Vol. 25, pp. 103-111 (1998).
61. Lauchle, G.C. and A.R. Jones, "Unsteady Lift Force on a Towed Sphere," J. Fluids and Structures **112** (1998).
62. Davis, C.L. and G.A. Lesieutre, "An Actively Tuned Solid State Vibration Absorber Using Capacitive Shunting of Piezoelectric Stiffness," J. Sound & Vibration (1998). [accepted]

#### 9.0. PAPERS SUBMITTED FOR PUBLICATIONS

1. Shepard Jr., J.F., S. Trolier-McKinstry, and J.-P. Maria, "The Effects of Applied Biaxial Stress on the Low and High-Field Characteristics of Thin Film PZT," J. Mat. Res. (1998). [submitted]
2. Xu, F., F. Chu, and S. Trolier-McKinstry, "Longitudinal Piezoelectric Coefficient Measurement for Bulk Ceramics and Thin Films Using Pneumatic Pressure Rig," J. Appl. Phys. (1998). [submitted]
3. Maria, J.P., H.L. McKinstry, and S. Trolier-McKinstry, "The Origin of Preferential Orthorhombic Twinning in SrRuO<sub>3</sub> Epitaxial Thin Films," Applied Physics Letters (1998). [submitted]
4. Maria, J.P., J. F. Shepard Jr., S. Trolier-McKinstry, T.R. Watkins and A.E. Payzant, "Piezoelectric Analysis of Pb(Mg<sub>1/3</sub>Nb<sub>2/3</sub>)O<sub>3</sub>-PbTiO<sub>3</sub> Epitaxial Thin Films," Journal of Applied Physics (1998). [submitted]
5. Rehrig, P.W., S.-E. Park, S. Trolier-McKinstry, G.L. Messing, B. Jones, T.R. Shrout, "Piezoelectric Properties of Zirconium-Doped Barium Titanate Single Crystals Grown by Templated Grain Growth," J. Appl. Phys. (1998). [submitted]
6. Zhao, J., V. Mueller, and Q.M. Zhang, "The Influence of External Stress on the Electromechanical Response of Electrostrictive 0.9PMN-0.1PT in the DC Field Biased State," J. Mater. Res. (1999). [in print]
7. Mueller, V., H. Geige, and Q.M. Zhang, "Nonlinear Ferroelectric Domain Wall Response," Ferroelectrics (1999). [in print]
8. Liu, R., Q. Wang, Q.M. Zhang, and L.E. Cross, "Piezoelectric Pseudo-Shear Universal Actuator Made by L-Shape Joint Bonding," J. Mat. Sci: Mat. in Electro. (1999). [in print]

9. Liu, R., Q.M. Zhang, and L.E. Cross, "Experimental Investigation of Field Induced Direct Piezoelectric Properties in Polyurethane Elastomer Under Quasistatic Condition," *J. Appl. Polym. Sci.* (1999). [in print]
10. Cheng, Z.-Y., S. Gross, J. Su, and Q.M. Zhang, "Pressure-Temperature Phase Diagram for A Polyurethane Elastomer," *J. Polym. Sci.* (1999). [in print]
11. Cheng, Z.-Y., T.-B. Xu, V. Bharti, S. Wang, and Q.M. Zhang, "Transverse Strain Response in the Electrostrictive P(VDF-TrFE) Copolymer," *Appl. Phys. Lett.* (1999). [in print]
12. Cheng, Z.-Y., S.J. Gross, J. Su, and Q.M. Zhang, "The Converse Electrostrictive Effect and the Pressure Dependence of Dielectric Response of Amorphous Polymers," *J. Appl. Phys.* (1998). [submitted]
13. Glazounov, A.E., Q.M. Zhang, and C. Kim, "Torsional Actuator Based on Mechanically Amplified Shear Piezoelectric Response," *Sensors and Actuators* (1998). [submitted]
14. Bharti, V., G. Shanthi, H. Xu, Q.M. Zhang, and K. Liang, "Evolution of Transitional Behavior and Structure of Electron Irradiated P(VDF-TrFE) Copolymer Films," *Appl. Phys. Lett.* (1999). [submitted]
15. Wang, Q.-M., Q.M. Zhang, B. Xu, R. Liu, and L.E. Cross, "Nonlinear Piezoelectric Behavior of Ceramic Bending Mode Actuators Under Strong Electric Fields," *J. Appl. Phys.* (1998). [submitted]
16. Zhang, Q.M. and J. Zhao, "Electromechanical Responses of Lead Zirconate Titanate Piezoceramics under the Influence of Mechanical Stresses," *IEEE UFFC* (1999). [submitted]
17. Cheng, Z.-Y., V. Bharti, T.B. Xu, S. Wang, Q.M. Zhang, T. Ramotowski, F. Tito, and R. Ting, "Transverse Strain Responses in Electrostrictive P(VDF-TrFE) Films and Development of a Dilatometer for the Measurement," *J. Appl. Phys.* (1999). [submitted]
18. Xu, H.-S., Z.-Y. Cheng, Q.M. Zhang, P.-C. Wang, and A. MacDiarmid, "Conduction Behavior of Doped Polyaniline Film at High Current Density and the Effect of High Energy Electron Irradiation on It," *J. Poly. Sci.* (1999). [submitted]
19. Xu, H.-S., Z.-Y. Cheng, V. Bharti, S. Wang, and Q.M. Zhang, "All-Polymer Electromechanical Systems Consisting of Electrostrictive Poly(vinylidene fluoride-trifluoroethylene) and Conductive Polyaniline," *J. Appl. Poly. Sci.* (1999). [submitted]
20. Bastyr, K.J., G.C. Lauchle, and J.A. McConnell, "A Velocity Gradient Underwater Acoustic Intensity Sensor," *J. Acoust. Soc. Am.* (February 1999). [submitted]
21. McGuinn, R.S., G.C. Lauchle, and D.C. Swanson, "Low Flow-Noise Pressure Measurements Using a 'Hot-Mic'," *J. Acoust. Soc. Am.* (April 1998). [submitted]
22. Brungart, T.A., G.C. Lauchle, S. Deutsch, and E. Riggs, "Outer Flow Modifications on Turbulent Boundary Layer Wall Pressure Fluctuations," *J. Acoust. Soc. Am.* **105** (April 1999).
23. Brungart, T.A., G.C. Lauchle, S. Deutsch, and E. Riggs., "Wall Pressure Fluctuations Induced by Non-Equilibrium Turbulent Boundary Layer Flow," *J. Sound and Vib.* (December 1998). [submitted]

24. Brungart, T.A., G.C. Lauchle, and R.K. Ramanujam, "Installation Effects on Fan Acoustic and Aerodynamic Performance," *Noise Control Eng. J.* 47 (January/February 1999).
25. Brungart, T.A., G.C. Lauchle, S. Deutsch, and E. Riggs, "Effect of a Moving Wall Boundary Conditions on a Fully-Developed, Equilibrium Turbulent Boundary Layer," *Phys. Fluids* (February 1998). [submitted]
26. Bernard, J., G.A. Lesieutre, and G.H. Koopmann, "Active Broadband Force Isolation using a Flexural Piezoelectric Inertial Actuator," *J. Sound and Vibration* (1999). [submitted]
27. Meng, J.F., R. Katiyar, E. Alberta, R. Guo and A.S. Bhalla, "Optical and Raman Spectroscopic Studies of PIN-PST Solid Solutions," *Ferroelectrics* (1998). [accepted]
28. Alberta, E.F. and A.S. Bhalla, "Dielectric and Piezoelectric Properties of the  $\text{Pb}(\text{In}_{1/2}\text{Ta}_{1/2})\text{O}_3$  -  $\text{PbTiO}_3$  Solid Solution System," *Proceedings of the 10th Annual International Symposium on the Applications of Ferroelectric* (1998). [accepted]
29. Alberta, E.F. and A.S. Bhalla, "Investigation of The Lead Indium Niobate-Lead Magnesium Niobate Solid Solution System," *Materials Letters* (1998). [accepted]
30. Alberta, E.F. and A.S. Bhalla, "Electrical Property Diagram and Morphotropic Phase Boundary in the  $\text{Pb}(\text{In}_{1/2}\text{Ta}_{1/2})\text{O}_3$  -  $\text{PbTiO}_3$  Solid Solution System," *Ferroelectric Letters* (1998). [accepted]
31. Alberta, E.F., A.S. Bhalla, and M. Adachi, "Temperature Dependence of The Piezoelectric and Dielectric Coefficients of Niobium-Doped  $\text{Pb}[(\text{Sc}_{1/2}\text{Nb}_{1/2})_{0.575}\text{Ti}_{0.425}]\text{O}_3$ ," *Ferroelectric Letters* (1998). [accepted]
32. Alberta, E.F., A.S. Bhalla, and T. Takenaka, "Large Hydrostatic Piezoelectric Constant and Temperature Dependence of The Piezoelectric Properties of  $\text{Bi}(\text{Ni}_{1/2}\text{Ti}_{1/2})\text{O}_3\text{:PbTiO}_3$  Ceramics," *Ferroelectrics Letters* (1998). [accepted]
33. Erhart, J. and W. Cao, "Effective Material Properties in Twinned Ferroelectric Crystals," *J. Appl. Phys.* (January 1999). [submitted]
34. Zhu, S.N. and W. Cao, "Pyroelectric and Piezoelectric Imaging of Ferroelectric Domains in  $\text{LiTaO}_3$  by Scanning Electron Microscopy," *Phys. Status Solidi* (1998). [submitted]
35. Du, X.H., Q.M. Wang, U. Belegundu, and K. Uchino, "Piezoelectric Property Enhancement in Polycrystalline Lead Zirconate Titanate by Changing Cutting Angle," *J. Ceram. Soc. Jpn.* (1999). [accepted]
36. Du, X.H., Q.M. Wang, U. Belegundu, A. Bhalla, and K. Uchino, "Crystal Orientation Dependence of Piezoelectric Properties of Single Crystal Barium Titanate," *Mater. Lett.* (1999). [accepted]
37. Yao, K., W. Zhu, K. Uchino, Z. Zhang, and L. C. Lim, "Design and Fabrication of a High Performance Multilayer Piezoelectric Actuator with Bending Deformation," *IEEE Trans. UFFC* (1998). [accepted]
38. Uchino, K. and H. Aburatani, "Field Induced Acoustic Emission in Ferroelectric Ceramics," *Proc. IEEE Ultrasonic Symp., Sendai, Japan* (October, 1998). [in press]

39. Belegundu, U., M. Pastor, X.H. Du, L.E. Cross, and K. Uchino, "Domain Formation in  $0.90\text{Pb}(\text{Zn}_{1/3}\text{Nb}_{2/3})\text{O}_3\text{-}0.1\text{PbTiO}_3$  Single Crystals under the Electric Field along [111] Direction," IEEE Int'l Ultrasonic Symp., TT-3, Sendai, Japan (October 1998).
40. Xu, Y., B. Koc, and K. Uchino, "Engineering Chart of Resonance Frequency of PZT Rings at Different Clamping Conditions," 2nd Asian Meeting on Ferroelectrics, International, AMF-2, Singapore (December 1998).
41. Uchino, K and B. Koc, "Compact Ultrasonic Motors," 2nd Asian Meeting on Ferroelectrics (AMF-2), Singapore (December 1998).
42. Abothu, I.R., P. Poosanaas, S. Komarneni, Y. Ito, and K. Uchino, "Nanocomposite Versus Monophasic Sol-Gel Processing of PLZT Ceramics," Proceedings in Asian Meeting on Ferroelectrics (AMF2), Singapore (December 1998).
43. Abothu, I.R., Y. Ito, P. Poosanaas, S. Kalpat, S. Komarneni, and K. Uchino, "Sol-Gel Processing of Piezoelectric Thin Films," Proceedings in Asian Meeting on Ferroelectrics (AMF2), Singapore (December 1998).
44. Liu, S.F., I.R. Abothu, S. Komarneni, P. Poosanaas, D-S. Paik, Y. Ito, and K. Uchino, "PLZT Ceramics Prepared From Conventional and Microwave Hydrothermal Powders," Proceedings in Asian Meeting on Ferroelectrics (AMF2), Singapore (December 1998).
45. Uchino, K., Wiley Encyclopedia of Electrical and Electronics Engineering, J.G. Webster, Edit., (Partial Charge "Piezoelectric Actuators"), John Wiley & Sons (1998). [in press]
46. Ito, Y. and K. Uchino, Wiley Encyclopedia of Electrical and Electronics Engineering, J.G. Webster, Edit., (Partial Charge "Piezoelectricity"), John Wiley & Sons (1998). [in press]
47. Poosanaas, P., A. Dogan, A.V. Prasadaraao, S. Komarneni, and K. Uchino, "Effect of Ceramic Processing Methods on Photostrictive Ceramics," J. Advanced Performance Mater. (1997). [submitted]
48. Poosanaas, P., and K. Uchino, "Photostrictive Effect in Lanthanum-Modified Lead Zirconate Titanate Ceramics near the Morphotropic Phase Boundary," J. Mater. Chem. and Phys. (1998). [submitted]
49. Witham, J.P. and K. Uchino, "Effect of Grain Size on Dielectric and Piezoelectric Properties of PLZT X/65/35 and X/40/60 Ceramics," J. Electroceramics (1998). [submitted]
50. Witham, J.P. and K. Uchino, "Optical Studies of Domains in PLZT Ceramics Under Applied AC Fields at Room Temperature," J. Amer. Ceram. Soc. (1998). [submitted]
51. Uchino, K., Encyclopedia of Vibration, Partial Charge "Electrostrictive Materials," Academic Press, London (1998). [submitted]
52. Uchino, K., Encyclopedia Smart Materials, J. Harvey, Edit., Partial Charge "Smart Ceramics: Transducers, Sensors and Actuators," John Wiley & Sons, New York (1998). [submitted]
53. Zhang, J., W.J. Hughes, A.C. Hladky-Hennion, and R.E. Newnham, "Concave Cymbal Transducers," Materials Research Innovation (1998).



54. Moret, M.P., R. Zallen, R.E. Newnham, P.C. Joshi, and S.B. Deshu, "Infrared Activity in the Aurivillius Layered Ferroelectric  $\text{SrBi}_2\text{Ta}_2\text{O}_9$ ," J. Amer. Phys. Soc. (1998). [submitted]
55. Villegas, M., C. Moure, P. Duran, J.F. Fernandez, and R.E. Newnham, "Influence of Processing Method on Sintering and Electrical Properties of  $\text{Pb}(\text{Zn}_{1/3}\text{Nb}_{2/3})\text{O}_3$  - Based Ceramics, J. Amer. Ceram. Soc. (1998). [submitted]

#### 10.0 PAPERS APPEARING IN NON REFEREED PUBLICATIONS

1. Koc, B. and K. Uchino, "Ceramic Metal Composite Piezoelectric Motors," IEEE Int'l Ultrasonic Symp., YY-6, Sendai, Japan (October 1998).
2. Abothu, I.R., P. Poosanaas, S. Komarneni, Y. Ito, and K. Uchino, "Nanocomposite Versus Monophasic Sol-Gel Processing of PLZT Ceramics," 2nd Asian Meeting on Ferroelectrics (AMF2), Singapore (December 1998).
3. Abothu, I.R., Y. Ito, P. Poosanaas, S. Kalpat, S. Komarneni, and K. Uchino, "Sol-Gel Processing of Piezoelectric Thin Films," 2nd Asian Meeting on Ferroelectrics (AMF2), Singapore (December 1998).
4. Liu, S.F., I.R. Abothu, S. Komarneni, P. Poosanaas, D-S. Paik, Y. Ito, and K. Uchino, "PLZT Ceramics Prepared From Conventional and Microwave Hydrothermal Powders," 2nd Asian Meeting on Ferroelectrics (AMF2), Singapore (December 1998).
5. Thakoor S., P. Poosanaas, J.M. Morookian, A. Yavrovian, L. Lowry, N. Marzwell, J. Nelson, R.R. Neurgaonkar and K. Uchino, "Optical Microactuation in Piezoceramics," Proc. 5th SPIE Mtg., San Diego (1998).
6. Belegundu, U., X.H. Du and K. Uchino, "In-Situ Observation of Domain Orientation in  $\text{Pb}(\text{Zn}_{1/3}\text{Nb}_{2/3})\text{O}_3$ - $\text{PbTiO}_3$  Single Crystals," Proc. 5th Int'l Symp. Ferroic Domains and Mesoscopic Structures, University Park, PA (April 1998).
7. Uchino, K. and P. Poosanaas, "Photostriction in PLZT and Its Applications," Proc. CIMTEC '98, Florence, Italy (June 1998).
8. Atherton, P.D. and K. Uchino, "New Developments in Piezo Motors and Mechanisms," Proc. 6th Int'l Conf. on New Actuators (Actuator 98), Bremen, Germany, p.164-169 (June 1998).
9. Poosanaas, P., A. Dogan, S. Thakoor, and K. Uchino, "Thick-Film Type Photostrictive Actuators," Proc. 6th Int'l Conf. on New Actuators (Actuator 98), Bremen, Germany, p.345-348 (June 1998).
10. Dogan, A., P. Poosanaas, and K. Uchino, "Surface Characteristics and Photostrictive Behavior of PLZT Ceramics," Proc. Ceram. Congress IV, Eskisehir, Turkey (September 1998).
11. Uchino, K. and P. Poosanaas, "Photostriction in PLZT and Its Application," 4<sup>th</sup> International Conference on Intelligence Materials (ICIM'98), Makuahari, Japan, pp. 68-69 (1998).
12. Koc, B., Y. Xu, and K. Uchino, "Roto-Linear Ultrasonic Motors," Proc. 6th Int'l Conf. on New Actuators (Actuator 98), Bremen, Germany, p.349-352 (June 1998).
13. Uchino, K., "New Trend in Ceramic Actuators," Proc. 6th Int'l Aerospace Symp. '98, Nagoya, Japan, p.S1-2, 1-10 (July 1998).



14. Koc, B., Y. Xu and K. Uchino, "Composite Ultrasonic Motors," IEEE Ultrasonic Symposium, Sendai, Japan, October (1998).
15. Pai, N.G., B. Xu, and L.E. Cross, "Compositional Dependence of Electrical Properties for PLZST Thin Films," ISIF-98 (A Special Issue of Integrated Ferroelectrics) (1998).
16. Wada, S., S.E. Park, L.E. Cross, and T.R. Shrout, "Domain Configuration and Ferroelectric Related Properties of Relaxor Based Single Crystals," J. Korean Phys. Soc. **32**, S1290-S1293 (1998).
17. Cross, L.E., "Piezoelectric Double Amplifier Systems for Air Acoustic Noise Control," Proceedings of the 4<sup>th</sup> European Conference on Smart Structures and Materials in Conjunction with the 2<sup>nd</sup> International Conference on Micromechanics, Intelligent Materials and Robotics, Harrogate, United Kingdom (July 1998).
18. Cross, L.E., "Recent Development in Piezoelectric Ferroelectric Materials and Composites," Proceedings of the 4<sup>th</sup> European Conference on Smart Structures and Materials in Conjunction with the 2<sup>nd</sup> International Conference on Micromechanics, Intelligent Materials and Robotics, Harrogate, United Kingdom (July 1998).
19. Tutwiler, R.L., "Ultrasonic Beamforming Architectures," SPIE Medical Imagint (1998).
20. Majahan, K., S. Madhavan, and R.L. Tutwiler, "High Frequency Data Acquisition System for Ultrasonic Transducer/Array Characterization," SPIE Medical Imaging (1998).
21. Howarth, T.R., D. VanTol, C. Allen, and W.J. Hughes, "A Study of 1-3 Piezocomposite High Drive Limits," ASA/ICA Proceedings (June 1998).
22. Alberta, E.F. and A.S. Bhalla, "Dielectric and Piezoelectric Properties of the  $\text{Pb}(\text{In}_{1/2}\text{Ta}_{1/2})\text{O}_3$  -  $\text{PbTiO}_3$  Solid Solution System," Proceedings of the 10th Annual International Symposium on the Applications of Ferroelectric, Montreux, Switzerland (August 1998).
23. Katiyar, R.S., I. Siny, R. Guo, and A.S. Bhalla, "Dielectric Behavior and Phonon Damping in Low-Dielectric Constant Perovskite Materials," Mat. Res. Soc. Symp. Proc. **511**, 165-170 Materials Res. Soc. (1998).
24. Gaskins, F. (mentor Ruyan Guo), "Thermal Expansion Study of Ferroelectric Relaxor Materials," The Pennsylvania State University Summer Research Opportunities Program Journal **6**, 53-60 (1998).
25. Williams, K.D. (Mentors E. Alberta and A. Bhalla), "Hydrostatic Measurements of Piezoelectric Ceramics," The Pennsylvania State University Summer Research Opportunities Program Journal **6**, 175-182 (1998).

#### 11.0 INVITED PAPERS PRESENTATIONS AT NATIONAL AND INTERNATIONAL MEETINGS

1. Cross, L.E., "Single Crystal Systems of Potential Interest for High-Strain Actuation," SPIE 5<sup>th</sup> Annual Int. Symp. On Smart Structures & Materials, San Diego, CA (March 1998).
2. Cross, L.E., "The Saga of Fine Grain Barium Titanate," 100<sup>th</sup> Annual Mtg. of the American Ceramic Society, Cincinnati, Ohio (May 1998).

3. Cross, L.E., "Recent Developments in Piezoelectric Ferroelectric Materials and Composites," 4<sup>th</sup> European Conference on Smart Structures & Materials, Harrogate, United Kingdom (June 1998).
4. Cross, L.E., "Piezoelectric Double Amplifiers for Air Acoustic Noise Control," 4<sup>th</sup> European Conference on Smart Structures and Materials, Harrogate, United Kingdom (June 1998).
5. Cross, L.E., "Balance of Intrinsic and domain Related Responses in Some Practical Ferroelectric Systems," ISAF XI '98, Montreux, Switzerland (August 1998).
6. Cross, L.E., "Recent Advances in Ferroelectric Sensor and Actuator Materials and Devices," First China International Conference on High-Performance Ceramics CICCI, Beijing, China (October 31-November 3, 1998). [Plenary]
7. Cross, L.E., "Influence of Relaxor Character on the Lower Temperature Ferroelectric Behavior," Second Asia Meeting on Ferroelectricity (AMF 2), Singapore (December 1998).
8. Newnham, R.E., "Ceramic Engineering in the 21<sup>st</sup> Century: Scaling Up and Scaling Down," 100<sup>th</sup> Annual Mtg. of the American Ceramic Society, Cincinnati, Ohio (May 1998).
9. Newnham, R.E., "Persistent Disequilibrium in Smart Materials," Gordon Research Conference on Disorder in Materials, New London, NH (July 1998).
10. Yimnirun, R., V. Sundar, P. Moses, and R.E. Newnham., "Predicting Electrostriction," Innovation in Materials Conference, Washington, DC (July 1998).
11. Newnham, R.E., "Electroceramics in the 21<sup>st</sup> Century," Intl. Symp. On Appl. Of Ferroelectrics (ISAF XI), Montreux, Switzerland (August 1998).
12. Newnham, R.E., "Structure-Property Relation in Smart Materials," Kreidl Lecture, 10<sup>th</sup> Annual Rio Grande Symposium on Advanced Materials, Albuquerque, New Mexico (October 1998).
13. Newnham, R.E., "Structure-Property Relations in Smart Materials," Maddin Lecture, University of Pennsylvania (December 1998).
14. Uchino, K., "New Trend in Multilayer Ceramic Actuators," 100<sup>th</sup> Annual Mtg. of Amer. Ceram. Soc. Intl. Symp. Multilayer Electronic Ceramic Devices, Cincinnati, Ohio (May 1998).
15. Uchino, K. and P. Poosanaas, "Photostriction in PLZT and Its Applications," 9<sup>th</sup> Intl. Conf. on Modern Materials & Technologies," SVIII-1:IL02, Florence, Italy (June 1998).
16. Atherton, P.D. and K. Uchino, "New Developments in Piezo Motors and Mechanisms," 6<sup>th</sup> Intl. Conf. on New Actuators (Actuator 98), Bremen, Germany (June 1998).
17. Uchino, K., "New Trend in Ceramic Actuators," 6<sup>th</sup> Intl. Aerospace Symp. '98, Nagoya, Japan (July 1998).
18. Uchino, K. and P. Poosanaas, "Photostriction in PLZT and Its Applications," 4<sup>th</sup> Intl. Conf. Intelligent Materials, Makuhari, Japan (October 1998).
19. Hatch, D.M. and W. Cao, "Determination of Domain and Domain Wall Formation at Ferroic Transitions," The 5<sup>th</sup> International Symposium on Domains and Mesoscopic Structures, The Pennsylvania State University, University Park, Pennsylvania (April 1998).
20. Cao, W., "Review on Finite Element Design Modeling of Medical Ultrasonic Transducers," Medical Imaging 1999, San Diego, California (February 1999).

21. Lauchle, G.C., A.R. Jones, J.J. Dreyer, and J. Wang, "Flow-Induced Lift Forces on a Towed Sphere," ASME Winter Annual Meeting, Anaheim, California (November 1998).
22. Zhang, Q., "Massive Electrostriction and Relaxor Behavior in Electron Irradiated P(VDF-TrFE) Copolymer," Innovations in Materials Conference, Washington, DC (July 1998).
23. Zhang, Q., "Relaxor Ferroelectric Polymers for Actuators and Transducers," IEEE International Ultrasonic Symposium, Sendai, Japan (October 1998).
24. Bhalla, A., "Nanostructure Science and Technology," Short Course at the Second Asian Meeting on Ferroelectrics, Singapore (December 1998).
25. Bhalla, A., "Perovskite Quantum Paraelectrics for Tunable Devices," ACerS 1998 Annual Meeting, Cincinnati, Ohio (May 1998).
26. Bhalla, A., "Relaxor Ferroelectrics," Electronics Materials Symposium, Baton Rouge, Louisiana (1998).
27. Bhalla, A., "Low and High Frequency Dielectric Constant Materials," ACerS 1998 Annual Meeting, Cincinnati, Ohio (May 1998).
28. Bhalla, A., "Properties of Nanoregions and Boundaries in Ferroelectrics," Third Pacific Rim International Conference on Advance Materials and Processing, Honolulu, Hawaii (July 1998).
29. Bhalla, A., "Self-Assembled Nano Materials," University of Puerto Rico, San Piedras, Puerto Rico (November 1998).
30. Bhalla, A. and R. Guo, "Microwave Substrates of the Third Kind," International Conference on New Development of HTSC, Baton Rouge, Louisiana (February 1998). [keynote]
31. Guo, R., "Ferroelectric Tungsten Bronze Solid Solution Compositions Near Morphotropic Phase Boundaries," International Symposium on Dielectric Ceramics, Cincinnati, Ohio (May 1998).
32. Guo, R., "Morphotropic Phase Boundaries in Ferroelectric Tungsten Bronze," Second Asian Meeting on Ferroelectrics, Singapore (December 1998).
33. Guo, R., "Crystal Structure Analysis and Polarization Mechanisms of Ferroelectric Tungsten Bronzes," The 56<sup>th</sup> Annual Pittsburgh Diffraction Conference, Pittsburgh, PA (November 1998).
34. Trolrier-McKinstry, S., J.P. Maria, R. Polcawich, J.F. Shepard, Jr., W. Ren, and F. Xu, "Ferroelectric Films for MEMS Applications," International Conference on Metallurgical Coatings and Thin Films, San Diego, CA (April 1999).
35. Trolrier-McKinstry, S., J.P. Maria, and J.H. Park, "Epitaxial and Oriented  $\text{Pb}(\text{Mg}_{1/3}\text{Nb}_{2/3})\text{O}_3$ - $\text{PbTiO}_3$  Films," Materials Research Society Meeting, San Francisco, CA (April 1999).
36. Trolrier-McKinstry, S. and J.P. Maria, "Structure-Property Relations in Epitaxial  $\text{Pb}(\text{Mg}_{1/3}\text{Nb}_{2/3})\text{O}_3$ - $\text{PbTiO}_3$ / $\text{SrRuO}_3$ / $\text{LaAlO}_3$  Heterostructures," Pittsburgh Diffraction Conference, Pittsburgh, PA (November 1998).
37. Wasa, K., Y. Haneda, T. Sato, H. Adachi, I. Kanno, D.G. Schlom, S. Trolrier-McKinstry, Q. Gang, and C.B. Eom, "Step-Flow Growth of Perovskite  $\text{PbTiO}_3$  Thin Films Epitaxially Grown on a Miscut  $\text{SrTiO}_3$  Substrate," SPIE Meeting, San Diego, CA (July 1998).

## 12.0 INVITED PAPERS PRESENTED AT UNIVERSITY, INDUSTRY, AND GOVERNMENT LABORATORIES

1. Cross, L.E., "Past Experience and Future Trend," 1998 ONR Transducer Materials and Transducers Workshop, State College, PA (May 1998).
2. Cross, L.E., Short Courses, "Actuators," "Ferroelectric Relaxors," "Ferroelectric Domain Structures," Cranfield University, United Kingdom (March 29-April 3, 1998)
3. Cross, L.E., "Phenomenology of Ferroelectricity," ISAF XI '98, Montreux, Switzerland (August 1998). [tutorial]
4. Cross, L.E., "US Research Activities," Nikko Workshop on Smart Materials and Systems, Nikko, Japan (October 1998).
5. Cross, L.E. and J. Fousek, "Domains in Ferroelectrics," AMF2, Singapore (December 1998). [tutorial]
6. Cross, L.E., "Recent Advances in Ferroelectric Sensors and Actuators," Technology Seminar, Institute of Technology, Linkoping, Sweden (1998).
7. Newnham, R.E., "Molecular Mechanisms in Smart Materials," Raychem Corporation, Menlo Park, CA (January 1998).
8. Newnham, R.E., "Molecular Mechanisms in Smart Materials, Materials Science Department Seminar, University of California-Berkeley (January 1998).
9. Newnham, R.E., "Molecular Mechanisms in Smart Materials," Physics Department Seminar, Indiana University of Pennsylvania (February 1998).
10. Newnham, R.E., "Molecular Mechanisms in Smart Materials," Materials Department, Virginia Polytechnic Institute (February 1998).
11. Newnham, R.E., "Molecular Mechanisms in Smart Materials, Alfred School of Ceramics, Alfred, NY (March 1998).
12. Newnham, R.E., "Smart Composites," Seminar, Lincoln University (March 1998).
13. Newnham, R.E., "Ceramic Engineering in the 21<sup>st</sup> Century: Scaling Up and Scaling Down," International Center for Actuators and Transducers Dinner Banquet, The Pennsylvania State University, University Park, PA (May 1998).
14. Newnham, R.E., "Composite Transducers," Philips Laboratory Seminar, Eindhoven, Holland (May 1998).
15. Newnham, R.E., "Molecular Mechanisms in Smart Materials," RWTH Seminar, Aachen, Germany (May 1998).
16. Newnham, R.E., "Molecular Mechanisms in Smart Materials," Chalmers University, Goteborg, Sweden (May 1998).
17. Newnham, R.E., "Molecular Mechanisms in Smart Materials," Institute of Solid State Physics, Riga, Latvia (June 1998).
18. Newnham, R.E., "Symmetry and Physical Properties," Intl. Symp. On Applications of Ferroelectrics (ISAF XI), Montreux, Switzerland (August 1998). [tutorial]
19. Newnham, R.E., "Molecular Mechanisms in Smart Materials," Dept. of Materials and Nuclear Engineering, University of Maryland (September 1998).
20. Newnham, R.E., "Lectures in Modern Chemistry Series," University of British Columbia and Simon Fraser University (September 1998).
21. Newnham, R.E., "Biomimetic Transducers," Tokyo Institute of Technology, Tokyo, Japan (September 1998).

22. Newnham, R.E., "Smart Materials and Smart Structures," National Academy of Engineering Annual Meeting, Washington, DC (October 1998).
23. Newnham, R.E., "Ceramic Engineering in the 21<sup>st</sup> Century," Future of Ceramics Meeting, Corning, NY (October 1998).
24. Newnham, R.E., "Ceramic Engineering in the 21<sup>st</sup> Century," Pennsylvania Ceramics Association Meeting, Penn State University, University Park, PA (October 1998).
25. Newnham, R.E., "Biomimetic Transducers," Ceramics Department Seminar, Rutgers University (October 1998).
26. Newnham, R.E., "Smart Materials," 56<sup>th</sup> Annual Pittsburgh Diffraction Conference, Pittsburgh, PA (November 1998).
27. Newnham, R.E., "Structure-Property Relations in Smart Materials," Seminar at Motorola, Inc., Albuquerque, New Mexico (November 1998).
28. Cao, W., "Ferroelectric Materials and Their Applications," Los Alamos National Lab, New Mexico (June 1998).
29. Cao, W., "Property Variation with Scaling in Ferroic Materials," Los Alamos National Lab., New Mexico (June 1998).
30. Cao, W., "Medical Ultrasonic Research at Penn State," Acoustic Institute, Nanjing University, Nanjing, China (September 1998).
31. Cao, W., "Interdisciplinary Research on Transducer Designs," Department of Physics, Jilin University, Changchun, China (October 1998).
32. Cao, W., "High Frequency Medical Ultrasound," Department of Bioengineering and Information Systems, Xian Jiaotong University, Xian, China (October 1998).
33. Cao, W., "Landau-Ginzburg Theory for Inhomogeneous Structures Resulting a Ferroelectric Phase Transition," Department of Physics, Nanjing University, Nanjing (October 1998).
34. Cao, W., "Observation of Ferroelectric Domains and Computer Simulations," Laboratory of Solid State Microstructures, Nanjing University, Nanjing, China (October 1998).
35. Cao, W., "Phase Transitions, Domains, and Material Properties," Department of Physics, Suzhou University, Suzhou, China (October 1998).
36. Cao, W., "Simulation Design of High Frequency Medical Ultrasonic Transducers," Smart Materials Research Laboratory, Tongji University, Shanghai, China (October 1998).
37. Lauchle, G.C. and D.E. Capone, "Flow-Induced Flow Noise Modeling for Acoustic Velocity Hydrophones," ONR Underseas Warfare Systems Technology, Applications, and Tactics Conference, Austin, TX (February 1998).
38. McConnell, J.A., G.C. Lauchle, and K.J. Bastyr, "The Development of Underwater Acoustic Intensity Sensors," ONR Underseas Warfare Systems Technology, Applications, and Tactics Conference, Austin, TX (February 1998).
39. Zhang, Q., "Relaxor Ferroelectric Polymers," Allied Signal Inc., New Jersey (1998).
40. Zhang, Q., "Ferroelectric Materials for Actuators and Transducers, Research Center, Daimler-Benz AG, Germany (1998).
41. Zhang, Q., "Electrostrictive Polymers," Science University of Tokyo, Japan (1998).
42. Hughes, W.J., S. Trolier-McKinstry, R.L. Tutwiler, R.J. Davis, and W.W. Cao, "Ultrasonic Transducer Efforts at Penn State," DARPA/ONR Workshop on Medical Ultrasound Imaging Technology Development for Combat Care, Lansdowne, Virginia (February 1998).

43. Hughes, W.J., S. Trolier-McKinstry, R.L. Tutwiler, and R.J. Davis, "MURI:Micro-Tonpitz Transducer, and DARPA/ONR: Sonoelectronics," Advisory Committee for the NIH Transducer Resource Center, Penn State (April 1998).

### 13.0 CONTRIBUTED PAPERS AT NATIONAL AND INTERNATIONAL MEETINGS

1. Watkins, T.R., E.A. Payzant, J.P. Maria, S. Trolier-McKinstry, S.T. Misture, and S.M. Pilgrim, "Electroactive Characterization of PMN by X-Ray Diffraction," Pittsburgh Diffraction Conference, Pittsburgh (November 1998).
2. Maria, J.P., E.A. Payzang, J.F. Shepard, Jr., and S. Trolier-McKinstry, "Epitaxial  $\text{Pb}(\text{Mg}_{1/3}\text{Nb}_{2/3})\text{O}_3$ - $\text{PbTiO}_3$  Thin Films," Intl. Symp. On Applications of Ferroelectrics, Montreux, Switzerland (August 1998).
3. Zeto, R.J., B.J. Rod, M.H. Ervin, R.C. Piekarz, S. Trolier-McKinstry, T. Su, and J.F. Shepard, "High Resolution Dry Etch Patterning of PZT for Piezoelectric MEMS Devices," Intl. Symp. on Applications of Ferroelectrics, Montreux, Switzerland (August 1998).
4. Shepard, Jr., J.F., F. Xu, F. Chu, R. Polcawich, and S. Trolier-McKinstry, "Direct Techniques for the Characterization of the Piezoelectric Coefficients ( $d_{33}$  and  $d_{31}$ ) of Thin Films,' Intl. Symp. on Applications of Ferroelectrics, Montreux, Switzerland (August 1998).
5. Rehrig, P.W., C. Duran, E.M. Sabolsky, S. Trolier-McKinstry, and G.L. Messing, "Templated Grain Growth of Perovskite Ferroelectrics," Intl. Symp. on Applications of Ferroelectrics, Montreux, Switzerland (August 1998).
6. Sabolsky, E.M., G.L. Messing, and S. Trolier-McKinstry, "Templated Grain Growth (TGG) in  $0.65\text{Pb}(\text{Mg}_{1/3}\text{Nb}_{2/3})\text{O}_3$ - $0.35\text{PbTiO}_3$ , Gordon Research Conference (1998).
7. Trolier-McKinstry, S., F. Xu, J.P. Maria, R. Polcawich, W. Ren, and J.F. Shepard, Jr., "Piezoelectric Thin Films for MEMS Applications, Intl. Symp. on Integrated Ferroelectrics, Colorado Springs, CO (March 1999).
8. Rehrig, P.W., G.L. Messing, and S. Trolier-McKinstry, "Properties of  $\text{BaTiO}_3$  Single Crystals Grown by Templated Grain Growth," ACerS Mtg, Indianapolis, Indiana (1999).
9. Poosanaas, P., K. Uchino, and S. Thakoor, "Composition and Surface Effects in Photostrictive Behavior," 100th Annual Mtg. of Amer. Ceram. Soc., Int'l Symp. Dielectric Ceramics, Cincinnati, Ohio (May 1998).
10. Belegundu, U., M. Pastor, X. Du, and K. Uchino, "Observation of Domain Orientation Process in  $\text{Pb}(\text{Zn}_{1/3}\text{Nb}_{2/3})\text{O}_3$ - $\text{PbTiO}_3$  Using Optical Microscope," 100th Annual Mtg. of Amer. Ceram. Soc., Int'l Symp. Dielectric Ceramics, Cincinnati, Ohio (May 1998).
11. Tonooka, K., P. Poosanaas, and K. Uchino, "Mechanism of the Bulk Photovoltaic Effect in Ferroelectrics," Proc. 5th SPIE Mtg., San Diego, CA (March 1998).
12. Thakoor S., P. Poosanaas, J. M. Morookian, A. Yavrovian, L. Lowry, N. Marzwell, J.Nelson, R.R. Neurgaonkar, and K. Uchino, "Optical Microactuation in Piezoceramics," Proc. 5th SPIE Mtg., San Diego, CA (March 1998).



13. Poosanaas, P. and K. Uchino, "Surface Characteristics on Photostriction of PLZT Ceramics," 13th Annual Graduate Research Exhibition, PennState University, University Park, Pennsylvania (March 1998).
14. Chen, Y.H. and K. Uchino, "High-Power Characteristics of PMN-PT with Constant Current/Constant Voltage Measurements," ICAT 24th Smart Actuator Symposium, University Park, PA (April 1998).
15. Chen, Y. H. and K. Uchino, "High-Power Characteristics of PMN-PT with Constant Current/Constant Voltage Measurements," ONR Transducer Workshop, University Park, PA (April 1998).
16. Belegundu, U., X. H. Du, and K. Uchino, "In-Situ Observation of Domain Orientation in  $\text{Pb}(\text{Zn}_{1/3}\text{Nb}_{2/3})\text{O}_3\text{-PbTiO}_3$  Single Crystals," 5th Int'l Symp. Ferroic Domains and Mesoscopic Structures, University Park, PA (April 1998).
17. Poosanaas, P., A. Dogan, S. Thakoor, and K. Uchino, "Thick-Film Type Photostrictive Actuators," 6th Int'l Conf. on New Actuators (Actuator 98), Bremen, Germany (June 1998).
18. Koc, B., Y. Xu, and K. Uchino, "Roto-Linear Ultrasonic Motors," 6th Int'l Conf. on New Actuators (Actuator 98), Bremen, Germany (June 1998).
19. Uchino, K., "Compact Piezoelectric Ultrasonic Motors," 1st NASA/JPL Workshop on Biomorphc Explorers for Future Missions, Pasadena, CA (Aug. 1998).
20. Uchino, K. and I. Hayashi, "New Solid State Actuators for Biomorphc Explorers," 1st NASA/JPL Workshop on Biomorphc Explorers for Future Missions, Pasadena, CA (Aug. 1998).
21. Dogan, A., P. Poosanaas, and K. Uchino, "Surface Characteristics on Photostrictive Behavior of PLZT Ceramics," Proceedings in Ceramic Congress IV, Eskisehir, Turkey (September 1998).
22. Uchino, K. and H. Aburatani, "Field Induced Acoustic Emission in Ferroelectric Ceramics," IEEE Int'l Ultrasonic Symp., B-6, Sendai, Japan (October 1998).
23. Belegundu, U., M. Pastor, X. H. Du, L. E. Cross, and K. Uchino, "Domain Formation in  $0.90\text{Pb}(\text{Zn}_{1/3}\text{Nb}_{2/3})\text{O}_3\text{-}0.1\text{PbTiO}_3$  Single Crystals under the Electric Field along [111] Direction," IEEE Int'l Ultrasonic Symp., TT-3, Sendai, Japan (October 1998).
24. Erhart, J., W. Cao, and J. Fousek, "A Study of S-Walls in a m3m-mmm Ferroelastic Phase Transitions," Intl. Symp. on Application of Ferroelectrics (ISAF XI), Montreux, Switzerland (August 1998).
25. Wang, H., T.A. Ritter, W. Cao, and K. Shung, "Passive Materials for High Frequency Ultrasonic Transducers," Medical Imaging 1999, San Diego, CA (February 1999).
26. Yin, J.H., B. Jiang, and W. Cao, "Elastic, Piezoelectric and Dielectric Properties of PZN-PT Single Crystals," Medical Imaging 1999, San Diego, CA (February 1999).
27. Cao, W., "Physical Principles on Domain Engineering in PZN-PT, PMN-PT Single Crystal Systems," Medical Imaging 1999, Conference on Ultrasonic Transducer Engineering, San Diego, CA (February 1999).
28. Cao, W., A. Saxena, D. Hatch, and G. Barsch, "Theory of Domain Walls in Improper Ferroelastic Phase Transition Driven by Zone Boundary Phonon," American Physical Society March Meeting, Atlanta, Georgia (March 1999).

29. Glazounov, A., J. Zhao, and Q.M. Zhang, "Nano-polar Regions and Electrostriction in Relaxor Ferroelectric PMN," ONR Workshop on Transducer and Transducer Materials, Penn State University (May 1998).
30. Glazounov, A., Q.M. Zhang, and C. Kim, "Piezoceramic Torsional Actuator," ONR Workshop on Transducer and Transducer Materials, Penn State University (May 1998).
31. Liu, R., Q.M. Zhang, and L.E. Cross, ONR Workshop on Transducer and Transducer Materials, Penn State University (May 1998).
32. Zhao, J., A. Glazounov, and Q.M. Zhang, "Influence of the Electrical and Mechanical Boundary Conditions on the Electromechanical Performance of PMN-PT," ONR Workshop on Transducer and Transducer Materials, Penn State University (May 1998).
33. Zhao, J. and Q.M. Zhang, "Polarization and Electrostriction in PMN-PT Ceramics," American Ceramic Meeting, Cincinnati, Ohio (May 1998).
34. Zhang, Q.M., V. Bharti, X. Zhao, T. Ramotowski, F. Tito, and R. Ting, "Relaxor Ferroelectric Polymers," ONR Workshop on Transducer and Transducer Materials, Penn State University (May 1998).
35. Zhang, Q.M. and L.E. Cross, "Noval P(VDF-TrFE) Copolymer Actuators and Sensors," DSRC Meeting on Electroactive Polymers, Washington, DC (June 1998).
36. Kim, C., D. Lewis III, C.C. Wu, M. Kahn, A. Glazounov, and Q.M. Zhang, "Torsional Actuators," DARPA Actuator Programs Technology Interchange Meeting, NASA-Langley, VA (June 1998).
37. Zhang, Q.M., V. Bharti, X. Zhao, "Relaxor Ferroelectric Behavior and Massive Electrostriction in Electron Irradiated P(VDF-TrFE) Copolymer," Innovations in Materials Conference, Washington, DC (July 1998).
38. Zhang, Q.M., "Relaxor Ferroelectric Polymers," Materials Innovation at Penn State MRL, The Osborn Symposium, Penn State University (July 1998).
39. Zhang, Q.M., V. Bharti, Z-Y Cheng, and X. Zhao, "Relaxor Ferroelectric Polymers," Proc. 1998 ISAF XI, Montreux, Switzerland (August 1998).
40. Mueller, V. and Q.M. Zhang, "Universal Nonlinear Behavior of Soft PZT-Piezoceramics," Proc. 1998 ISAF XI, Montreux, Switzerland (August 1998).
41. Zhao, J., V. Mueller, and Q.M. Zhang, "Stress Dependence of Electromechanical Response of PMN-PT in the DC-Electrical Field Biased State," Proc. 1998 ISAF XI, Montreux, Switzerland (August 1998).
42. Kim, C., D. Lewis, III, V. Degiorgi, D. Flippen, B. Bender, T. Jesson, C.C. Wu, M. Kahn, A. Pattnaik, A. Glazounov, and Q.M. Zhang, "High Authority Piezoelectric Torsional Actuators," Proc. 1998 ISAF XI, Montreux, Switzerland (August 1998).
43. Zhang, Q.M., "Relaxor Ferroelectric Polymers for Actuators and Transducers," 1998 IEEE International Ultrasonics Symposium. Sendai, Japan (October 1998).
44. Bharti, V., Z.-Y. Cheng, T.B. Xu, and Q.M. Zhang, "Modified P(VDF-TrFE) Copolymer Systems and their Associated Dielectric and Electromechanical Properties," Center for Dielectric Study Fall Meeting, Penn State University (October 1998).
45. Glazounov, A.E., Q.M. Zhang, and C. Kim, "Torsional Actuator Based on Mechanically Amplified Shear Piezoelectric Response," Center for Dielectric Study Fall Meeting, Penn State University (October 1998).



46. Zhang, Q.M., "Relaxor Ferroelectric Polymer-Modified P(VDF-TrFE) Polymer," The 56th Annual Pittsburgh Diffraction Conference, Pittsburgh, PA (1998).
47. Bharti, V., Z.-Y. Cheng, and Q.M. Zhang, "Giant Electrostriction and Relaxor Ferroelectric Behavior in Electron Irradiated P(VDF-TrFE) Copolymers," MRS Fall Meeting, Boston, MA (December 1998).
48. Cheng, Z.-Y., S. Gross, J. Su, and Q.M. Zhang, "The Pressure Effect on Dielectric Response of an Electrostrictive Polymer: Polyurethane Elastomer," MRS Fall Meeting, Boston, MA (December 1998).
49. Bharti, V., Z.-Y. Cheng, T.B. Xu, S. Wang, and Q.M. Zhang, "Electrostrictive Properties of Electron Irradiated P(VDF-TrFE) Copolymers," MRS Fall Meeting, Boston, MA (December 1998).
50. Alberta, E.F. and A.S. Bhalla, "Piezoelectric and Dielectric Properties of PSNT:PZNT Ceramics near the Morphotropic Phase Boundary," 1998 ONR Transducer Materials and Transducers Workshop, State College, PA (May 1998).
51. Alberta, E.F. and A.S. Bhalla, "Electrical and Mechanical Properties of Perovskite  $o$ -d Ferroelectric Relaxor  $\text{Pb}(\text{InNb})_{1/2}\text{O}_3$  and  $\text{Pb}(\text{ScNb})_{1/2}\text{O}_3 : \text{PbTiO}_3$  Systems," Third Pacific Rim International Conference on Advanced Materials and Processing, Honolulu, Hawaii (July 1998).
52. Alberta, E.F. and A.S. Bhalla, "Piezoelectric Properties of  $\text{Pb}(\text{InTa})\text{O}_3$ - $\text{PbTiO}_3$  Solid Solution Systems", IEEE International Symposium on Applications of Ferroelectrics (ISAF XI), Montreux, Switzerland (Aug. 1998).
53. Alberta, E.F., "Piezoelectric Properties of Ceramics in the  $(1-x) \text{Pb}(\text{In}_{1/2}\text{Ta}_{1/2})\text{O}_3 : (x) \text{PbTiO}_3$  ( $\text{Ta} = \text{Nb}, \text{Ta}$ ) Solid Solution Systems," Pennsylvania State University MURI Group Meeting, University Park, PA (October 1998).
54. Pandya, K., Y. Jiang, R. Guo, and A.S. Bhalla, "Lead-Containing Ferroelectric Tungsten Bronze Single Crystals Grown by Laser Heated Pedestal Growth Technique," 1998 ONR Transducer Materials and Transducers Workshop, State College, PA (May 1998).
55. Gaskins, F. and R. Guo, "Ferroelectric Lead Barium Niobate Structure and Cation Site Preference Analysis Using Rietveld Refinement Method," 1998 ONR Transducer Materials and Transducers Workshop, State College, PA (May 1998).
56. Gaskins, F. (mentor Ruyan Guo), "Thermal Expansion Study of Ferroelectric Relaxor Materials," The Pennsylvania State University Summer Research Symposium, University Park, PA (August 1998).
57. Williams, K.D. (Mentors E. Alberta and A. Bhalla), "Hydrostatic Measurements of Piezoelectric Ceramics," The Pennsylvania State University Summer Research Opportunities Program Research Symposium, University Park, PA (August 1998).
58. Chen, A., Y. Zhi, J. Scott, A. Loidl, R. Guo, A.S. Bhalla, and L.E. Cross, "Dielectric Polarization Processes in  $\text{Bi:SrTiO}_3$ ," Workshop on Relaxors, Colonial Williamsburg, Virginia (February 1999).
59. Venkateshwaran, B., R. Guo, and A. Bhalla, "Low Temperature Dielectric Properties of the  $(\text{LnNa})\text{TiO}_3$  Family," ACerS 1998 Annual Meeting, Cincinnati, Ohio (May 1998).
60. Pandya, K., Y. Jiang, R. Guo, and A. Bhalla, "Single Crystal Fiber Growth and Ferroelectric Properties of  $2(\text{Pb,Sr})\text{Nb}_2\text{O}_6:(\text{K,Na})\text{NbO}_3$  System," Intl. Symp. on Dielectric Ceramics, Cincinnati, Ohio (May 1998).

61. Guo, R., Y. Jiang, and A.S. Bhalla, "Ferroelectric Properties of A-site Filled Tungsten Bronze Single Crystals  $(\text{Ba}_{1-x}\text{Sr}_x)_2\text{Na}_{1-y}\text{K}_y\text{Nb}_5\text{O}_{15}$ ," Intl. Symp. on Applications of Ferroelectrics (ISAF XI), Montreux, Switzerland (August 1998).
62. Guo, R., H.T. Evans, Jr., and A.S. Bhalla, "Ionic Site Occupancy and Displacement in Ferroelectric Lead Barium Niobate Single Crystals," Intl. Symp. on Applications of Ferroelectrics, Montreux, Switzerland (August 1998).
63. Jiang, Y., K. Pandya, R. Guo, and A.S. Bhalla, "Lead Containing PSKNN Ferroelectric Single Crystals Grown by the Laser Heated Pedestal Growth Technique," Intl. Symp. on Electronic Materials, Beijing, China (October 1998).
64. Siny, I.G., R. Katiyar, R. Guo, and A. Bhalla, "Dielectric Behavior and Phonon Damping in Low Dielectric Constant Perovskite Materials," MRS 1998 Spring Meeting, Sna Francisco, CA (April 1998).
65. Amin, S., R. Guo, and A.S. Bhalla, "Potassium Lithium Niobate Single Crystal Growth and Low Temperature Properties," ACerS 1998 Annual Meetings, Cincinnati, Ohio (May 1998).
66. Jiang, Y., R. Guo, and A. Bhalla, "Ferroelectric Properties of Filled Tungsten Bronze Single Crystals  $(\text{Ba}_{1-x}\text{Sr}_x)_3\text{Na}_{1-y}\text{K}_y\text{Nb}_5\text{O}_{15}$ ," ACerS 1998 Annual Meeting, Cincinnati, Ohio (May 1998).
67. Bastyr, K.J. and G.C. Lauchle, "Calibration and Testing of a Neutrally Buoyant u-u Intensity Probe," Joint 16<sup>th</sup> International Congress on Acoustics and 135<sup>th</sup> Meeting on the Acoust. Soc. A., Seattle, Washington [J. Acoust. Soc. Am. **103**, Pt. 2, 2755 (1998)].
68. McConnell, J.A. and G.C. Lauchle, "Calibration and Testing of a Neutrally Buoyant p-u Intensity Probe," Joint 16<sup>th</sup> International Congress on Acoustics and 135<sup>th</sup> Meeting on the Acoust. Soc. A., Seattle, Washington [J. Acoust. Soc. Am. **103**, Pt. 2, 2755 (1998)].
69. VanTol, D. and W.J. Hughes, "Micro-Tonpilz Transducer," ONR Workshop on Transducer Materials and Transducers, State College, PA (May 1998).
70. Hebert, C.A. and G.A. Lesieutre, "Flexural Piezoelectric Transducers with Frequency Agility Obtained Via Membrane Loads," AIAA/ASME/AHS Adaptive Structures Forum, St. Louis, MO (April 1999).
71. Bernard, J.E. and G.A. Lesieutre, "Active Broadband Force Isolation Using a Flexible Piezoelectric Actuator," AIAA/ASME/AHS Adaptive Structures Forum, St. Louis, MO (April 1999).
72. Lesieutre, G.A., C.L. Davis, and C.A. Hebert, "Making Piezoelectric Transducers More Effective: Can Device Electromechanical Coupling Be Higher Than Material Coupling," ONR Transducer Materials and Transducers Workshop, State College, PA (May 1998).
73. Lesieutre, G.A. and C.L. Davis, "An Actively-Tuned, Solid-State Piezoelectric Vibration Absorbers," ONR Transducer Materials and Transducers Workshop, State College, PA (May 1998).
74. Hebert, C.A. and G.A. Lesieutre, "Rotocraft Blade Lag Damping using Highly Distributed Tuned Vibration Absorbers," 39<sup>th</sup> AIAA/ASME/ASCE/AHS/ASC Structures, Structural Dynamics and Materials Conference, Long Beach, CA (April 1998).

75. Lesieutre, G.A. and C.L. Davis, "An Actively-Tuned Solid-State Piezoelectric Vibration Absorber," SPIE Smart Structures and Materials Conference: Smart Structures and Integrated Systems, San Diego, CA (March 1998).
76. Yimnirun, R., S. Eury, P. Moses, V. Sundar, and R.E. Newnham, "Measurements of Electrostriction Coefficients Using Interferometer and Compressometer Based Methods," 56<sup>th</sup> Annual Pittsburgh Diffraction Conference, Pittsburgh, PA (November 1998).
77. Alkoy, S., J. Cochran, and R.E. Newnham, "An Application of Smart Materials: Piezoelectric Hollow Spheres, 56<sup>th</sup> Annual Pittsburgh Diffraction Conference, Pittsburgh, PA (November 1998).
78. Zhang, J., W.J. Hughes, A.C. Hladky-Hennion, and R.E. Newnham, "Concave Cymbal Transducers," 56<sup>th</sup> Annual Pittsburgh Diffraction Conference, Pittsburgh, PA (November 1998).
79. Zhang, J., R.E. Newnham, and W.J. Hughes, "Acoustic Measurements on Cymbal Arrays," MURI Review Meeting, Penn State University (November 1998).
80. Yimnirun, P. Moses, V. Sundar, and R.E. Newnham, "Interferometric and Compressometric Studies of Electrostrictive Properties in Low-K Ceramics, ACerS Mtg., Cincinnati Ohio (May 1998).
81. Alkoy, S. and R.E. Newnham, "PZT-Polymer Composite Hydrophones Prepared from Hollow Ceramic Spheres," Centennial Symposium of the American Ceramic Society, Cincinnati, Ohio (May 1998).
82. Yimnirun, R., S. Eury, V. Sundar, P. Moses, and S.-J. Jang, "Electrostriction Measurements on Low Permittivity Ceramics and Polymers," ISAF XI, Montreux, Switzerland (August 1998).
83. Zhang, J., J.F. Tressler, A. Dogan, and R.E. Newnham, "Concave Cymbal Transducers," ISAF XI, Montreux, Switzerland (August 1998).
84. Alkoy, S., A.C. Hladky-Hennion, J.K. Cochran, and R.E. Newnham, "Miniature Hydrophones from Hollow Ceramic Spheres," ISAF XI, Montreux, Switzerland (August 1998).
85. Hladky-Hennion, A.C., R. Bosout, S. Alkoy, and R.E. Newnham, "Finite Element Modeling of Transduction Materials with Application to Piezoelectric Hollow Sphere Transducers," IEEE Frequency Control Symposium, Pasadena, CA (1998).

#### 14.0 BOOKS (AND SECTIONS THERE OF)

1. Hughes, W.J., "Transducers, Underwater Acoustics," Encyclopedia of Applied Physics, Vol. 22 (1998). Wiley-VCH Verlag GmbH.
2. Uchino, K., "Shape Memory Materials," Chapter 8 in *Shape Memory Ceramics*, edit. K. Otsuka and C.M. Wayman, Cambridge Univ. Press, Cambridge (1998).
3. Cross, L.E., Section on Electroceramics, Encyclopedia of Materials: Science and Technology, ed. S.K. Dey, Elsevier Science.
4. Fousek, J. and L.E. Cross, "Domains and Switching in Ferroics," Elsevier Science. [book 90% completed]

# **GENERAL SUMMARY PAPERS**

# **APPENDIX 1**

## Recent Developments in Piezoelectric Ferroelectric Materials and Composites

L. Eric Cross  
Intercollege Materials Research Laboratory  
The Pennsylvania State University  
University Park, Pennsylvania 16802-4800 USA

**Abstract.** Thinking with regard to piezoelectric sensing and actuation has recently been revolutionized by the discovery of quite exceptional piezoelectric response in single crystals of new solid solution systems with morphotropic phase boundaries. In the systems lead zinc niobate:lead titanate  $\text{PbZn}_{1/3}\text{Nb}_{2/3}\text{O}_3\text{:PbTiO}_3$  (PZN:PT) and lead magnesium niobate:lead titanate  $\text{PbMg}_{1/3}\text{Nb}_{2/3}\text{O}_3\text{:PbTiO}_3$  (PMN:PT) Drs. Thomas ShROUT and Seung-Eek "Eagle" Park at Penn State have demonstrated that for certain orientation of crystal and electric field  $d_{33}$  piezoelectric constants up to 2300 pC/N and coupling coefficient  $k_{33} \sim 95\%$  can be achieved. For the converse effect, driving the crystals as actuators in the  $d_{33}$  mode, linear anhysteretic strain of 0.6% can be achieved and total strains up to 1.7% have been demonstrated. These outstanding properties only occur for specific orientations of the electric field with respect to the crystal axes and the anisotropy in response is exceptionally and surprisingly large. In practical transducing structures for first impact of these new capabilities will be in high frequency medical ultrasound where the capability to engineer very fine scale 1:3 type composites is already being demonstrated.

Preliminary studies of the mechanism giving rise to these outstanding properties suggest that the behavior is intrinsic and not domain related, and may thus persist in thin film structures broadening the potential area of applicability to many MEMS type systems.

In the more conventional polycrystal lead zirconate titanate composite systems the elegant injection molding method by Materials Systems Inc. is providing large area 1:3 PZT polymer composites of excellent sensitivity in both send and receive modes, and new types of smart panel incorporating both capabilities will be briefly reviewed.

For the modified flextensional "moonie" and "cymbal" structures it is pleasing to see that the moonie is now moving into substantial commercial production for hydrophone application. Recent work has focused upon the resonant characteristics of the cymbal and the possibility of dual frequency resonators by modifying the cap structures of upper and lower surfaces of the ceramic. Recent studies on large area cymbal arrays suggest that they may be even more effective than the 1:3 composite for large area low frequency sound in water transmission.

### 1. Introduction

In all the perovskite structure ferroelectric oxides which form the materials base for piezoelectric ceramic actuators and sensors, the electric polarization and shape changing processes are complex, involving both intrinsic changes within the ferroelectric domain and polarization and shape changes associated with domain and phase boundary motions (fig. 1). For the lead zirconate titanate (PZT) family which is much the most widely used piezoceramic, the poling which is essential to induce piezo-response in the randomly axed




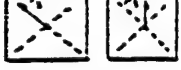
(A) HIGH FIELD		$E \uparrow$	
(1) INTRINSIC SINGLE DOMAIN POLARIZABILITY	$\alpha_i$		Normal piezoelectricity in the polar domain.
(2) 180° DOMAIN WALL MOTION	$\alpha_D(180)$		Polarization change with no shape change.
(3) FERROELASTIC WALL MOTION	$\alpha_D(e)$		Shape changing ferroelastic wall motion.
(4) FERROELECTRIC PHASE CHANGE	$\alpha_{FE}$		Shape changing phase boundary motion.

Figure 1  
Polarization and Deformation Mechanisms in Perovskite Oxide Ferroelectrics

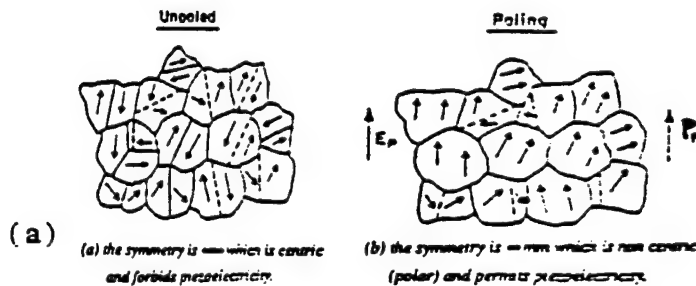


Figure 2a  
Poling in a Ferroelectric Ceramics

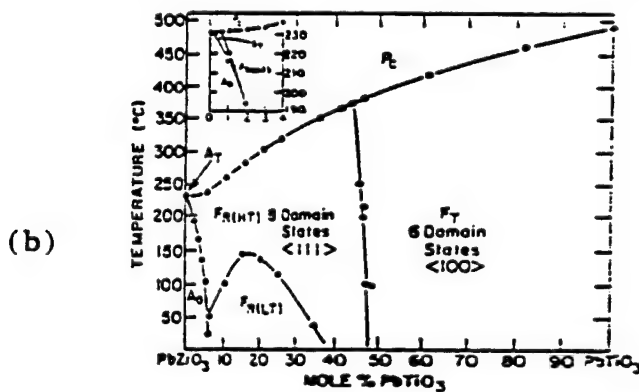


Figure 2b  
Lead Zirconate Titanate (PZT)  
Phase Diagram

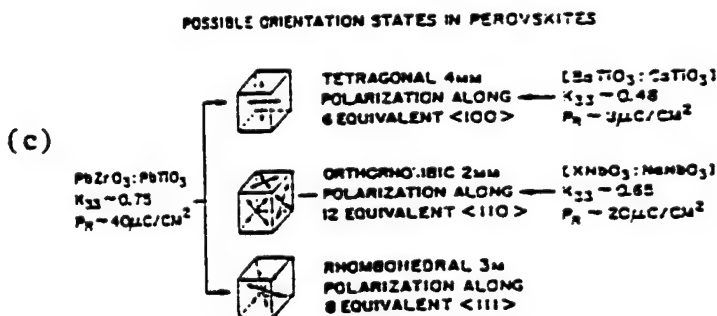


Figure 2c  
Domain Orientation States  
Available for Poling in Different  
Perovskite Ceramics



polycrystal (fig. 2a) is markedly aided by the presence of a morphotropic phase boundary (MPB) between tetragonal and rhombohedral ferroelectric phases (fig. 2b). This vertical boundary in the composition/temperature phase diagram is a first order phase change, so that metastable two-phase regions can persist and the poling process can make use of both tetragonal and rhombohedral domain states in compositions close to the 52/48 Zr/Ti ratio of the MPB.

A wide range of aliovalent substituents have been used to modify and control the extrinsic domain contribution to piezoelectric response in practical transducer ceramics however for a very broad range of PZT and similar compositions in the poled ceramic form there is a clear trend between the maximum achieved piezoelectric constant  $d_{33}$  and the Curie temperature of the ferroelectric phase (fig. 3) which suggests a strong intrinsic contribution, at least in these higher sensitivity systems.

To separate and understand the response mechanisms it would be most valuable to have single crystals which could be converted to single domain states where the full three dimensional elasto-dielectric response could be explored. In the PZT composition near the 'magic' MPB, crystal growth has proven impossibly difficult, however there are a number of lead based relaxor-ferroelectric compositions such as lead magnesium niobate ( $\text{PbMg}_{1/3}\text{Nb}_{2/3}\text{O}_3$  PMN) and lead zinc niobate ( $\text{PbZn}_{1/3}\text{Nb}_{2/3}\text{O}_3$  PZN) which form three component solid solutions with PZT where the MPB extends over to the relaxor:lead titanate join (fig. 4). It is single crystals of composition close to morphotropy in the PZN:PT and PMN:PT systems which are the subject of the major part of this report.

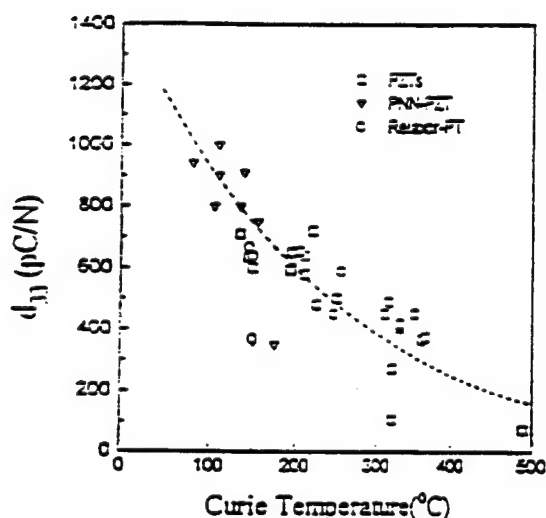


Figure 3

Piezoelectric Response  $d_{33}$  as a Function of Curie Temperature for a Wide Range of 'Soft' PZT Based and Relaxor Ferroelectric Ceramics

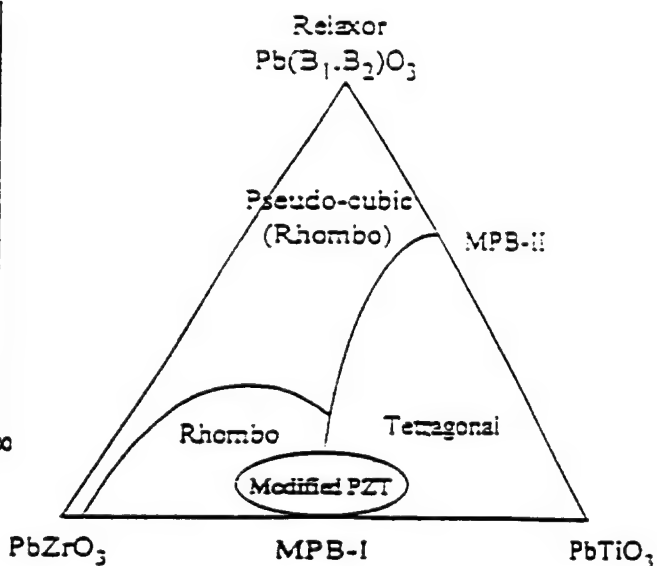


Figure 4

Typical Phase Diagram for a Three Component Lead Zirconate:Lead Titanate Relaxor Ferroelectric Solid Solution, Showing the Location of the MPB

## 2. Crystal Growth

In the Materials Research Laboratory at Penn State, Park and Shrout [1] have grown single crystals of PMN:PT and PZN:PT at compositions close to the pseudo-MPB systems by flux methods. Using excess lead oxide as the flux and a soak temperature in the range 1100 to 1200°C, followed by slow cooling, crystals in the range 3 to 20 mm cube were grown. Crystals in the systems PMN:PT have also been grown by Bridgman method in a sealed crucible [2], by enhanced grain growth in a polycrystal matrix [3], and by hydrothermal methods [4].

Crystals grown by the flux method can be extracted from the melt using hot nitric acid. In general the PMN:PT system would appear to be the more tractable, and even in pure PZN, care must be exercised to avoid incorporation of the alternative pyrochlore structure form. Crystals can be oriented using Laue method and thin sections cut in 001 and 111 orientation have been extensively explored.

## 3. Dielectric and Piezoelectric Properties

In PZN:PT, the morphotropic phase boundary occurs at 0.09 mole fraction PT with a Curie temperature (Diffuse) at 170°C, whilst in PMN:PT the MPB composition is 0.33 PT with  $T_c$  at 150°C. Early studies of PZN, PZN:PT, and PMN:PT (Table 1) showed most exciting properties for 001 cut sections which is surprising since these compositions are in the rhombohedral ferroelectric phase, where the  $\langle 111 \rangle$  family of directions are the domain polar vector orientations. More detailed studies of  $d_{33}$  as a function of composition in PZN:PT confirms the massive values of  $d_{33}$  for the  $\langle 001 \rangle$  cut, and the much smaller values for  $\langle 111 \rangle$  (fig. 5). Both dielectric response and piezoelectric coupling  $k_{33}$  show exceptionally large values over the full range from 20°C to over 100°C (fig. 6).

That the single crystal behavior breaks completely new ground in piezoelectricity may be judged from the jump in  $d_{33}$  value afforded by the PZN:PT system over all earlier piezoceramics (fig. 7).

Of even more compelling interest is the potential actuator performance in the poled 001 oriented PZN:PT. The almost linear response both in  $P_3$  and in  $S_{33}$  up to strain levels of  $\sim 0.6\%$  is evident in fig. 8, and the ultra high strain capability for both families as compared to conventional ceramics is evidenced in fig. 9.

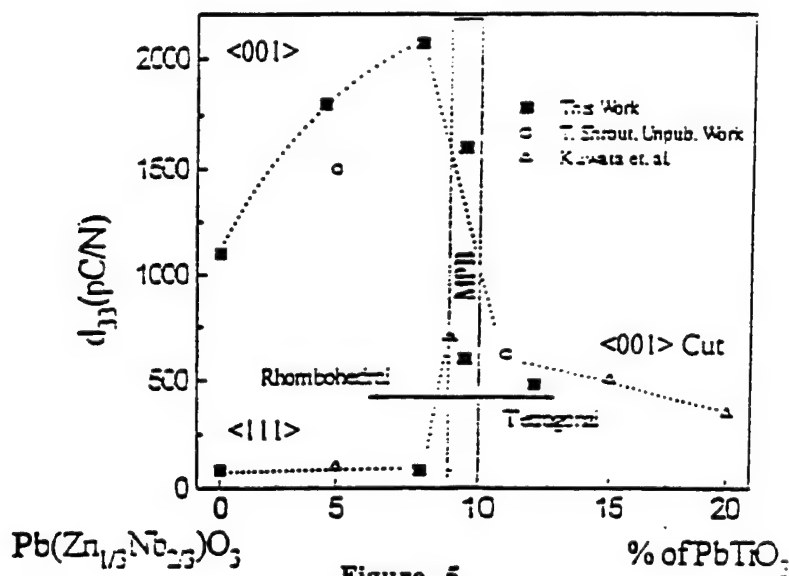


Figure 5  
Piezoelectric  $d_{33}$  in Poled PZN:PT Solid Solutions as a  
Function of Composition for 111 Oriented and 001 Oriented Crystal Cuts

Table 1

Evidence of Exceptional Dielectric and Piezoelectric Response in 111 Oriented PZN:PT and PMN:PT Single Crystals for Rhombohedral Symmetry Compositions Close to the Morphotropic Phase Boundary

Material	Transiti on Temp. $T_c$	Dielectric Constant (loss) K	Piezoelectric $d_{31}, d_{33}$ : $\times 10^{-12}$ C/N	Properties $k_{31}, k_{33}$ : Coupling	Elastic $s_{11}$ $\times 10^{-12}$	Constants $s_{33}$ $m^2/N$	Freq. Consts. (Hz:m)
PZN							
$\langle 111 \rangle$	$-140^\circ\text{C}$	900	-57,92	: -12%;	29.9	7.2	1,000; 2,058
$\langle 001 \rangle$		2850	-470,1612	: 37.7% -39.7%; 85.2%	55.1	42.0	743; 1,521
PZN-PT							
$\langle 111 \rangle$	$-176^\circ\text{C}$	4300 (0.007)	-1020,509  -320,1815	: -79.8%; 64.4%	42.9	9.6	842; 2,240
$\langle 001 \rangle$		1400 (0.004)		: -55.3%; 89.4%	26.8	66.2	1,065; 1403
PMN-PT	$-160^\circ\text{C}$	3120 (0.014)	-320, 2,900	: -41.4%; 91.9%	22.0	55.9	1,175; 1,730
PZT-5H	$-190^\circ\text{C}$	3,400 (.02)	-274,590	: -38%; 75%	16.5	9.0	1,400; 2,000
DOD Type II							

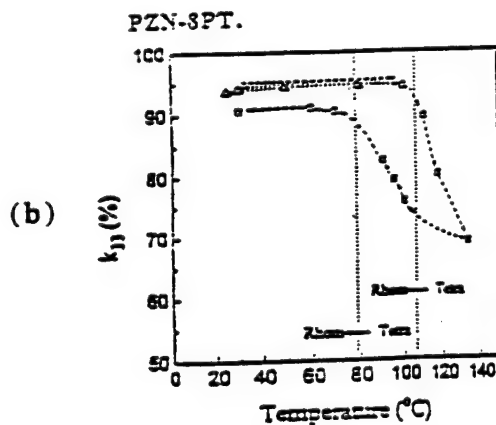
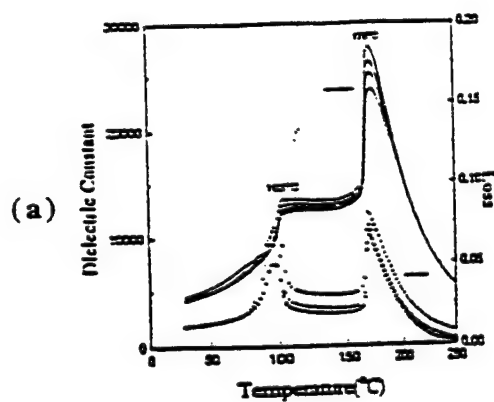
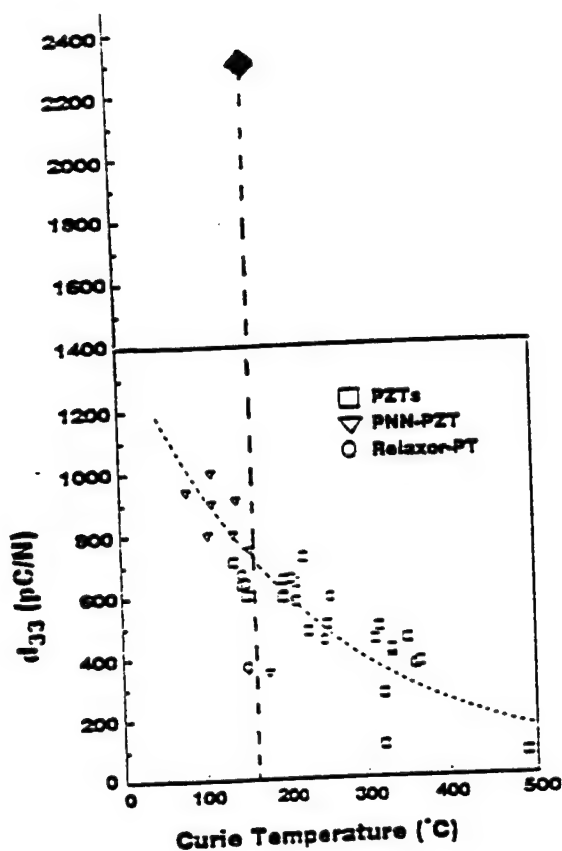
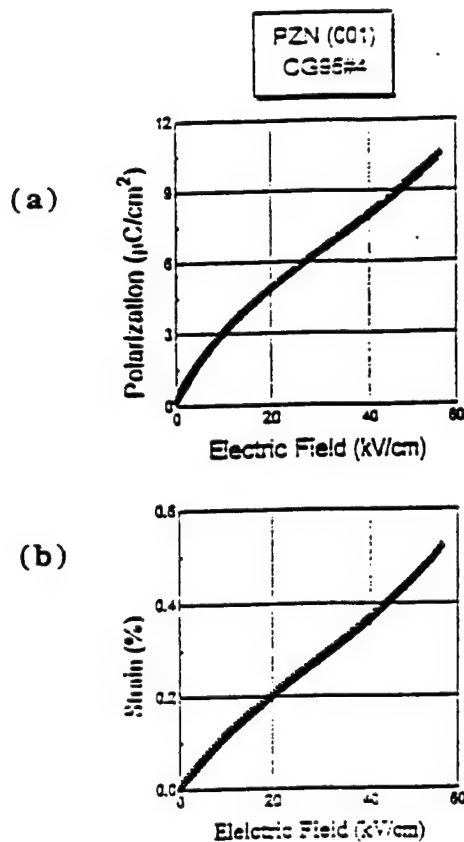


Figure 6

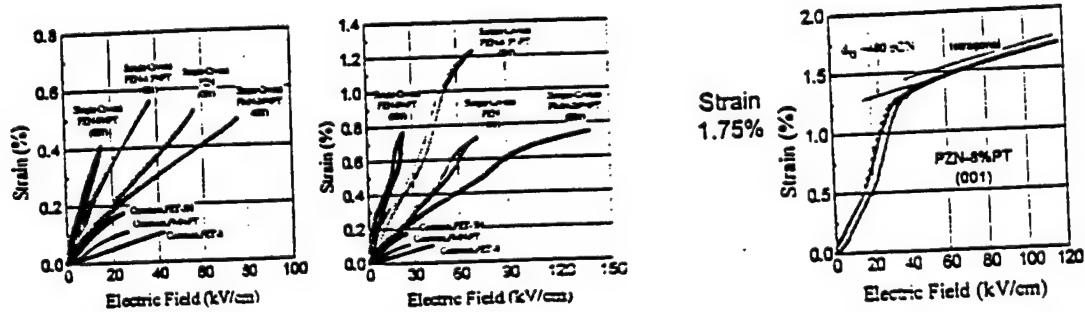
- (a) Dielectric Response for PZN:0.08 PT vs Temperature.  
 (b) Piezoelectric Coupling Constant  $k_{33}$  vs T for PZN:0.08 PT 111 Poled Single Crystal.



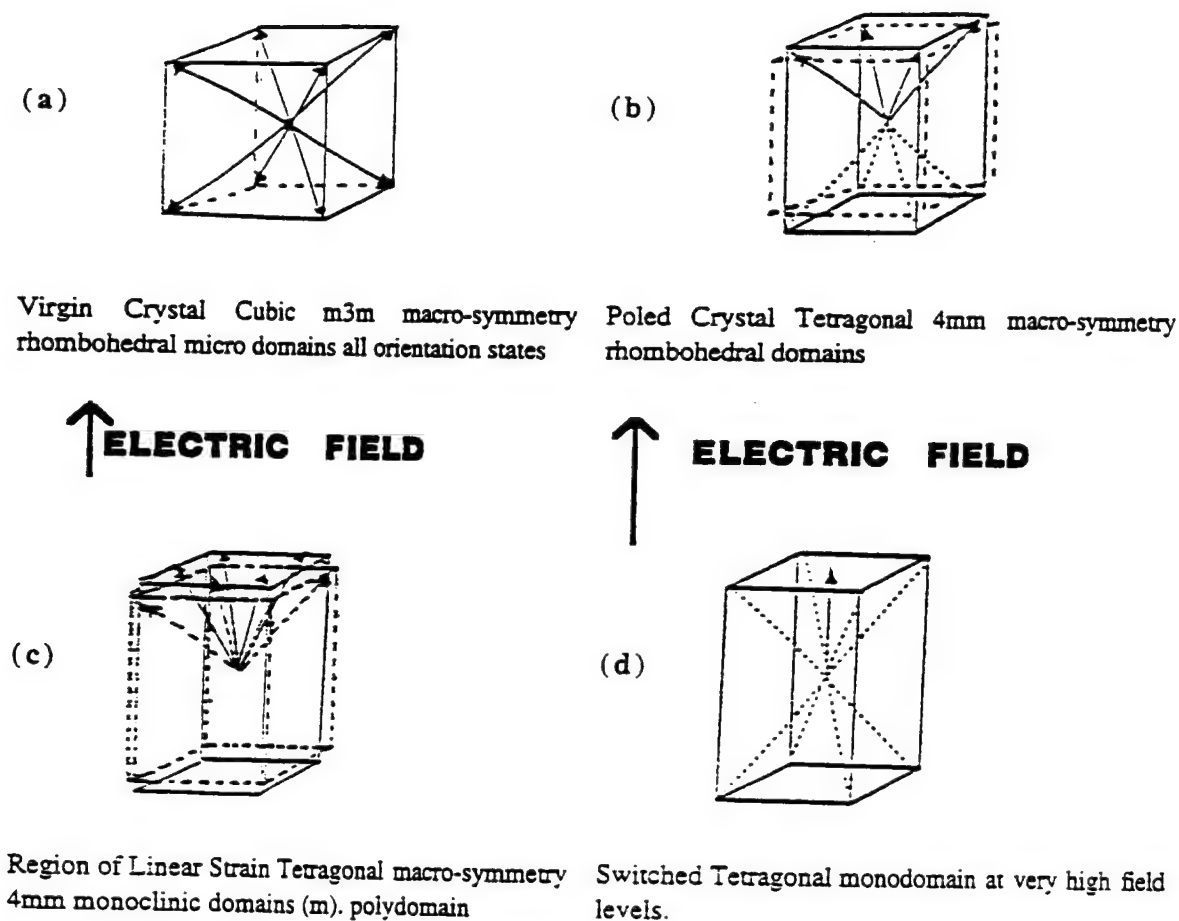
**Figure 7**  
Piezoelectric  $d_{33}$  of PZN:0.08 PT 111 Oriented  
Poled Single Crystal. Compared to a Wide Range  
of Soft PZT Ceramics.



**Figure 8**  
Polarization and Elastic Strain  $S_3$  vs E field in  
111 Poled Pure PZN.



**Figure 9**  
**High Field High Strain Behavior in PZN:PT and PMN:PT Single Crystals.**



**Figure 10**  
Possible Polarization Changes in PZN:PT under High  $E_3$  Fields.

Just for the 001 oriented field in the rhombohedral phase, it is evident that once  $180^\circ$  domain switch has been accomplished to the poled state (fig. 10b), there is no longer any drive to more domain walls between the different remaining  $\langle 111 \rangle$  orientation.

We believe that the balance of polarization change may then be tilting of  $P_s$  towards 001 (fig. 10c), until the phase switch to the 001 tetragonal orientation. If indeed the polarization mechanism is dominantly intrinsic of this form, then perhaps similar performance may be expected in epitaxial single crystal films which could address a much wider market.

#### 4. Composite Transducers

For more than twenty years, the ferroelectric group in MRL has been exploring a wide range of composite approaches to modify and control the piezoelectric tensor properties available in PZT piezoceramics. Early work on the 1:3 connected composite (fig. 11a) was taken up strongly by the medical ultrasound community and is now widely used in imaging arrays. The original design was in fact for Naval undersea

application, and it is only very recently through the imaginative injection moulding techniques pioneered by MSI, Inc. that large area 1:3 PZT:polymer panels have become available, and smart systems which incorporate both accelerometer sensor and actuator are becoming available (fig. 11b).

A very simple modification of the classical Navy flexensional transducer, the moonie (fig. 12) was also pioneered in our laboratory and a more recent variant, the cymbal (fig. 12b) is much simpler to fabricate. It is pleasing to note that the moonie, which has excellent hydrostatic response and very wide dynamic range is now coming into extensive use in towed arrays and in oil exploration and monitoring systems. An interesting facet of both moonie and cymbal actuators is that by modification of upper and lower cap geometry it is possible to make the composite resonate at two widely separated frequencies (fig. 13).

Currently the interest is in two dimensional cymbal arrays which promise to have even better hydrostatic sensitivity than the best 1:3 composites, both in send and receive modes.

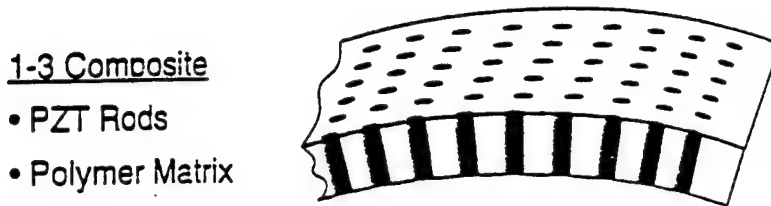


Figure 11 (a)  
Typical 1:3 PZT Polymer Composite.

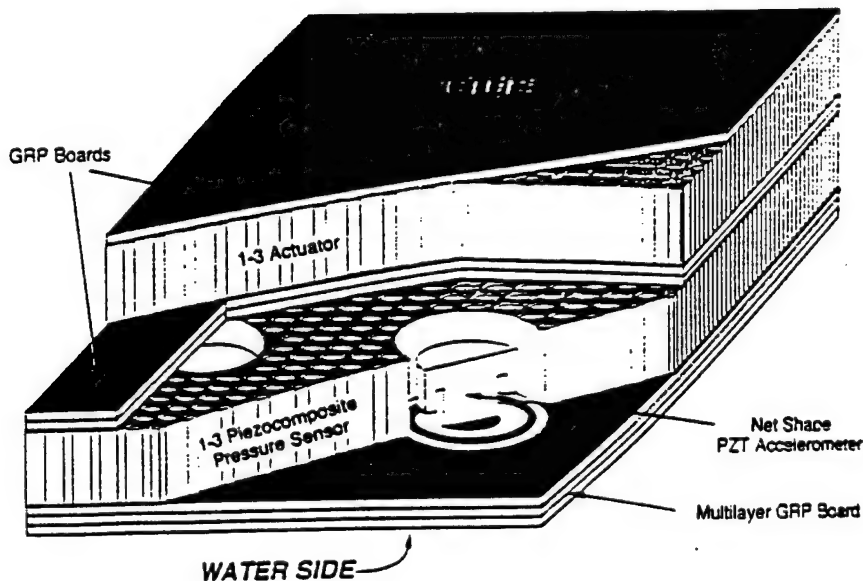
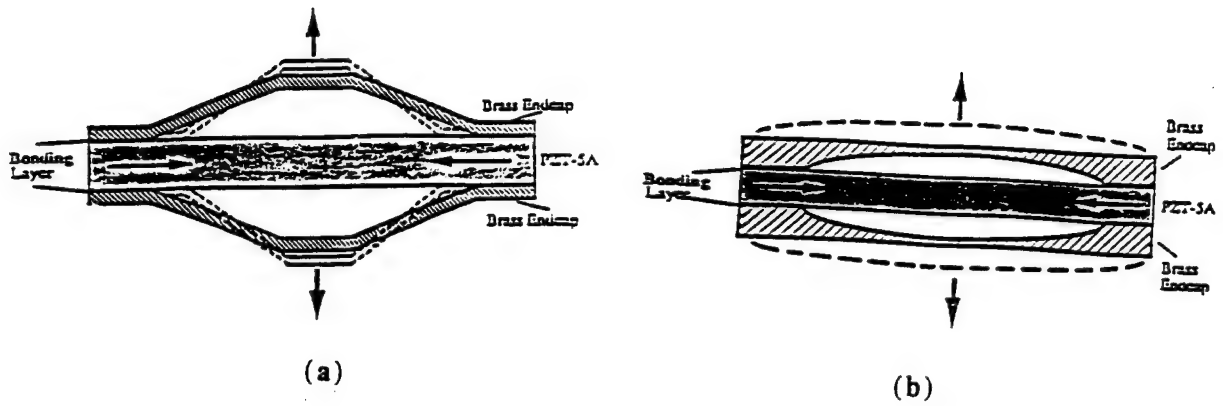
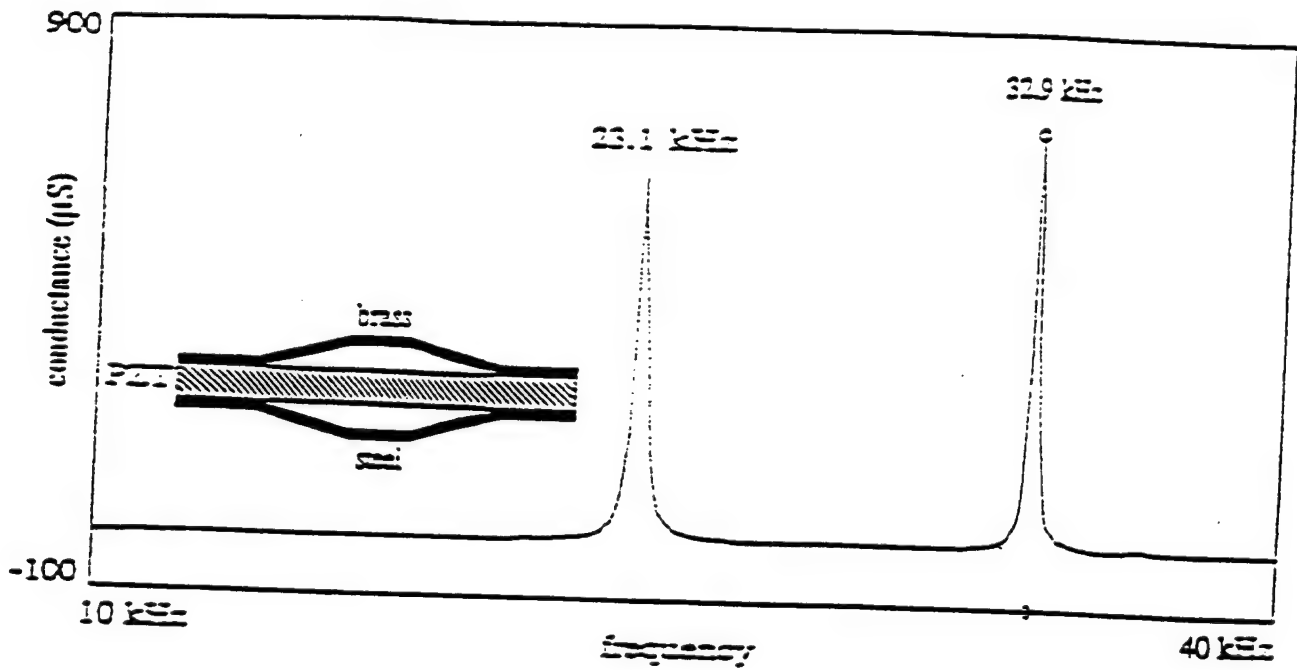


Figure 11 (b)  
MSI Smart Skin Incorporating Sensor, Actuator and Accelerometer Components.



**Figure 12**

- (a) Cymbal Actuator in Cross-Section.  
 (b) Moonie Composite Actuator Cross Section.



**Figure 13**

Dual Resonance Characteristics of a Cymbal Actuator with Different Amplifier Plates on Upper and Lower Surfaces.



# **APPENDIX 2**

## *Chapter Thirteen*

# **FUNCTIONAL COMPOSITES FOR SENSORS AND ACTUATORS: Smart Materials**

**ROBERT E. NEWNHAM**

Materials Research Laboratory  
Pennsylvania State University  
University Park, PA 16802

### **ABSTRACT**

"Smart" materials have the ability to perform both sensing and actuating functions. Passively smart materials respond to external change in a useful manner without assistance, while actively smart materials have a feedback loop which allows them to both recognize the change and initiate an appropriate response through an actuator circuit.

One of the techniques used to impart intelligence into materials is "Biomimetics," the imitation of biological functions in engineering materials. Composite ferroelectrics fashioned after the lateral line and swim bladders of fish are used to illustrate the idea. "Very Smart" materials, in addition to sensing and actuating, have the ability to "learn" by altering their property coefficients in response to the environment. Field-induced changes in the nonlinear properties of relaxor ferroelectrics and soft rubber are utilized to construct tunable transducers. Integration of multifunctional ferroic ceramics into compact, robust packages is a major goal in the development of smart materials.

### **INTRODUCTION**

It has been said that life itself is motion, from the single cell to the most complex organism: the human body. This motion, in the form of mobility, change, and adaptation, is what elevates living beings above the lifeless forms (Rogers, 1990). This concept of creating a higher form of materials and structures by

providing the necessary life functions of sensing, actuating, control, and intelligence to those materials is the motivation for studying smart materials.

Smart materials are part of smart systems - functional materials for a variety of engineering applications. Smart medical systems for the treatment of diabetes with blood sugar sensors and insulin delivery pumps. Smart airplane wings that achieve greater fuel efficiency by altering their shape in response to air pressure and flying speed. Smart toilets that analyze urine as an early warning system for health problems. Smart structures in outer space incorporating vibration cancellation systems that compensate for the absence of gravity and prevent metal fatigue. Smart houses with electrochromic windows that control the flow of heat and light in response to weather changes and human activity. Smart tennis rackets with rapid internal adjustments for overhead smashes and delicate drop shots. Smart muscle implants made from rubbery gels that respond to electric fields, and smart dental braces made from shape memory alloys. Smart hulls and propulsion systems for navy ships and submarines that detect flow noise, remove turbulence, and prevent detection. Smart water purification systems that sense and remove noxious pollutants. As indicated later, modern automobiles already contain a wide variety of sensors and actuators, but there are many more to come. In a recent newspaper cartoon, Blondie and Dagwood encountered a smart automobile that drives itself back to the finance company when the owner misses a payment!

In this chapter the idea of "smartness" in a material is discussed, along with a number of examples involving ferroelectric components. Some of these smart ceramics are in production, while others have great potential but are thus far limited to laboratory investigations.

To begin our discussion, we first define "smart" to set the limits for classifying smart materials.

## PASSIVE SMARTNESS

A passively smart material has the ability to respond to environmental conditions in a useful manner. It differs from an actively smart material in that there are no external fields or forces or feedback systems used to enhance its behavior. Many passively smart materials incorporate self-repair mechanisms or stand-by phenomena which enable the material to withstand sudden changes in the surroundings. The crack-arresting mechanisms in partially stabilized zirconia are a good example. Here the tetragonal-monoclinic phase change accompanied by ferroelastic twin wall motion are the stand-by phenomena capable of generating compressive stresses at the crack tip. In a similar way, toughness can be improved by fiber pull-out or by multiple crack-branching as in the structural composites used in aircraft, or in machinable glass-ceramics.

Ceramic varistors and PTC thermistors are also passively smart materials. When struck by high-voltage lightning, a zinc oxide varistor loses most of its electrical resistance and the current is by-passed to ground. The resistance change is

reversible and acts as a stand-by protection phenomenon. Varistors also have a self-repair mechanism in which its highly nonlinear I-V relationship can be restored by repeated application of voltage pulses. Barium titanate PTC thermistors show a very large increase in electrical resistance at the ferroelectric phase transformation near 130°C. The jump in resistance enables the thermistor to arrest current surges, again acting as a protection element. The R(V) behavior of the varistor and the R(T) behavior of the PTC thermistor are both highly nonlinear effects which act as standby protection phenomena, and make the ceramics smart in a passive mode.

### ACTIVE SMARTNESS

A smart ceramic can also be defined with reference to sensing and actuating functions, in analogy to the human body. A smart ceramic senses a change in the environment, and using a feedback system, makes a useful response. It is both a sensor and an actuator. Examples include vibration damping systems for outer space platforms and electrically-controlled automobile suspension systems using piezoelectric ceramic sensors and actuators. Other sensor-actuator combinations are illustrated in Figure 1.

A video tape head positioner developed by Piezoelectric Products, Inc., operates on this principle. A bilaminate bender made from tape-cast PZT ceramic has a segmented electrode pattern dividing the sensing and actuating functions of the positioner. The voltage across the sensing electrode is processed through the feedback system resulting in a voltage across the positioning electrodes. This causes the cantilevered bimorph to bend, following the video tape track path. Articulated sensing and positioning electrodes operating at 450Hz near the tape head help keep the head perpendicular to the track.

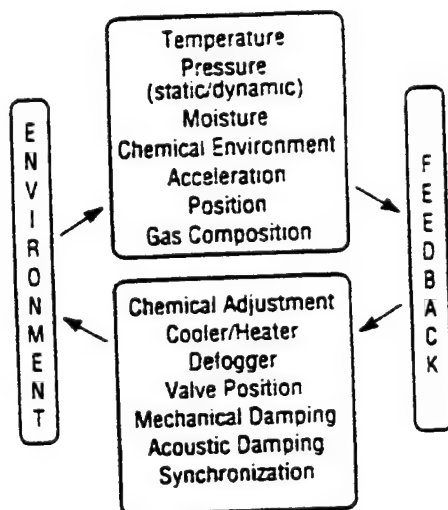


FIGURE 1. Examples of sensing and actuating functions in actively smart system.

## RUBBER-LIKE CERAMICS

Every baseball and cricket player knows the importance of "soft hands." In catching a baseball, it is important to withdraw the hands slightly on making contact with the ball. This reduces the momentum of the ball gradually and creates a soft landing. Soft landings are achieved on ceramics in the same way, making them feel as soft as rubber.

To test the concept, controlled compliance experiments have been carried out using PZT sensors and actuators (Newnham et al., 1989). In the test set-up, (Figure 2) one actuator is used as the external driver, and the other as the responder. Sandwiched between the two actuator stacks are two sensors and a layer of rubber.

The upper actuator is driven at a frequency of 100 Hz and the vibrations are monitored with the upper sensor. The pressure wave emanating from the driver passes through the upper sensor and the rubber separator and impinges on the lower sensor. The resulting signal is amplified using a low noise amplifier and fed back through a phase shifter to the lower actuator to control the compliance.

A smart sensor-actuator system can mimic a very stiff solid or a very compliant rubber. This can be done while retaining great strength under static loading, making the smart material especially attractive for vibration control.

If the phase of the feedback voltage is adjusted to cause the responder to contract in length rather than expand, the smart material mimics a very soft, compliant substance. This reduces the force on the sensors and partially eliminates the reflected signal. The reduction in output signal of the upper sensor is a measure of the effectiveness of the feedback system. In our experiments, the compliance of the actuator-sensor composite was reduced by a factor of six compared to rubber (Newnham et al., 1989).

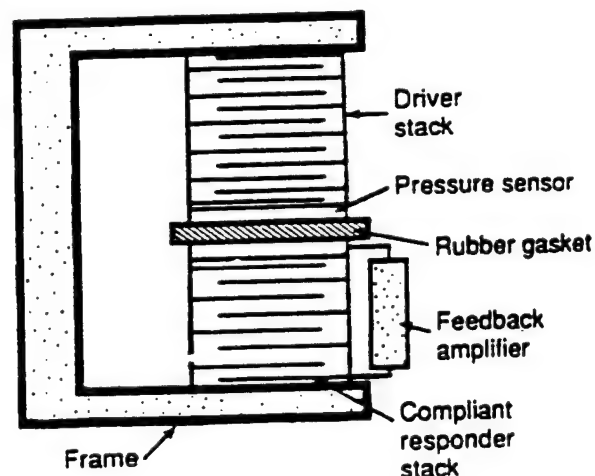


FIGURE 2. Fixture for experimental evaluation of smart materials with controlled compliance.

## MODULATED SUSPENSION SYSTEMS

The automobile industry is a very large market in which smart composites and sensors are already widely used. More than fifty electroceramic components can be found in today's high-tech autos, ranging from the air-fuel oxygen sensors used in most autos to the more exotic piezoelectric raindrop sensor, which automatically senses the amount of rain falling, and adjusts the windshield wipers to the optimum speed (Taguchi, 1987).

Controlled compliance with piezoelectric ceramics is utilized in Toyota's piezoTEMS (Toyota Electronic Modulated Suspension), a system which has been developed to improve the drivability and stability of the automobile, and at the same time enhance passenger comfort (Fukami et al., 1994). The TEMS is basically a road stability sensor and shock adjustor, which detects bumps, dips, rough pavement, and sudden lurches by the vehicle, then rapidly adjusts the shock absorbers to apply a softer or firmer damping force, depending on what is necessary to minimize discomfort while maintaining control of the vehicle. The shock absorbers are continuously readjusted as the road conditions change so that rocking or wobbling on soft shocks is eliminated.

The TEMS road surface sensor consists of a five-layer piezoelectric ceramic sensor mounted on the piston rod of the shock absorber. When a bump in the road is encountered, the resulting stress applied to the sensor produces a voltage which is fed into an electronic control unit that amplifies the signal and supplies a high voltage to the piezoelectric actuator. The 88-layer PZT actuator produces a 50  $\mu\text{m}$  displacement on the oil system which is hydraulically enlarged to two millimeters, enough to change the damping force from firm to soft: the entire process takes only about twenty milliseconds (not even enough time to slam on the brakes!). Also figured into the actuator output are the vehicle speed and the driver's preference for a generally softer (American) or firmer (European) ride.

Alternatively, it is possible to damp stresses and vibrations without the need for a sensor-actuator feedback loop; materials which can perform this function are called passive damping materials. In a piezoelectric passive damper, a piezoelectric ceramic is connected in parallel with a properly matched resistor. The external stress creates a polarization in the piezoelectric, which induces a current in the resistor, leading to energy dissipation. A high piezoelectric coupling coefficient is required to induce the maximum voltage and energy dissipation (Suzuki, et al., 1991) (Figure 3).

## ACTUATOR MATERIALS

Two of the most popular actuators are the multilayer and bimorph designs shown in Figure 4. The multilayer has fast response, low drive voltage, and high generative force, but only micron-size motions, whereas bimorphs are capable of millimeter movements, but are slow, weak, and unreliable. The moonie is an

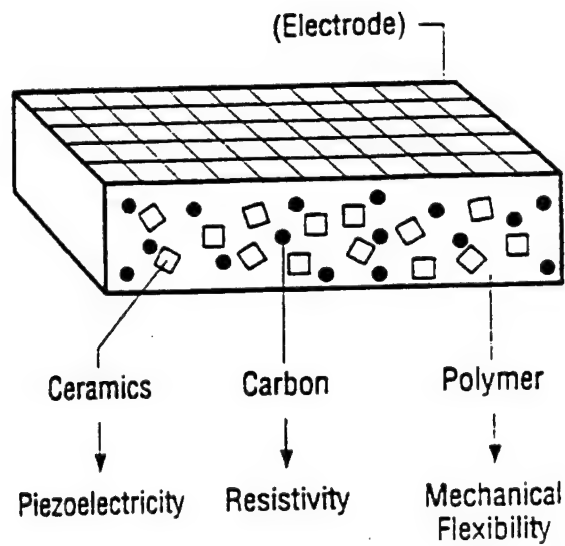


FIGURE 3. Composite damper consisting of piezoelectric PZT grains and conducting carbon grains embedded in a flexible polymer matrix.

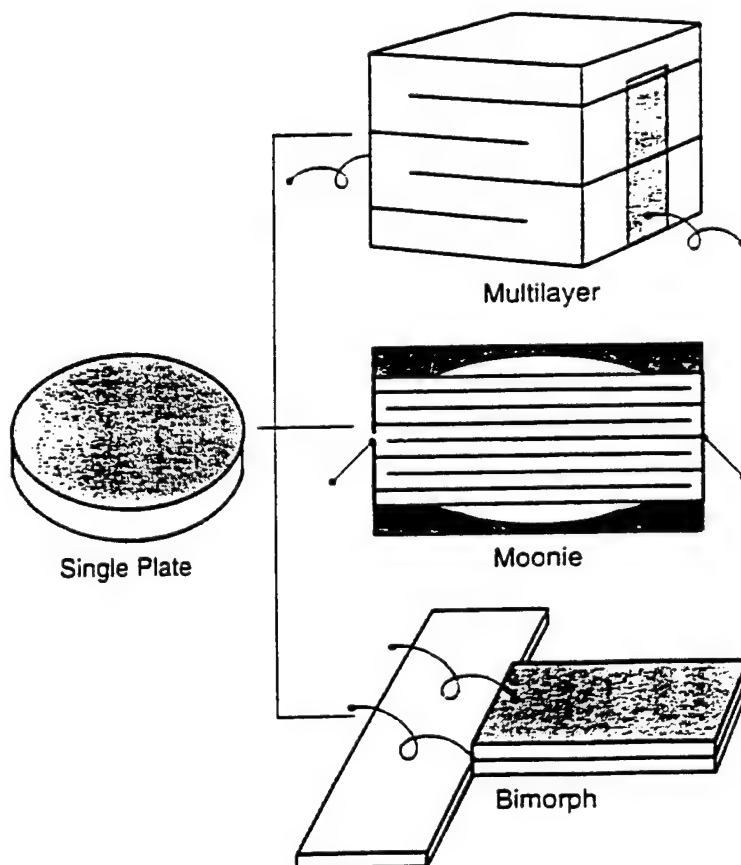


FIGURE 4. Typical designs for ceramic actuators: multilayer, moonie, and bimorph.



excellent compromise which retains the low drive voltage and amplifies the motion with bonded metal caps operating in a flextensional mode (Uchino, 1993).

There are many approaches to controlling vibration and structural deformation. Actuation strain can be controlled by piezoelectric materials (Burke and Hubbard, 1987), electrostrictive materials (Uchino, 1986), magnetostrictive materials (Hathaway and Clark, 1993), shape-memory metal alloys (Schetky, 1979), and thermally-controllable materials (Edberg, 1987). Utilizing a system with distributed actuators, it is possible to design structures with intrinsic vibration and shape control capabilities. Among the most important actuator materials are shape memory metals and ceramics. The shape memory effect is exhibited by alloys which undergo thermoelastic martensite transformations. This is a first order displacive transformation in which a body centered cubic metal transforms by shear on cooling to a martensitic phase. When deformed in the martensitic low temperature phase, shape memory alloys will recover this deformation and return to the original shape when heated to a temperature where the martensite reverts back to the parent body-centered cubic structure. Unlike most ferroelectric and ferromagnetic transitions, the shape memory transformation has a large hysteresis which can be troublesome in practice. Non-ferrous shape memory alloys of nickel-titanium alloy (Nitinol) have been developed by Goodyear Aerospace Corporation for spacecraft antennae (Schetky, 1979). A wire hemisphere of the material is crumpled into a tight ball, less than five centimeters across. When heated above 77°C, the ball opens up into its original shape—a fully formed antenna. Although it has seldom been used in service, this antenna demonstrates the magnitude of deformation and reformation possible in shape memory alloys.

While shape memory alloys are more like a solution looking for a problem, it has been suggested that transient and steady state vibration control can be accomplished with hybrid structures in which the shape memory alloy is embedded inside the material (Rogers et al., 1989).

Some ceramic materials also possess a sizeable shape-memory effect; of particular interest are materials which are simultaneously ferroelectric and ferroelastic. Their ferroelasticity ensures that recoverable spontaneous strain is available for contributing to the shape memory effect, and the ferroelectricity implies that their spontaneous strain can be manipulated not only by mechanical forces but also by electric fields (Wadhawan et al., 1981).

## ELECTRORHEOLOGICAL FLUIDS

One of the criteria which separates "smart" materials from "very smart" or "intelligent" materials is the ability of the material to not only sense a change and actuate a response, but to automatically modify one or more of its property coefficients during the sensing/actuating process. In effect, this type of material not only warns the user of a change in its environmental conditions and responds to it, but can in addition adjust itself to compensate for future change.

Electrorheological (ER) fluids (Ghandi and Thompson, 1989), and their magnetic analog, ferrofluids (Rosenweg, 1985), are an example of materials that have great potential for use in smart materials and systems. ER fluids are typically suspensions of fine particles in a liquid medium: the viscosity of the suspension can be changed dramatically by applying an electrical field. The electric field causes alignment of the particles in fibril-like branches in the direction of the applied field. The alignment disappears when the electric field is removed, thus creating the desired property of complete cyclic reproducibility.

ER fluids represent an advanced class of composite materials with self-tuning properties, that will find considerable use in vibration control applications. In addition, the compatibility of this technology with modern solid state electronics makes it an attractive component for integration into multifunction, self-contained smart material packages.

### BIOMIMETICS - FISH EARS

The word "biomimetic" is not found in most dictionaries so it needs to be defined. It comes from the Greek words "bios," meaning "life," and "mimetikos," meaning "to imitate." Biomimetic means to imitate life, or to use the biological world as a source of ideas for device concepts.

Fish and the other inhabitants of the underwater world have some interesting ways of talking and listening which have been copied using piezoelectric ceramics. For most fish, the principal sensors are the *lateral line* and the *inner ear* coupled to the *swim bladder*. The pulsating swim bladder also acts as a voice, as do chattering teeth in certain fish species.

The lateral line runs from the head to the tail of the fish and resembles a towed array with sensing organs (stitches) spaced at intervals along the nerve fiber. Each stitch contains several neuromasts made up of gelatinous cupulae resembling pimples in shape, and within each cupula are several fibers which vibrate as the fish swims through water and act as sensors for flow noise. The hair-like fibers are extremely thin in diameter ranging from 0.5 to 10  $\mu\text{m}$ . When stimulated by turbulence, the motion of the hairs produces changes in the synapses which are in turn connected to the nerve fiber. The electric signal originates from impedance changes in cell walls which modulate the flow of  $\text{K}^+$  ions. The lateral line is especially sensitive to low frequency fluid motion parallel to the length of the fish. In the 50 Hz range, threshold signals are observed for displacements as small as 30 nm! (Bond, 1979; Moyle and Cech, 1988).

The 1-3 composite hydrophones described later are patterned after the hair-filled cupulae of the lateral line. Thin PZT fibers embedded in polymer provide excellent electromechanical coupling to a liquid medium and can be used as both sensors and actuators.

The primary function of the gas-filled swim bladder is to provide buoyancy, but

it is also used for sound and pressure reception and in some species is equipped with drumming muscles for sound production. The flexible swim bladder responds to hydrostatic pressure waves by changing volume. Fish with swim bladders can perceive relative pressure changes equivalent to less than 0.5% of the ambient hydrostatic pressure. Direct or indirect linkages from the swim bladder to the inner ear promote the hearing sensation. Fish with no connections perceive low frequency sound (less than 500 Hz), while those with good connections have an upper frequency response of 5000 Hz. As might be expected, the swim bladder is reduced in size with depth, and loses much of its sensitivity as a sensor. The flextensional Moonie transducer (Figure 4) mimics the swim bladder of a fish.

## HYDROPHONE MATERIALS

The knowledge which comes from the understanding of "fish talk" can be directly applied to research in materials destined to someday "sleep with the fishes". Hydrophones are underwater listening devices made from piezoelectric materials which respond to hydrostatic pressure waves. Among the applications for hydrophones are sonar systems for submarines, off-shore oil platforms, geophysical prospecting equipment, fish finders, and earthquake monitors.

As the earth's population continues to increase, mankind must continue to search for new and efficient sources of food and nutrition. The world's oceans may provide a solution to this problem, not only through fish farming but through the use of new and varied salt water vegetation that could provide an abundant source of food, especially for third world countries in which poor soil and harsh climates prohibit conventional farming. Smart hydrophone transceivers will receive and transmit fish talk and monitor the growth of underwater vegetation.

The figure of merit for hydrophone materials is the product of the hydrostatic piezoelectric charge coefficient ( $d_h$ ) and the piezoelectric voltage coefficient ( $g_h$ ). While good piezoelectric materials such as PZT have high  $d_{33}$  and  $d_{31}$  piezoelectric coupling coefficients, the  $d_h$  value is only about 45 pC/N because  $d_{33}$  and  $d_{31}$  are opposite in sign, and  $d_h = d_{33} + 2d_{31}$ .  $d_h g_h$  is also inversely related to the dielectric permittivity,  $\epsilon_{33}$ , so that low dielectric constants are desirable as well.

Rather than abandon PZT in search of the ultimate hydrophone material, avoiding this problem is often a matter of appropriate engineering of existing materials. Too often in the field of materials research we put too much emphasis on the synthesis of new materials and too little emphasis on new and unique designs for old materials.

A composite design with 1-3 connectivity is similar in design to the hair-filled gelatinous cupula with thin PZT rods embedded in a polymer matrix. The 1-3 piezocomposites have excellent sensitivity to pressure waves in water (Klicker et al., 1981; Gurusaraja et al., 1984). The large  $d_{33}$  is maintained because the parallel connection results in stress transfer from polymer to piezoceramic, while the  $d_{31}$  is destroyed because of series connection in the lateral dimension where the

mechanical load is absorbed by the polymer and not transferred to the PZT rods. Finally,  $\epsilon_{33}$  is minimized due to the large volume of low  $\epsilon_{33}$  polymer present. The  $d_{hg}$  values are improved by more than an order of magnitude when very thin rods are used.

Another piezoelectric hydrophone composite maximizes  $d_h$  by simply redirecting the applied stresses using specially shaped electrodes (Xu et al., 1991). These are flextensional transducers which mimic the motions of the swim bladder. Shallow air spaces are positioned under the metal electrodes while the PZT ceramic plays the role of the muscle lining the swim bladder. When subjected to a hydrostatic stress, the thick metallic electrodes convert a portion of the  $z$ -direction stress into large radial and tangential stresses of opposite signs. The result is that  $d_{31}$  changes from negative to positive, so that its contribution now adds to  $d_{33}$  rather than subtracting from it. The  $d_{hg}$  of these composites is approximately 250 times that of pure PZT.

### VERY SMART COMPOSITES: THE TUNABLE TRANSDUCER

By building in a learning function, the definition of a smart material can be extended to a higher level of intelligence: *A very smart material senses a change in the environment and responds by changing one or more of its property coefficients. Such a material can tune its sensor and actuator functions in time and space to optimize future behavior.* With the help of a feedback system, a very smart material becomes smarter with age, something even human beings strive for. The distinction between smart and very smart materials is essentially one between linear and nonlinear properties. The physical properties of nonlinear materials can be adjusted by bias fields or forces to control response.

To illustrate the concept of a very smart material, we describe the tunable transducer recently developed in our laboratory. Five important properties of a transducer are the resonant frequency  $f_r$ , the acoustic impedance  $Z_A$ , the mechanical damping coefficient  $Q$ , the electromechanical coupling factor  $k$ , and the electrical impedance  $Z_E$ . The resonant frequency and acoustic impedance are controlled by the elastic constants and density, as discussed in the next section. The mechanical  $Q$  is governed by the damping coefficient ( $\alpha$ ) and is important because it controls "ringing" in the transducer. Definitions of the coefficients are given in Table 1.

Electromechanical coupling coefficients are controlled by the piezoelectric coefficient which, in turn, can be controlled and fine-tuned using relaxor ferroelectrics with large electrostrictive effects. The dielectric "constant" of relaxor ferroelectrics depends markedly on DC bias fields, allowing the electrical impedance to be tuned over a wide range as well. In the following sections we describe the nature of nonlinearity and how it controls the properties of a tunable transducer.

TABLE 1.  
Important characteristics of an electromechanical transducer.

Fundamental resonant frequency, $f$ , of the thickness mode	$f = \frac{1}{2t} \sqrt{\frac{c}{\rho}}$	where $t$ = thickness dimension. $c$ = elastic stiffness. $\rho$ = density
Acoustic Impedance $Z_A$	$ Z_A  = \sqrt{\rho \cdot c}$	where $c$ = elastic stiffness. $\rho$ = density
Mechanical Q	$Q = \frac{\pi}{\lambda_s \cdot \alpha}$	where $\lambda_s$ = acoustic wavelength $\alpha$ = damping coefficient
Electromechanical coupling coefficient $k$	$k = d \sqrt{\frac{c}{\epsilon}}$	$d$ = piezoelectric charge coefficient. $\epsilon$ = electric permittivity
Electrical impedance $Z_e$	$ Z_e  = \frac{t}{\omega \cdot \epsilon \cdot A}$	where $\omega$ = angular frequency. $A$ = electrode area

## ELASTIC NONLINEARITY: TUNING THE RESONANT FREQUENCY

Rubber is a highly nonlinear elastic medium. In the unstressed compliant state, the molecules are coiled and tangled, but under stress the molecules align and the material stiffens noticeably. Experiments carried out on rubber-metal laminates demonstrate the size of the nonlinearity. Young's modulus was measured for a multilayer laminate consisting of alternating steel shim and soft rubber layers each 0.1 mm thick. Under compressive stresses of 200 Mpa, the stiffness is quadrupled from about 600 to 2400 Mpa (Rivin, 1983). The resonant frequency  $f$  is therefore doubled, and can be modulated by applied stress.

Rubber, like most elastomers, is not piezoelectric. To take advantage of the elastic nonlinearity, it is therefore necessary to construct a composite transducer consisting of a piezoelectric ceramic (PZT) transducer, thin rubber layers, and metal head and tail masses, all held together by a stress bolt.

The resonant frequency and mechanical Q of such a sandwich structure has been measured as a function of stress bias. Stresses ranged from 20 to 100 Mpa in the experiments. Under these conditions the radial resonant frequency changed from 19 to 37 kHz, approximately doubling in frequency as predicted from the elastic nonlinearity. At the same time the mechanical Q increases from about 11 to 34 as the rubber stiffens under stress.

The changes in resonant frequency and Q can be modeled with an equivalent

circuit in which the compliance of the thin, rubber layers are represented as capacitors coupling together the larger masses (represented as inductors) of the PZT transducer and the metal head and tail masses. Under low stress bias, the rubber is very compliant and effectively isolates the PZT transducer from the head and tail masses. At very high stress, the rubber stiffens and tightly couples the metal end pieces to the resonating PZT ceramic. For intermediate stresses the rubber acts as an impedance transformer giving parallel resonance of the PZT - rubber - metal - radiation load.

Continuing the biomimetic theme, it is interesting to compare the change in frequency of the tunable transducer with the transceiver systems used in the biological world. The biosonar system of the flying bat is similar in frequency and tunability to our tunable transducer. The bat emits chirps at 30 kHz and listens for the return signal to locate flying insects. To help it differentiate the return signal from the outgoing chirp, and to help in timing the echo, the bat puts an FM signature on the pulse. This causes the resonant frequency to decrease from 30 to 20 kHz near the end of each chirp. Return signals from the insect target are detected in the ears of the bat where neural cavities tuned to this frequency range measure the time delay and flutter needed to locate and identify its prey. Extension of the bat biosonar principle to automotive, industrial, medical and entertainment systems is underway.

### PIEZOELECTRIC NONLINEARITY: TUNING THE ELECTROMECHANICAL COUPLING COEFFICIENT

The difference between a smart and a very smart material can be illustrated with piezoelectric and electrostrictive ceramics. PZT (lead zirconate titanate) is a piezoelectric ceramic in which the ferroelectric domains have been aligned in a very large poling field. Strain is linearly proportional to electric field in a fully poled piezoelectric material which means that the piezoelectric coefficient is a constant and cannot be electrically tuned with a bias field. Nevertheless it is a smart material because it can be used both as a sensor and an actuator.

PMN (lead magnesium niobate) is not piezoelectric at room temperature because its Curie temperature lies near 0°C. Because of the proximity of the ferroelectric phase transformation, however, and because of its diffuse nature, PMN ceramics exhibit very large electrostrictive effects.

Electromechanical strains comparable to PZT can be obtained with electrostrictive ceramics like PMN, and without the troubling hysteretic behavior shown by PZT under high fields. The nonlinear relation between strain and electric field (Figure 5) in electrostrictive transducers can be used to tune the piezoelectric coefficient and the dielectric constant.

The piezoelectric  $d_{33}$  coefficient is the slope of the strain-electric field curve when strain is measured in the same direction as the applied field. Its value for

$\text{Pb}(\text{Mg}_{0.3}\text{Nb}_{0.6}\text{Ti}_{0.1})\text{O}_3$  ceramics is zero at zero field and increases to a maximum value of 1300 pC/N (about three times larger than PZT) under a bias field of 3.7 kV/cm.

This means that the electromechanical coupling coefficient can be tuned over a very wide range, changing the transducer from inactive to extremely active. The dielectric constant also depends on DC bias. The polarization saturates under high fields causing decreases of 100% or more in the capacitance. In this way the electrical impedance can be controlled as well.

Electrostrictive transducers have already been used in a number of applications including adaptive optic systems, scanning tunneling microscopes, and precision micropositioners (Uchino, 1986).

### CONDUCTOR FILLED COMPOSITES

Up to this point, our discussion has focused primarily on piezoelectric transducers in which the sensing and actuating functions are electromechanical in nature. But the idea of a smart material is much more general than that. There are many types of sensors and many types of actuators, and many different feedback circuits. Composites consisting of a highly conductive filler powder dispersed in a flexible, insulating polymer matrix are commonly used in electronic applications for thermistors (Hu et al., 1987), pressure sensing elements (Yoshikawa et al., 1990) and chemical sensors (Ruschau et al., 1989).

The electrical properties of these materials are described by conventional percolation theory (Ruschau and Newnham, 1992). When a sufficient amount of conductive filler is loaded into an insulating matrix, the composite transforms from an insulator to a conductor, arising through the continuous linkages of particles. Figure 6. As the volume fraction of filler is increased, the probability of continu-

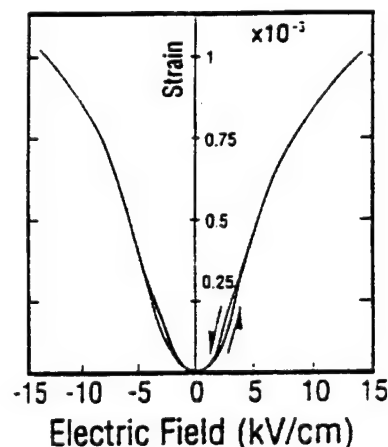


FIGURE 5. Electrostriction in PMN ( $\text{Pb}_3\text{MgNb}_2\text{O}_9$ )-based ceramics leads to strains of 0.1%. An attractive feature of these ceramics is the near absence of hysteresis (Cross et al., 1980)



ity increases until the critical volume fraction is reached, beyond which the electrical conductivity is high, closer to the filler material.

Thermistors or temperature dependent resistors, are typically made from doped ceramics ( $\text{BaTiO}_3$ ). The desire for improved properties and ease of processing has spurred the development of composite thermistors. This type of composite combines a low resistivity filler powder, such as carbon black, vanadium sesquioxide, or nickel with a high resistivity polymer matrix such as polyethylene or polystyrene. In the dormant room temperature state the thermistor has a resistivity similar to the filler. On being activated by heating, however, the polymer expands pulling the particles apart and causing the resistivity to increase to a value close to the polymer matrix resistivity, an increase as large as eight orders of magnitude (Hu et al., 1987).

Conductive composites exposed to a solvent, in order to produce chemical sensing capabilities, have also been shown to take advantage of percolation phenomena. A conductive composite which shows some sensitivity to chemical vapors undergoes a four-step resistance change during exposure to the solvent. First, adsorption of solvent onto the surface of the composite results in a small, quick increase in resistance. Secondly, as the solvent diffuses through the sensor sample, the number of percolated chains decreases and the remaining chains become less conductive; a gradual increase in resistance occurs during this step. Third, when the last remaining percolated linkage is disrupted, there is a large increase in resistivity, usually several orders of magnitude; this conductor-to-insulator switch is the most important step for application purposes. Finally, as more solvent diffuses into the composite, the resistivity saturates at a level determined primarily by the conductivity of the solvent/polymer solution, although some effects from the filler are evident (Ruschau et al., 1989).

#### SMART ELECTROCERAMIC PACKAGES

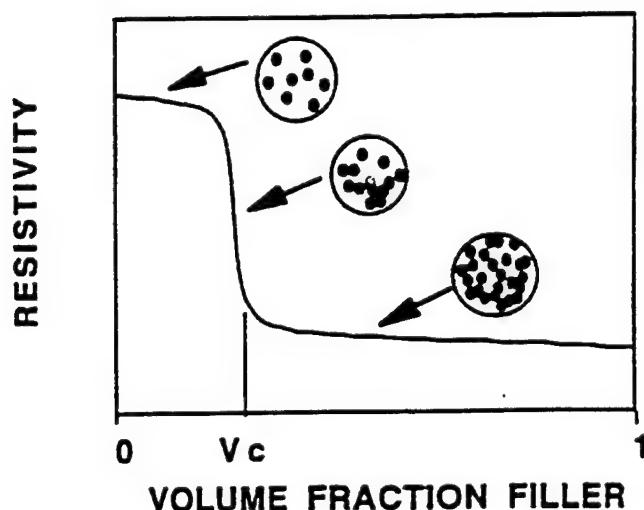


FIGURE 6. Percolation theory as applied to conductive composites, showing the development of conductive pathways with an increase in volume fraction of filler.

Many sensors and actuators can be fabricated in the form of multilayer ceramic packages. Until recently multilayer packages consisted of low permittivity dielectric layers with metal circuitry printed on each layer and interconnected through metallized via holes between layers. Buried capacitors and resistors have now been added to the three-dimensional packages, and other components will follow shortly. Smart sensors, adaptive actuators, and display panels, together with thermistors and varistors to guard against current and voltage overloads, are next in line for development (Newnham, 1988).

Integration and miniaturization of electroceramic sensors and actuators is an ongoing process in the automotive and consumer electronics areas. Multilayer packages containing signal processing layers made up of low-permittivity dielectrics and printed metal interconnections are in widespread production. Further integration with embedded resistors and capacitors are under development, and it seems likely that intelligent systems will make use of the same processing technology. Tape casting and screen printing are used most often. Varistors, chemical sensors, thermistors, and piezoelectric transducers can all be fabricated in this way, opening up the possibility of multicomponent, multifunction ceramics with both sensor and actuator capabilities. Silicon chips can be mounted on these multifunctional packages to provide all or part of the control network. Processing is a major challenge because of the high firing temperatures of most ceramics, typically in the range 800°C to 1500°C. Differences in densification shrinkage and thermal contraction, together with adverse chemical reactions between the electroceramic phases, create formidable problems. Nevertheless, the rewards for such an achievement are substantial. An all-ceramic multifunction package would be small, robust, inexpensive, and sufficiently refractory to withstand elevated temperatures.

The next logical step is to combine the sensor and actuator functions with the control system. This can be done by depositing electroceramic coatings on integrated circuit silicon chips. Electroceramics have a vital role to play in intelligent systems, and many new developments will take place in the coming decade and the next century.

## REFERENCES

- Bond, C.E. 1979. "Biology of Fishes." Saunders College Publishing Co. Philadelphia.
- Burke, S. and J.E. Hubbard. 1987. "Active Vibration Control of a Simply-Supported Beam Using a Spatially-Distributed Actuator." *IEEE Control Systems Magazine* 7, 25-30.
- Cross, L.E., Jang, S.J., Newnham, R.E., Nomura, S., and K. Uchino. 1980. "Large Electrostriction Effects in Relaxor Ferroelectrics", *Ferroelectrics* 23 187-193.
- Edberg, D.L. 1987: "Control of Flexible Structures by Applied Thermal

- Gradients," *AIAA Journal*, 25, 877-883.
- Fukami, A., Yano, M., Tokuda, H., Ohki, M. and R. Kizu. 1994. "Development of Piezoelectric Actuators and Sensors for Electronically Controlled Suspension", *Int. J. of Vehicle Design*, 15 348-357.
- Ghandi, M.V. and B.S. Thompson. 1989. "Smart Materials, Structures, and Mathematical Issues," ed. by C.A. Rogers. Technomic Publishers, Lancaster, PA. 63-68.
- Gururaja, T.R., Schulze, W.A., Cross, L.E., Newnham, R.E., Auld, B.A., and J. Wang. 1984. "Resonant Modes in Piezoelectric PZT Rod-Polymer Composite Materials," *Proc. of IEEE Ultrasonic Symposium*, 523-527.
- Hathaway, K.B. and A.E. Clark. 1993. "Magnetostrictive Materials", *Mat. Res. Soc. Bull.* 18 34-41.
- Hu, K.A., Moffat, D., Runt, J., Safari, A., and R.E. Newnham. 1987. "V3O3-Polymer Composite Thermistors." *J. Am. ceram. Soc.* 70: 583-585.
- Klicker, K.A., Biggers, J.V. and R.E. Newnham. 1981. Composites of PZT and Epoxy for Hydrostatic Transducer Applications." *J.Amer.Cer.Soc.* 64, 5-9.
- Moyle, P.B. and J.J. Cech, Jr. 1988. "Fishes: An Introduction to Ichthyology." Prentice Hall, Englewood Cliffs, N.J.
- Newnham, R.E. 1988. "The Golden Age of Electroceramics," *Adv. Ceram. Mat.* 3, 12-16.
- Newnham, R.E., Xu, Q.C., Kumar, S., and L.E. Cross. 1989. "Smart Ceramics." *J.Wave-Matl.Int.* 4, 3-10.
- Rivin, E.I. 1983. "Properties and Prospective Applications of Ultra Thin Layered Rubber-Metal Laminates for Limited Travel Bearings," *Tribology Int.* 16, 17-25.
- Rogers, C.A. 1990. "From the Editor." *Journal of Intelligent Material Systems and Structures* 1, 3.
- Rogers, C.A., Liang, C., and D.K. Barker. 1989. In "Smart Materials, Structures, and Mathematical Issues," ed. by C.A. Rogers, Technomic Publishers, Lancaster, PA, 39-62.
- Rosenweig, R.E. 1985. "Ferrohydrodynamics," Cambridge University Press, New York.
- Ruschau, G.R., Newnham, R.E., Runt, J., and B.E. Smith. 1989. "O-3 Ceramic-Polymer Composite Chemical Sensors, Sensors and Actuators, 20: 269-275.
- Ruschau, G. and R.E. Newnham. 1992. "Critical Volume Fractions in Conductive Composites", *J. Comp. Mat.* 26: 2727-2735.
- Ruschau, G.R., Yoshikawa, S., and R.E. Newnham. 1992. *J. Appl. Phys.* 72:953-959.
- Schetky, L. 1979. "Shape Memory Alloys," *Scientific American* 241, 74-82.
- Sullivan, R.J. and R.E. Newnham. 1992. "Composite Thermistors", pp. 351-367, in: C.N.R.Rao (Ed.) *Chemistry of Advanced Materials*, Blackwell Scientific Publications London, U.K.
- Suzuki, Y., Uchino, K., Gouda, H., Sumita, M., Newnham, R.E., and A.R. Ramachandran. 1991. *J. Japan Ceram. Soc.*, 99, 1135-1140.
- Taguchi, M., 1987. "Applications of High-Technology Ceramics in Japanese Automobiles," *Adv. Ceram. Mat.* 2, 754-762.

- Takagi, T. 1989. "The Concept of Intelligent Materials and the Guidelines on R&D Promotion", Japan Science and Technology Agency Report.
- Tsuka, H., Nakomo, J., and Y. Yokoya. 1990: "A New Electronic Controlled Suspension Using Piezoelectric Ceramics." IEEE Workshop on Electronic Applications in Transportation.
- Uchino, K. 1986. "Piezoelectric/Electrostrictive Actuators." Morikita Publishers. Tokyo.
- Uchino, K. 1993. "Ceramic Actuators: Principles and Applications", Mat. Res. Soc. Bull. 18, 42-48.
- Urick, R.J. 1975. "Principles of Underwater Sound." McGraw Hill, New York.
- Wadhawan, V.K., Kernion, M.C., Kimura, T. and R.E. Newnham. 1981. "The Shape Memory Effect in PLZT Ceramics." *Ferroelectrics* 37, 575-578.
- Xu, Q.C., Belsick, J., Yoshikawa, S., Srinivasan, T.T., and R.E. Newnham. 1991: "Piezoelectric Composites with High Sensitivity and High Capacitance for Use at High Pressures." IEEE Transactions. UFFC 38, 634-639.
- Xu, Q.C., Newnham, R.E., Blaskiewicz, M., Fang, T.T., Srinivasan, T.T., and S. Yoshikawa. 1990. "Nonlinear Multilayer Composite Transducers." Presented at the 7th International Symposium on Applications for Ferroelectrics. June 6-8. Urbana, IL.
- Yoshikawa, S., Ota, T., and R.E. Newnham. 1990. "Piezoresistivity in Polymer-Ceramic Composites." J. Am. Ceram. Soc., 73: 263-267.

# **APPENDIX 3**

# Piezoelectric ultrasonic motors: overview

Kenji Uchino

International Center for Actuators and Transducers, Intercollege Materials Research Laboratory, The Pennsylvania State University, University Park, PA 16802, USA

Received 26 July 1997, accepted for publication 20 October 1997

**Abstract.** This paper reviews recent developments of ultrasonic motors using piezoelectric resonant vibrations. Following the historical background, ultrasonic motors using standing and traveling waves are introduced. Driving principles and motor characteristics are explained in comparison with conventional electromagnetic motors. After a brief discussion on speed and thrust calculation, finally, reliability issues of ultrasonic motors are described.

## 1. Introduction

In office equipment such as printers and floppy disk drives, market research indicates that tiny motors smaller than  $1\text{ cm}^3$  would be in large demand over the next ten years. However, using the conventional electromagnetic motor structure, it is rather difficult to produce a motor with sufficient energy efficiency. Piezoelectric ultrasonic motors, whose efficiency is insensitive to size, are superior in the mm-size motor area.

In general, piezoelectric and electrostrictive actuators are classified into two categories, based on the type of driving voltage applied to the device and the nature of the strain induced by the voltage: (1) rigid displacement devices for which the strain is induced unidirectionally along an applied dc field, and (2) resonating displacement devices for which the alternating strain is excited by an ac field at the mechanical resonance frequency (ultrasonic motors). The first category can be further divided into two types: servo displacement transducers (positioners) controlled by a feedback system through a position-detection signal, and pulse-drive motors operated in a simple on/off switching mode, exemplified by dot-matrix printers.

The AC resonant displacement is not directly proportional to the applied voltage, but is, instead, dependent on adjustment of the drive frequency. Although the positioning accuracy is not as high as that of the rigid displacement devices, very high speed motion due to the high frequency is an attractive feature of the ultrasonic motors. Servo displacement transducers, which use feedback voltage superimposed on the DC bias, are used as positioners for optical and precision machinery systems. In contrast, a pulse drive motor generates only on/off strains, suitable for the impact elements of dot-matrix or ink-jet printers.

The materials requirements for these classes of devices are somewhat different, and certain compounds will be

better suited for particular applications. The ultrasonic motor, for instance, requires a very hard piezoelectric with a high mechanical quality factor  $Q$ , in order to minimize heat generation and maximize displacement. Note that the resonance displacement is equal to  $\alpha dEL$ , where  $d$  is a piezoelectric constant,  $E$ , applied electric field,  $L$ , sample length and  $\alpha$  is an amplification factor proportional to the mechanical  $Q$ . The servo-displacement transducer suffers most from strain hysteresis and, therefore, a PMN electrostrictor is preferred for this application. Notice that even in a feedback system the hysteresis results in a much lower response speed. The pulse-drive motor requires a low-permittivity material aiming at quick response with a limited power supply rather than a small hysteresis, so that soft PZT piezoelectrics are preferred to the high-permittivity PMN for this application.

This paper deals with ultrasonic motors using resonant vibrations. Following the historical background, various ultrasonic motors are introduced. Driving principles and motor characteristics are explained in comparison with the conventional electromagnetic motors. After a brief discussion on speed and thrust calculation, finally, reliability issues of ultrasonic motors are described.

## 2. Classification of ultrasonic motors

### 2.1. Historical background

Electromagnetic motors were invented more than a hundred years ago. While these motors still dominate the industry, a drastic improvement cannot be expected except through new discoveries in magnetic or superconducting materials. Regarding conventional electromagnetic motors, tiny motors smaller than  $1\text{ cm}^3$  are rather difficult to produce with sufficient energy efficiency. Therefore, a new class of motors using high power ultrasonic energy—ultrasonic motors—is gaining widespread attention. Ultrasonic motors made with piezoceramics whose efficiency is insensitive to

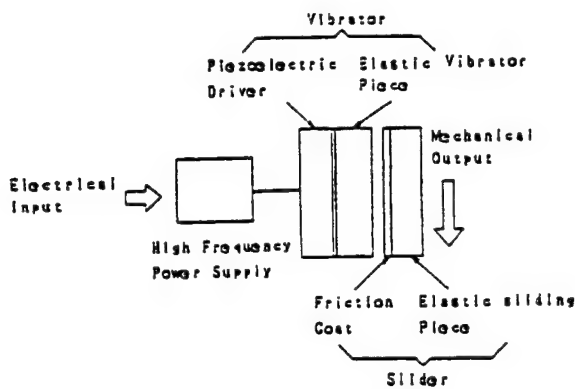


Figure 1. Fundamental construction of ultrasonic motors.

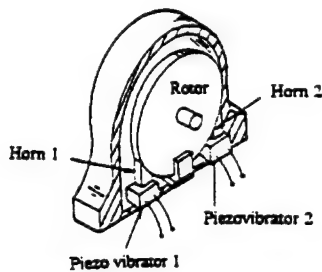


Figure 2. Ultrasonic motor by Barth.

size are superior in the mini-motor area. Figure 1 shows the basic construction of ultrasonic motors, which consist of a high-frequency power supply, a vibrator and a slider. Further, the vibrator is composed of a piezoelectric driving component and an elastic vibratory part, and the slider is composed of an elastic moving part and a friction coat.

Though there had been some earlier attempts, the practical ultrasonic motor was proposed firstly by H V Barth of IBM in 1973 [1]. As shown in figure 2, the rotor was pressed against two horns placed at different locations. By exciting one of the horns, the rotor was driven in one direction, and by exciting the other horn, the rotation direction was reversed. Various mechanisms based on virtually the same principle were proposed by V V Lavrinenko *et al* [2] and P E Vasiliev *et al* [3] in the former USSR. Because of difficulty in maintaining a constant vibration amplitude with temperature rise, wear and tear, the motors were not of much practical use at that time.

In the 1980s, with increasing chip pattern density, the semiconductor industry began to request much more precise and sophisticated positioners which do not generate magnetic field noise. This urgent request has accelerated the developments in ultrasonic motors. Another advantage of ultrasonic motors over the conventional electromagnetic motors with expensive copper coils, is the improved availability of piezoelectric ceramics at reasonable cost. Japanese manufacturers are producing piezoelectric buzzers around the 30–40 cent price range at the moment.

Let us summarize the merits and demerits of the ultrasonic motors.

#### Merits.

- (1) Low speed and high torque—direct drive.
- (2) Quick response, wide velocity range, hard brake and no backlash: excellent controllability; fine position resolution.
- (3) High power/weight ratio and high efficiency.
- (4) Quiet drive.
- (5) Compact size and light weight.
- (6) Simple structure and easy production process.
- (7) Negligible effect from external magnetic or radioactive fields, and also no generation of these fields.

#### Demerits.

- (8) Necessity for a high frequency power supply.
- (9) Less durability due to frictional drive.
- (10) Drooping torque-speed characteristics.

## 2.2. Classification and principles of ultrasonic motors

From a customer's point of view, there are rotary and linear type motors. If we categorize them from the vibrator shape, there are rod type,  $\pi$ -shaped, ring (square) and cylinder types, which are illustrated in figure 3. Two categories are being investigated for ultrasonic motors from a vibration characteristic viewpoint: a standing-wave type and a propagating-wave type. Refresh your memory on the wave formulas. The standing wave is expressed by

$$u_s(x, t) = A \cos kx \cos \omega t \quad (1)$$

while the propagating wave is expressed as

$$u_p(x, t) = A \cos(kx - \omega t). \quad (2)$$

Using a trigonometric relation, (2) can be transformed as

$$u_p(x, t) = A \cos kx \cos \omega t + A \cos(kx - \pi/2) \cos(\omega t - \pi/2). \quad (3)$$

This leads to an important result, i.e. a propagating wave can be generated by superimposing two standing waves whose phases differ by  $90^\circ$  from each other both in time and in space. This principle is necessary to generate a propagating wave on a limited volume/size substance, because only standing waves can be excited stably in a finite size.

**2.2.1. Standing-wave type.** The standing-wave type is sometimes referred to as a vibratory-coupler type or a 'woodpecker' type, where a vibratory piece is connected to a piezoelectric driver and the tip portion generates flat-elliptical movement. Figure 4 shows a simple model proposed by T Sashida [4]. A vibratory piece is attached to a rotor or a slider with a slight cant angle  $\theta$ . Take the  $x$ - $y$  coordinate so that the  $x$  axis is normal to the rotor face. When a vibration displacement

$$u_x = u_0 \sin(\omega t + \alpha) \quad (4)$$

is excited at the piezoelectric vibrator, the vibratory piece generates bending because of restriction by the rotor, so that the tip moves along the rotor face between  $A \rightarrow B$ , and freely between  $B \rightarrow A$ . If the vibratory piece and the

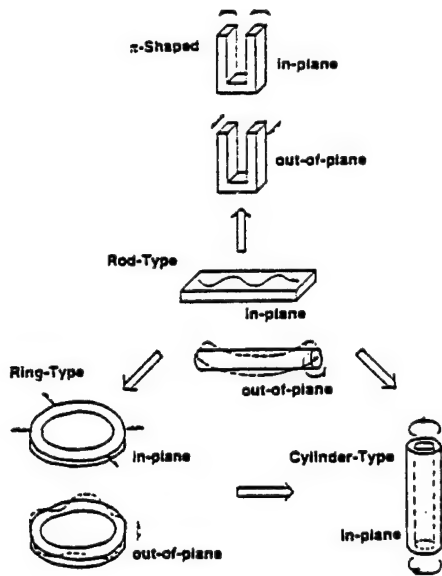


Figure 3. Vibrator shapes for ultrasonic motors.

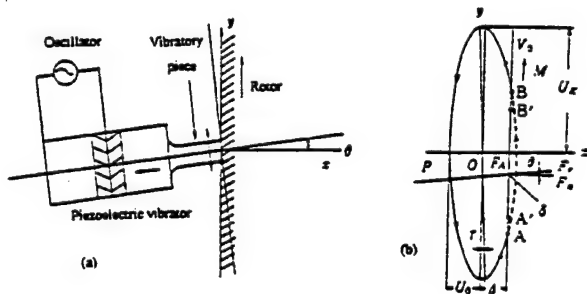


Figure 4. Vibratory coupler type motor (a) and its tip locus (b).

piezo-vibrator are tuned properly, they form a resonating structure, and if the bending deformation is sufficiently small compared with the piece length, the tip locus during the free vibration ( $B \rightarrow A$ ) is represented by

$$\begin{aligned} x &= u_0 \sin(\omega t + \alpha) \\ y &= u_1 \sin(\omega t + \beta) \end{aligned} \quad (5)$$

which is an elliptical locus. Therefore, only the duration  $A \rightarrow B$  provides a unidirectional force to the rotor through friction, i.e. intermittent rotational torque or thrust. However, because of the inertia of the rotor, the rotation speed ripple is not large to observe. The standing-wave type, in general, is low in cost (one vibration source) and has high efficiency (up to 98% theoretically), but lack of control in both clockwise and counterclockwise directions is a problem.

**2.2.2. Propagating-wave type.** By comparison, the propagating-wave type (a surface-wave or 'surfing' type) combines two standing waves with a 90 degree phase difference both in time and in space. The principle is shown in figure 5. A surface particle of the elastic body draws an elliptical locus due to the coupling of longitudinal

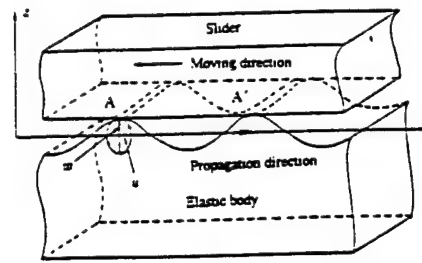


Figure 5. Principle of the propagating-wave type motor.

and transverse waves. This type requires, in general, two vibration sources to generate one propagating wave, leading to low efficiency (not more than 50%), but it is controllable in both the rotational directions.

### 3. Standing-wave type motors

#### 3.1. Rotary motors

T Sashida developed a rotary type motor similar to the fundamental structure [4]. Four vibratory pieces were installed on the edge face of a cylindrical vibrator, and pressed onto the rotor. This is one of the prototypes which triggered the present development fever on ultrasonic motors. A rotation speed of 1500 rpm, torque of 0.08 N m and output of 12 W (efficiency 40%) were obtained under an input of 30 W at 35 kHz. This type of ultrasonic motor can provide a speed much higher than the inchworm types, because of high frequency and an amplified vibration displacement at the resonance frequency.

Hitachi Maxel significantly improved the torque and efficiency by using a torsional coupler replacing Sashida's vibratory pieces (figure 6), and by increasing the pressing force with a bolt [5]. The torsional coupler looks like an old fashioned TV channel knob, consisting of two legs which transform longitudinal vibration generated by the Langevin vibrator to a bending mode of the knob disk, and a vibratory extruder. Notice that this extruder is aligned with a certain cant angle to the legs, which transforms the bending to a torsion vibration. This transverse moment coupled with the bending up-down motion leads to an elliptical rotation on the tip portion, as illustrated in figure 6(b). The optimum pressing force to obtain the maximum thrust is obtained, when the ellipse locus is deformed roughly by half. A motor 30 mm × 60 mm in size and 20–30° in cant angle between a leg and a vibratory piece provided torque as high as 1.3 N m and the efficiency of 80%. However, this type provides only unidirectional rotation. Notice that even though the drive of the motor is intermittent, the output rotation becomes very smooth because of the inertia of the rotor.

The Penn State University has developed a compact ultrasonic rotary motor as tiny as 3 mm in diameter. As shown in figure 7, the stator consists of a piezoelectric ring and two concave/convex metal endcaps with 'windmill' shaped slots bonded together, so as to generate a coupled vibration of up-down and torsional type [6]. Since the component number and the fabrication process were



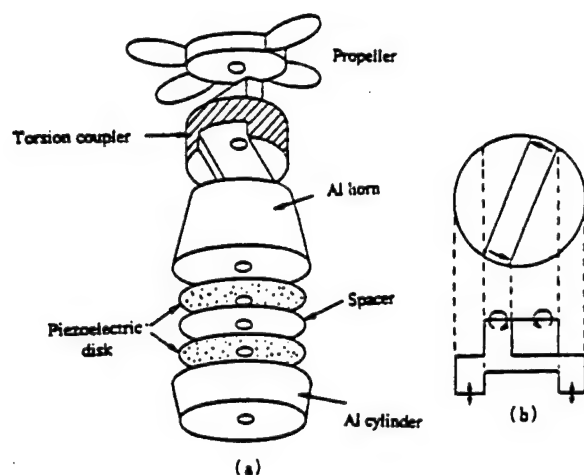


Figure 6. Torsional coupler ultrasonic motor (a) and the motion of the torsional coupler (b).

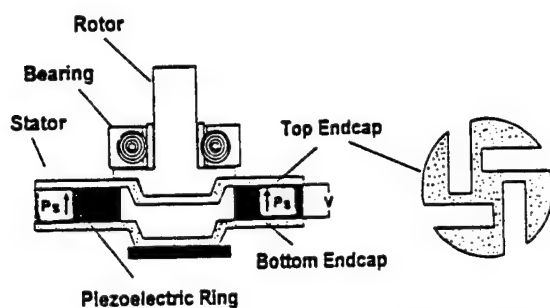


Figure 7. 'Windmill' motor with a disk-shaped torsional coupler.

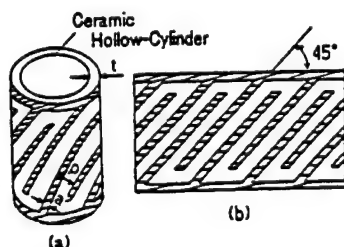


Figure 8. Piezoelectric cylinder torsional vibrator (a) and the electrode pattern (b).

minimized, the fabrication price would be decreased remarkably, and it would be adaptive to disposable usage. When driven at 160 kHz, the maximum revolution 600 rpm and the maximum torque 1 mN m were obtained for a 11 mm diameter motor.

Tokim developed a piezoelectric ceramic cylinder for a torsional vibrator (figure 8) [7]. Using an interdigital type electrode pattern printed with 45° cant angle on the cylinder surface, torsion vibration was generated, which is applicable to a simple ultrasonic motor.

S Ueha *et al* proposed a two-vibration-mode coupled type (figure 9), i.e. a torsional Langevin vibrator was combined with three multilayer actuators to generate larger longitudinal and transverse surface displacement of the stator, as well as to control their phase difference [8]. The

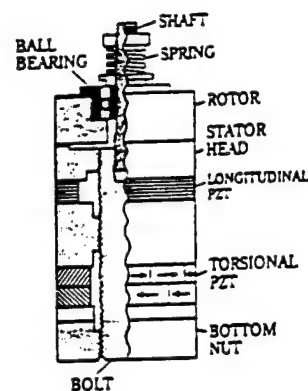


Figure 9. Two-vibration-mode coupled type motor.

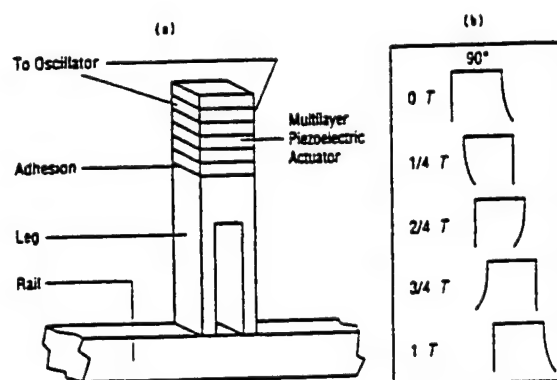


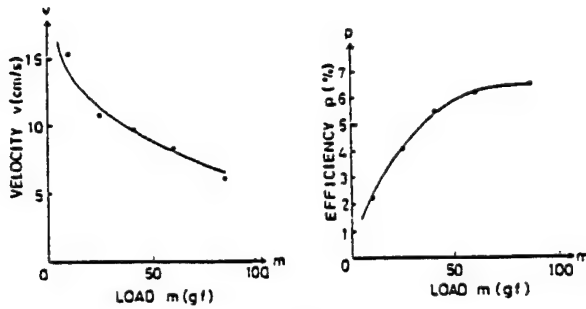
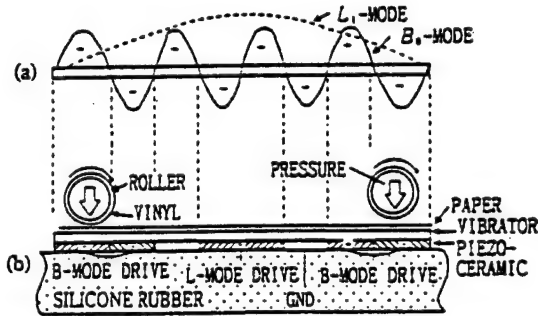
Figure 10.  $\pi$ -shaped linear ultrasonic motor: (a) construction and (b) walking principle. Note the 90 degree phase difference like a human walk.

phase change can change the rotation direction.

### 3.2. Linear motors

K Uchino *et al* invented a  $\pi$ -shaped linear motor [9]. This linear motor is equipped with a multilayer piezoelectric actuator and fork-shaped metallic legs as shown in figure 10. Since there is a slight difference in the mechanical resonance frequency between the two legs, the phase difference between the bending vibrations of both legs can be controlled by changing the drive frequency. The walking slider moves in a way similar to a horse using its fore and hind legs when trotting. A test motor  $20 \times 20 \times 5 \text{ mm}^3$  in dimension exhibited a maximum speed of  $20 \text{ cm s}^{-1}$  and a maximum thrust of 0.2 kgf with a maximum efficiency of 20%, when driven at 98 kHz at 6 V (actual power = 0.7 W). Figure 11 shows the motor characteristics of the linear motor. This motor has been employed in a precision X-Y stage.

Tomikawa's rectangular plate motor is also intriguing [10]. As shown in figure 12, a combination of the two modes forms an elliptical displacement motion. The two modes chosen were the first longitudinal mode ( $L_1$  mode) and the eighth bending mode ( $B_8$ ), whose resonance frequencies were almost the same. By applying voltages with a phase difference of 90° to the L-mode and B-mode drive electrodes, elliptical motion in the same direction can

Figure 11. Motor characteristics of the  $\pi$ -shaped motor.Figure 12.  $L_1$  and  $B_3$  double-mode vibrator motor.

be obtained at both ends of this plate, leading to rotation of the rollers in contact with these points. Anticipated applications are paper or card senders. The reader can find other linear motor ideas in Ueha and Tomikawa's book [11].

## 4. Propagating wave type motors

### 4.1. Linear motors

T Sashida and S Ueha *et al* manufactured a linear motor as illustrated in figure 13 [12,13]. The two piezoelectric vibrators installed at both ends of a transmittance steel rod excite and receive the traveling transverse wave (antisymmetric fundamental Lamb wave mode). Adjusting a load resistance in the receiving vibrator leads to a perfect traveling wave. Exchanging the role of exciting and receiving piezo-components provided a reverse moving direction.

The bending vibration transmitting via the rail rod is represented by the following differential equation:

$$(\partial^2 w(x, t) / \partial t^2) + (EI / \rho A) (\partial^4 w(x, t) / \partial x^4) = 0 \quad (6)$$

where  $w(x, t)$  is a transverse displacement (see figure 5),  $x$ , the coordinate along the rod axis,  $E$ , Young's modulus of the rod,  $A$ , the cross sectional area,  $\rho$ , density and  $I$  is the moment of inertia of the cross-section. Assuming a general solution of (6) as

$$w(x, t) = W(x)(A \sin \omega t + B \cos \omega t) \quad (7)$$

the wave transmission velocity  $v$  and wavelength  $\lambda$  are calculated as

$$v = (EI / \rho A)^{1/4} \sqrt{\omega} \quad (8)$$

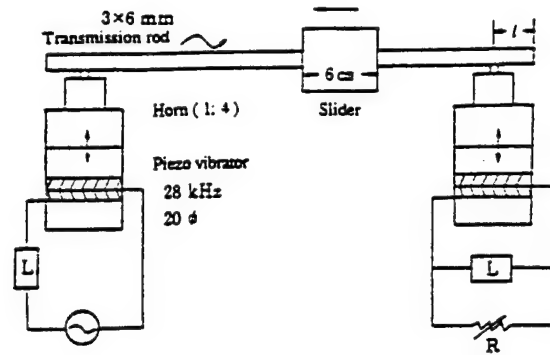


Figure 13. Linear motor using a bending vibration.

$$\lambda = 2\pi(EI / \rho A)^{1/4} / \sqrt{\omega}. \quad (9)$$

Using the bending vibration, the wavelength  $\lambda$  can be easily chosen as short as several mm to satisfy a stable surface contact with the slider by changing the cross section area  $A$  or the moment of inertia  $I$  of the transmission rod. In the case of figure 13,  $\lambda = 26.8$  mm.

A slider, the contact face of which is coated with rubber or vinyl resin sheet, clamps the transmission rod with an appropriate force. The transmission efficiency is strongly affected by the vibration source position on the rod, showing a periodic change with the distance from the free end of the rod to the position of the vibrator. Taking account of the wave phase, the vibration source should be fixed at the distance of the wavelength  $\lambda$  (i.e. 26.8 mm) from the rod end.

The slider made of a steel clasper 60 mm in length, which theoretically covers two waves, was driven at a speed of  $20 \text{ cm s}^{-1}$  with a thrust of 50 N at 28 kHz. A serious problem with this type is found in low efficiency around 3% because the whole rod must be excited even when only a small portion is utilized for the output. Thus, ring type motors were invented by Sashida, where the whole rod can be utilized, because the lengths of the stator and rotor are the same.

### 4.2. Rotary motors

When we deform the rod discussed in the previous section to make a ring by connecting the two ends topologically, we can make a rotary type motor using a bending vibration. Two types of 'ring' motor design are possible: (a) bending mode and (b) extensional mode [14]. Though the principle is similar to the linear type, more sophisticated structures are employed in the ceramic poling and in the mechanical support mechanism.

**4.2.1. Principle of 'surfing' rotary motors.** In general, when a vibration source is driven at one position on a closed ring (circular or square) at a frequency corresponding to the resonance of this ring, only a standing wave is excited, because the vibration propagates in two directions symmetrically to the vibration source and these interfere with each other. When multiple vibration sources are installed on the ring, displacements can be obtained

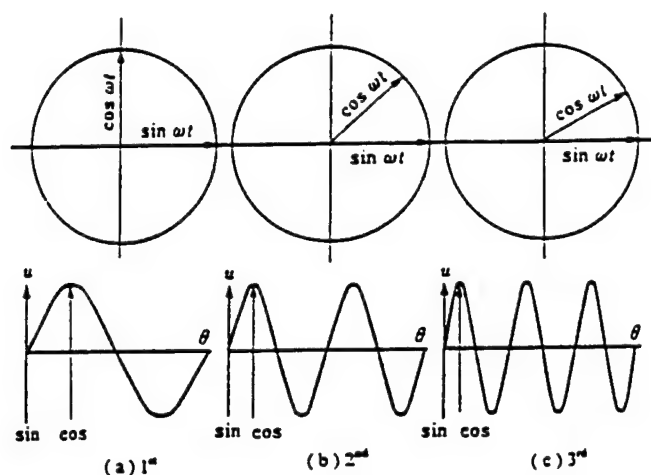


Figure 14. Vibration source positions for generating a propagating wave in a ring.

by superimposing all the waves (two waves from each vibration source). Using this superposition principle, we can generate a propagating wave which is a rotation of the standing-wave shape, even in a closed ring.

Assuming a vibration source of  $A \cos \omega t$  at the point  $\theta = 0$  of the elastic ring, the  $n$ th mode standing wave can be expressed by

$$u(\theta, t) = A \cos n\theta \cos \omega t \quad (10)$$

and the traveling wave by

$$u(\theta, t) = A \cos(n\theta - \omega t). \quad (11)$$

Since the traveling wave can be expressed as a superimposition of two standing waves as

$$u(\theta, t) = A \cos n\theta \cos \omega t + A \cos(n\theta - \pi/2) \cos(\omega t - \pi/2) \quad (12)$$

we derive an important principle: a propagating wave can be generated by superimposing two standing waves whose phases differ by  $90^\circ$  from each other both in time and in space. More generally, the phase difference can be chosen arbitrarily (except  $0, -\pi, \pi$ ), as long as the phase difference is the same in space and in time. The vibration source positions for generating a propagating wave on a ring are illustrated in figure 14. In principle, the excitation at only two parts of the ring is sufficient to generate a traveling wave. However, in practice, the number of the vibration sources is increased to as many as possible to increase the mechanical output. The symmetry of the electrode structure needs to be considered.

**4.2.2. Examples of 'surfing' rotary motors.** Figure 15 shows the famous Sashida motor [15]. By means of the traveling elastic wave induced by a thin piezoelectric ring, a ring-type slider in contact with the 'rippled' surface of the elastic body bonded onto the piezoelectric is driven in both directions by exchanging the sine and cosine voltage inputs. Another advantage is its thin design, which makes it suitable for installation in cameras as an automatic focusing

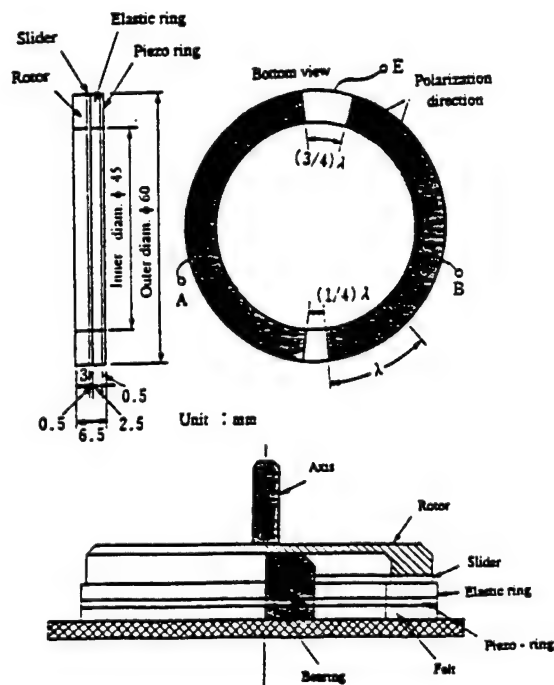


Figure 15. Stator structure of Sashida's motor.

device. Eighty percent of the exchange lenses in Canon's 'EOS' camera series have already been replaced by the ultrasonic motor mechanism. Most of the studies on ultrasonic motors done in the US and Japan have been modifications of Sashida's type.

The PZT piezoelectric ring is divided into 16 positively and negatively poled regions and two asymmetric electrode gap regions so as to generate a ninth mode propagating wave at 44 kHz. A proto-type was composed of a brass ring of 60 mm in outer diameter, 45 mm in inner diameter and 2.5 mm in thickness, bonded onto a PZT ceramic ring of 0.5 mm in thickness with divided electrodes on the back-side. The rotor was made of polymer coated with hard rubber or polyurethane. Figure 16 shows Sashida's motor

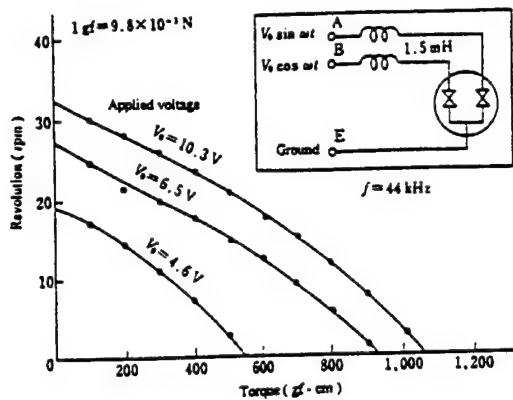


Figure 16. Motor characteristics of Sashida's motor.

characteristics.

Canon utilized the 'surfing' motor for a camera automatic focusing mechanism, installing the ring motor compactly in the lens frame. It is noteworthy that the stator elastic ring has many teeth, which can magnify the transverse elliptical displacement and improve the speed. The lens position can be shifted back and forth through a screw mechanism. The advantages of this motor over the conventional electromagnetic motor are:

- (1) Silent drive due to the ultrasonic frequency drive and no gear mechanism (i.e. more suitable to video cameras with microphones).
- (2) Thin motor design and no speed reduction mechanism such as gears, leading to space saving.
- (3) Energy saving.

A general problem encountered in these traveling wave type motors is the support of the stator. In the case of a standing wave motor, the nodal points or lines are generally supported; this causes minimum effects on the resonance vibration. In contrast, a traveling wave does not have such steady nodal points or lines. Thus, special considerations are necessary. In figure 15, the stator is basically fixed very gently along the axial direction through felt so as not to suppress the bending vibration. It is important to note that the stop pins which latch onto the stator teeth only provide high rigidity against the rotation.

Matsushita Electric proposed a nodal line support method using a higher order vibration mode (see figure 17(b)) [16]. Figure 17(a) shows the stator structure, where a wide ring was supported at the nodal circular line and 'teeth' were arranged on the maximum amplitude circle to obtain larger revolution.

Seiko Instruments miniaturized the ultrasonic motor to as tiny as 10 mm in diameter using basically the same principle [17]. Figure 18 shows the construction of this small motor with 10 mm diameter and 4.5 mm thickness. A driving voltage of 3 V and a current 60 mA provides 6000 rev min<sup>-1</sup> (no load) with torque of 0.1 mN m. AlliedSignal developed ultrasonic motors similar to Shinsei's, which would be utilized as mechanical switches for launching missiles [18].

It is important to note that the unimorph (bonded type of a piezoceramic plate and a metal plate) bending actuation

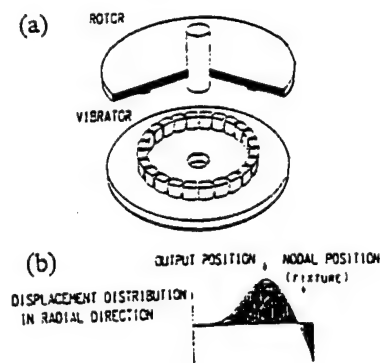


Figure 17. (a) Tooth shaped stator and (b) a higher order vibration mode with a nodal line for fixing.

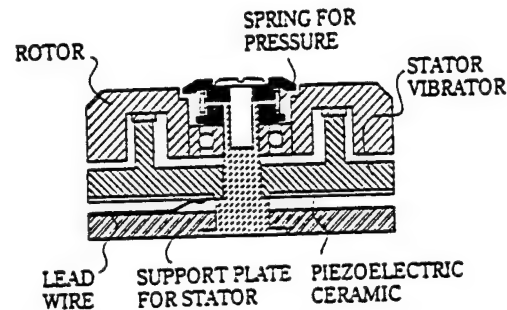


Figure 18. Construction of Seiko's motor.

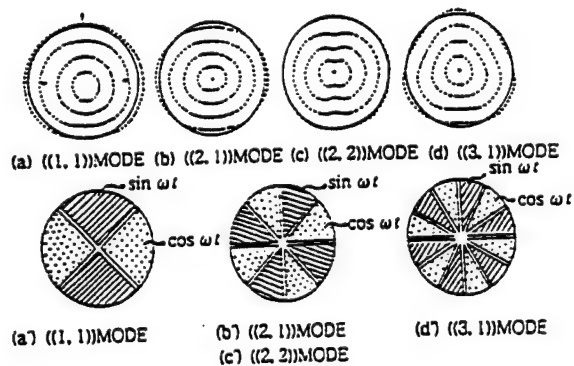


Figure 19. Disk type hula-hoop motor.

can not provide high efficiency theoretically, because the electromechanical coupling factor  $k$  is usually less than 10%. Therefore, instead of the unimorph structure, a simple disk was directly used to make motors [19, 20]. Figure 19 shows (1,1), (2,1) and (3,1) modes of a simple disk, which are axial-asymmetric modes. Both the inner and outer circumferences can provide a rotation like a 'hula hoop'.

Another intriguing design is a 'plate-spinning' type proposed by Tokin [21]. Figure 20 shows its principle. A rotary bending vibration was excited on a PZT rod by a combination of sine and cosine voltages, then a cup was made to contact the 'spinning' rod with the internal face for achieving rotation.

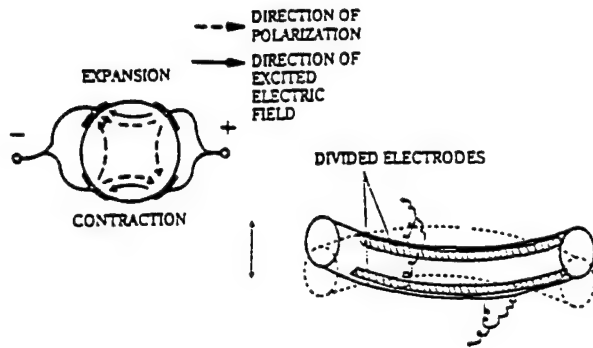


Figure 20. 'Plate-spinning' type motor by Tokin.

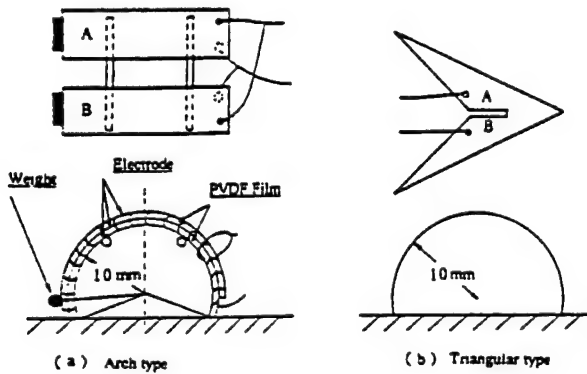


Figure 21. PVDF walking mechanism.

#### 4.3. Comparison among various ultrasonic motors

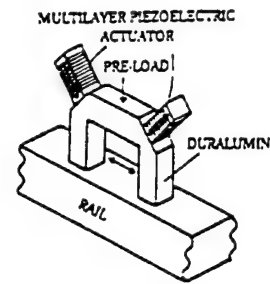
The standing-wave type, in general, is low in cost (one vibration source) and has high efficiency (up to 98% theoretically), but lack of control in both clockwise and counterclockwise directions is a problem. By comparison, the propagating-wave type combines two standing waves with a 90 degree phase difference both in time and in space. This type requires, in general, two vibration sources to generate one propagating wave, leading to low efficiency (not more than 50%), but is controllable in both rotational directions.

Table 1 summarizes the motor characteristics of the vibration coupler standing wave type (Hitachi Maxel), surface propagating wave type (Shinsei Industry) and a compromised 'teeth' vibrator type (Matsushita) [22].

### 5. Micro-walking machines

Recent biomedical experiments and medical surgery require sophisticated tiny actuators for micro-manipulation of optical fibers, catheters, micro-surgery knives etc. Thus, microactuators, particularly micro-walking devices, have been studied intensively.

The first systematic study was performed by T Hayashi on PVDF bimorph actuators [23]. Figure 21 shows two designs of micro-machines. The devices were fabricated using two 30  $\mu\text{m}$  thick PVDF films bonded together with a curvature of  $1\text{ cm}^{-1}$ . The curved bimorph is electrically

Figure 22.  $\pi$ -shaped ultrasonic linear motor.

driven at the mechanical resonance, which generates a large opening and closing motion at the contact point with the floor. In order to control the device in both clockwise and counter-clockwise rotations, a slight difference of the leg width between the right and left legs was intentionally made, so as to provide a slight difference between their resonance frequencies. By choosing a suitable drive frequency, the right or left leg pair is more mechanically excited, leading to curving.

The  $\pi$ -shape ultrasonic motor described in section 3.2 can be modified to be driven in a propagating wave manner. K Ohnishi *et al* developed a motor as shown in figure 22, where two multilayer actuators were installed at the two corners of the  $\pi$ -shaped frame, and driven with a 90 degree phase difference, revealing a 'trotting' leg motion [24].




One ceramic multilayer component actuator was proposed by Mitsui Sekka [25]. Figure 23 shows the electrode pattern. Only by the external connection, a combined vibration of the longitudinal  $L_1$  and bending  $B_2$  modes could be excited. The motor characteristics are shown in figure 24.

Let us introduce a surface acoustic wave motor proposed by Kurosawa and Higuchi [26]. As shown in figure 25(a), Rayleigh waves were excited in two crossed directions on a  $127.8^\circ$  rotation  $\text{Y-LiNbO}_3$  plate with two pairs of interdigital electrode patterns. Figure 25(b) shows a slider structure with three balls as legs. The driving vibration amplitude and the wave velocity of the Rayleigh waves were adjusted to 6.1 nm and  $22\text{ cm s}^{-1}$  for both  $x$  and  $y$  directions. It is important to note that even though the up-down vibrational amplitude is much smaller ( $<1/10$ ) than the surface roughness of the  $\text{LiNbO}_3$ , the slider was transferred smoothly. The mechanism has not been clarified yet; it might be due to the locally enhanced friction force through a ball-point contact. This may be categorized as a nano-actuator.

### 6. Speed/thrust calculation

We will introduce the speed and thrust calculation for ultrasonic motors roughly in this section [27]. These calculations depend on the type of motor as well as the contact conditions. The intermittent drive must be considered for the vibratory coupler type motors, while the surface wave type provides the continuous drive in the calculation. The contact models include:

Table 1. Comparison of the motor characteristics of the vibration coupler standing wave type (Hitachi Maxel), surface propagating wave type (Shinsei Industry) and a compromised 'teeth' vibrator type (Matsushita).

CHARACTERISTICS TYPES	Rotation	Rotation Speed (rpm)	Rotation Torque (kg-cm)	Efficiency (%)	Size	Analogy
Vibratory Coupler Type 	Uni- Direction	600	13	80	Slim & Long	Euglena
Compromise Type 	Reversible	600	1	45	· · ·	Paramecium
Surface Wave Type 	Reversible	600	0.5	30	Wide & Thin	Amoeba

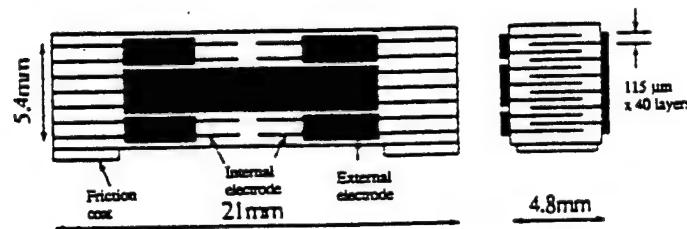


Figure 23. Multilayer ceramic simple linear motor.

- (1) rigid slider and rigid stator,
- (2) compliant slider and rigid stator,
- (3) compliant slider and compliant stator.

### 6.1. Surface wave type

If the rigid slider and rigid stator model is employed, the slider speed can be obtained from the horizontal velocity of the surface portion of the stator (see figure 26). If the frequency and wavelength of the stator vibration are  $f$  and  $\lambda$ , respectively, and the normal vibration amplitude (up-down) is  $Z$ , and the distance between the surface and the neutral plane is  $e_0$ , the wave propagation speed is given by

$$V = f\lambda. \quad (13)$$

This is the sound phase velocity of the vibration mode! In contrast, the speed of the slider is given by

$$\dot{v} = 4\pi^2 Z e_0 f / \lambda. \quad (14)$$

It is noteworthy that the slider moves in the opposite direction with respect to the wave traveling direction.

### 6.2. Vibration coupler type

Here, the compliant slider—rigid stator model is introduced. As shown in figure 27, the horizontal and vertical displacements of the rigid stator are given by

$$\begin{aligned} a &= a_0 \cos \omega t \\ b &= b_0 \sin \omega t. \end{aligned} \quad (15)$$

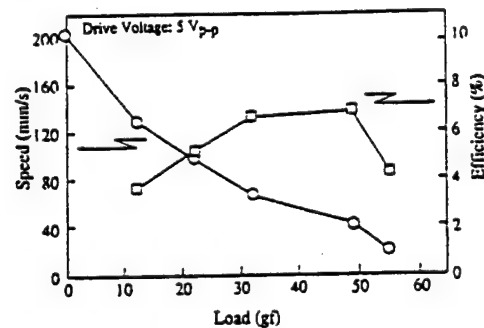


Figure 24. Motor characteristics of the Mitsui Sekka motor.

Thus, the horizontal velocity becomes

$$v_h = (\partial a / \partial t) = -a_0 \omega \sin \omega t. \quad (16)$$

We usually employ the following three hypotheses for further calculations:

*Hypothesis 1.* Normal force is given as follows, using a characteristic angle  $\phi$  (between  $P_1$  and  $P_2$ ):

$$\begin{aligned} n &= \beta [\sin \omega t - \cos(\phi/2)] \\ &\text{for } (\pi/2 - \phi/2) < \omega t < (\pi/2 + \phi/2) \text{ (in contact)} \\ n &= 0 \quad \text{for } 0 < \omega t < (\pi/2 - \phi/2), (\pi/2 + \phi/2) < \omega t < 2\pi \text{ (out of contact).} \end{aligned} \quad (17)$$

*Hypothesis 2.* The slider speed is constant ( $V_0$ ).



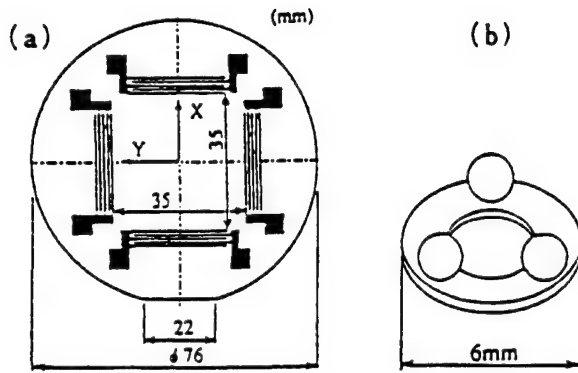


Figure 25. (a) Stator structure of the surface acoustic wave motor. (b) Slider structure of the SAW motor.

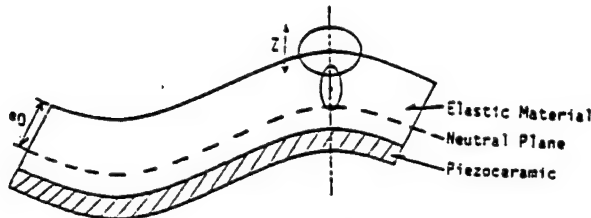


Figure 26. Displacement configuration of the stator of the surface wave type motor.

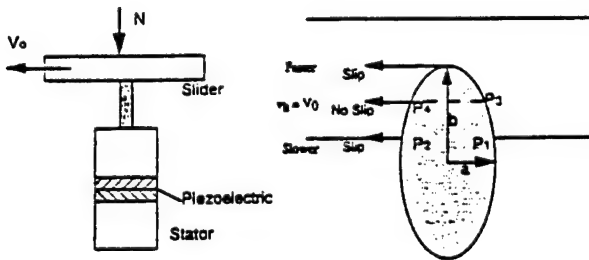


Figure 27. Compliant slider and rigid stator model.

**Hypothesis 3.** The maximum thrust is given by the dynamic friction constant  $\mu_d$ :

$$\begin{aligned} f &= -\mu_d n && \text{accelerating force for } (\pi/2 - \psi/2) \\ &< \omega t < (\pi/2 + \psi/2) \\ f &= \mu_d n && \text{dragging force for } (\pi/2 - \phi/2) \\ &< \omega t < (\pi/2 - \psi/2), (\pi/2 + \psi/2) < \omega t \\ &< (\pi/2 + \phi/2). \end{aligned} \quad (18)$$

The main results are summarized. If we know  $\phi$  experimentally (or theoretically taking into account the geometry and elasticity) under a certain normal force  $N$ , we can calculate the no-load speed  $V_0$  from

$$V_0 = -a_0 \omega \sin(\phi/2)/(\phi/2) \quad (19)$$

and no-slip position angle  $\psi$  from the following relation:

$$\cos(\psi/2) = \sin(\phi/2)/(\phi/2). \quad (20)$$

Then, finally, we can obtain the thrust from

$$F = \mu_d N \{1 - 2[\sin(\psi/2) - (\psi/2) \cos(\phi/2)]/[\sin(\phi/2) - (\phi/2) \cos(\phi/2)]\}. \quad (21)$$

In the case of  $\phi = 0$ ,  $\psi = 0$ ,  $V_0 = -a_0 \omega$ ,  $F = -0.155 \mu_d N$ ; while in the case of  $\phi = \pi$ ,  $\cos(\psi/2) = 2/\pi$ ,  $V_0 = -(2/\pi) a_0 \omega$  and  $F = -0.542 \mu_d N$ . With increasing contact period of the vibratory piece, the thrust  $F$  increases by sacrificing the speed.

For other model calculations, refer to the book [11].

## 7. Reliability of ultrasonic motors

In the development of ultrasonic motors, the following themes should be systematically studied:

- (1) Measuring methods for high-field electromechanical couplings.
- (2) Materials development (low loss and high vibration velocity).
- (3) Piezo-actuator designs.
  - (a) Heat generation mechanism.
  - (b) Degradation mechanisms.
  - (c) New multilayer actuator designs.
- (4) USM designs.
  - (a) Displacement magnification mechanisms (horn, hinge-lever).
  - (b) USM types (standing-wave type, propagating-wave type).
  - (c) Frictional contact part.
- (5) Drive/control.
  - (a) High frequency/high power supply.
  - (b) Resonance/antiresonance usage.

We will discuss the reliability issues in this section: heat generation, friction materials and drive/control techniques in the ultrasonic motors.

### 7.1. Heat generation

The largest problem in ultrasonic motors is heat generation, which sometimes drives temperatures up to 120°C and causes a serious degradation of the motor characteristics through depoling of the piezoceramic. Therefore, the ultrasonic motor requires a very hard type piezoelectric with a high mechanical quality factor  $Q$ , leading to the suppression of heat generation. It is also notable that the actual mechanical vibration amplitude at the resonance frequency is directly proportional to this  $Q$  value.

Figure 28 shows mechanical  $Q$  versus basic composition  $x$  at effective vibration velocity  $v_0 = 0.05 \text{ m s}^{-1}$  and  $0.5 \text{ m s}^{-1}$  for  $\text{Pb}(\text{Zr}_x\text{Ti}_{1-x})\text{O}_3$  doped with 2.1 at.% of Fe [28]. The decrease in mechanical  $Q$  with an increase of vibration level is minimum around the rhombohedral-tetragonal morphotropic phase boundary (52/48). In other words, the worst material at a small vibration level becomes the best at a large vibration level, and the data obtained by a conventional impedance analyser are not relevant to high power materials.

Figure 29 shows an important notion on heat generation from the piezoelectric material. The resistances  $R_d$  and

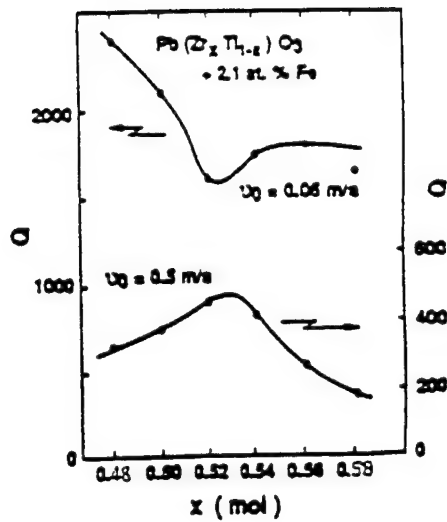


Figure 28. Mechanical quality factor  $Q$  against basic composition  $x$  at vibration velocity  $v_0 = 0.05$  and  $0.5 \text{ m s}^{-1}$  for  $\text{Pb}(\text{Zr}_x\text{Ti}_{1-x})\text{O}_3 + 2.1 \text{ at.}\% \text{ Fe}$  ceramics.

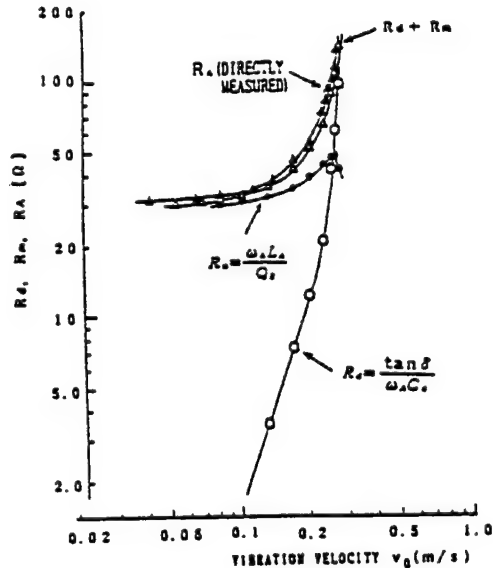


Figure 29. Vibration velocity dependence of the resistances  $R_d$  and  $R_m$  in the equivalent electric circuit.

$R_m$  in the equivalent electrical circuit are separately plotted as a function of vibration velocity [29]. Note that  $R_m$ , mainly related to the mechanical loss, is insensitive to the vibration velocity, while  $R_d$ , related to the dielectric loss, changes significantly around a certain critical vibration velocity. Thus, the resonance loss at a small vibration velocity is mainly determined by the mechanical loss, and with increasing vibration velocity, the dielectric loss contribution significantly increases. We can conclude that heat generation is caused by dielectric loss (i.e.  $P$ - $E$  hysteresis loss).

Zheng *et al* reported the heat generation from various sizes of multilayer type piezoelectric ceramic actuators [30]. The temperature change was monitored in the actuators when driven at  $3 \text{ kV mm}^{-1}$  and  $300 \text{ Hz}$ , and figure 30 plots

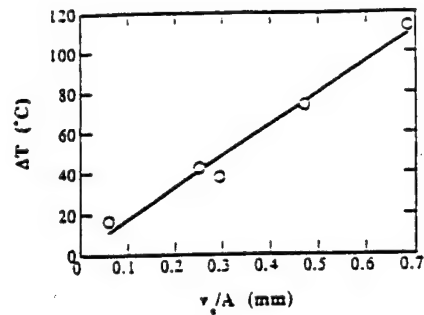


Figure 30. Temperature rise versus  $V_e/A$  ( $3 \text{ kV mm}^{-1}$ ,  $300 \text{ Hz}$ ), where  $V_e$  is the effective volume generating the heat and  $A$  is the surface area dissipating the heat.

the saturated temperature as a function of  $V_e/A$ , where  $V_e$  is the effective volume (electrode overlapped part) and  $A$  is the surface area. This linear relation is reasonable because the volume  $V_e$  generates the heat and this heat is dissipated through the area  $A$ . Thus, if you need to suppress the heat, a small  $V_e/A$  design is preferred.

## 7.2. Frictional coating and lifetime

Figure 31 plots the efficiency and maximum output of various friction materials [31]. High ranking materials include PTFE (polytetrafluoroethylene, Teflon), PPS (Ryton), PBT (polybutyl terephthalate) and PEEK (polyethylethylketone). In practical motors, Econol (Sumitomo Chemical), carbon fiber reinforced plastic (Japan Carbon), PPS (Sumitomo Bakelite) and polyimide have been popularly used. Figure 32 shows the wear and driving period for CFRP, which indicates that the  $0.5 \text{ mm}$  thick coat corresponds to  $6000$ – $8000$  hours life [32]. Although the lifetime of the ultrasonic motor is limited by the characteristics of the friction material, this problem has been nearly solved in practice for some cases. The durability test of the Shinsei motor (USR 30) is shown below:

continuous drive (CW 1 min and CCW 1 min) under revolution  $250 \text{ rpm}$  and load  $0.5 \text{ kg cm}$

→ after 2000 hours, the revolution change is less than 10%

intermittent drive (CW 1 rotation and CCW 1 rotation) under no load

→ after 250 million revolutions, no degradation in motor characteristics.

Taking into account the usual lifetime specifications, e.g.  $2000$ – $3000$  hours for VCRs, the lifetime of the ultrasonic motor is no longer a problem.

Of course, the lifetime of the motor itself is not identical to the lifetime installed in a device system. We need further clarification on this issue under severe drive conditions such as large load and high temperature and humidity.



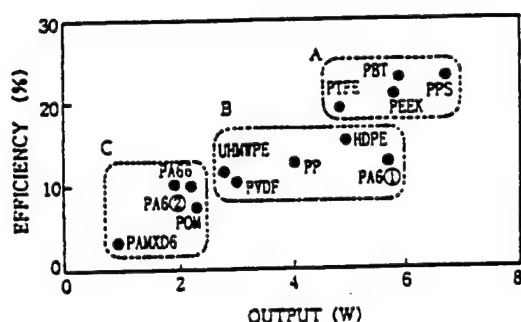


Figure 31. Efficiency and maximum output of the Shinsei ultrasonic motor for various friction materials.

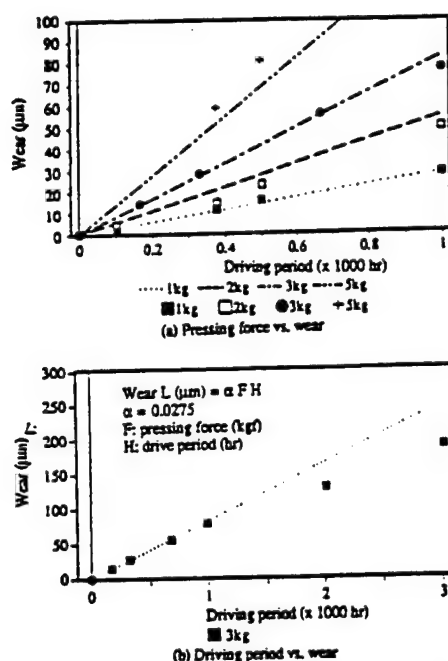


Figure 32. Wear and driving period of the ultrasonic motor for CFRP friction material.

### 7.3. Drive/control technique

Figure 33 summarizes the control methods of the ultrasonic motors. Taking account of the controllability and efficiency, pulse width modulation is most highly recommended.

Driving the motor at the antiresonant frequency, rather than at the resonant state, is also an intriguing technique to reduce the load on the piezo-ceramic and the power supply. Mechanical quality factor  $Q_m$  and temperature rise have been investigated on a PZT ceramic rectangular bar, and the results for the fundamental resonance (A-type) and antiresonance (B-type) modes are plotted in figure 34 as a function of vibration velocity [33]. It is recognized that  $Q_B$  is higher than  $Q_A$  over the whole vibration velocity range. In other words, the antiresonance mode can provide the same mechanical vibration level without generating heat. Moreover, the usage of 'antiresonance', whose admittance is very low, requires low current and high voltage for driving, in contrast to high current and low voltage for 'resonance'. This means that a conventional inexpensive power supply may be utilized for driving the ultrasonic

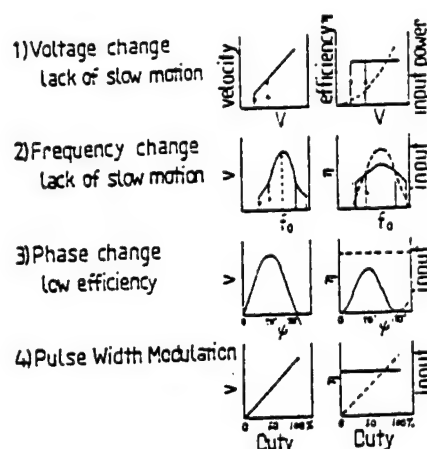


Figure 33. Control methods of the ultrasonic motors.

motor.

## 8. Summaries

### 8.1. Merits and demerits of ultrasonic motors

Ultrasonic motors are characterized by 'low speed and high torque', which are contrasted with 'high speed and low torque' of the conventional electromagnetic motors. Thus, the ultrasonic motors do not require gear mechanisms, leading to very quiet operation and space saving. Negligible effects from external magnetic or radioactive fields, and no generation of these fields are suitable for the application to electron beam lithography etc relevant to the semiconductor technology. Moreover, high power/weight ratio, high efficiency, compact size and light weight are very promising for the future micro-actuators adopted for catheter or tele-surgery.

### 8.2. Classifications of ultrasonic motors

There are various categories to classify ultrasonic motors such as:

- (1) operation: rotary type and linear type;
- (2) device geometry: rod type,  $\pi$ -shaped, ring (square) and cylinder types;
- (3) generating wave: standing wave type and propagating wave type.

### 8.3. Contact models for speed/thrust calculations

The following models have been proposed to calculate the speed/thrust of the ultrasonic motors:

- (1) rigid slider and rigid stator,
- (2) compliant slider and rigid stator,
- (3) compliant slider and compliant stator.

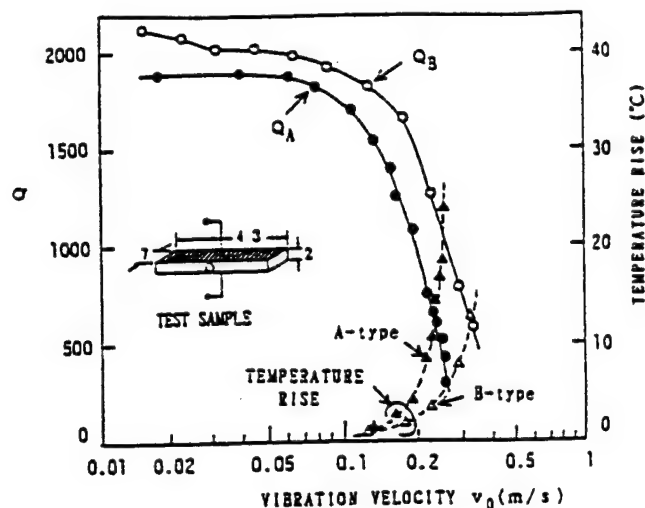


Figure 34. Vibration velocity dependence of the quality factor  $Q$  and temperature rise for both A (resonance) and B (antiresonance) type resonances of a longitudinally vibrating PZT rectangular transducer through  $d_{31}$ .

#### 8.4. The ultrasonic motor development requirements

For the further applications of ultrasonic motors, systematic investigations on the following issues will be required:

- (1) low loss and high vibration velocity piezo-ceramics,
- (2) piezo-actuator designs with high resistance to fracture and good heat dissipation,
- (3) USM designs:
  - (a) displacement magnification mechanisms (horn, hinge-lever),
  - (b) USM types (standing-wave type, propagating-wave type),
  - (c) frictional contact part,
- (4) high frequency/high power supplies.

#### References

- [1] Barth H V 1973 *IBM Tech. Disclosure Bull.* 16 2263
- [2] Lavrinenko V V, Vishnevski S S and Kartashev I K 1976 *Izv. Vyssh. Uchebn. Zaved. Radioelektron.* 13 57
- [3] Vasiliev P E et al 1979 *UK Patent Application* GB 2020857 A
- [4] Sashida T 1982 *Oyo Butsuri* 51 713
- [5] Kumada A 1985 *Japan. J. Appl. Phys.* 24 (Supplement 2) 739
- [6] Koc B 1998 *PhD Thesis* Electrical Engineering Department, The Pennsylvania State University
- [7] Fuda Y and Yoshida T 1994 *Ferroelectrics* 160 323
- [8] Nakamura K, Kurosawa M and Ueha S 1993 *Proc. Japan. Acoust. Soc.* No 1-1-18, 917
- [9] Uchino K, Kato K and Tohda M 1988 *Ferroelectrics* 87 331
- [10] Tomikawa Y, Nishituka T, Ogasawara T and Takano T 1989 *Sensors Mater.* 1 359
- [11] Ueha S and Tomikawa Y 1993 *Ultrasonic Motors (Monographs in Electrical and Electronic Engineering 29)* (Oxford: Oxford Science)
- [12] 1983 *Nikkei Mech.* 28 Feb. 44
- [13] Kurosawa M, Ueha S and Mori E 1985 *J. Acoust. Soc. Am.* 77 1431
- [14] Ueha S and Kuribayashi M 1986 *Ceramics* 21 9
- [15] Sashida T 1983 *Mech. Automation Japan* 15 31
- [16] Ise K 1987 *J. Acoust. Soc. Japan* 43 184
- [17] Kasuga M, Satoh T, Tsukada N, Yamazaki T, Ogawa F, Suzuki M, Horikoshi I and Itoh T 1991 *J. Soc. Precision Eng.* 57 63
- [18] Cummings J and Stutts D 1994 *Am. Ceram. Soc. Trans.* 147
- [19] Kumada A 1989 *Ultrason. Technol.* 1 51
- [20] Tomikawa Y and Takano T 1990 *Nikkei Mech. Suppl.* 194
- [21] Yoshida T 1989 *Proc. 2nd Memorial Symp. on Solid Actuators of Japan: Ultra-precise Positioning Techniques and Solid Actuators for Them* p 1
- [22] Uchino K 1988 *Solid State Phys. Special Issue Ferroelectrics* 23 632
- [23] Hayashi T 1984 *Proc. Japan. Electr. Commun. Soc.* US84-8 25
- [24] Ohnishi K, Naito K, Nakazawa T and Yamakoshi K 1991 *J. Acoust. Soc. Japan* 47 27
- [25] Saigo H 1994 *15th Symp. on Ultrasonic Electronics, USE '94* PB-46 p 253
- [26] Takahashi M, Kurosawa M and Higuchi T 1994 *Proc. 6th Symp. on Electro-Magnetic Dynamics '94* 940-26 II, D718, p 349
- [27] Uchino K 1996 *Piezoelectric Actuators and Ultrasonic Motors* (Dordrecht: Kluwer)
- [28] Takahashi S and Hirose S 1993 *Japan. J. Appl. Phys.* 32 2422
- [29] Hirose S, Aoyagi M, Tomikawa Y, Takahashi S and Uchino K 1995 *Proc. Ultrasonics Int. '95 (Edinburgh, 1995)* p 184
- [30] Zheng J, Takahashi S, Yoshikawa S, Uchino K and de Vries J W C 1996 *J. Am. Ceram. Soc.* 79 3193
- [31] Tada Y, Ishikawa M and Sagara N 1991 *Polym. Preprints* 40 1408
- [32] Ohnishi K et al 1993 *SAW Device 150 Committee, Japan. Acad. Promotion Inst., Abstract 36th Mtg* p 5
- [33] Hirose S, Takahashi S, Uchino K, Aoyagi M and Tomikawa Y 1995 *Mater. Res. Soc. Symp. Proc.* vol 360 (Pittsburgh, PA: Materials Research Society) p 15

# **APPENDIX 4**

## Phase Transformations in Smart Materials

ROBERT E. NEWNHAM

The Pennsylvania State University, Materials Research Laboratory, University Park, PA 16802, USA.  
E-mail: bobnewnham@psu.edu

(Received 1 February 1998; accepted 6 July 1998)

### Abstract

One of the qualities that distinguishes living systems from inanimate matter is the ability to adapt to changes in the environment. Smart materials have the ability to perform both sensing and actuating functions and are, therefore, capable of imitating this rudimentary aspect of life. Four of the most widely used smart materials are piezoelectric  $\text{Pb}(\text{Zr}, \text{Ti})\text{O}_3$ , electrostrictive  $\text{Pb}(\text{Mg}, \text{Nb})\text{O}_3$ , magnetostrictive  $(\text{Tb}, \text{Dy})\text{Fe}_2$  and the shape-memory alloy  $\text{NiTi}$ . All four are ferroic with active domain walls and two phase transformations, which help to tune the properties of these actuator materials.  $\text{Pb}(\text{Zr}, \text{Ti})\text{O}_3$  is a ferroelectric ceramic which is cubic at high temperature and becomes ferroelectric on cooling through the Curie temperature. At room temperature, it is poised on a rhombohedral–tetragonal phase boundary which enhances the piezoelectric coefficients. Terfenol,  $(\text{Tb}, \text{Dy})\text{Fe}_2$ , is also cubic at high temperature and then becomes magnetic on cooling through its Curie temperature. At room temperature, it too is poised on a rhombohedral–tetragonal transition which enhances its magnetostriction coefficients.  $\text{Pb}(\text{Mg}, \text{Nb})\text{O}_3$  and nitinol ( $\text{NiTi}$ ) are also cubic at high temperatures and on annealing transform to a partially ordered state. On further cooling,  $\text{Pb}(\text{Mg}, \text{Nb})\text{O}_3$  passes through a diffuse phase transformation at room temperature where it exhibits very large dielectric and electrostrictive coefficients. Just below room temperature, it transforms to a ferroelectric rhombohedral phase. The partially ordered shape-memory alloy  $\text{NiTi}$  undergoes an austenitic (cubic) to martensitic (monoclinic) phase change just above room temperature. It is easily deformed in the martensitic state but recovers its original shape when reheated to austenite. The structural similarities between these four superb actuator

materials are remarkable, and provide a key to the development of future smart materials.

### 1. Introduction

The concept of a smart material can be illustrated with the smart shock absorber used to suppress road vibrations (Fig. 1). Inside the smart absorber developed by Toyota, there is a multilayer piezoelectric ceramic which has five layers for sensing road vibrations. The multilayer stacks positioned near each wheel of the auto also have about 100 layers which act as the actuator, all part of the same  $\text{Pb}(\text{Zr}, \text{Ti})\text{O}_3$  (PZT) ceramic. After analyzing the vibration signals, a voltage is fed back to the actuator stack and a response is made by pushing on the hydraulic system of the auto to enlarge the motion. In this way, the auto is able to analyze acceleration signals from road bumps and respond with a motion that cancels the vibration. This is the Toyota Electronic Modulated System, which produces force in the kilonewton range and displacements in the micrometer range.

In the smart shock absorber, the *direct piezoelectric effect* is used as a *sensor* by converting mechanical stress into an electrical voltage. Working through a feedback circuit, a larger electrical voltage with the appropriate frequency spectrum and phase angles is then applied to the piezoelectric material. Using the *converse piezoelectric effect*, the actuator creates a vibration that is out of phase with the incoming vibration and cancels it. In this device, the piezoelectric ceramic acts as *both* a sensor and an actuator.

This combination of sensing and actuating mimics two of the functions of a living system, namely being aware of the surroundings and then being able to respond to that signal with a useful response, usually in the form of a motion. By way of definition, then, a smart material is not simply a sensor. A sensor receives a stimulus and responds with a signal. A smart material is not simply an actuator. An actuator produces a useful motion or action. Smart materials function as both sensors and actuators. Smart materials sometimes have a control system and sometimes not. Some function like our spinal cord in that they are *passively smart* and respond without thought or signal processing going on. They are

---

*Robert E. Newnham recently retired as Alcoa Professor of Solid State Science at the Pennsylvania State University, where he taught courses in crystal chemistry, crystal physics and electroceramics. He has written more than 400 papers on ferroelectric and piezoelectric materials and devices, and is a member of the US National Academy of Engineering and the International Academy of Ceramics.*

---

analogous to the reflex responses of the human body. In other cases, smart systems analyze the sensed signal, perhaps for its frequency components, and then make a choice as to what type of response to make. An *actively smart system* such as this acts like a cognitive response in the human body (Newnham & Ruschau, 1991).

## 2. Molecular mechanisms

Crystallographic phase transformations are a prominent feature of the best smart materials. All four of the major families exhibit at least two transitions with different order parameters.

Nitinol and other shape-memory alloys have a broad phase transition with partially ordered caesium chloride-like structures transforming to a martensitic-like phase of lower symmetry. Both atomic ordering and atomic displacements are involved. In lead magnesium niobate (PMN), an outstanding electrostrictive material with the perovskite structure, there is a similar diffuse phase transition from a partially ordered high-temperature state to a ferroelectric low-temperature state. PMN is a ferroelectric analog to ferroelastic nitinol.

Terfenol is a typical magnetostrictive actuator with strong coupling between magnetic field and mechanical motion. It is an iron-rare-earth alloy with a paramagnetic-to-ferrimagnetic phase change at high temperature. Magnetostrictive actuators are operated near a second phase transformation where the magnetic spins undergo reorientation to different crystallographic directions. In piezoelectric PZT, the best known of the actuator materials, there are similar changes in symmetry. PZT is cubic at high temperatures and is operated near a boundary between rhombohedral and tetragonal states. Terfenol is a magnetic analog to ferroelectric PZT.

## 3. Ferroelectrics

To illustrate the behavior of piezoelectric and electrostrictive actuators, we have chosen  $\text{Pb}(\text{Zr}, \text{Ti})\text{O}_3$  and  $\text{Pb}(\text{Mg}, \text{Nb})\text{O}_3$ , usually referred to as PZT and PMN, respectively. PZT (lead zirconate titanate) is a well behaved normal ferroelectric with a large spontaneous polarization appearing at the Curie temperature. PMN (lead magnesium niobate) is a relaxor ferroelectric with a partially ordered perovskite structure and a broad diffuse phase transition. Very large dielectric constants and electrostriction coefficients are observed in this temperature range.

The multimillion dollar market for PZT multilayer actuators includes  $d_{33}$  thickness mode transducers,  $d_{31}$  transverse mode transducers and various bender types. Multilayer actuators have about a hundred layers and overall dimensions in the millimeter to centimeter range. Piezoelectric printers, fuel injectors and pneumatic

valves are well developed markets for these multilayer actuators.

Multilayer actuators make use of ferroelectric oxides such as lead zirconate titanate (PZT) and lead magnesium niobate (PMN) with the perovskite structure. Ferroelectric oxides with the perovskite, tungsten bronze, pyrochlore and bismuth titanate layer structures all have high dielectric constants, high refractive indices, and large electromechanical coupling coefficients, and all contain corner-linked octahedral networks of  $\text{Ti}^{4+}$ ,  $\text{Nb}^{5+}$  or other  $d^0$  ions. These transition-metal elements are the highly polarizable 'active' ions promoting ferroelectricity and the high permittivities and piezoelectric constants required for transducers and capacitors. With reference to the periodic system, there are two major groups of active ions, and both are near electronic 'crossover' points where different types of atomic orbitals are comparable in energy and where hybrid bond formation is prevalent. The first group, typified by  $\text{Ti}^{4+}$ ,  $\text{Nb}^{5+}$  and  $\text{W}^{6+}$ , are  $d^0$  ions octahedrally coordinated to oxygen. For  $\text{Ti}^{4+}$ , the electronic crossover involves the 3d, 4s and 4p orbitals, which combine with the s and p orbitals of its six  $\text{O}^{2-}$  neighbors to form a number of molecular orbitals for the  $(\text{TiO}_6)^{8-}$  complex. The bond energy of the complex can be lowered by distorting the octahedron to a lower symmetry. This leads to molecular dipole moments, ferroelectricity, large dielectric constants, piezoelectricity and electrostriction. A second group of active elements contributing to polar distortions in ceramic dielectrics are the lone-pair ions having two electrons outside a closed shell in an asymmetric hybrid orbital. Among oxides, the most important of these lone-pair ions are  $\text{Pb}^{2+}$  and  $\text{Bi}^{3+}$ , which are involved in a number of ferroelectrics ( $\text{PbTiO}_3$ ,  $\text{Bi}_4\text{Ti}_3\text{O}_{12}$ ,  $\text{PbNb}_2\text{O}_6$ ) with high Curie temperatures. In many of these compounds,  $\text{Pb}^{2+}$  and  $\text{Bi}^{3+}$  are in pyramidal coordination with oxygen and therefore contribute to the spontaneous polarization.

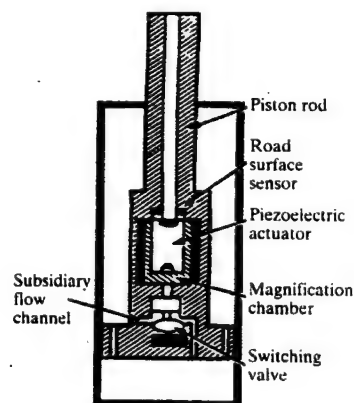


Fig. 1. Cross section of the principal portion of a shock absorber (Uchino, 1997).

### 3.1. Piezoelectric PZT

Most piezoelectric transducer formulations are based on  $\text{Pb}(\text{Zr}, \text{Ti})\text{O}_3$ , one of a number of ferroelectric substances crystallizing with the perovskite structure (Megaw, 1957). Pb atoms are located at the corners of the unit cell and O atoms at the face centers. Both Pb and O ions have radii of about 1.4 Å and together they make up a face-centered cubic array having a lattice parameter near 4 Å. Octahedrally coordinated Ti or Zr ions are located at the center of the unit cell.

On cooling from high temperature, the crystal structure of PZT undergoes a displacive phase transformation with atomic displacements of about 0.1 Å. For titanium-rich compositions, the point symmetry changes from cubic  $m\bar{3}m$  to tetragonal  $4mm$  at the Curie temperature. The tetragonal state with its spontaneous polarization along  $[001]$  persists down to 0 K. The structural changes are illustrated in Fig. 2.

To make use of these piezoelectric ceramics with their large polarizations, compositions near a second phase transition are chosen. At the Curie point, PZT converts from a paraelectric state with the ideal cubic perovskite structure to a ferroelectric phase located near a morphotropic phase boundary between the tetragonal and rhombohedral states. Very large piezoelectric coupling between electric and mechanical variables is obtained near this phase boundary. Much of the current research in this field involves looking for other morphotropic phase boundaries to further enhance the electromechanical coupling factors.

The two effects that are utilized in PZT transducers are the direct and the converse piezoelectric effects. The direct effect relates polarization to stress and is used in sensors. The converse effect relates strain to electric field and is used in actuators.

For a poled ceramic having symmetry  $\infty m$ ,  $d_{31}$ ,  $d_{33}$  and  $d_{15}$  are the appropriate tensor coefficients. There are

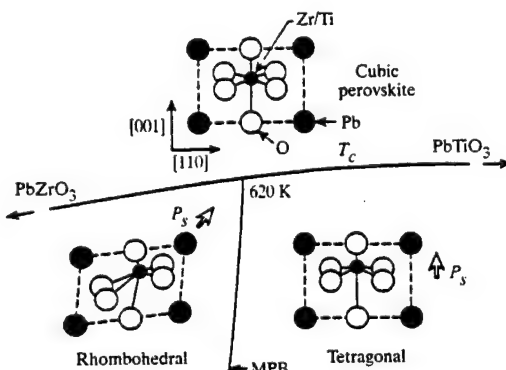


Fig. 2. A portion of the  $\text{PbZrO}_3$ - $\text{PbTiO}_3$  phase diagram showing the structure changes at the Curie temperature ( $T_c$ ) and the morphotropic phase boundary (Jaffe *et al.*, 1971). Compositions near a morphotropic phase boundary have 14 possible poling directions.

both intrinsic and extrinsic contributions to these piezoelectric coefficients. The intrinsic effects coming from the distortions of the crystal structure under mechanical stress are pictured in Fig. 3.

Under mechanical stress parallel to the dipole moment, there is an enhancement of  $P_s$  along  $X_3$ . When stress is applied perpendicular to that dipole moment, electric charges are developed transversely. These are the  $d_{33}$  and  $d_{31}$  effects, respectively. When the dipole is tilted by shear stress, charges appear on the side faces, the  $d_{15}$  coefficient. There are extrinsic contributions to the piezoelectric coefficient as well and these can be extremely large, often involving the domain wall motions.

Ferroelectric ceramics such as lead zirconate titanate do not become piezoelectric until electrically poled. Poling is carried out under intense electric fields at elevated temperatures below the ferroelectric Curie point where the domains are easily aligned.

Titanium-rich compositions in the PZT system favor a tetragonal modification with sizable elongation along  $[001]$  and a large spontaneous polarization in the same direction. There are six equivalent polar axes in the tetragonal phase corresponding to the  $[100]$ ,  $[\bar{1}00]$ ,  $[010]$ ,  $[0\bar{1}0]$ ,  $[001]$ ,  $[00\bar{1}]$  directions of the cubic paraelectric state. A rhombohedral ferroelectric state is favored for zirconium-rich compositions. Here the distortion and polarization are along  $[111]$  directions, giving rise to eight possible domain states:  $[111]$ ,  $[\bar{1}\bar{1}1]$ ,  $[1\bar{1}\bar{1}]$ ,  $[\bar{1}11]$ ,  $[11\bar{1}]$ ,  $[\bar{1}\bar{1}1]$ ,  $[\bar{1}1\bar{1}]$  and  $[111]$ .

The compositions that pole best lie near the morphotropic boundary between the rhombohedral and tetragonal ferroelectric phases. For these compositions,

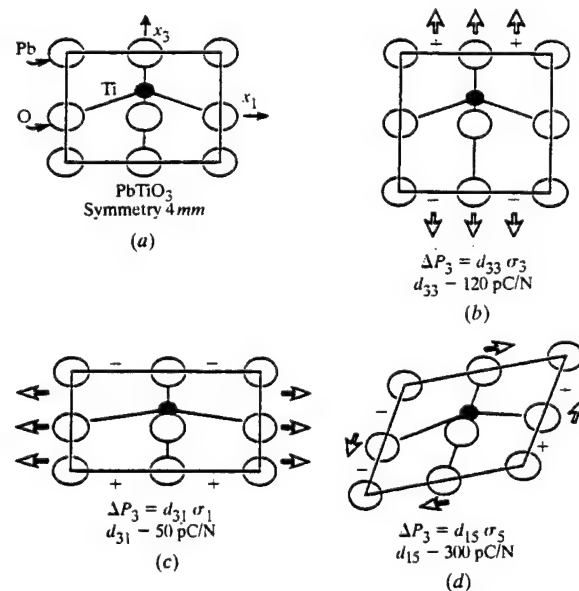


Fig. 3. Intrinsic piezoelectric effect in polar lead titanate.

there are 14 possible poling directions over a very wide temperature range. This explains in part why the ceramic piezoelectric coefficients are largest near the morphotropic boundary. Phase changes between the rhombohedral and tetragonal phases also occur during the poling process.

### 3.2. Electrostrictors

Piezoelectricity is a third-rank tensor relating strain and electric field. Electrostriction is a fourth-rank tensor relating strain to the square of the electric polarization.

Above the Curie temperature, the perovskite structure is cubic and the electrostriction effect is more important than the piezoelectric effect because third-rank tensors disappear in centrosymmetric media. This leads to what we call very smart ceramics. In a smart ceramic, the direct piezoelectric effect is used for sensing followed by feedback through the converse piezoelectric effect. In a very smart material, we monitor the change in capacitance of the material. We then monitor feedback with both direct-current (DC) and alternating-current (AC) fields to tune the magnitude of the electromechanical-coupling coefficient and then to drive it. For higher-order coupling coefficients like electrostriction, there are three rather than two coupled effects: the change in the dielectric constant with stress, the field dependence of the piezoelectric voltage coefficient and the electrically driven mechanical strain. The electrostrictive ceramic becomes a tunable transducer (Newnham, 1991).

We began work on a number of these electrostrictive materials nearly 20 years ago (Uchino *et al.*, 1980) for active optic systems. Much of this work was performed with the ITEK Corporation in Lexington, MA, USA. During the cold war, there were many satellites flying over the old Soviet Union utilizing active optic systems to eliminate atmospheric turbulence. In adjusting the position of optical components, electrostrictive materials have an advantage over piezoelectrics because there is much less hysteresis associated with the motions.

Work on active optic systems has continued over the years and similar multilayer actuators were used to correct the positioning of the optical elements in the Hubble telescope. Supermarket scanners use actuators and flexible mirrors to optically interrogate bar codes.

### 3.3. Relaxor ferroelectrics

Ordered perovskites generally have low dielectric constants because the linkage between 'active' ions is severed. In partially disordered structures such as the relaxor ferroelectrics, the dielectric constant can be extremely large, making them useful as capacitor dielectrics and as electrostrictive actuators. The most widely used compositions are modifications of lead magnesium niobate,  $\text{Pb}_{1-x}\text{Mg}_x\text{Nb}_2\text{O}_9$ .

Relaxor ferroelectrics consist of temperature-sensitive microdomains resulting from the many different 'active' ion linkages in the disordered octahedral framework. Each  $\text{NbO}_6$  octahedron may be bonded to anywhere from zero to six other  $\text{NbO}_6$  octahedra. Connections between these octahedra are assumed to be essential to ferroelectricity and high dielectric constant values. As temperature decreases from the high-temperature paraelectric state, ferroelectric microdomains gradually coalesce to macrodomains giving rise to a diffuse phase transformation. These polarization fluctuations are also dependent on bias field and measurement frequency. The dielectric constant drops off rapidly with frequency (hence the name 'relaxor') because it takes time for the polarization fluctuations to respond. DC bias fields favor coalescence, giving the same effect as lowering the temperature.

Relaxor behavior is very common along Pb-based perovskites, suggesting that  $\text{Pb}^{2+}$  and its 'lone-pair' electrons play a role in the microdomain process, possibly by adjusting the orientation of the lone pair.

Electrostriction is described by a  $6 \times 6$  matrix,  $Q$ , relating strain to the square of the electric polarization. This type of matrix is familiar to most materials scientists because electrostriction is a fourth-rank tensor almost identical in form to elasticity. For a cubic crystal, we are dealing with the same coefficients, 11, 12 and 44, that would normally be used to describe the elastic properties of a cubic crystal. In the case of electrostriction, strain is induced electrically rather than mechanically.

Compared to piezoelectric transducers which utilize a polar material, electrostrictive transducers use a cubic material, a material that is poised on an instability with micro regions that are fluctuating in polarization. On average, the atoms are located in the ideal cubic sites but are continually shifting off these positions. An atomic view of the  $Q_{11}$ , the  $Q_{12}$  and the  $Q_{44}$  motions (Newnham, 1991) in an electrostrictive material is shown in Fig. 4. The underlying origin of these effects is a partial ordering of the PMN perovskite structure in which the Nb and the Mg atoms of lead magnesium niobate alternate but only over short ranges, typically 30–50 Å, just a few unit cells. Within these ordered islands, there are fluctuating dipoles that are acted upon by an external field to make large electrostrictive motion.

## 4. Magnetostrictive actuators

PZT and PMN ceramics are outstanding ferroelectric actuators, but equally interesting developments are taking place in ferroelastic and ferromagnetic materials. All these ferroic materials have a domain structure in which the walls can be moved with electric fields, magnetic fields or mechanical stresses.

Magnetostrictive alloys like terfenol-D ( $\text{Tb}_{1-x}\text{Dy}_x\text{Fe}_2$ ) function well as both sensors and



actuators (Hathaway & Clark, 1993). High-power actuators can deliver forces greater than 50 MPa with strains up to 0.6%, while magnetostrictive sensor materials can provide hundreds of times the sensitivity of semiconductor strain gauges. Magnetoelastic materials also have tunable elastic moduli that can be controlled by external magnetic fields.

A large number of magnetomechanical transducers and actuators utilizing terfenol-D have been designed and manufactured. The high-energy density of these actuators, plus their ruggedness and reliability, make them attractive for vibration suppression and high-power sonar. Thin films of magnetostrictive rare-earth-iron alloys can be sputtered on silicon and patterned by etching or sputtering through masks. Micropump and microvalve membranes and cantilevers appear to be promising microelectromechanical systems (MEMS) components (Wun-Fogle *et al.*, 1987).

The rare-earth atoms in terfenol have large orbital moments that interact with magnetic fields to give large magnetostrictive strains. Rotation of the magnetization

is largely responsible for the shape change. The field-induced strain in terfenol-D is about a hundred times larger than those in iron and nickel.

The iron in terfenol produces the high Curie temperature. The rare-earth Tb and Dy atoms produce the large magnetostriction. In combination, these three elements produce useful alloys. What I wish to point out here is the analogy to PZT. Plotted in Fig. 5 is a portion of the magnetic phase diagram of the material. It is cubic and paramagnetic at high temperature and then undergoes a magnetic phase transformation to a rhombohedral structure with magnetic spins parallel to  $\langle 111 \rangle$  directions. Near room temperature, it is poised on an instability with the spins ready to reorient into the tetragonal directions, the former  $\langle 100 \rangle$  directions of the cube. There is a complex domain structure both above and below the transition and, like PZT, it is poised on a rhombohedral-tetragonal phase boundary. The phase diagram of terfenol is the magnetic equivalent to the morphotropic boundary of PZT.

The figure of merit for magnetostrictive actuators is proportional to the saturation strain coefficient. But, in addition to a large shape change, the strain must be easy to move. Therefore, the anisotropy coefficient  $K$ , which controls the rotation of the magnetization, also comes into the figure of merit,  $\lambda/K$ , where  $\lambda$  is the saturation strain. TbFe<sub>2</sub> has a very large  $\lambda$  coefficient, but also has a large anisotropy constant  $K$ , which reduces the figure of merit. DyFe<sub>2</sub> has an anisotropy coefficient of opposite sign. So by tuning the composition to be near the point where the anisotropy coefficient goes to zero, one can make an easily movable strain in this magnetostrictive alloy. This maximizes the figure of merit.

Fig. 6 shows the two magnetic phase changes for terfenol-D. At high temperature, it is paramagnetic and,

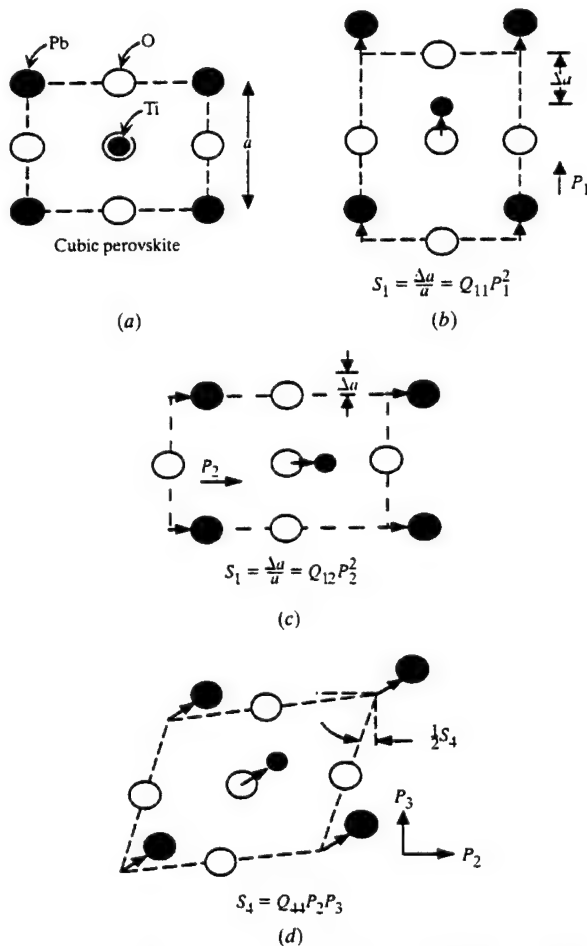


Fig. 4. Electrostriction in cubic perovskites showing the physical origin of the electrostrictive coefficients  $Q_{11}$ ,  $Q_{12}$  and  $Q_{44}$ .

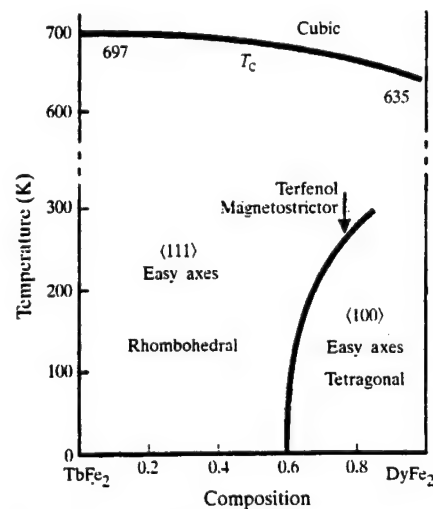


Fig. 5. Binary phase diagram for the Tb<sub>1-x</sub>Dy<sub>x</sub>Fe<sub>2</sub> system. Compositions near the magnetic spin boundary at  $x = 0.7$  are used in magnetostrictive applications (Purdy & Parr, 1961).



below  $T_c$  near 700 K, the spins are aligned along a  $[111]$  direction giving a rhombohedral distortion of the unit cell. The strong antiferromagnetic interactions between the iron and rare-earth spins make the alloy ferrimagnetic rather than ferromagnetic. Near room temperature, there is a spin reorientation to the tetragonal  $\langle 100 \rangle$  directions of the cube. The magnetic point group changes from  $3m'$  (the prime indicating time reversal operator) to  $4/mmm'$ .

An explanation of the large magnetostrictive effect in  $\text{TbFe}_2$  and rare-earth-iron intermetallic compounds has been put forward by Clark and co-workers (Clark, 1980). Pure rare-earth metals possess large magnetostrictive strains but are not used as actuators because of their low Curie temperatures. When alloyed with iron, however, the  $R\text{Fe}_2$  compounds are magnetic at room temperature with  $T_c$  values near 700 K.

The large magnetostriction coefficients are caused by the orbital motion of the rare-earth  $4f$  electrons, which impart a shape anisotropy to the atoms. Trivalent Tb and Dy ions resemble flattened oblate ellipsoids while Er, Sm and Tm ions have elongated prolate shapes. Under strong magnetic fields, the magnetization rotates to a new orientation and is accompanied by a shape change as the ellipsoids change orientation.

The resulting magnetostrictive strain is especially large for  $R\text{Fe}_2$  compounds with the cubic Laves C15 structure. The structure distorts to a pseudocubic ferrimagnetic phase below the Curie temperature with the iron sublattice magnetization opposed to that of the rare earths. At room temperature, the preferred directions for magnetization are the six  $\langle 100 \rangle$  cube axes for domains in  $\text{DyFe}_2$ . For  $\text{TbFe}_2$ , the eight  $\langle 111 \rangle$  body diagonals are the easy axes of magnetization.

The magnetostriction coefficients are largest for the rhombohedrally distorted alloys with  $\langle 111 \rangle$  easy axes. This can be understood by examining the crystal structure. In the C15 structure, the rare-earth ions form a diamond-like lattice in which each rare-earth atom is bonded along  $\langle 111 \rangle$  directions to four other rare-earth

atoms. When a magnetic field is applied along  $[111]$ , and the  $R\text{Fe}_2$  compound magnetizes in this direction, there is a redistribution of electron density and a change in the  $R-R$  bonding. For oblate atoms like terbium, the bonds along  $\langle 111 \rangle$  are enhanced when the  $4f$  electron contribution to the Tb-Tb bond along  $[111]$  is decreased. This causes expansion along  $[111]$  and contraction in the perpendicular directions. For  $\text{ErFe}_2$ , the prolate Er ions also align along  $\langle 111 \rangle$  directions but a field along  $[111]$  causes a contraction along  $[111]$  rather than an expansion. In this case, the Er-Er bond along  $[111]$  grows stronger and shorter as magnetization develops along  $[111]$ . Thus,  $\text{TbFe}_2$  has a large positive magnetostriction coefficient and  $\text{ErFe}_2$  has a large negative coefficient.

Other  $R\text{Fe}_2$  compounds magnetize along  $\langle 100 \rangle$  directions and have rather modest magnetostrictive coefficients. The enhancement in electron density is the same for all four  $R-R$  bonds pointing along different  $\langle 111 \rangle$  directions. This applies to both oblate and prolate rare-earth atoms. As a result, the magnetostriction coefficient of  $\text{DyFe}_2$  is an order of magnitude smaller than that of  $\text{TbFe}_2$ .

Nevertheless, it is important to alloy  $\text{TbFe}_2$  with  $\text{DyFe}_2$ . In actuators and transducers, it is very useful to have a large shape change but it is also important to be able to control the shape change with small applied fields. A large shape change frozen in position is of no practical value. To lower the driving field, a second phase change is positioned near room temperature. This can be performed by lowering the Curie temperature but this has the effect of demagnetizing the actuator and greatly reducing the magnetostriction coefficient. It is preferable to choose a composition near the rhombohedral-tetragonal phase boundary where the easy axis switches from  $\langle 111 \rangle$  to  $\langle 100 \rangle$ . Compositions near  $\text{Dy}_{0.7}\text{Tb}_{0.3}\text{Fe}_2$  have large magnetostrictive coefficients with easily controlled shape changes. Below room temperature, the magnetic symmetry changes from rhombohedral to tetragonal with a large decrease in the magnetostrictive shape change.

## 5. Shape-memory metals

My last example of an actuator material involves the shape-memory alloys that are thermally driven rather than the magnetic drive of magnetostrictors or the electrical drive of piezoelectric and electrostrictive materials. This material too has phase transitions associated with the large thermomechanical coupling coefficients. A commonly used material is nitinol, nickel titanium alloys, investigated initially at the Navy laboratories. Working near 1:1 compositions, the nickel-titanium intermetallic compound melts congruently at about 1570 K and has a martensitic phase transformation near room temperature.

Shape-memory alloys undergo martensitic transformations similar to those observed in the processing of

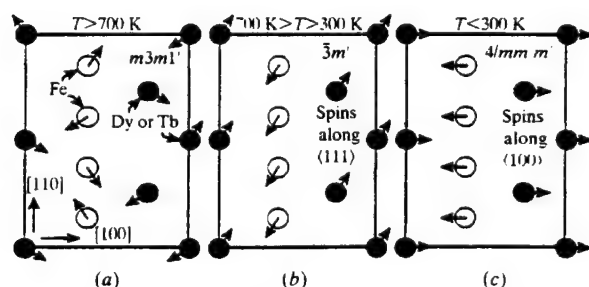


Fig. 6. Magnetic phase transformation in terfenol-D,  $\text{Tb}_{0.3}\text{Dy}_{0.7}\text{Fe}_2$ , magnetostrictive actuator. At the Curie temperature, the paramagnetic phase converts to a rhombohedral ferrimagnetic phase (b) with spins parallel to  $\langle 111 \rangle$  directions. Under operating conditions near room temperature, terfenol is poised on a second transition to a tetragonal ferrimagnetic state (c) with spins parallel to  $\langle 100 \rangle$  axes.

steel. Two characteristics of martensitic phase changes are the absence of long-range diffusion and the appearance of a shape change (Wayman, 1993). Ferroelastic phase transformations are also distortive and diffusionless, and have much in common with the martensites. Ferroelastic crystals exhibit mechanical hysteresis between stress and strain caused by the stress-induced movement of domain walls. Martensites are also internally twinned but mechanical stress causes phase changes as well as domain-wall movements.

Typically, these materials are partially ordered as they undergo a transition from a body-centered cubic structure to a partially ordered CsCl structure (Fig. 7). The shape-memory effect takes place at a martensitic transformation from the caesium chloride-like structure into a distorted multidomain martensite phase. Under stress, the martensite easily deforms and when re-heated goes back to the original morphology of the high-temperature structure. This is the shape-memory effect.

Some of the martensitic structures are very complex (Fig. 8). The monoclinic structure of nickel-titanium belongs to point group  $2/m$  and has a  $\beta$  angle about  $8^\circ$  different from  $90^\circ$ . This generates a large spontaneous strain accompanying the martensitic phase change and is the shape change that external mechanical stresses and thermally induced stresses act upon. In the case of

ferroelectrics, external fields act upon electric dipoles. For magnetic actuators, there are magnetic dipoles and with ferroelastics there is a shape change.

In the diffuse martensitic phase change, the partially ordered high-temperature austenite phase partially transforms into the martensitic phase (Fig. 9). Then, under mechanical stress, two things happen. Domain reorientation takes place as indicated by the little bars in Fig. 9 and phase changes occur as well. This behavior is very similar to the electrical behavior of the PMN relaxor ferroelectrics.

High-performance products utilizing shape-memory alloys include aircraft hydraulic couplings and electric connectors where they are used as substitutes for solenoids, motors and bimetallic actuators. Additionally, the alloys are used in shower heads and cut-off valves to provide thermal protection, and in dental prostheses and other medical products.

## 6. Concluding remarks

There are several common themes in this discussion of piezoelectric, electrostrictive, magnetostrictive and shape-memory materials. Two transformations are involved in most of these smart materials, often a primary ferroic (ferroelastic, ferroelectric or ferromagnetic) with domain-wall motions that assist in the sensing and actuating processes. The ferroics are operated near an instability to make these domain walls with their associated dipoles and strains movable. We have identified two main types among the commonly used actuators, although others appear to be possible too. In one type, there is a high Curie temperature as in PZT or terfenol and the actuator is operated near an orientational change of the electric or the magnetic dipole moment.

The second type involves a partially ordered phase, as in electrostrictive PMN or the shape-memory alloys. These materials are operated near a diffuse phase transition with two coexisting phases, the high

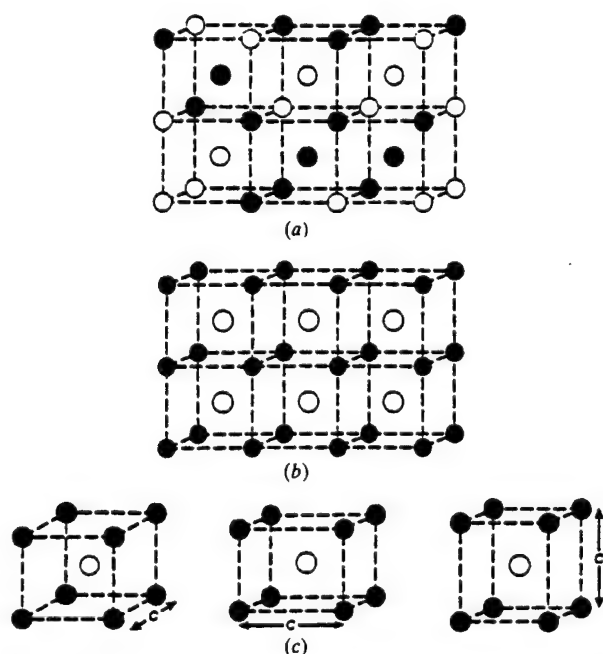


Fig. 7. Body-centered intermetallics often show a structural transformation from a high-temperature disordered body-centered-cubic phase (space group  $Im\bar{3}m$ ) (a) to an annealed-ordered austenite phase with the CsCl structure (space group  $Pm\bar{3}m$ ). (b) At lower temperatures, there is a second phase transition from austenite to a twinned martensite phase, pictured here as three variants of a body-centered tetragonal phase (space group  $P4/mmm$ ) (c) with ferroelastic and antiphase domain walls.

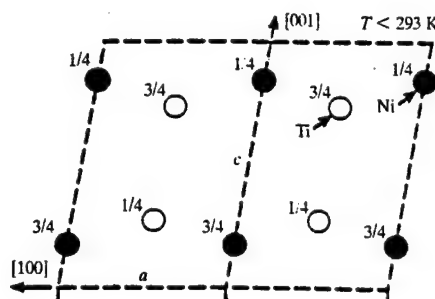


Fig. 8. Crystal structure of the martensitic phase of nitinol, NiTi. The space group is  $P2_1/m$  with lattice parameters  $a = 2.884$ ,  $b = 4.110$ ,  $c = 4.665$  Å,  $\beta = 98.10^\circ$ . Sometimes referred to as the low AuCd structure, there are 12 orientation states of this monoclinic phase with respect to the cubic austenite phase (Kudoh *et al.*, 1985).

temperature or austenite-like phase and the low-temperature or martensitic type phase.

The underlying reasons are fairly obvious. Why use a primary ferroic? These provide a big handle for external fields or forces, whether it be a strain or an electric dipole or magnetic dipole. Why use a cubic prototype phase? The answer is that it gives many equivalent orientation states and makes it possible then to use polycrystalline materials without the necessity of growing single crystals. Why is partial ordering helpful? This type of structure provides many nucleation sites for generating a diffuse phase transformation. Why is a morphotropic transition used? This kind of instability ensures persistent disequilibrium over quite a wide range of temperatures.

In his recent book, *Out of Control*, author Kevin Kelly (1994) describes how biological systems evolve into more complex life forms: neither constancy nor

relentless change will support a complex dynamic system. Equilibrium is death and complete chaos leads to explosive behavior, also followed by death. On the other hand, persistent disequilibrium optimizes dynamic behavior by staying on the hairy edge of rapid response (Kelly, 1994). The behavior of the sensor and actuator materials used in smart systems appears to be consistent with this idea.

As we look to the future, many new types of smart systems will be developed. Aerospace engineers are interested in smart air foils to control drag and turbulence. Diabetics need medical systems to sense the sugar level and deliver insulin. Architects are designing smart buildings that incorporate selfadjusting windows to control the flow of energy into the house. Tennis players will want smart racquets to make overhead smashes and delicate drop shots. Smart systems will identify burglars and other dishonest people and control their movements. Smart toilets are capable of analyzing urine to identify health problems. Smart irrigation systems are needed to optimize the world's food supply. Fish are the leading source of protein in many parts of the world. We can farm the oceans using smart transducers to talk to the fish and herd them like cattle. The word 'smart' is being used everywhere including the comic strips. Dagwood and Blondie recently visited a used car dealer who told them about a smart car, and they asked what is meant by a 'smart car'? The dealer replied that the car is so smart that if the payments are not made, it will drive itself back to the dealership!

It is a pleasure for me to acknowledge Eric Cross and my other colleagues in the ferroelectrics group at Penn State. We have worked together in great harmony for many years. The financial support of the Office of Naval Research, the National Science Foundation, the Advanced Research Projects Agency, and the Alcoa Corporation are also acknowledged with gratitude. Mrs Debora Shay has been very helpful in preparing the manuscript.

#### References

- Clark, A. E. (1980). *Ferromagnetic Materials I*, edited by E. P. Wohlfarth. Amsterdam: North Holland.
- Hathaway, K. B. & Clark, A. E. (1993). *Mater. Res. Soc. Bull.* **18**, 34-41.
- Jaffe, B., Cook, W. R. & Jaffe, H. (1971). *Piezoelectric Ceramics*. New York: Academic Press.
- Kelly, K. (1994). *Out of Control*. New York: Addison-Wesley.
- Kudoh, Y., Tokonami, M., Miyazaki, S. & Otsuka, K. (1985). *Acta Metall.* **33**, 2049-2051.
- deLange, R. G. & Zijderveld, J. (1968). *J. Appl. Phys.* **39**, 2195-2197.
- Megaw, H. D. (1957). *Ferroelectricity in Crystals*. London: Methuen.
- Newnham R. E. (1991). *NIST Spec. Publ.* No. 804, pp. 39-51.

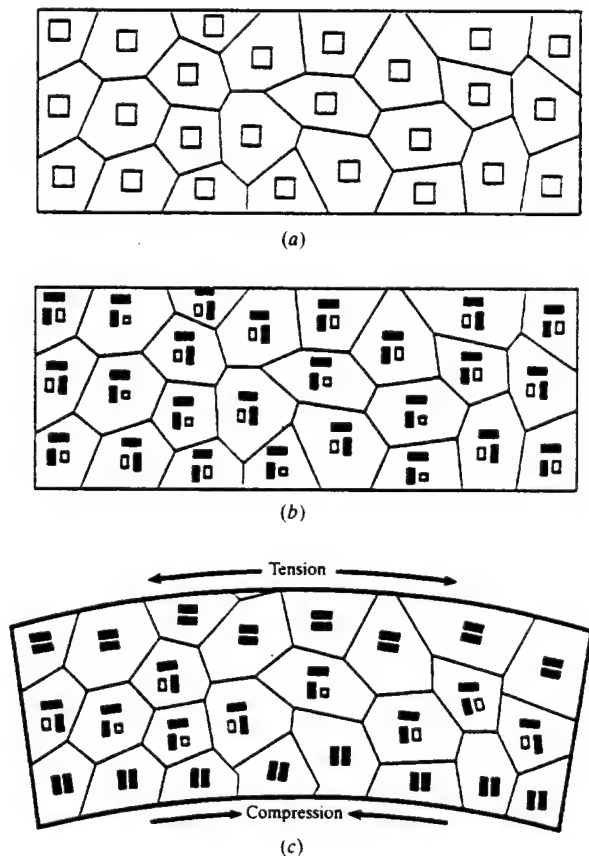


Fig. 9. Shape-memory alloys transform from a partially ordered high-temperature cubic austenitic phase (a) to a mixed austenite-martensitic partially transformed low-temperature state (b) at the operating temperature. When deformed under mechanical stress (tension and compression) (c), phase changes and domain-wall movements take place. The metal returns to its original shape when the austenite phase reappears under heating (deLange & Zijderveld, 1968). Both twin orientation and phase changes occur.

- Newnham, R. E. & Ruschau, G. R. (1991). *J. Am. Ceram. Soc.* **74**, 463-480.
- Purdy, G. R. & Parr, J. G. (1961). *Trans. Am. Inst. Min. Metall. Pet. Eng.* **221**, 631-633.
- Uchino, K. (1997). *Piezoelectric Actuators and Ultrasonic Motors*. Boston: Kluwer Academic Publishers.
- Uchino, K., Nomura, S., Cross, L. E. & Newnham, R. E. (1980). *J. Phys. Soc. Jpn.* **49B**, 45-48.
- Wayman, C. M. (1993). *Mater. Res. Soc. Bull.* **18**, 49-56.
- Wun-Fogle, M. H., Savage, T. & Clark, A. E. (1987). *Sens. Actuators*, **12**, 323-328.

# **MATERIALS STUDIES**

## **Polycrystal Perovskite Ceramics**

# **APPENDIX 5**

## PLZT CERAMICS PREPARED FROM CONVENTIONAL AND MICROWAVE HYDROTHERMAL POWDERS

SHI-FANG LIU, ISAAC ROBIN ABOTHU<sup>a</sup>, SRIDHAR KOMARNENI,  
PATCHARIN POOSANAAS, DONG-SOO PAIK, YUKIO ITO<sup>a</sup>  
AND KENJI UCHINO

Materials Research laboratory, The Pennsylvania State university,  
University Park PA 16802 U.S.A; <sup>a</sup>Permanent address: Institute of Materials  
Research and Engineering (IMRE), National University of Singapore,  
Singapore -119260

Phase pure PLZT (3/52/48) powders were synthesized at a low temperature of 138°C by both conventional and microwave hydrothermal (MH) methods without using excess lead content. PLZT ceramics fabricated from the above powders resulted in 96% of theoretical density upon sintering. Properties such as crystallinity, morphology of the as prepared MH powders and densification and microstructure of the sintered pellets were studied. These properties of MH samples were compared with the properties of those prepared by conventional hydrothermal method (CH).

Keywords: Microwave and conventional hydrothermal; PLZT ceramics.

### INTRODUCTION

Lanthanum doped lead zirconate titanate (PLZT) ceramics have emerged as the most promising family of materials<sup>[1]</sup> for electrooptic<sup>[2]</sup> and photostriction<sup>[3]</sup> applications. Many solid state reaction processes have been reported<sup>[4,5]</sup> and the studies suggest the importance of chemical homogeneity and powder sinterability for low processing temperatures in fabricating high quality ceramics. It is well recognized now that high quality sinterable powder is an essential prerequisite for multicomponent ceramics. Sol-gel process is a

versatile technique to prepare very fine powders because of distinct advantages such as low processing temperature, better control over stoichiometry and chemical homogeneity. We have reported PLZT ceramics with greater than 93% of theoretical density by sol-gel process<sup>[3]</sup>. Besides the above two methods for the fabrication of fine powders, hydrothermal method has gained its importance in the fabrication of highly dense electroceramics from very fine powders. In CH method the reactions are carried out in an aqueous environment in the presence of hydroxide ion<sup>[6]</sup>. The advantages of hydrothermal method are (i) low temperature process, (ii) environmentally friendly as the reactions are carried out under closed system conditions, (iii) teflon-lined bombs are used which is very important for highly caustic solutions when used and (iv) ultrafine powder synthesis. There are no reports on the synthesis of PLZT powders by hydrothermal method to the authors' knowledge.

A recent innovation of the hydrothermal process is the introduction of microwaves into the reaction vessels to produce fine ceramic powders rapidly<sup>[7]</sup>. The primary advantages of using microwaves in the hydrothermal system are (i) rapid kinetics leading to savings of time and energy (ii) rapid internal heating and (iii) synthesis of new materials. In view of the above advantages, an attempt is made here to prepare PLZT by MH method and evaluate this method for its phase formation, sinterability and microstructure in comparison to that prepared by CH method.

### **Experimental**

Aqueous solutions of lead nitrate  $[\text{Pb}(\text{NO}_3)_2]$ , lanthanum chloride  $[\text{LaCl}_3]$ , niobium chloride  $[\text{NbCl}_5]$ , oxyzirconium chloride  $[\text{ZrOCl}_2 \cdot 8\text{H}_2\text{O}]$  and titanium tetrachloride  $[\text{TiCl}_4]$  of reagent grade (Aldrich) were the starting chemicals to get the composition  $(\text{Pb}_{0.96}\text{La}_{0.03})(\text{Zr}_{0.51}\text{Ti}_{0.47}\text{Nb}_{0.01})\text{O}_3$ . Stoichiometric inorganic salts of (1M) lead nitrate, (0.5M) oxyzirconium chloride, (0.3M) lanthanum chloride and (0.01M) niobium chloride were dissolved in 20 ml of 0.5 M aqueous solution of  $\text{TiCl}_4$  followed by the addition of KOH (to make the solution 10M with respect to KOH) as a catalyst of the hydrothermal reaction



## PLZT CERAMICS PREPARED FROM CONVENTIONAL AND MICROWAVE HYDROTHERMAL POWDERS

(Table 1). The mixture was stirred with teflon bar for 30 minutes in 125 ml capacity teflon vessel of Parr bomb (Parr Instrument Co., USA). The experimental set up for MH and CH were described in our earlier work [7]. It was assumed in this study that 49 psi was equivalent to 138°C. After the MH and CH treatments, the solid and solution phases were separated by centrifugation before characterization. For powder XRD studies, the solid fractions were dried below 100°C after they were washed with deionized water. Powder XRD patterns of the dried samples were recorded using X-ray diffractometer (Scintag model DMC 105), with  $\text{CuK}\alpha$  radiation in the range of 20-60° 2 $\theta$ . The powders were pressed into disks and sintered at 1150, 1250°C for 4hrs & 1270°C for 2hrs. Densities of the sintered bodies were measured by the Archimedes' method. Microstructural studies were done on samples thermally etched at 1200°C for 20 mins. A gold layer was then sputter coated on the samples. Microstructural investigation was performed with a scanning electron microscope (Model ISI-DS-130, Akashi Beam Tech. Corp., Japan).

### Results and discussion

The experimental data obtained in the synthesis of PLZT by MH and CH methods are shown in Table 1. From the data, it is clear that phase pure PLZT was obtained at the lowest temperature used i.e., 138°C by MH as well as CH methods. In the case of MH method, 2 hrs of treatment time was used to obtain the phase pure PLZT powders while 2.5 hrs was used in the case of CH method. XRD patterns for both MH and CH as prepared powders are depicted in Figure 1. SEM micrographs for the PLZT powders prepared by MH and CH methods are shown in Figure 2. It is obvious from the figure that both MH and CH methods yielded aggregated powders with particle diameter in the range of 1-4 $\mu\text{m}$ , the crystals were of cubic morphology. The pellets prepared from the powders obtained by both MH and CH processing conditions were sintered at 1150, 1250°C for 4hrs and 1270°C/2hrs. All the characterization studies were

done on the pellets with the highest density prepared from powders obtained by both MH and CH at 138°C and sintered at 1250°C for 4 hrs.

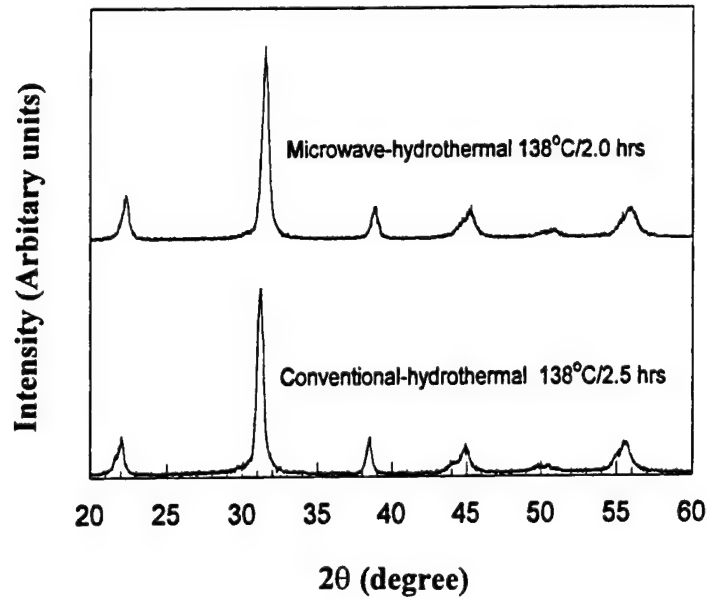


FIGURE 1. XRD patterns of PLZT powders

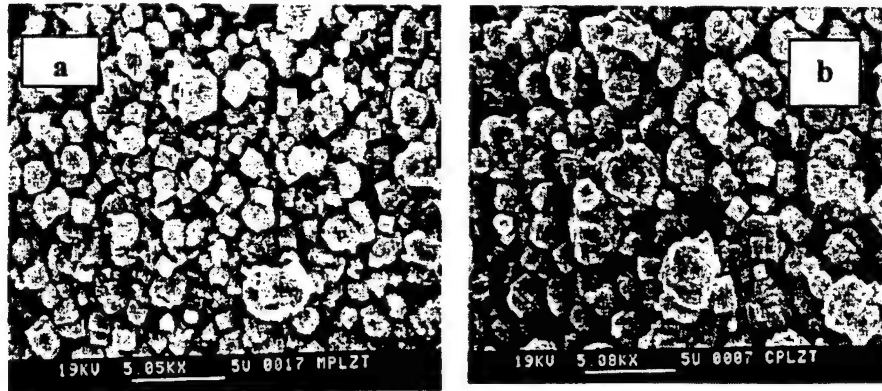


FIGURE 2. SEM micrographs of PLZT powders synthesized at 138°C by (a) microwave and (b) conventional hydrothermal methods

Figure 3 shows SEM microstructures of PLZT sintered pellets. From the figure it is clear that in MH method the average grain size is about 2.5  $\mu\text{m}$  whereas CH method yielded ceramics with average grain size around 2  $\mu\text{m}$  with high density (96%) ceramics in both the cases.

## PLZT CERAMICS PREPARED FROM CONVENTIONAL AND MICROWAVE HYDROTHERMAL POWDERS

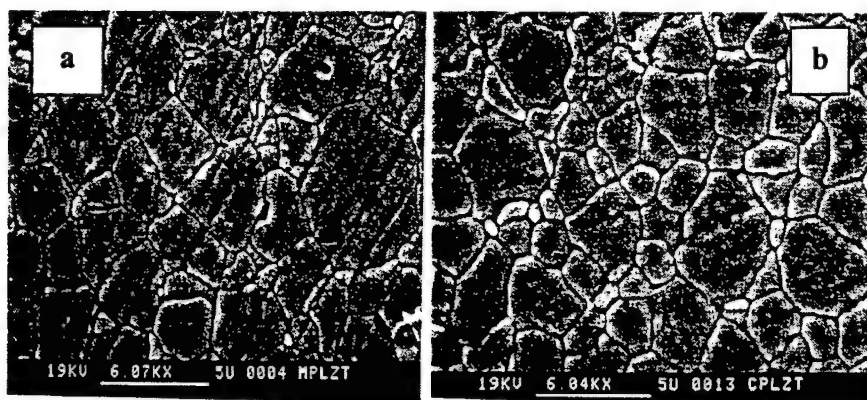


FIGURE 3. SEM micrographs of thermally etched PLZT pellets derived from (a) microwave and (b) conventional hydrothermal powders synthesized at 138°C and sintered at 1250°C for 4h.

### Conclusion

Phase pure PLZT powders were successfully prepared at a low temperature of 138°C by MH and CH methods. However, the former method may lead to energy savings because of rapid heating to temperature. No excess lead content was used during this process. The pellets sintered at 1250°C for 4 hrs showed 96% of theoretical densities and grain sizes of around 3 $\mu$ m. No lead vapors were apparently released during these processes as the reactions were done in closed system.

### References

- [1.] G.H. Haertling and C.E. Land, J. Am.Ceram. Soc. **54**, 1 (1971).
- [2.] J.R. Matdonado and A.H. Meitzler, IEEE, Trans. Electronic Devices ED, **17**, 148 (1970).
- [3.] P. Poosanas, A. Dogan, A.V.P. Rao, S. Komarneni and K. Uchino, J.of Electroceramics **1**, 105 (1997).
- [4.] S.S. Chandratreya, R. M. Fulrath, and J.A. Pask, J. Am.Ceram. Soc. **64**, 422 (1981).
- [5.] B.V. Hiremath, A.I. Kingon, and J.V. Biggers, J. Am.Ceram. Soc. **66**, 790 (1983).
- [6.] Q.H. Li, M.S. thesis, The Pennsylvania State University, U.S.A. (1993).
- [7.] S. Komarneni, R. Roy and Q.H. Li, Mater. Res. Bull. **27**, 1393 (1992).

TABLE 1: XRD analyses of  $(\text{Pb}_{0.90}\text{La}_{0.03})(\text{Zr}_{0.51}\text{Ti}_{0.47}\text{Nb}_{0.01})\text{O}_3$  Powders and sintering properties of pellets prepared by microwave and conventional hydrothermal methods.

Concentration (M)				Temperature (°C)	Duration (Hrs)	Reaction Product	Sintering Condition (°C/hrs)	% Theo.	Density
Microwave-hydrothermal				138	2.0	PLZT	1270/2	94	
TiCl <sub>4</sub>	Pb(NO <sub>3</sub> ) <sub>2</sub>	LaCl <sub>3</sub>	ZrOCl <sub>2</sub>	NbCl <sub>5</sub>	KOH				
0.5	1.0566	0.0317	0.5416	0.0106	10				
						PLZT	1270/2	96	
							1250/4	96	
							1150/4	77	
							1270/2	96	
							1250/4	96	
							1150/4	76	
						PLZT	1270/2	96	
							1250/4	92	
							1150/4	83	
Conventional-hydrothermal				138	2.5	PLZT	1270/2	95	
TiCl <sub>4</sub>	Pb(NO <sub>3</sub> ) <sub>2</sub>	LaCl <sub>3</sub>	ZrOCl <sub>2</sub>	NbCl <sub>5</sub>	KOH				
0.5	1.0566	0.0317	0.5416	0.0106	10				
						PLZT	1270/2	96	
							1250/4	94	
							1150/4	91	
							1270/2	95	
							1250/4	93	
							1150/4	81	

# **APPENDIX 6**

# NANOCOMPOSITE VERSUS MONOPHASIC SOL-GEL PROCESSING OF PLZT CERAMICS

ISAAC ROBIN ABOTHU<sup>a</sup>, PATCHARIN POOSANAAS,  
SRIDHAR KOMARNENI, YUKIO ITO<sup>a</sup>, and KENJI UCHINO

Materials Research Laboratory, The Pennsylvania State University, University Park, PA 16802, USA; <sup>a</sup>Permanent Address: Institute of Materials Research and Engineering (IMRE), National University of Singapore, Singapore -119260.

Very fine PLZT powders with particle size of ~ 200 nm were synthesized by a nanocomposite method from relatively inexpensive precursors. Pellets made from these powders were sintered to 96% of theoretical density at 1250°C for 4 hrs. The crystallization, densification and microstructure were studied for nanocomposite PLZT in comparison with sintered compacts made from monophasic processing of the same composition.

Keywords: Nanocomposite processing; Sol-gel processing; PLZT ceramics.

## INTRODUCTION

The solid solution system lead-lanthanum-zirconate-titanate (PLZT) has been widely investigated among ferroelectric ceramics due to their interesting ferroelectric, piezoelectric, pyroelectric and electro-optic properties<sup>[1]</sup>. Over the years, this material has been prepared by traditional mixed oxide (MO) method in which solid state reaction of mixed metal oxides occurred<sup>[2]</sup>. Since such reactions, however, often lead to compositional and structural inhomogeneities due to repeated calcination and grinding steps, much higher heating schedules are required to overcome large diffusion distances. Therefore, this method was subsequently replaced by suitable chemical routes such as coprecipitation process (CP)<sup>[3]</sup>, spray drying, freeze drying, evaporation and sol-gel processes

[4,5]. Even though sol-gel method offers distinct advantages such as low processing temperature, better control over stoichiometry and chemical homogeneity, the excessive cost and special handling of extremely moisture sensitive alkoxide precursors preclude the adoption of this technique for routine ceramic synthesis. Nanocomposites have been shown to exhibit superior properties as compared to single phases of the same composition prepared by sol-gel method [6]. Recent research in our laboratory has been focussed on low temperature nanocomposite processing technique as an alternative to sol-gel process. We have demonstrated that electroceramics prepared by nanocomposite method densify better than monophasic sol-gel process because of a narrower temperature interval between crystallization and densification temperatures in nanocomposite mixed powder as compared to sol-gel processing techniques [7]. Also, impurities which may be introduced into the system during intermediate calcination and grinding steps of the solid-state method can be eliminated with this nanocomposite technique. In view of the above advantages, an attempt is made here to prepare and evaluate PLZT ferroelectric material by nanocomposite route. This paper discusses the nanocomposite versus monophasic sol-gel processing of PLZT (3/52/48) powders, their sinterabilities and corresponding microstructures.

### **Experimental**

The experimental procedure adopted for the synthesis of PLZT (3/52/48) by sol-gel was reported in our earlier work [8]. In the nanocomposite approach lead hydroxide [Pb(OH)<sub>2</sub>] (prepared from lead nitrate and ammonia at pH 10), lanthanum hydroxide [La(OH)<sub>3</sub>], zirconium oxide [ZrO<sub>2</sub>], and titanium oxide [TiO<sub>2</sub>] (hydrothermal powders) were the starting materials. All the precursors for nanocomposite route prior to their use were individually heat treated at 600°C for 1hr to determine loss of adsorbed water and also loss due to dehydration so that respective metal oxide content in the precursors is exactly known. Stoichiometric quantities of lead hydroxide, lanthanum hydroxide, zirconium oxide and titanium oxide to yield 0.02 mole PLZT (3/52/48) were

## NANOCOMPOSITE VERSUS MONOPHASIC SOL-GEL PROCESSING OF PLZT CERAMICS

mixed in about 30cc of ethanol to form a slurry and stirred for 12 hrs, after which the slurry was dried and mixed with PVA as binder for pelletization. The resultant gel powder from sol-gel process and the nanocomposite precursor powder were each mixed with 2 wt% polyvinyl alcohol as binder and pressed into pellets using a pressure of 1500 psi. The pellets were sintered at 1150°C/4hrs, 1250°C/2hrs, 1250°C/4hrs and 1270°C/2hrs in lead rich atmosphere to determine the densification behavior. Phase identification of the heat treated powders was done using x-ray diffractometer (Scintag model DMC 105) with copper K $\alpha$  radiation. Densities of the sintered samples were measured by Archimedes' method. Powder morphology and microstructural studies were performed with a scanning electron microscope (Model ISI-DS-130, Akashi Beam Technology Corporation, Japan). For microstructural studies the samples were polished with 0.5 $\mu$ m alumina powder. The samples were ultrasonically cleaned in acetone and thermally etched at 1200°C for 20 minutes. A gold layer was thin sputter coated on the samples before SEM analysis.

### Results and discussion

It has been reported in our earlier work <sup>[8]</sup>, that PLZT precursor gel powder heat treated at 600°C for 1 hr yielded crystalline cubic PLZT. However, in the case of nanocomposite mixed powder heat treated at 850°C, no formation of the PLZT pure phase was achieved under this firing condition as it contains a small amount of PbZrO<sub>3</sub>. On the other hand, the XRD patterns shown in Figure 1, for sol-gel and nanocomposite pellets sintered at 1250°C exhibited single phase PLZT tetragonal structure. Scanning electron micrographs of sol-gel PLZT powder and heat treated nanocomposite powder are shown in Figure 2. From the figure, it is clear that the nanocomposite process yielded fine PLZT spherical particles with particle size around 100 nm and with little agglomeration. On the contrary, the sol-gel process yielded PLZT powder with particle size around 200 nm and with somewhat higher agglomeration. It was observed that the pellets prepared from nanocomposite processing showed a



high density of 95% theoretical at 1250°C for 4hrs while the sol-gel pellets and nanocomposite pellets sintered at 1250°C for 2hrs showed 92 and 90% theoretical densities, respectively. High densification in compacts prepared from nanocomposite powders can be attributed to crystallization and densification occurring within a short temperature interval<sup>[7]</sup>. Nanocomposite and sol-gel processing led to similar densification at 1250°C/2hrs. However, the latter powder underwent an additional calcination step that led to crystallization of the equilibrium phase <sup>[7]</sup>. The avoidance of this additional step in the nanocomposite process is expected to save time and energy.

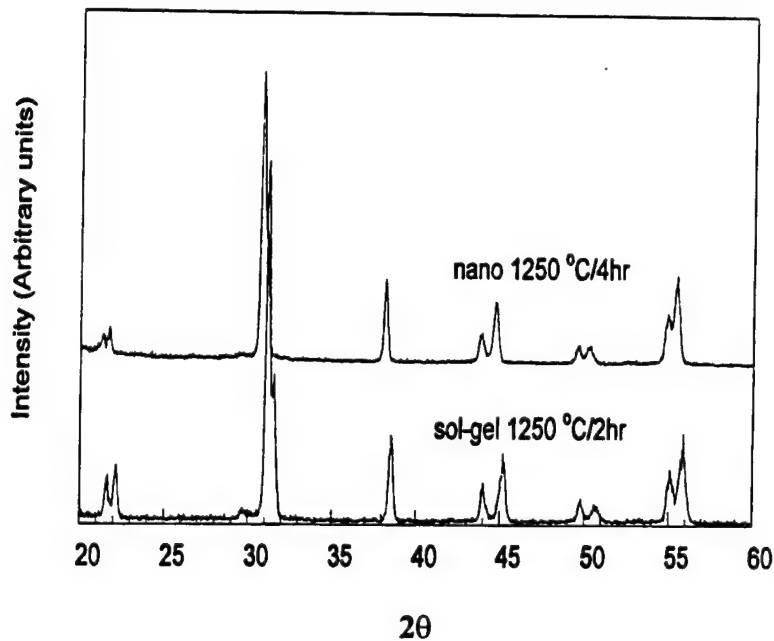


FIGURE 1 XRD patterns of PLZT nanocomposite and sol-gel sintered pellets.

Even though crystallization of sol-gel powder occurred at a lower temperature of 600°C when compared with that of nanocomposite mixed powder, densification of sol-gel powder can occur only at a relatively higher temperature because the interval between crystallization and densification is wider in the former than in the later<sup>[7]</sup>. When the equilibrium phase crystallizes, it is very

## NANOCOMPOSITE VERSUS MONOPHASIC SOL-GEL PROCESSING OF PLZT CERAMICS

difficult to densify and this is the case with sol-gel process. Figure 3 shows the microstructures of thermally etched pellets sintered at 1250°C. Average grain size of about 1.40  $\mu\text{m}$  was seen in pellets prepared from nanocomposite approach sintered for 4 hrs while it was  $\sim 1.45 \mu\text{m}$  in the case of sol-gel pellets sintered for 2 hrs. It was observed that the grain sizes of both nanocomposite and sol-gel pellets were much lower than for conventional oxide mixing process [8,9].

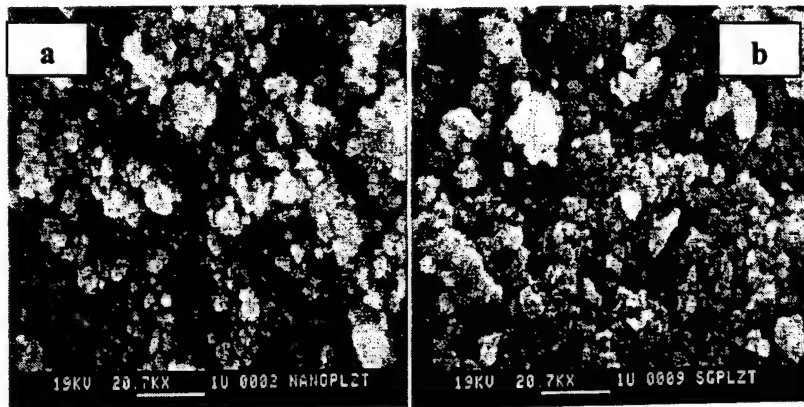


FIGURE 2 SEM for PLZT powders synthesized by (a) nanocomposite (b) sol-gel processing.

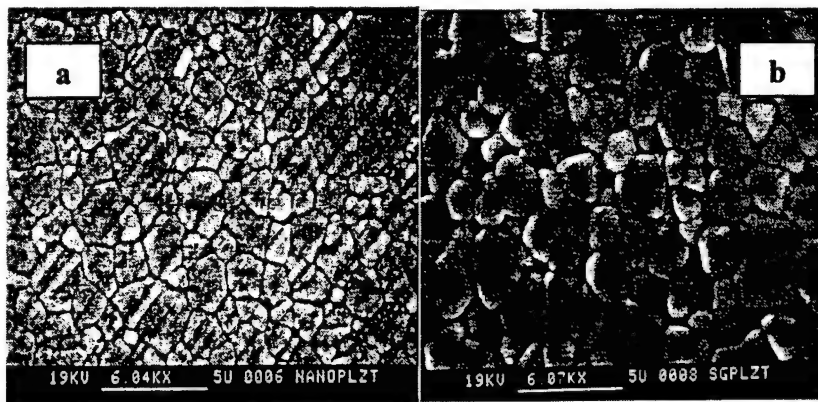


FIGURE 3 Microstructure of PLZT ceramics obtained by (a) nanocomposite processing / sintered at 1250°C/4hr (b) sol-gel processing / sintered at 1250°C/2hr.

Another advantage of nanocomposite approach is that inorganic salts can be used to prepare nanophases which are the precursors of the nanocomposite method. In the case of sol-gel process, some of the metal alkoxide precursors are highly reactive and should be handled in a glove box and this may add to the cost of the preparation.

### Conclusions

Very fine PLZT powders were synthesized with particle size of 200 nm by nanocomposite approach. A high density of 95% theoretical was obtained for nanocomposite PLZT ceramics at 1250°C/4hrs while 92 and 90% theoretical densities were obtained for sol-gel and nanocomposite PLZT ceramics sintered at 1250°C for 2hrs, respectively. Because of the narrower temperature interval between crystallization and densification, nanocomposite powders are good for densification. The nanocomposite method needs no intermediate calcination, grinding steps and requires no special handling of precursors.

### Acknowledgements

This research was supported by the Division of Materials Research, National Science Foundation under grant No. DMR-9319809.

### References

- [1.] M. Takahashi, Jap. J. Appl. Phys. **9**, 1236, (1970).
- [2.] B.H. Chu, R.M. Sun and Z.W. Yin, Proc. Int. Sump. Factors in Densification and sintering of oxide and nonoxide ceramics, Japan (1978)
- [3.] G. Haertling and C. Land, Ferroelectrics **3**, 269, (1972).
- [4.] D.W. Johnson Jr. Am. Ceram. Soc. Bull. **64**, 1597 (1985).
- [5.] Colomban, Ph. Ceram. Int. **15**, 23 (1989).
- [6.] S. Komarneni, J. Mater. Chem., **2**, 1219, (1990).
- [7.] A.V.P. Rao, A.I. Robin, and S. Komarneni, Ceram. Trans., **70**, 253 (1997).
- [8.] P. Poosanas, A. Dogan, A.V. Prasada Rao, S. Komarneni, and K. Uchino, J. of Electroceramics, **1**, 5 (1997).
- [9.] P. Poosanaas, , and K. Uchino, Submitted to the special issue of The Journal of Materials Chemistry and Physics, (1998).

# **APPENDIX 7**

# Dielectric and Piezoelectric Properties of Fe<sub>2</sub>O<sub>3</sub>-doped 0.57PSN-0.43PT Ceramics

Jin Soo KIM

Department of Technology Education, Korea National University of Education, Chungbuk 363-791, Korea

Yun Han CHEN and Kenji UCHINO

Materials Research Laboratory, The Pennsylvania State University, University Park, PA 16802, USA

Dielectric and piezoelectric properties of iron-doped 0.57Pb(Sc<sub>1/2</sub>Nb<sub>1/2</sub>)O<sub>3</sub>-0.43PbTiO<sub>3</sub> were investigated. The maximum dielectric constant ( $\epsilon_{33}/\epsilon_0 = 2551$ ) and the minimum dielectric loss ( $\tan\delta = 0.51\%$ ) at room temperature were obtained at 0.1 wt% and 0.3 wt% of Fe<sub>2</sub>O<sub>3</sub> additions, respectively. The temperature dependence of the dielectric constant was measured between 20 °C and 350 °C. With the additions of Fe<sub>2</sub>O<sub>3</sub>, the piezoelectric constant  $d_{33}$  and electromechanical coupling factor  $k_p$  were slightly decreased, but the mechanical quality factor  $Q_m$  was significantly increased. The highest mechanical quality factor ( $Q_m=297$ ) was obtained at 0.3 wt% Fe<sub>2</sub>O<sub>3</sub>, which is 4.4 times larger than that of non-doped 0.57PSN-0.43PT ceramics.

## I. INTRODUCTION

The composition of PSN-PT solid solutions exhibits a morphotropic phase boundary (MPB) at 42.5 mol% PT [1,2]. Only five papers were reported about the PSN-PT system [2-6]. Tennery *et al.* initially reported about properties of solid solutions for the Pb(Sc<sub>1/2</sub>Nb<sub>1/2</sub>)O<sub>3</sub>-PbTiO<sub>3</sub> system [2]. Yamashita reported on the effect of Nb<sub>2</sub>O<sub>5</sub> additions to 0.575PSN-0.425PT ceramics [3]. The electrical properties of Niobium-doped (1-x)PSN-xPT (x=0.4-0.45) ceramics near the MPB were also investigated by Yamashita [4,5]. Adachi *et al.* [6] reported the piezoelectric properties of 0.575PSN-0.425PT ceramics. For high-power piezoelectric actuator devices, such as ultrasonic motors and piezoelectric transformers, it is necessary to have a high  $Q_m$  and low  $\tan\delta$ . In this paper, the addition of Fe<sub>2</sub>O<sub>3</sub> to the 0.57PSN-0.43PT composition was carried out so as to improve the value of mechanical quality factor for high-power device applications, and the resulting dielectric and piezoelectric properties of the samples were studied.

## II. EXPERIMENT

The specimens were prepared from high-purity PbO, Sc<sub>2</sub>O<sub>3</sub>, Nb<sub>2</sub>O<sub>5</sub>, TiO<sub>2</sub> and Fe<sub>2</sub>O<sub>3</sub>. Six compositions of 0.57PSN-0.43PT+x wt% Fe<sub>2</sub>O<sub>3</sub> (x=0, 0.1, 0.3, 0.5, 0.7, 0.9) were selected. Mixtures of the raw materials were ball-milled. Dried powders were calcined at 850 °C for 2 h. The calcined powders were granulated and cold-pressed at a pressure of 1000 kg/cm<sup>2</sup>. The binder was burned out at 600 °C for 2 h. The specimens were sintered at 1250 °C for 3 h and polished. Electrodes were applied both sides of the sample with silver paste and firing

at 650 °C. The samples were poled in a silicone oil bath at 120 °C by DC 2.5 kV/m for 15 min. The final sample dimension was 12.9 mm in diameter and 0.84 mm in thickness. Dielectric constant and dielectric loss of samples at 1 kHz were measured using LCR meter (SR715). Temperature dependence of the dielectric constant was measured using a computer-controlled system consisting of a temperature controller (Delta9010), multi-frequency LCR meter (HP4274A) and PC (HP9121). The resonance and antiresonance frequencies were measured using an impedance/gain-phase analyzer (HP4194A). Electromechanical coupling factor and mechanical quality factor were calculated. The P-E loops were examined using a polarization measuring system with DSP lock-in amplifier (SR830), high voltage DC amplifier (TREK 609C-6) and IBM PC. After poling, piezo  $d_{33}$  meter (ZJ-2) was used to measure  $d_{33}$ .

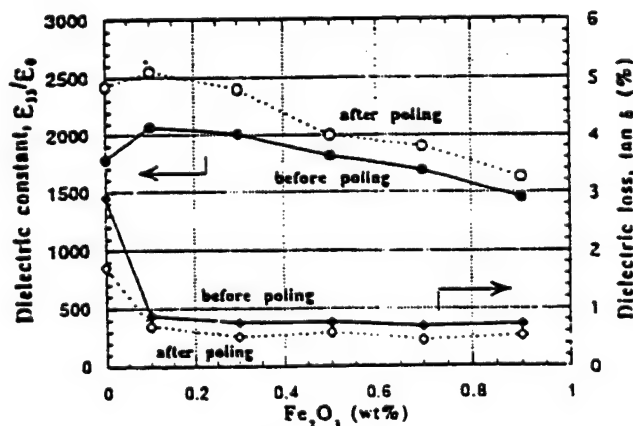


Fig. 1. Dielectric constant and dielectric loss before and after poling of 0.57PSN-0.43PT ceramics as a function of Fe<sub>2</sub>O<sub>3</sub> additions.

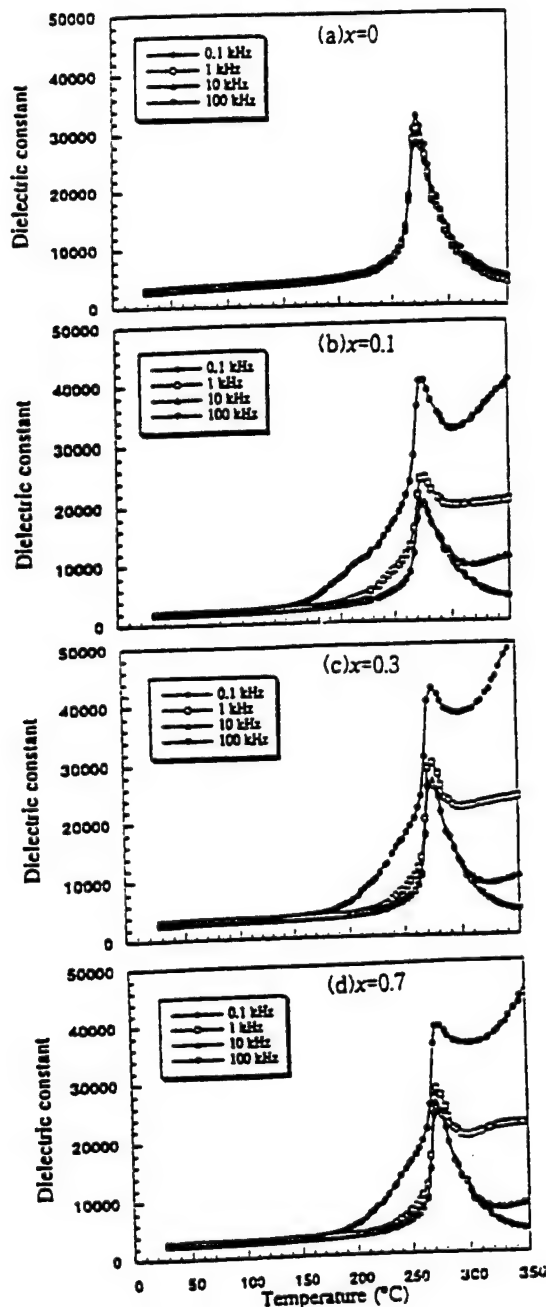


Fig. 2. Temperature dependence of the dielectric constant as a function of  $\text{Fe}_2\text{O}_3$  in 0.57PSN-0.43PT + x wt%  $\text{Fe}_2\text{O}_3$  samples. Samples are being measured while being heated to 350 °C.

### III. RESULTS AND DISCUSSION

Figure 1 shows the dielectric constant and dielectric loss of 0.57PSN-0.43PT ceramics as a function of  $\text{Fe}_2\text{O}_3$  addition. The dielectric constant after poling showed a maximum value (2551) at 0.1 wt%  $\text{Fe}_2\text{O}_3$  addition, and then decreased with increasing  $\text{Fe}_2\text{O}_3$  addition. The decrease of dielectric constant for the  $\text{Fe}_2\text{O}_3$ -doped samples suggests an acceptor effect by the Fe atoms [8,9]. Dielectric loss after poling of iron-doped samples are less than 0.7%. In case of 0.3 wt%  $\text{Fe}_2\text{O}_3$  addition, the dielectric

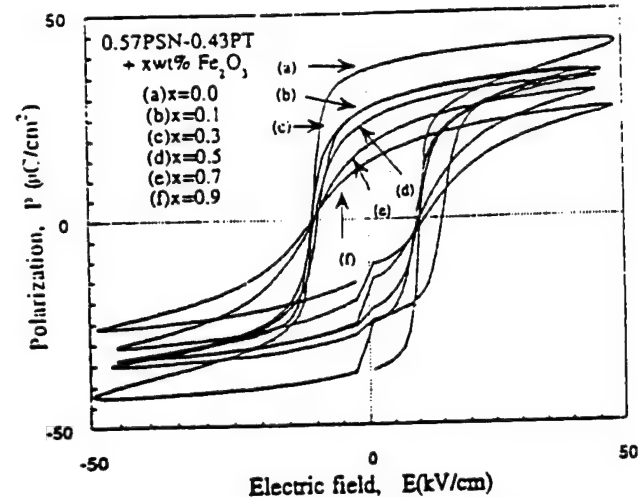


Fig. 3. P-E hysteresis loops of 0.57PSN-0.43PT + x wt%  $\text{Fe}_2\text{O}_3$  samples measured at room temperature at 1.0 Hz.

loss is 0.51 %. The acceptor dopant  $\text{Fe}_2\text{O}_3$  decreases the dielectric loss of 0.57PSN-0.43PT ceramic [3].

Figure 2 shows the dielectric constant as a function of temperature and frequencies for 0.57PSN-0.43PT of  $\text{Fe}_2\text{O}_3$ -doped samples. The Curie temperature of the non-doped sample is at 271.5 °C, and maximum dielectric constant of the sample at  $T_C$  point is 32680. For both non-doped and iron-doped samples Curie temperature did not depend on the measuring frequency. Above  $T_C$ , the dielectric constant of iron-doped samples increases at 0.1 kHz. This higher dielectric constant may be attributed to the higher electrical conductivity due to iron doping [10,11]. When increasing the amount of  $\text{Fe}_2\text{O}_3$ , Curie temperature was slightly decreased. Generally, the introduction of additives into a ferroelectric material with a perovskite structure results in a decrease of Curie temperature, but maximum values of dielectric constant at the Curie temperature were increased [11].

Figure 3 shows the P-E hysteresis loops. This measurement was performed under the condition such that

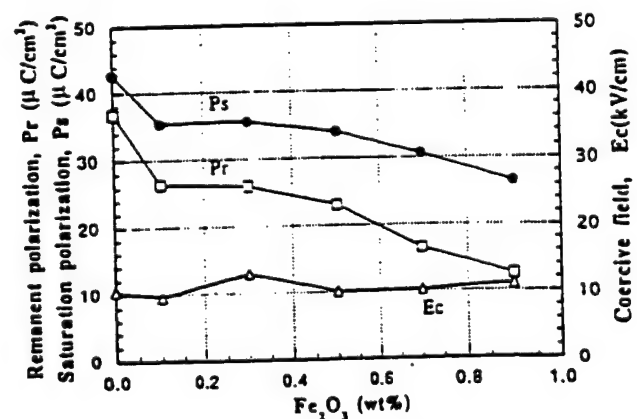


Fig. 4. Remanent and saturation polarizations and coercive field of 0.57PSN-0.43PT ceramics as a function of  $\text{Fe}_2\text{O}_3$  addition.

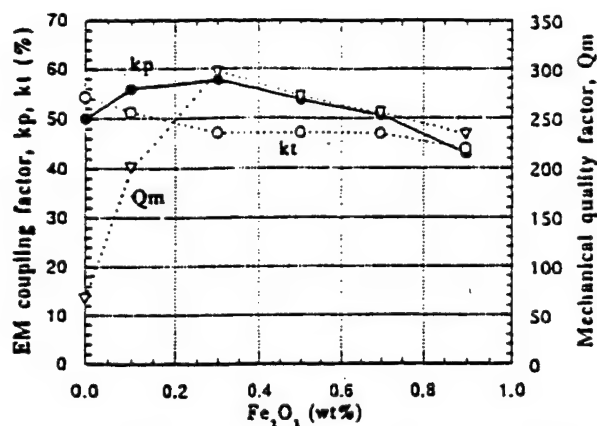


Fig. 5. Electromechanical coupling factor for planar and thickness modes and mechanical quality factor of 0.57PSN-0.43PT ceramics as a function of  $\text{Fe}_2\text{O}_3$  addition.

samples were poled to full saturation. A remanent polarization  $P_r$  of  $36.8 \mu\text{C}/\text{cm}^2$  and a coercive field  $E_c$  of  $10.47 \text{ kV}/\text{cm}$  were obtained for non-doped 0.57PSN-0.43PT ceramics. By acceptor doping with  $\text{Fe}_2\text{O}_3$ , the introduction of oxygen vacancies decreased the domain wall mobility, which subsequently decreases the hysteresis loss [12].

Figure 4 shows the remanent polarization and coercive field of 0.57PSN-0.43PT ceramics at RT as a function of  $\text{Fe}_2\text{O}_3$  addition. Remanent polarization values gradually decrease with increasing  $\text{Fe}_2\text{O}_3$  additions. Coercive field reached a maximum value of  $12.83 \text{ kV}/\text{cm}$  at  $0.3 \text{ wt}\%$   $\text{Fe}_2\text{O}_3$  amount, but the  $E_c$  values slightly increased with increasing  $\text{Fe}_2\text{O}_3$  addition above  $0.3 \text{ wt}\%$ .

Figure 5 shows the electromechanical coupling factors  $k_p$  and  $k_t$ , and mechanical quality factor  $Q_m$  of 0.57PSN-0.43PT ceramics. The largest value of  $k_p=57.5\%$  was observed at  $0.3 \text{ wt}\%$   $\text{Fe}_2\text{O}_3$  addition. The  $Q_m$  value reached a maximum of 297 at  $0.3 \text{ wt}\%$   $\text{Fe}_2\text{O}_3$ ; This leads to the conclusion that this particular 0.57PSN-0.43PT composition is very suitable for high-power applications. It is well known that the additions of acceptor dopants, like  $\text{Fe}_2\text{O}_3$ , improve the  $Q_m$  value, while decreasing  $d_{33}$  and  $k_p$  values [12,13]. Oxygen vacancies inhibit the movement of domain walls, and therefore decrease the piezoelectric constant, the dielectric constant and the electromechanical coupling factor [3,7,14].

#### IV. CONCLUSION

The dielectric constant after poling of the samples increased. Dielectric loss for poled, iron-doped samples is less than  $0.7\%$ . The dielectric constant after poling showed a maximum value (2551) at  $0.1 \text{ wt}\%$   $\text{Fe}_2\text{O}_3$  addition. The Curie temperature of non-doped 0.57PSN-0.43PT ceramics is at  $271.5^\circ\text{C}$ . For composition with  $0.3 \text{ wt}\%$   $\text{Fe}_2\text{O}_3$  addition, an electromechanical coupling factor  $k_p=57.7\%$  and a mechanical quality factor  $Q_m=297$  were observed, respectively. It was determined that the  $0.3 \text{ wt}\%$  iron-doped 0.57PSN-0.43PT is the most suitable composition for high-power device applications.

#### ACKNOWLEDGMENTS

Jin Soo KIM would like to acknowledge to the financial support of the Korea Science and Engineering Foundation (KOSEF) for research at Penn State Univ. from Jan. 1996 to Jan. 1997.

#### REFERENCES

- [1] G. A. Smolenskii, V. A. Isupov and A. I. Agranovskaya, *Sov. Phys. Solid State* **1**, 150 (1959).
- [2] V. J. Tennery, K. W. Hang and R. E. Novak, *J. Am. Ceram. Soc.* **51**, 671 (1968).
- [3] Y. Yamashita, *Jpn. J. Appl. Phys.* **32**, 5036 (1993).
- [4] Y. Yamashita, *Jpn. J. Appl. Phys.* **33**, 4652 (1994).
- [5] Y. Yamashita, *Jpn. J. Appl. Phys.* **33**, 5328 (1994).
- [6] M. Adachi, E. Miyabukuro and A. Kawabata, *Jpn. J. Appl. Phys.* **33**, 5420 (1994).
- [7] F. Kulscar, *J. Am. Ceram. Soc.* **42**, 43 (1959).
- [8] X. Wang and X. Yao, *Ferroelectrics* **154**, 307 (1994).
- [9] J. H. Moon and H. M. Jang and B. D. You, *J. Mater. Res.* **8**, 3184 (1993).
- [10] N. Ichinose and N. Kato, *Jpn. J. Appl. Phys.* **33**, 5423 (1994).
- [11] W. R. Xue, P. W. Lu and W. Huebner, *Proc. of IEEE*, 101 (1995).
- [12] S. Takahashi and S. Hirose, *Jpn. J. Appl. Phys.* **32**, 2422 (1993).
- [13] H. Ouchi, M. Nishida and S. Hayakawa, *J. Am. Ceram. Soc.* **49**, 577 (1966).
- [14] K. Uchino, *Piezoelectric Actuators and Ultrasonic Motors* (Kluwer Aca. Pub., 1997), Chap. 2.

# **APPENDIX 8**



## Electrical Property Diagram and Morphotropic Phase Boundary in The $\text{Pb}(\text{In}_{1/2}\text{Ta}_{1/2})\text{O}_3 - \text{PbTiO}_3$ Solid Solution System.

Edward F. Alberta and Amar S. Bhalla  
Materials Research Laboratory, The Pennsylvania State University, University Park.  
Pennsylvania, USA.

**Abstract** Dielectric, pyroelectric and piezoelectric properties of the solid solution:  $(1-x) \text{Pb}(\text{In}_{1/2}\text{Ta}_{1/2})\text{O}_3 - (x) \text{PbTiO}_3$  [PIT : PT] have been investigated. High dielectric constant of 2300 at room temperature and 13000 at approximately 248°C, remnant polarization of approximately 26  $\mu\text{C}/\text{cm}^2$ , and coercive field of 11 kV/cm were measured for compositions near the morphotropic phase boundary [MPB] at  $x = 38$  mol% PT. Poled ceramics of this composition gave a piezoelectric coefficient,  $d_{33}$ , of 302 pC/N and piezoelectric coupling coefficients,  $k_p$  and  $k_{31}$ , of 37% and 20%, respectively.

## INTRODUCTION

Perovskite lead indium tantalate (PIT) was first prepared, in crystalline form, by Kania [1,2] and Bokov [3]. This material displays typical relaxor behavior, with a maximum in the dielectric constant of 900 occurring at approximately 100°C. Several other groups [4-7] have attempted the preparation of ceramic PIT. However, due to the persistence of an undesirable pyrochlore phase, these studies have had limited success. The groups reporting the synthesis of PIT also report dielectric properties inferior to reported by Kania and Bokov.

In this work, the solid solution system  $\text{Pb}(\text{In}_{1/2}\text{Ta}_{1/2})\text{O}_3$  (PIT) :  $\text{PbTiO}_3$  (PT) is explored. Lead titanate was chosen for two reasons: (1) to stabilize the perovskite phase of PIT, and (2) to identify the morphotropic phase boundary (MPB) in this system. This paper reports on the compositional dependence of the dielectric, pyroelectric, and piezoelectric properties of the  $(1-x)$  PIT :  $(x)$  PT system, with emphasis on those compositions near the morphotropic phase boundary.

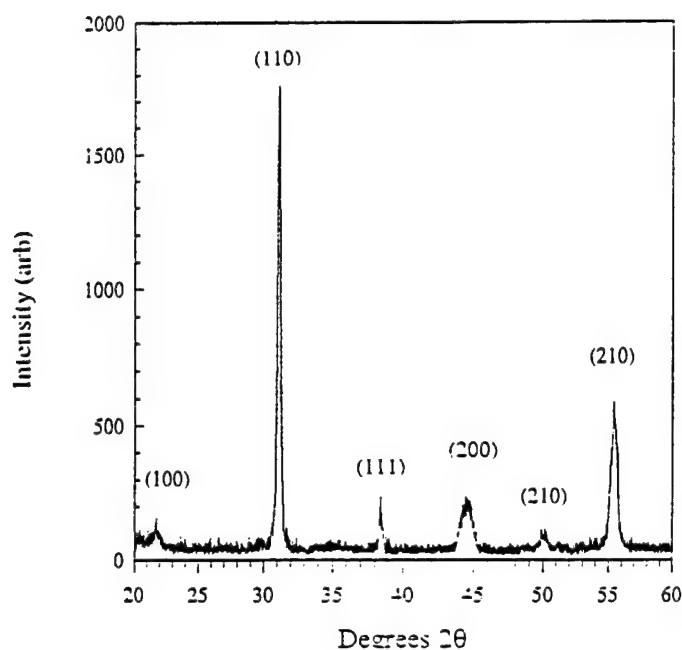


Figure 1. X-Ray diffraction pattern for a (0.64) PIT : (0.36) PT ceramic at room temperature.

### EXPERIMENTAL PROCEDURE

The Columbite precursor method was used to prepare the ceramics for this study[8]. First, the  $\text{InTaO}_4$  precursor phase was prepared by ball milling  $\text{In}_2\text{O}_3$  and  $\text{Ta}_2\text{O}_5$  using  $\text{ZrO}_2$  Balls. The slurry was then dried and calcined in an  $\text{Al}_2\text{O}_3$  crucible at  $1100^\circ\text{C}$  for 4 hours. The resulting  $\text{InTaO}_4$  was then mixed in stoichiometric proportions with  $\text{PbO}$  and  $\text{TiO}_2$  and re-milled. The dried powder was calcined at  $900^\circ\text{C}$  for 4 hours. After an additional milling step, the powder was pressed into disks and sintered between  $1000^\circ\text{C}$  and  $1300^\circ\text{C}$ . Both calcined powders and sintered ceramics were analyzed for phase purity using X-ray diffraction (Pad V, Sintag Inc.). The sintered ceramics were found to be at least 95 % theoretical density.

The sintered ceramics were polished and then coated with sputtered-gold electrodes. The temperature dependence of the dielectric properties was measured using a multifrequency LCR meter (HP4274A, Hewlett Packard Co.) and computer controlled oven (Delta Design, Inc.). Pyroelectric measurements were made using a similar system including a picoammeter (HP4140B, Hewlett Packard Co.). The ceramics were poled in a high-temperature stirred silicone bath (DC-200, Dow Corning,

Inc. and EX-250 HT, Exacal. Inc.). Piezoelectric measurements were then made using an impedance analyzer (HP4194A, Hewlett Packard Co.) following the IEEE resonance method.

## RESULTS AND DISCUSSION

The addition of PT to the PIT:PT system was found to stabilize to perovskite phase. Using X-Ray diffraction, it was found that the calcined powders of PIT:PT with PT concentrations of at least 30 mol% were phase-pure. After sintering, only traces of the pyrochlore phase were present in these compositions, figure 1.

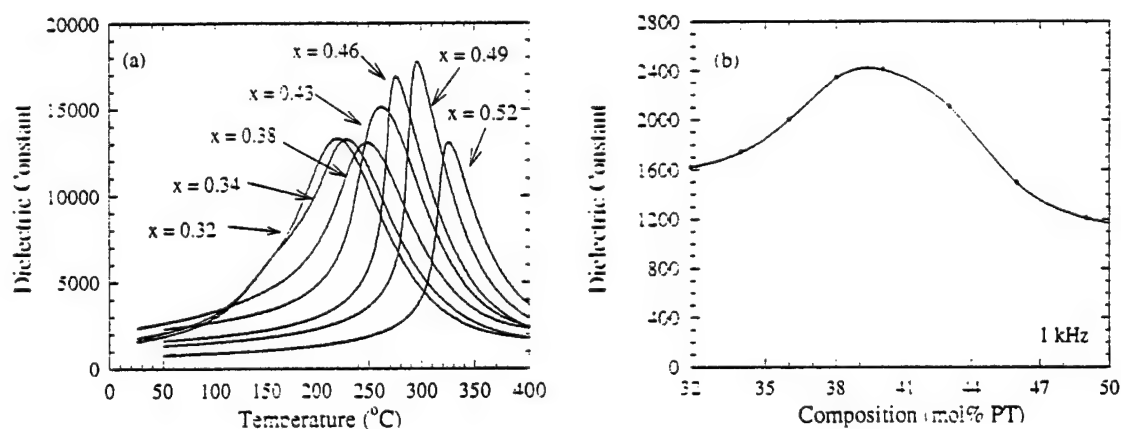


Figure 2. Compositional dependence of the dielectric constant for poled ceramics in the  $(1-x)$  PIT :  $(x)$  PT system measured at 1 kHz: (a) temperature dependence and (b) room temperature values.

The temperature dependence of the dielectric constant (measured at 1 kHz) for various poled ceramics with  $0.30 \leq x \leq 0.48$  is shown in figure 2(a). As expected, the addition of PT the system shifts the Curie temperature from 200°C to 300°C. Careful examination of the curves in figure 2(a) shows an additional anomaly in the dielectric constant for compositions with  $x < 0.38$ . These anomalies indicate a transition between the pseudo-cubic and tetragonal phases. The temperature at which this anomaly occurs was found to decrease with the addition of PT. The compositional dependence of the dielectric constant, figure 3(a), also indicates the MPB in the PIT:PT system. From these observations, the phase boundary was determined to be at  $x = 0.38$ . Figure 3(a)

shows the temperature dependence of the dielectric constant and loss for this composition.

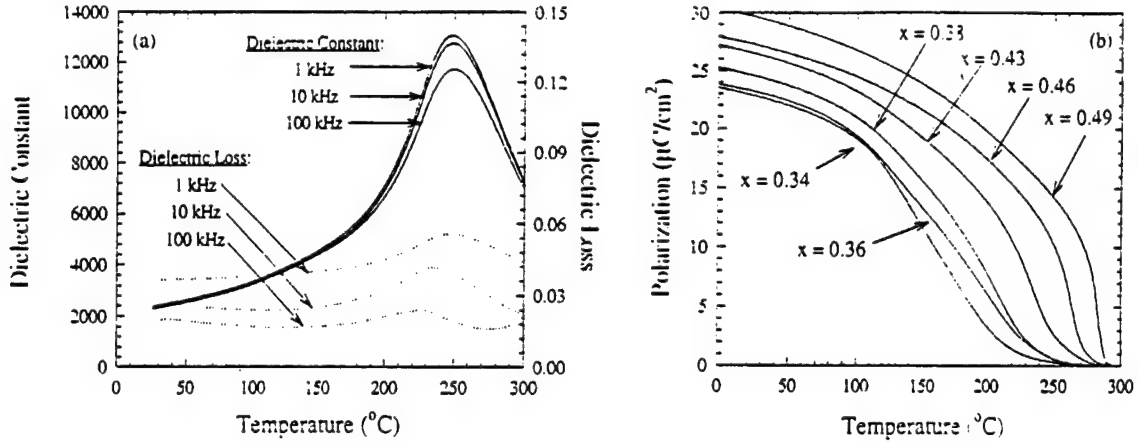


Figure 3. Temperature dependence of (a) the dielectric constant for poled ceramics with  $x = 0.38$  and (b) the polarization for ceramics with  $0.34 < x < 0.49$ .

The temperature dependence of the remnant polarization in the  $(1-x)$  PIT :  $(x)$  PT solid solution system was determined from pyroelectric measurements, figure 3(b). Again, the transition temperature increased, as expected, with increasing  $x$ . The polarization also increased with the addition of PT. As with the dielectric data, the pseudo-cubic to tetragonal phase boundary was identified by the slope changes that occur in the data for compositions with  $x < 0.40$ .

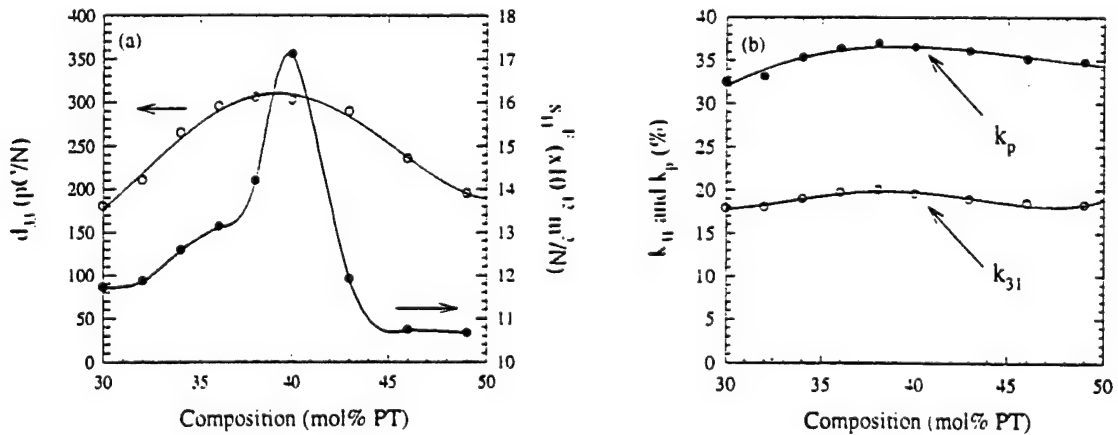


Figure 4. Compositional dependence of the piezoelectric properties for PIT:PT ceramics: (a) the piezoelectric constant,  $d_{33}$ , and elastic compliance,  $s_{11}^E$ , and (b) the electromechanical coupling factors,  $k_p$  and  $k_{31}$ .

The Morphotropic Phase Boundary in  $\text{Pb}(\text{In}_{1/2}\text{Ta}_{1/2})\text{O}_3$  :  $\text{PbTiO}_3$  Ceramics.

The piezoelectric properties of the  $(1-x)$  PIT :  $(x)$  PT solid solution system are shown in figure 4. The samples were poled in a stirred silicone bath at  $25^\circ\text{C}$  for 30 min, using a field of  $30 \text{ kV/cm}$ . After allowing the sample to age 24 hours, the piezoelectric coefficient,  $d_{33}$ , was measured and found to be on the order of  $302 \text{ pC/N}$  for the composition  $x = 0.38$ . The piezoelectric coupling factors ( $k_p$  and  $k_{31}$ ) are also maximized in this composition, with values of 37% and 20%, respectively. The elastic compliance was found to increase to a maximum of  $\sim 17 \times 10^{-12} \text{ m}^2/\text{N}$  at  $x = 0.40$ .

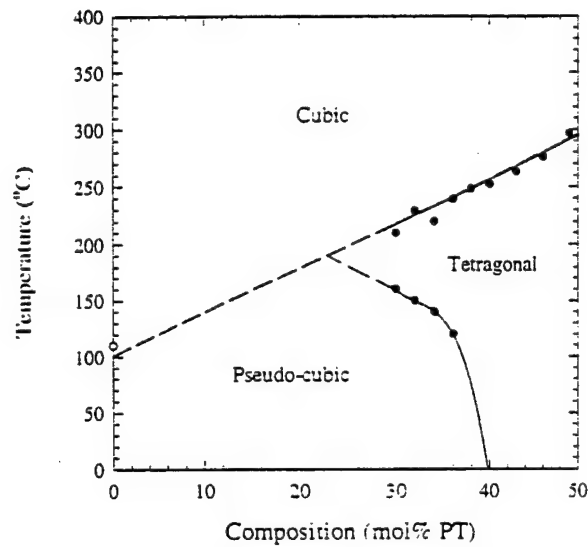


Figure 5. Phase diagram for  $(1-x)$  PIT :  $(x)$  PT ceramics based on dielectric data.

Finally, a phase diagram based on dielectric data was constructed (figure 5). It was rather difficult to obtain phase-pure perovskite samples for compositions with PT content less than 30%. This coexistence region, between the pyrochlore and perovskite phases, is shown by the dashed line between  $x = 0.00$  and  $0.36$ . The temperature of the ferroelectric to paraelectric phase transition for each composition was determined from the maximums in the dielectric constant (figure 2). The pseudo-cubic to tetragonal phase boundary was identified from the lower temperature anomalies in the dielectric data.

Table 1: Electrical properties of (1-x) PIT : (x) PT ceramics.

Property:	PIT:PT
Composition (mol% PT)	38.0
Dielectric constant:	
at 25°C (unpoled)	1900
at 25°C (poled)	2300
at $T_c$	13000
Dielectric Loss:	
at 25°C (unpoled)	0.021
at 25°C (poled)	0.019
at $T_c$	0.025
Transition temperature (°C)	248
Piezoelectric:	
$\sigma$	0.41
$s_{11}E$ ( $\times 10^{-12} \text{ m}^2/\text{N}$ )	14.08
$d_{33}$ (pC/N)	302
$d_{31}$ (pC/N)	-114
$k_p$ (%)	37
$k_{31}$ (%)	20

## CONCLUSIONS

This paper reports the first successful study of the preparation of single-phase perovskite (1-x) PIT : (x) PT ceramics. Based on anomalies in the dielectric data, a phase diagram was constructed. Piezoelectric, pyroelectric and dielectric data suggests the presence of a morphotropic phase boundary in this system at  $x \sim 0.38$  mol% PT.

## REFERENCES

1. Kania, A., "A New Perovskite  $\text{Pb}(\text{In}_{0.5}\text{Ta}_{0.5})\text{O}_3$  (PIT)," *Ferroelectric Letters*, Vol. 11, pp. 107-110, (1990).
2. Kania, A. and M. Pawelczyk, "Order-Disorder Aspects in  $\text{PbIn}_{0.5}\text{Ta}_{0.5}\text{O}_3$  Crystals," *Ferroelectrics*, Vol. 124, pp. 261-264, 1991.
3. Bokov, A.A., I.P. Rayevsky, V.V. Neprin and V.G. Smotrakov, "Investigation of Phase Transitions in  $\text{Pb}(\text{In}_{0.5}\text{Ta}_{0.5})\text{O}_3$  Crystals," *Ferroelectrics*, Vol. 124, pp. 271-273, (1990).
4. Jones, F.G., C.A. Randall, S.J. Jang, and T.R. Shrout, "Preparation and Characterization of Indium Based Complex Perovskites -  $\text{Pb}(\text{In}_{1/2}\text{Nb}_{1/2})\text{O}_3$  (PIN),  $\text{Ba}(\text{In}_{1/2}\text{Nb}_{1/2})\text{O}_3$  (BIN), and  $\text{Ba}(\text{In}_{1/2}\text{Ta}_{1/2})\text{O}_3$  (BIT)," *Ferroelectrics Letters*, Vol. 12, pp. 55-62, (1990).
5. Yasuda, N., S. Imamura, "Diffuse Phase Transition in A New Perovskite  $\text{Pb}(\text{In}_{1/2}\text{Ta}_{1/2})\text{O}_3$ ," *Appl. Phys. Lett.*, Vol. 59, No. 26, pp.3493-3495, (1991).

The Morphotropic Phase Boundary in  $\text{Pb}(\text{In}_{1-x}\text{Ta}_x)\text{O}_3$  :  $\text{PbTiO}_3$  Ceramics.

6. Yasuda, N., H., Inagaki, and S. Imamura. "Dielectric Properties of Perovskite Lead Indium Niobate and Tantalate Prepared by Fast Firing Technique," *Jpn. J. Appl. Phys.*, Vol. 31, pp. L 574 - L 575, (1992).
7. Yasuda, N., and S. Imamura. "Preparation and Characterization of Perovskite Lead Indium Tantalate", *Ferroelectrics*, Vol. 126. pp. 109-114. (1992).
8. Alberta, E.F., and A.S. Bhalla, "Preparation of Phase-Pure Lead Indium Niobate," *Mater. Lett.*, Vol. 29, pp. 127-129, (1996).
9. Alberta, E.F., and A.S. Bhalla, "Piezoelectric Properties of  $\text{Pb}(\text{In}_{1/2}\text{Nb}_{1/2})\text{O}_3$  -  $\text{PbTiO}_3$  Solid Solution Ceramics," *J. Korean Phys. Soc.*, Vol. 32. pp. S 1265 - S 1267, (1998).

# **APPENDIX 9**



# Photoluminescence in $\text{PbMg}_{1/3}\text{Nb}_{2/3}\text{O}_3$ – $\text{PbIn}_{1/2}\text{Nb}_{1/2}\text{O}_3$ systems

J. F. Meng, Z.-Y. Cheng, Brajesh K. Rai, and R. S. Katiyar

*Department of Physics, University of Puerto Rico, San Juan, Puerto Rico 00931*

E. Alberta, R. Guo, and A. S. Bhalla

*Materials Research Center, The Pennsylvania State University, University Park, Pennsylvania 16802*

(Received 12 March 1997; accepted 12 September 1997)

Photoluminescence for  $\text{PbMg}_{1/3}\text{Nb}_{2/3}\text{O}_3$  (PMN)– $\text{PbIn}_{1/2}\text{Nb}_{1/2}\text{O}_3$  (PIN) solid solutions in the temperature ranging from 35 to 295 K have been obtained for the first time. An abrupt photoluminescence enhancement of the system has been observed to occur at  $\sim 210$  K, which can be attributed to the growing and merging of dynamic polar microregions or to the phase transformation of the material at this temperature. The PIN content has been found to affect the photoluminescence of the PMN-PIN system significantly. The photoluminescence mechanism for PMN-PIN has been studied.

## I. INTRODUCTION

Like most typical relaxor ferroelectrics which exhibit reproducible electrostrictive strains, diffuse phase transition, and a high dielectric constant over a wide range of temperature,  $\text{PbMg}_{1/3}\text{Nb}_{2/3}\text{O}_3$  (PMN) is one of the most attractive materials for theoretical as well as practical application points of views.<sup>1–3</sup> At room temperature, PMN has a cubic symmetry and belongs to  $Pm\bar{3}m$  space group.<sup>4</sup> Several physical properties of PMN at temperatures below  $T_m = -8^\circ\text{C}$ , suitable to explain the dielectric relaxor behavior of the materials, are very attractive and have been widely studied.<sup>5–7</sup> It is well known that the dynamic polar microregions in PMN appear up to a temperature  $\sim 300^\circ\text{C}$ , and that there are nano-micro ordered clusters in the materials.<sup>8</sup> Nevertheless, the temperature dependence of the ordered clusters as well as their effects on the relaxor properties of materials are still under various studies. Additionally, in the case of PMN there are some questionable and incomplete reports about the phase transition at a temperature  $\sim 210$  K.<sup>9–11</sup> The origin and mechanism of the phase transition at this temperature is still unclear and worthwhile investigating further.  $\text{PbIn}_{1/2}\text{Nb}_{1/2}\text{O}_3$  (PIN) is another typical ferroelectric relaxor material with perovskite structure. Its ordered and disordered physical property is closely correlated with synthesis conditions.<sup>12</sup> The ordered PIN has a paraelectric to antiferroelectric phase transition at  $\sim 196^\circ\text{C}$ , while the disordered PIN is a typical relaxor ferroelectric,<sup>12,13</sup> and its dielectric constant peaks in the temperature range from 40 to  $60^\circ\text{C}$ .<sup>14,15</sup> Moreover, unlike in PMN, the 1:1 ordering on the B-sites in PIN is favorable and provides an electrically neutral region, and hence, the investigation of the PMN-PIN system would provide an insight about the behavior of the ordered clusters in this system.

Although photoluminescence (PL) technique is a very useful tool for studying phase transitions, inter-

faces, and atomic-distributions, and has been effectively applied to probe semiconductor materials, such as CdS and CdTe,<sup>16–19</sup> there are no reports on the PL as well as its field dependence in the PMN-PIN system. In this paper, on the basis of detailed PL measurements on the prepared PMN-PIN ceramics, we have investigated the effects of temperature and PIN content on dynamic polar microregions as well as phase transition in PMN ceramics.

## II. EXPERIMENTAL

The samples were prepared by the conventional oxide technique using the suitable precursors.<sup>20</sup> Four candidate compositions in PMN-PIN solid solutions, namely PMN, 0.8PMN-0.2PIN, 0.5PMN-0.5PIN, and PIN were investigated. Photoluminescence spectra were collected using a Spex-1402 double-grating monochromator with the 514.5 nm line from an argon-ion laser as the laser excitation. Low temperature photoluminescence measurements were performed using a closed cycle  $^4\text{He}$  cryosystem.

Using the excitation line of 514.5 nm, the PL spectra for four ceramic samples, i.e., PMN, 0.8PMN-0.2PIN, 0.5PMN-0.5PIN, and PIN, are shown in Figs. 1(a)–1(d). It is found that none of the four samples shows any distinct PL band in the energy range of 1.55 to 1.75 eV at room temperature. However, with decreasing temperature, an asymmetric luminescence spectrum containing two emission bands, as shown in Figs. 1(a) and 1(b) as A (the stronger emission) and B (the weaker emission), emerges. Also, an abrupt PL enhancement for the two emission bands is found to appear at  $\sim 210$  K. Figure 1 indicates that the PL bands of A and B in PMN-PIN system in the energy range of 1.55 to 1.75 eV decrease in intensity and approach disappearance with increasing PIN content. There are no PL bands to be detected for PIN. In addition, as the temperature is decreased, the PL

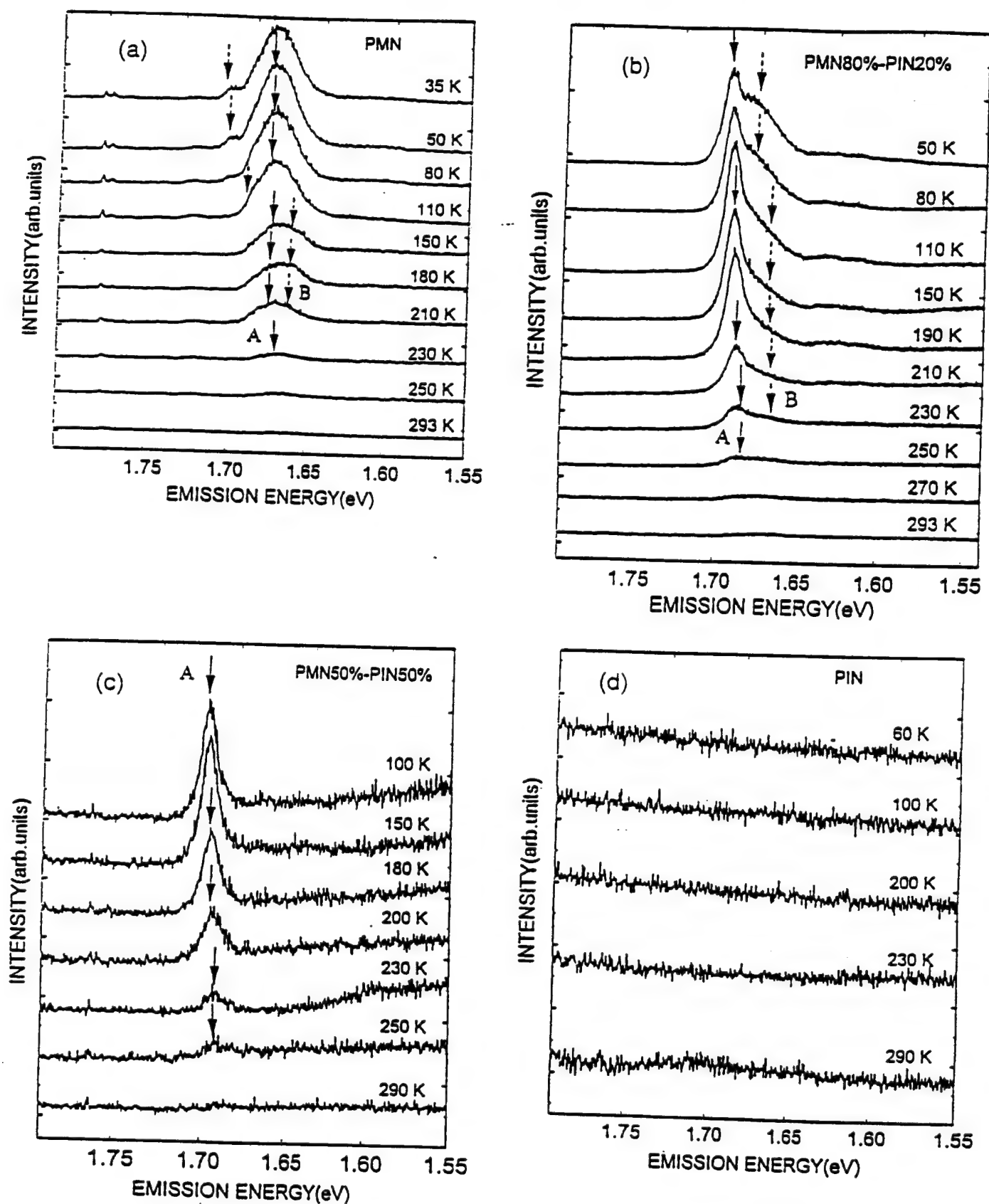


FIG. 1. Photoluminescence spectra of the PMN-PIN system with the excitation line of 514.5 nm at different temperatures and an energy region of 1.55–1.80 eV. (a) Pure PMN, (b) 0.8PMN-0.2PIN, (c) 0.5PMN-0.5PIN, and (d) pure PIN.

band-B of PMN seems to appear as a large shift in its peak position while the band-A shifts very little. On the other hand, the PIN content has an obvious effect on the B band. For 0.8PMN-0.2PIN, no higher emission energy for the band-B than that for the band-A is observed up to 50 K, whereas, for 0.5 PMN-0.5PIN, only a PL peak, e.g., the band-A can be detected.

### III. RESULTS

First, in the case of PMN, it is impossible to excite an electron from its valence to conduction band by using the laser line of 514.5 nm ( $\sim 2.41$  eV) so that the observed PL of PMN-PIN cannot be attributed to a band-to-band transition because the known band gap ( $\sim 3.4$  eV) of both PMN and PIN is much larger than the observed PL emission centered at 1.6–1.7 eV. The luminescence properties of niobate-oxygen octahedral in PMN can be compared to those of the titanate-oxygen octahedron<sup>21</sup> in  $\text{ATiO}_3$  (where A is a cation with  $-2$  valence), as both  $\text{Nb}^{5+}$  and  $\text{Ti}^{4+}$  have the same outer electronic configuration of  $nd^0$  (where  $n = 4$  for  $\text{Nb}^{5+}$  and  $n = 3$  for  $\text{Ti}^{4+}$ ). Furthermore, it has been recently shown that the luminescence properties of nanocrystalline  $\text{BaTiO}_3$  and  $\text{SrTiO}_3$  are predominantly determined by the  $d$ -surface states (which arise from  $\text{Ti}^{4+}$ ) in the bandgap, and very little so by Pb atoms.<sup>22</sup> which suggests the PL in PMN also probably to be Pb independent. Hence, we tend to associate the origin of PL bands in PMN with the Nb-O system, similar to that of  $\text{ATiO}_3$ , in the case in which the PL bands are determined mainly by the Ti-O system. In particular, the PL spectra in most of the titanium-activated stanates and zirconates are known to show two emission bands; one of which arises from a regular-titanate octahedron while the other from a defect-titanate octahedron, with both remaining independent of Mg.<sup>23</sup> Similarly, the PL of  $\text{Mg}_2\text{Nb}_2\text{O}_9$  (MNO) is also composed of two bands. The stronger one originates from the regular-Nb centers, whereas the weaker band originates from the defect-Nb centers.<sup>21</sup> Thus these facts make it possible to suggest that in the PMN-PIN system, the luminescence bands A (with a stronger intensity) and B (with a weaker intensity) can be analogously attributed to the emission of regular-Nb and defect-Nb centers, respectively.

In turn, we discuss the effects of PIN dopants on the PL of PMN. The PL intensity of the band-A for 0.5PMN-0.5PIN is significantly low as compared to that of PMN and 0.8PMN-0.2PIN. Especially, there is no PL to be observed in the energy range of 1.55 to 1.75 eV. That is, there is a PL "quenching" behavior [see Fig. 1(d)]. In fact, the PL quenching in PIN can be related to the influence of PIN on the known dynamic 1:1 ordered clusters of Mg and Nb in polar microregions. The volume fraction and dynamic nature of the 1:1 ordered

cluster, in the  $(1-x)\text{PMN}-x\text{PIN}$  system, decreases with increasing PIN content, which results in a decrease of Nb-octahedra and defect-Nb centers in microregions, and consequently, leads to the PL quenching in pure PIN. In addition, it is important to mention here that there is no polar microregion for PIN in the studied temperature range. It is thus thought that the PL quenching can be attributed to the decrease and disappearance of dynamic polar microregions with increasing PIN content.

The PL spectra of the PMN-PIN system in the other energy range of 1.80 to 2.25 eV are shown in Fig. 2 in order to reveal more detailed PL behavior in PIN. A well-defined PL spectrum for PIN has been observed, but it is interesting to note that the PMN does show no PL in the same energy range, which implies that the PL of the PIN system in the energy range could be independent of dynamic microregions. A detailed study on the PL in this energy region is in progress.

The 1:1 ordered clusters in PMN are not electrically neutral. Thus, a distribution of space charge, both within and outside of the clusters, is developed. A previous study of the dielectric properties on PLZT has shown the space charges to have a strong effect on the polar microregions of the material.<sup>24</sup> Analogously, the space charge distribution in PMN can be thought to have apparent effects on the properties of the 1:1 ordered clusters, such that the interaction between Nb-octahedra and defect-Nb centers in the microregions increases with decreasing temperature. From Fig. 1(a), it is seen that

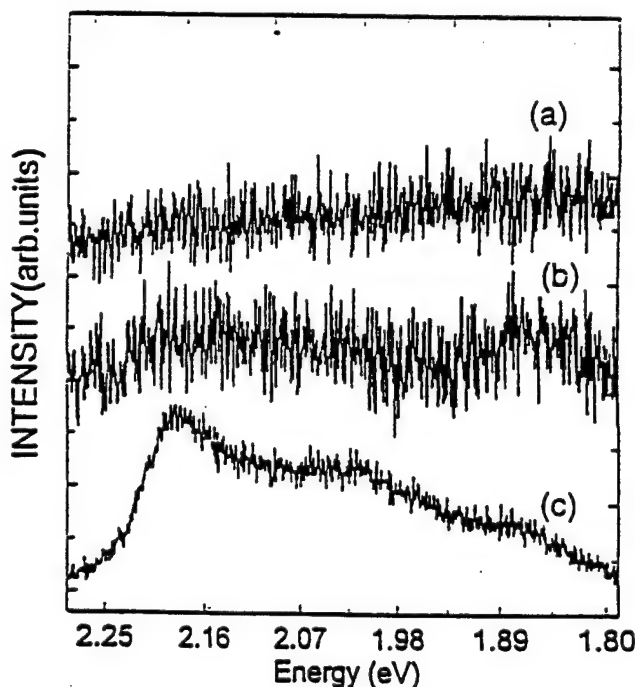


FIG. 2. Room temperature photoluminescence for the PMN-PIN system with the excitation line of 514.5 nm and energy region of 1.8–2.25 eV. (a) PMN, (b) 0.5PMN-0.5PIN, and (c) PIN.

the PL band A and B of PMN overlaps with each other at room temperature. However, as temperature is decreased, the band-B shows a more higher emission energy for temperatures below 130 K, whereas the band-A shifts very little. This seems to be related to an energy-exchange mechanism. That is, there is a possible energy transfer effect from regular- $\text{NbO}_6$  octahedra to defect-niobate centers.

Finally, we discuss the anomalous behavior of the PL intensity at  $\sim 210$  K. Previous investigations on the structure of PMN over the temperature range of 800 to 5 K show that a distortion from the cubic symmetry is present and the disordered cubic model becomes less and less satisfactory with decreasing temperature.<sup>23</sup> So, the B-site ions, exhibiting the well-known existence of 1:1 ordered cluster, shift from the center position to the off-center position of the octahedral along  $\langle 111 \rangle$  direction. Obviously, the deviation from cubic symmetry leads likely to a large change of the PL. Hence, the abrupt increase in the PL intensity at  $\sim 210$  K may be attributed to a phase transition from cubic to ferroelectric-rhombohedral phase. However, on the other hand, it is possible that with decreasing temperature, a few small dynamic polar microregions grow and as a result, merge into one large polar microregion. Thus, the PL of the material, exhibiting a strong temperature dependence, is likely related to the ordered length. In particular, the time dependence of merging process for some dynamic microregions makes it rather sensitive to the employed measurement technique. It is known that the dielectric measurement process involves a continuous, and somewhat rapid, variation of temperature, which inhibits the observation of any clear change in the time dependent dielectric behavior of the sample. Moreover, in the presence of a strong external electric field during the dielectric measurements, the space charges make the change in the dielectric properties occur at a very narrow temperature range like in PLZT.<sup>24</sup> However, in the present experiment, the sample was held at each temperature for a long time (30–60 min), which provided enough time for the merging of polar microregions. Therefore, the enhancement of the PL at  $\sim 210$  K can be likely associated with the merging process of the dynamic polar microregions at this temperature.

#### IV. CONCLUSIONS

The stronger PL band, i.e., the band-A, arises from the regular-Nb centers, while the weaker PL band, the band-B, originates from the defect-Nb centers. The PL quenching for PMN induced by increasing PIN content

is associated with the disappearance of dynamic polar microregions in the PMN-PIN system. The PL enhancement at  $\sim 210$  K has been attributed to the growing and merging of dynamic polar microregions or to some kind of phase transition at this temperature. The shift of the band-B in emission energy with decreasing temperature seems to originate from an energy-exchange process between regular- $\text{NbO}_6$  octahedra and defect-Nb centers.

#### ACKNOWLEDGMENTS

The work was supported by the Department of Energy Grant DE-FG02-94ER75764 and NASA-0088, and NSF-OSR-9452893.

#### REFERENCES

1. T. R. Shrout and A. H. Halliwell, *Am. Ceram. Soc. Bull.* 66, 704 (1987).
2. L. E. Cross, S. Jang, R. E. Newnham, S. Nomura, and K. Uchino, *Ferroelectrics* 23, 187 (1980).
3. K. Uchino, *Am. Ceram. Soc. Bull.* 65, 647 (1986).
4. H. B. Krause and D. L. Gibbon, *Zeits. Krist.* B4, 44 (1971).
5. G. Schmidt, *Phase Transition* 20, 127 (1990).
6. A. E. Giazounov, A. K. Tagantsev, and A. J. Bell, *Phys. Rev. B* 53 (17), 11 231 (1996).
7. Z.-G. Ye, *Ferroelectrics* 184, 193 (1996).
8. H. B. Krause, *Acta Crystallogr.* A35, 1015 (1979).
9. P. Bonneau, P. Garnier, G. Calvarin, E. Husson, J. R. Gavarri, A. W. Hewat, and A. Morell, *J. Solid State Chem.* 91, 350 (1990).
10. Z.-G. Ye and H. Schmid, *Ferroelectrics* 145, 83 (1993).
11. N. de Mathan, E. Husson, G. Calvarin, and A. Morell, *Mater. Res. Bull.* 26, 1167 (1991).
12. O. I. Prokhopalo, I. P. Raevskh, M. A. Malitskaya, Yu. M. Popov, A. A. Bokov, and V. G. Smotrakov, *Ferroelectrics* 45, 89 (1982).
13. N. Yasuda and S. Shibuya, *Ferroelectrics* 106, 281 (1990).
14. M. F. Kvpryanov, A. V. Turik, S. M. Zaisev, and E. G. Fesenko, *Phase Transition* 4, 65 (1983).
15. P. Groves, *Ferroelectrics* 65, 67 (1985).
16. N. Chestnoy, T. D. Harris, R. Hull, and L. E. Brus, *J. Phys. Chem.* 90, 3393 (1986).
17. R. Tenne and R. Jager-Waldau, *Phys. Rev. B* 36, 1204 (1987).
18. M. G. Bawendi, P. J. Carroll, W. L. Wilson, and L. E. Brus, *J. Chem. Phys.* 96, 946 (1992).
19. C. Barnett Davis, D. D. Allred, A. Reyes-Mena, J. Gonzalez-Hernandez, O. Gonzalez, B. C. Hess, and W. P. Allred, *Phys. Rev. B* 47, 13 363 (1993).
20. S. L. Swartz and T. R. Shrout, *Mater. Res. Bull.* 17, 1245 (1982).
21. A. J. H. Macke, *J. Solid State Chem.* 19, 221 (1976).
22. J. F. Meng, Y. B. Huang, W. F. Zhang, Z. L. Du, and G. T. Zou, *Phys. Lett. A* 205, 72 (1995).
23. A. J. Macke, Thesis, Utrecht, 1976. Chap. 2; A. J. H. Macke, Thesis, Utrecht, 1976. Chap. III; *J. Solid State Chem.* 18, 337 (1976).
24. Z.-Y. Cheng, L. Zhang, and X. Yao, *IEEE Trans. Electr. Insul.* 27, 773 (1992).
25. L. A. Shebanov, P. Kaspostins, and J. Zvirgzds, *Ferroelectrics* 56, 1057 (1984).

# **APPENDIX 10**

# Investigation of the Lead Indium Niobate - Lead Magnesium Niobate Solid Solution.

Edward F. Alberta and Amar. S. Bhalla

Materials Research Laboratory, The Pennsylvania State University  
University Park, PA 16802 USA

## Abstract:

This paper describes the first study on processing and electrical properties of ceramics in the  $(x) \text{Pb}(\text{In}_{1/2}\text{Nb}_{1/2})\text{O}_3 : (1-x) \text{Pb}(\text{Mg}_{1/3}\text{Nb}_{2/3})\text{O}_3$  [PIMN( $x/100$ - $x$ )] solid solution system with  $x = 50$  mol%. Pellets were sintered at  $1100^\circ\text{C}$  resulting in phase-pure perovskite ceramics with 98% theoretical density. These ceramics displayed typical relaxor ferroelectric behavior with a maximum dielectric constant of 8056 at  $26^\circ\text{C}$ . A slight polarization hysteresis was observed at  $25^\circ\text{C}$ . A maximum induced polarization of  $23.95 \mu\text{C}/\text{cm}^2$  and remanent polarization of  $1.2 \mu\text{C}/\text{cm}^2$  at the peak field level of  $48 \text{ kV}/\text{cm}$  was measured. The strain and electrostriction coefficient were measured, the values were in the range of  $x_{33} = 8.12 \times 10^{-4}$  and  $Q_{33} = 1.42 \times 10^{-2} \text{ m}^4/\text{C}^2$ , respectively. The low hysteresis in  $x_{33}$  and low values of  $P_r$  make this solid solution attractive for further study.

## Keywords:

Solid Solutions, Relaxor Ferroelectrics, Lead Indium Niobate, Lead Magnesium Niobate, Dielectric Properties, Electrostrictive Properties.

## Introduction:

Lead magnesium niobate  $\text{Pb}(\text{Mg}_{1/3}\text{Nb}_{2/3})\text{O}_3$  [PMN] is probably the most widely studied relaxor ferroelectric known. A maximum dielectric constant of nearly 18000 at its transition temperature,  $T_m$  of approximately  $-15^\circ\text{C}$  has been reported at a measurement frequency of  $1 \text{ kHz}$ . [1] There are also several reports on the properties of  $\text{PMN}:\text{PbTiO}_3$  [PMN:PT] solid solution with various concentrations of  $\text{PbTiO}_3$  [PT]. The PMN:PT solid solution also shows a morphotropic phase boundary at which further enhancement in some properties has been measured. PMN:PT compositions are highly promising for electrostrictive and piezoelectric devices. The composition (0.93) PMN : (0.07) PT has been shown to have a large piezoelectric effect under electrical field. [2] This composition, as well as others in this solid solution system appear to be promising candidates for some smart ferroic systems such as vibration control and actuators.

Lead indium niobate  $\text{Pb}(\text{In}_{1/2}\text{Nb}_{1/2})\text{O}_3$  [PIN] is an interesting order-disorder type relaxor. In its disordered state PIN is a relaxor ferroelectric with a pseudo cubic perovskite structure and a dielectric constant maximum ( $T_m$ ) of  $66^\circ\text{C}$ . [3] Annealing PIN at a suitable temperature causes the material to order into an antiferroelectric orthorhombic phase. This phase, which is isostructural with lead zirconate, has a



transition temperature of 190°C.[4] Another important and well-studied order-disorder relaxor is  $\text{Pb}(\text{Sc}_{1/2}\text{Ta}_{1/2})\text{O}_3$  [PST]. It's solid solution with PT has shown a variable order-disorder region as well as a morphotropic phase boundary.[5]

To our knowledge there are no reports so far on the PIMN solid solution. This system is expected to show some unique and unexplored characteristics. There is a possibility that additions of PMN may alter the order-disorder behavior of PIN such that it may fully disorder and display its relaxor ferroelectric behavior, or to produce ordering over a limited compositional range, and thereby transforming the composition into an antiferroelectric. The obvious stoichiometric differences between PIN and PMN may lead to other ordering phenomena, and even the existence of morphotropic phase boundaries. In order to study this interesting solid solution system this study has been undertaken and the first results on the PIN:PMN (50/50) compositions are reported here.

#### Experimental Procedures:

Ceramics with the composition PIMN(50/50) were fabricated using vibratory milled PIN and PMN powders. Stoichiometric PIN and PMN powders were prepared using the Columbite precursor method.[3,6] The precursor materials were synthesized using  $\text{In}_2\text{O}_3$ ,  $\text{Nb}_2\text{O}_5$  and  $\text{MgCO}_3$  to form stoichiometric  $\text{InNbO}_4$  and  $\text{MgNb}_2\text{O}_6$ .  $\text{PbO}$  was added to each precursor to form PIN and PMN, respectively. After calcining, the powders were mixed and milled for 24 hours in acetone with  $\text{ZrO}_2$  media. The powders were then dried for another 24 hours and then mixed with 3 wt% binder.

Pellets from the mixture were pressed and the binder removed. The green ceramics were sintered at various temperatures between 1050°C and 1200°C. Following the sintering step, x-ray diffraction was used to determine the concentration of the unwanted pyrochlore phase. For the electrical measurements the ceramic disks were polished using 1  $\mu\text{m}$   $\text{Al}_2\text{O}_3$ . Finally, the samples were cleaned in an ultrasonic bath, dried, and sputtered with gold.

Dielectric constant and loss measurements were made using an automated measurement system. This system consisted of an LCR meter (HP-4174A, Hewlett-Packard), a nitrogen-fed furnace (Model - 9023, Delta Design, Inc.), and a desktop computer (HP-200 series, Hewlett-Packard). Hysteresis measurements were made using a modified Sawyer-Tower circuit controlled by a PC. This system is also capable of simultaneous measurement of strain using an LVDT and lock-in amplifier (SR830 DSP, Stanford Research).

#### Results and Discussion:

Sintered densities of the PIMN(50/50) ceramics were found to vary between 8.13  $\text{g/cm}^3$  and 8.18  $\text{g/cm}^3$ . Weight loss was limited to less than 1 wt% between the sintering temperatures of 1050°C and 1200°C. At a sintering temperature of 1100°C both dielectric constant and density were found to be optimized (figure 1). Ceramics were determined, by X-ray diffraction, to be single-phase perovskite (figure 2).

Electrical measurements were made on samples sintered at 1100°C. The temperature dependence of the dielectric constant and loss of PIMN(50/50) shows typical relaxor ferroelectric behavior (figure 3). The maximum dielectric constant, measured at 1 kHz, is 8056 at 26°C and it shifts towards higher temperatures with increasing

frequency. The maximum loss measured at 1 kHz is 0.1043 at  $-4^{\circ}\text{C}$  and also shifts towards higher temperatures with increasing frequency.

Dielectric hysteresis behavior of PIMN(50/50) resembles that of a typical electrostrictive relaxor ferroelectric (figure 4). At room temperature, the maximum polarization,  $P_s$ , was  $23.95 \mu\text{C}/\text{cm}^2$  at an applied field of 48 kV/cm and the remanant polarization,  $P_r$ , was in the range of  $1.2 \mu\text{C}/\text{cm}^2$ . Electrostrictive measurements were made and the resulting strain was found to be non-hysteretic in nature with a maximum strain value of 0.0812% at a field of 48 kV/cm.  $Q_{33}$  as calculated from the strain data was on the order of  $1.42 \times 10^{-2} \text{ m}^4/\text{C}^2$ .

As expected from the hysteresis data, the sample was difficult to pole near or above room temperature. However, a remanent polarization of about  $12 \mu\text{C}/\text{cm}^2$  was observed at  $-75^{\circ}\text{C}$  using a 20 kV/cm poling field (applied while cooling). With increasing temperature the remanant polarization decreased to  $1 \mu\text{C}/\text{cm}^2$  at room temperature and decreases to zero at approximately  $90^{\circ}\text{C}$ . Table 1 summarizes the electrical measurements on the PIMN(50/50) samples.

#### Conclusions:

The composition  $(x) \text{Pb}(\text{In}_{1/2}\text{Nb}_{1/2})\text{O}_3 : (1-x) \text{Pb}(\text{Mg}_{1/3}\text{Nb}_{2/3})\text{O}_3$ ,  $x = 0.5$ , was synthesized for studying its relaxor behavior and electrical properties. A maximum dielectric constant of 8056 was observed at  $26^{\circ}\text{C}$  for the samples sintered at  $1100^{\circ}\text{C}$ . Only a slight dielectric hysteresis was observed at  $25^{\circ}\text{C}$  ( $P_r < 1.2 \mu\text{C}/\text{cm}^2$ ) for these samples which showed a maximum induced polarization of approximately  $23.95 \mu\text{C}/\text{cm}^2$  at 48 kV/cm. The strain levels and resulting electrostrictive coefficient,  $Q_{33}$ , were determined to be  $8.12 \times 10^{-4}$  and  $1.42 \text{ m}^4/\text{C}^2$  at 48 kV/cm, respectively. No room temperature piezoelectric activity was detected under zero bias conditions as the material is near  $T_m$ .

The solid solution compositions of PIN:PMN appear to be promising for electrostrictive devices. Further work is currently underway on both temperature and biasing effects on these materials and other compositions across the PIN:PMN phase diagram.



## References:

1. Z.-G. Ye and H. Schmid, Optical, Dielectric and Polarization Studies of the Electric Field-Induced Phase Transition in  $\text{Pb}(\text{Mg}_{1/3}\text{Nb}_{2/3})\text{O}_3$  [PMN], *Ferroelectrics* 145 (1993) 83.
2. D.J. Taylor, Electric and Elastic Coefficients of Lead Magnesium Niobate-Based Ceramics Under DC Bias For Active Smart Sensor Applications. Ph.D. Thesis. The Pennsylvania State University (1992).
3. E.F. Alberta and A.S. Bhalla, Preparation of Phase-Pure Perovskite Lead Indium Niobate Ceramics, *Materials Letters* 29 (1996) 127.
4. P. Groves, Fabrication and Characterization of Ferroelectric Perovskite Lead Indium Niobate, *Ferroelectrics* 65 (1985) 67.
5. J.R. Giniewicz, An Investigation of the Lead Scandium Tantalate-Lead Titanate Solid Solution System, Ph.D. Thesis, The Pennsylvania State University (1991).
6. S.L. Swartz and T.R. Shrout, Fabrication of Perovskite Lead Magnesium Niobate. *Mat. Res. Bull.* 17 (1982) 1245.
7. L.E. Cross, S.J. Jang, R.E. Newnham, S. Nomura, and K. Uchino, Large Electrostrictive Effects in Relaxor Ferroelectrics, *Ferroelectrics* 23 (1980) 187.

## Figures:

- Figure 1. Dielectric constant at room temperature and at  $T_m$  as a function of sintering temperature.
- Figure 2. X-ray diffraction pattern for PIMN(50/50) ceramic sintered at 1100°C.
- Figure 3. Temperature Dependence of the dielectric constant and loss for PIMN(50/50). (Measurement made while heating at 2°C/min).
- Figure 4. A) Room temperature dielectric hysteresis loop and B) strain for PIMN(50/50).
- Figure 5. Calculation of the electrostriction coefficient,  $Q_{33}$ , for PIMN(50/50).

## Tables:

- Table 1. Physical and electric properties of PIMN(50/50) ceramics.

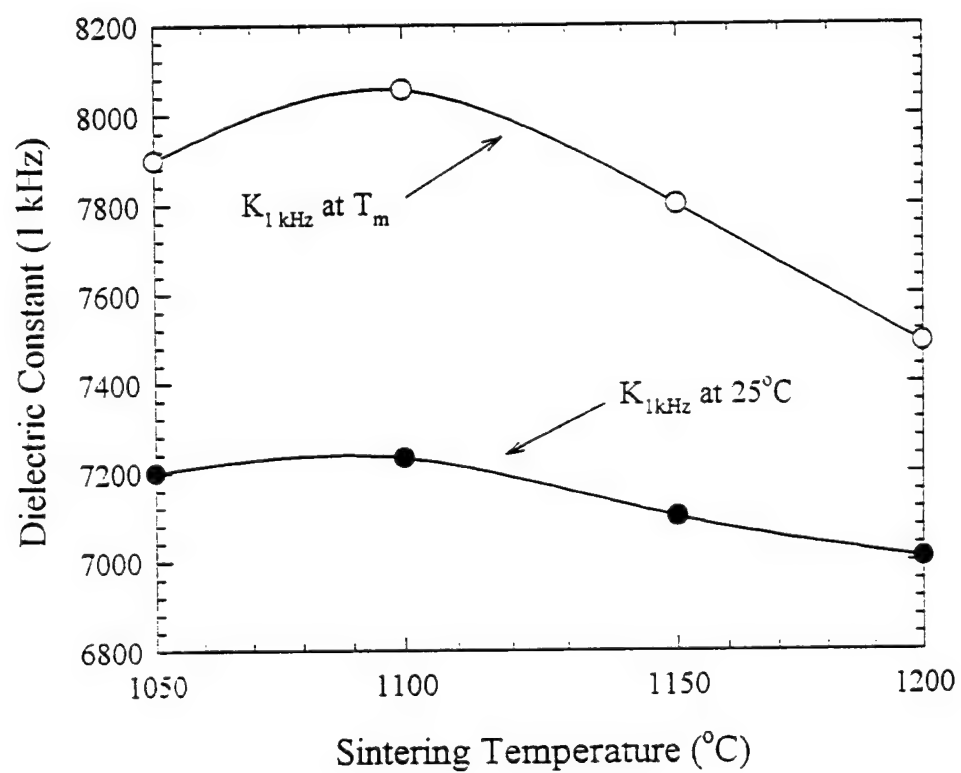


Figure 1

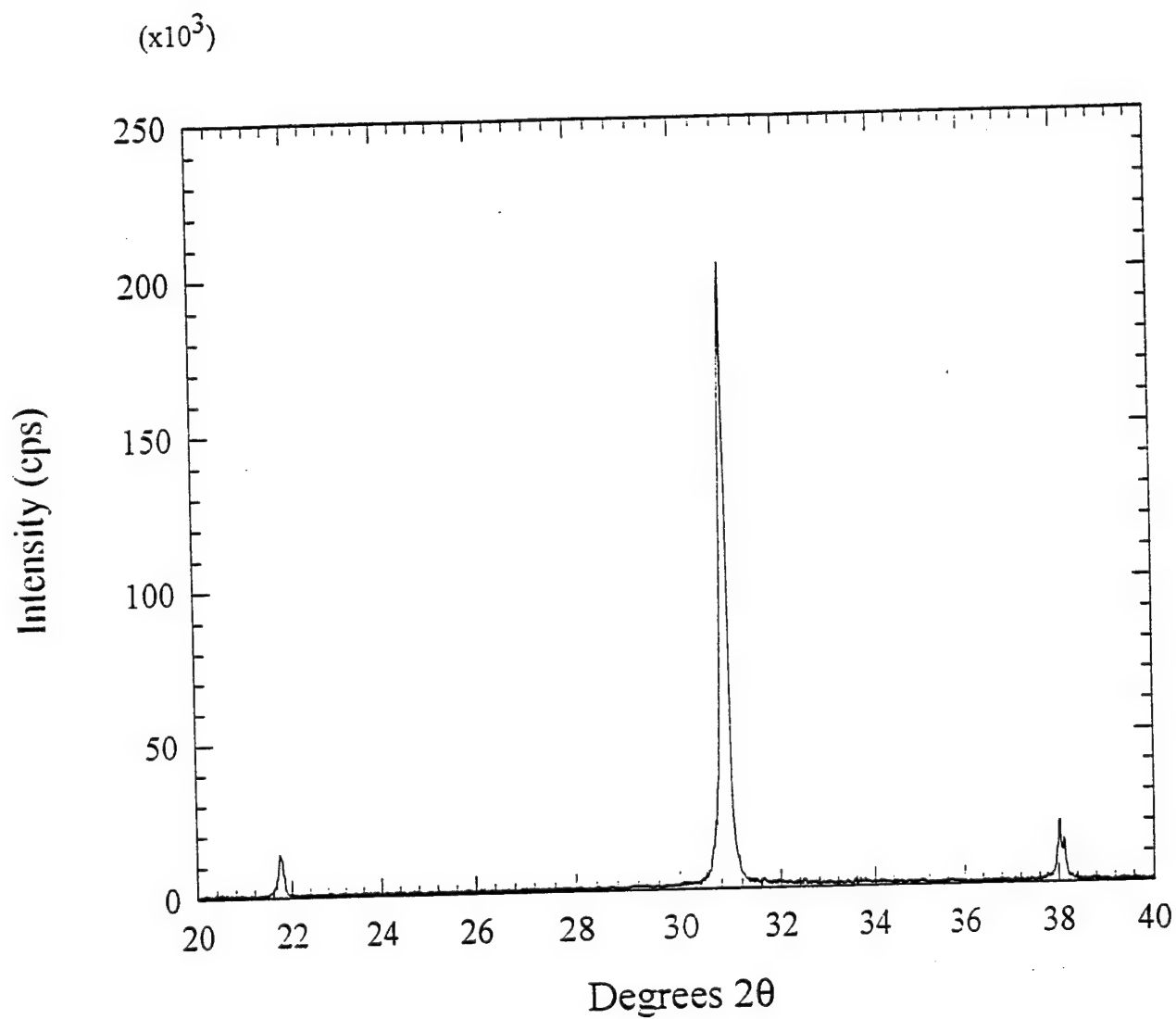


Figure 2

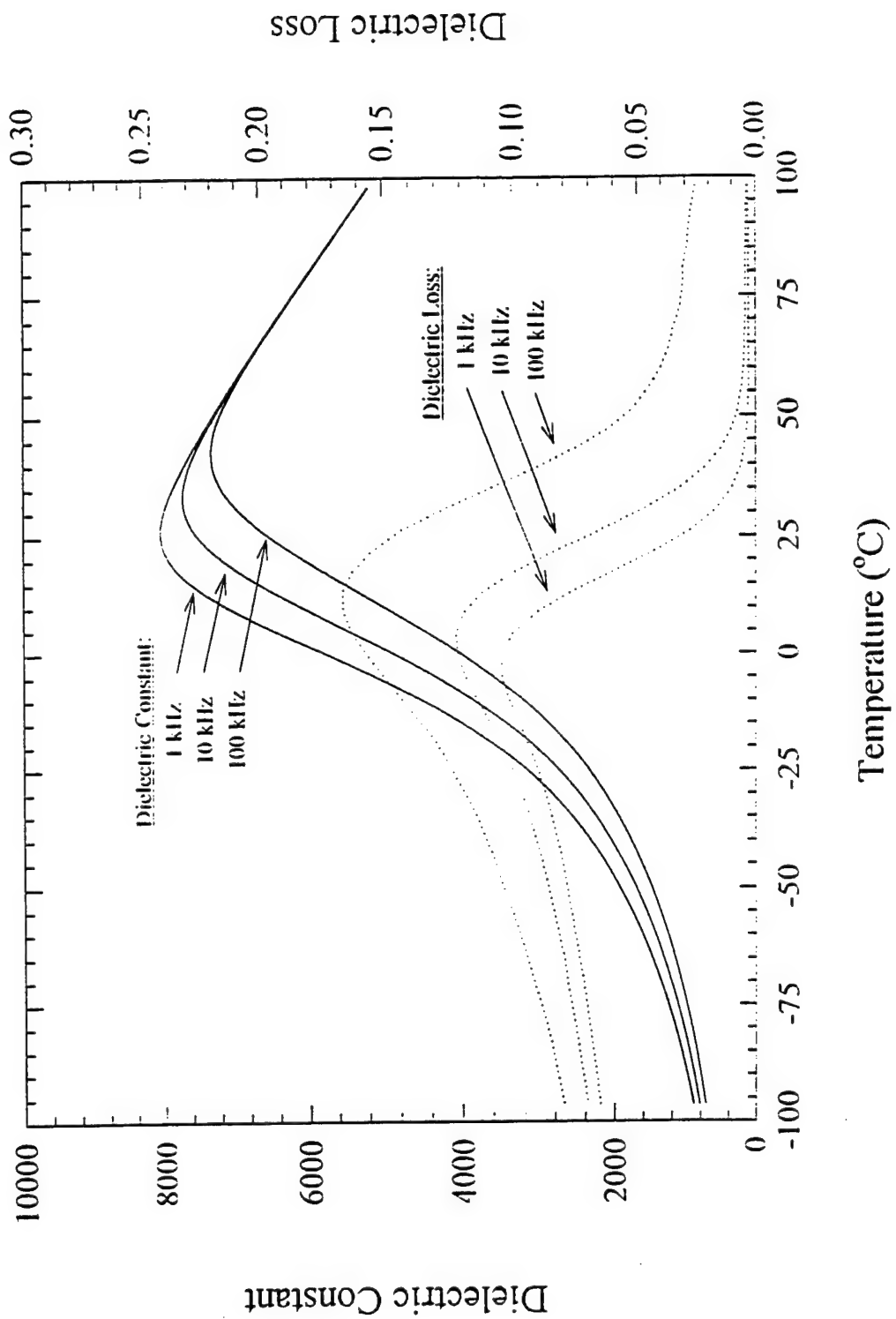


Figure 3

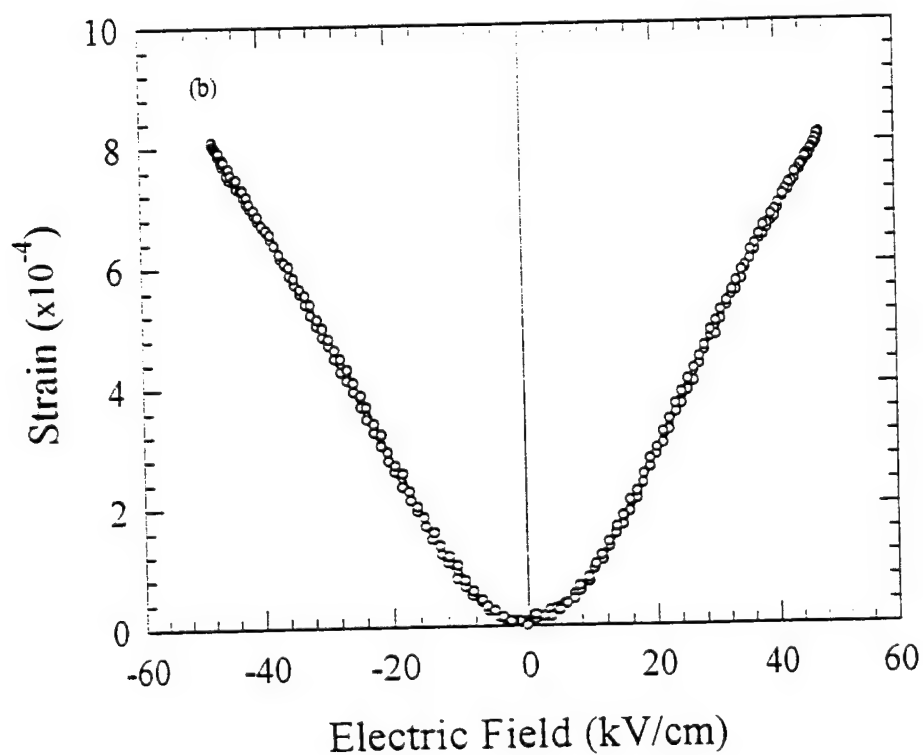
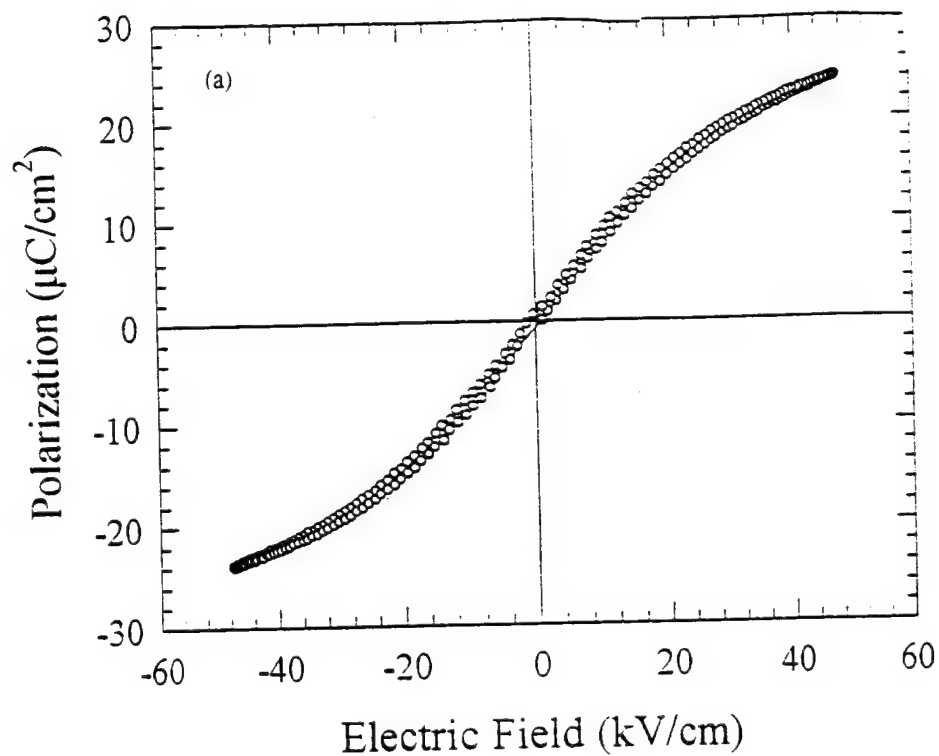


Figure 4

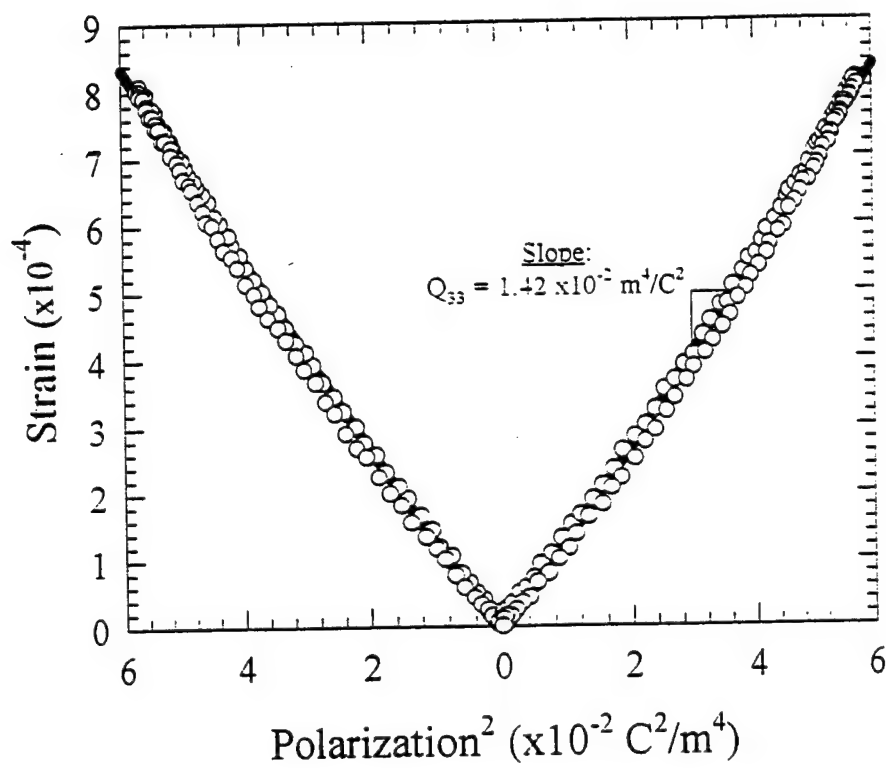


Figure 5

Table 1

Property:	PIN:PMN (50/50)
Sintering temperature (°C)	1100
Density (g/cm <sup>3</sup> )	8.18
Perovskite concentration (%)	100
Dielectric constant:	
at 25°C	7233
at T <sub>m</sub>	8056
Dielectric Loss:	
at 25°C	0.020
at T <sub>m</sub>	0.027
Transition temperature (°C)	26
Hysteresis:	
E <sub>max</sub> (kV/cm)	48.00
P <sub>max</sub> (μC/cm <sup>2</sup> )	23.95
P <sub>r</sub> (μC/cm <sup>2</sup> )	1.19
Q <sub>33</sub> (x10 <sup>-2</sup> m <sup>4</sup> /C <sup>2</sup> )	1.42

# **APPENDIX 11**



## Large Hydrostatic Piezoelectric Constant and Temperature Dependence of the Piezoelectric Properties of $\text{Bi}(\text{NiTi})_{0.4}\text{O}_3 : \text{PbTiO}_3$ Ceramics

Edward F. Alberta and Amar S. Bhalla  
Materials Research Laboratory, The Pennsylvania State University, University Park,  
Pennsylvania, USA.

T. Takenaka  
Faculty of Science and Technology, Science University of Tokyo, Noda, Chiba-ken,  
278 JAPAN.

**Abstract** Large hydrostatic piezoelectric coefficient,  $d_h \sim 111$  pC/N, for compositions in the system  $(1-x) \text{Bi}(\text{NiTi})_{0.4}\text{O}_3 : (x) \text{PbTiO}_3$  [BPNT] has been reported in this paper. Temperature dependencies of the dielectric, elastic, and piezoelectric properties of two compositions,  $x = 0.40$  and  $x = 0.50$ , around the morphotropic phase boundary of  $\text{Mn}^{2+}$  doped BPNT ceramics have been studied. Room temperature dielectric hysteresis loops with  $P_r = 37.86 \mu\text{C}/\text{cm}^2$  and  $E_c = 25.75 \text{ kV}/\text{cm}$  were observed for  $x = 0.40$ . Electromechanical coupling factors,  $k_p = 32.5\%$ ,  $k_{31} = 19.7\%$ , and  $k_t = 57.1\%$  and piezoelectric constants,  $d_{31} = 250$  pC/N,  $d_{11} = -57$  pC/N, and  $d_h = 111$  pC/N were measured in the BPNT-40 composition. The hydrophone figure of merit,  $d_h g_{31} \approx 1055 \times 10^{-13} \text{ m}^2/\text{N}$  was calculated from these measurements.

### INTRODUCTION

The solid solution bismuth nickel titanate - lead titanate,  $(1-x) \text{Bi}(\text{NiTi})_{0.4}\text{O}_3 : (x) \text{PbTiO}_3$  [BPNT- $x$ ], system has a morphotropic phase boundary at  $x = 0.445$ .<sup>1</sup> BPNT compositions have high Curie temperatures on the order of  $400^\circ\text{C}$  and have shown high mechanical strength ( $\sigma = 170 \text{ MPa}$ ). These features, as well as, the large remanent polarization values ( $30 \mu\text{C}/\text{cm}^2$ ) make BPNT- $x$  ceramics attractive for high temperature sensor applications. However, the large coercive fields ( $>45 \text{ kV}/\text{cm}$ ) and low breakdown strength could limit the ability to fully pole the ceramics. Takenaka, et al. has proposed  $\text{MnCO}_3$  additions to increase the breakdown strength and enhance the poling efficiency of these materials.<sup>2,3</sup>

In our earlier work large hydrostatic  $d_h$  values have been reported on these materials.<sup>5</sup> In this paper we report various ferroelectric and piezoelectric properties for these high temperature - low lead content - piezoelectric compositions. To enhance poling, 0.02 wt%  $\text{MnCO}_3$  was added to these compositions. Temperature dependencies of two selected BPNT-(x) compositions with  $x = 0.40$  and  $x = 0.50$  were measured. Hydrostatic piezoelectric coefficient,  $d_h$ , and hydrophone figure of merit,  $d_h g_h$  were determined on these samples.

### EXPERIMENTAL PROCEDURE

Ceramics were prepared using the conventional mixed-oxide method. The milled powders were calcined at  $800^\circ\text{C}$  for one hour and then re-milled. Pellets were then pressed and sintered at  $1100^\circ\text{C}$  for two hours in air. After polishing, fired-on silver-paste electrodes were applied to the ceramic samples.

The dielectric constant and loss were measured using a computer-controlled multifrequency LCR meter (HP 4174A, Hewlett-Packard, Inc.). The temperature dependence of the dielectric constant and loss was also measured using a liquid nitrogen fed furnace with a working range of  $-150^\circ\text{C}$  to  $500^\circ\text{C}$ . Dielectric hysteresis measurements were made using a modified Sawyer-Tower circuit.

Piezoelectric measurements were made on samples poled at  $42\text{ kV/cm}$  while cooling from  $100^\circ\text{C}$  to room temperature in a silicone oil bath. After aging for 24 hours,  $d_{33}$  was measured using a Berlincourt  $d_{33}$  meter. The rest of the piezoelectric and elastic constants were determined using the fundamental resonance and first overtone frequencies, as described in the IEEE standards on piezoelectricity.<sup>6</sup> Hydrostatic piezoelectric measurements were made using a hydraulic pump and pressure vessel. An actuator within the pressure vessel was used to apply a small dynamic hydrostatic pressure at a frequency of 30 Hz. The voltages produced by both the test specimen and a standard (PZT-5A) were measured with a spectrum analyzer. These voltages were then used to calculate the value of  $d_h$ .

The temperature dependence of the piezoelectric coefficients was evaluated using an impedance analyzer (HP-4194A, Hewlett-Packard, Inc.) and a nitrogen-fed furnace (DD-2300, Delta Design, Inc.). The same method previously mentioned was

used to calculate these coefficients between  $-150^\circ\text{C}$  and  $100^\circ\text{C}$ . After cycling through the temperature runs,  $d_{33}$  was re-measured.

### RESULTS AND DISCUSSION

Figure 1 shows the temperature dependence of the dielectric constant for the two compositions. The room temperature dielectric constant (measured at 1 kHz) is 860 and the dissipation factor 0.047 for BPNT-50 the values of 1289 and 0.084 are measured respectively for BPNT-40. At the transition temperature for BPNT-50,  $\sim 375^\circ\text{C}$ , the dielectric constant value of 30500 is measured as shown in the figure. Another weak anomaly can be seen near  $-25^\circ\text{C}$  in this composition. The transition temperature for BPNT-40 occurs at  $\sim 340^\circ\text{C}$  and corresponds to a maximum dielectric constant of 17000. The second, or lower temperature, anomaly for this composition occurs at the relatively higher temperature  $\sim 230^\circ\text{C}$ .

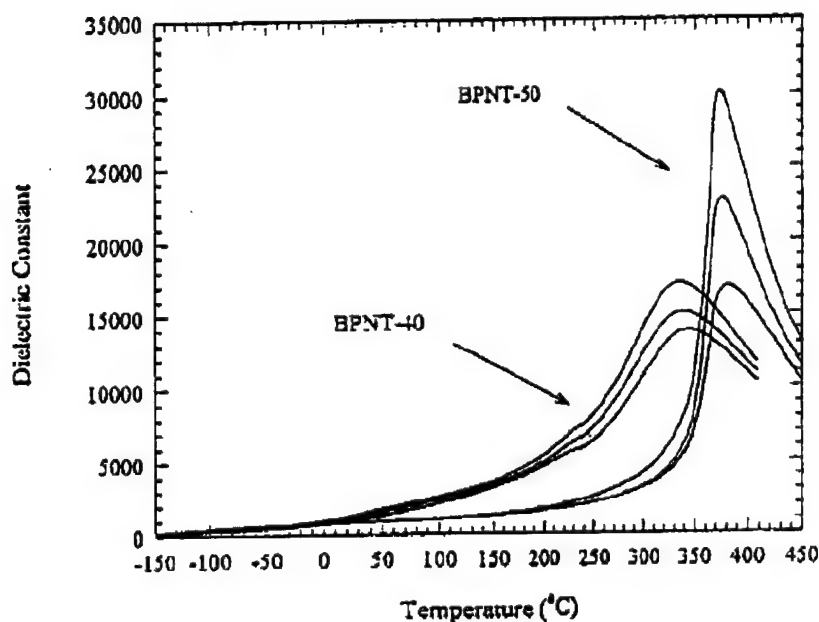


Figure 1. Variation of the dielectric constant with temperature for BPNT-40 and BPNT-50 ceramics measured at 1, 10, and 100 kHz.

Well-defined dielectric hysteresis loops are observed at room temperature for these compositions (figure 2). The saturation and remanent polarization values are on the order of  $50 \mu\text{C}/\text{cm}^2$  and  $37 \mu\text{C}/\text{cm}^2$ , respectively and are in the same range for both BPNT-40 and BPNT-50, in spite of the fact that the magnitudes of the coercive fields for these compositions are quite different. The composition on the rhombohedral side of the morphotropic phase boundary (BPNT-40) gives a typical value for the coercive field,  $\sim 26 \text{ kV}/\text{cm}$ , nearly half the value obtained for the composition on tetragonal side, (BPNT-50).

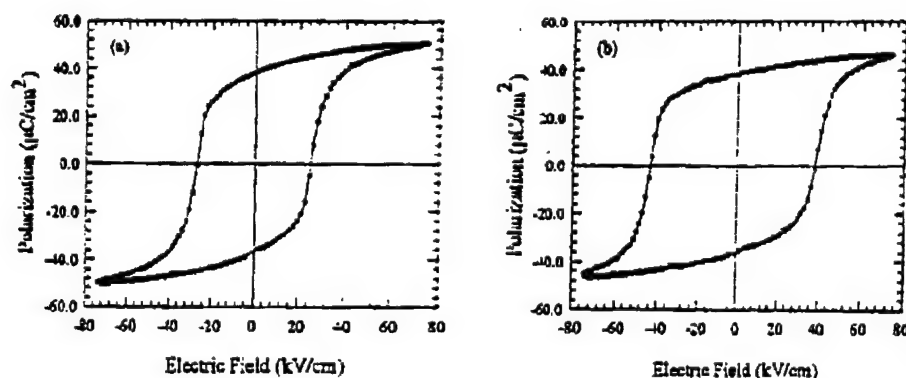


Figure 2. Dielectric hysteresis loops for: (a) BPNT-40 and (b) BPNT-50 ceramics.

Samples (of both compositions) were poled with a field of  $42 \text{ kV}/\text{cm}$  at  $100^\circ\text{C}$ . After allowing the samples to age for 24 hours, the measured  $d_{33}$  was in the range of  $250 \text{ pC}/\text{N}$  for BPNT-40 and  $105 \text{ pC}/\text{N}$  for BPNT-50. Resonance measurements at room temperature yield the coupling coefficients,  $k_p$ ,  $k_{31}$ , and  $k_t$  of: 32.5 %, 19.7 %, and 57.1 % for BPNT-40 and 20.1 %, 12.1 %, and 46.6 % for BPNT-50. The piezoelectric coefficient,  $d_{31}$ , is of the order  $-67 \text{ pC}/\text{N}$  and  $-35 \text{ pC}/\text{N}$  for BPNT-40 and BPNT-50, respectively.

The large anisotropy between  $d_{33}$  and  $d_{31}$  makes these compositions attractive for hydrophone applications. The hydrostatic piezoelectric coefficient for the poled ceramics was calculated using the relationship:  $d_h = d_{33} + 2d_{31}$ . High  $d_h$  values on the order of  $116 \text{ pC}/\text{N}$  were calculated for BPNT-40. Direct measurements of  $d_h$  were undertaken and the results show high  $d_h$  values of  $111 \text{ pC}/\text{N}$  for BPNT-40 and a

moderate  $d_h$  of 34 pC/N for BPNT-50. The hydrophone figure of merit,<sup>7</sup>  $d_h g_h$ , (as calculated from the measured  $d_h$  and  $g_h$ ) gives the values of  $1055 \times 10^{-15} \text{ m}^2/\text{N}$  for BPNT-40 and  $150 \times 10^{-15} \text{ m}^2/\text{N}$  for BPNT-50. For composites, much higher values of  $d_h g_h$  have been reported<sup>7</sup> but for a monolithic compound these values of  $d_h$  and  $d_h g_h$  are very attractive. The  $d_h g_h$  value for BPNT-40 compares well with  $\text{PbTiO}_3$  ( $d_h = 48 \text{ pC/N}$  and  $d_h g_h = 1248 \times 10^{-15} \text{ m}^2/\text{N}$ ) and is significantly larger than the value reported for PZT-5 ( $d_h = 21 \text{ pC/N}$  and  $d_h g_h = 42 \times 10^{-15} \text{ m}^2/\text{N}$ ).<sup>6</sup>

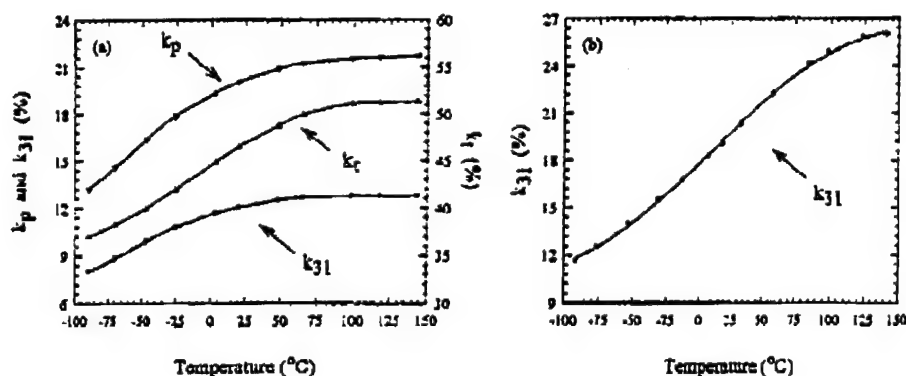


Figure 3. Variation of the coupling coefficients, ( $k_p$ ,  $k_{31}$ , and  $k_t$ ) with temperature for: (a) BPNT-40 and (b) BPNT-50 ceramics.

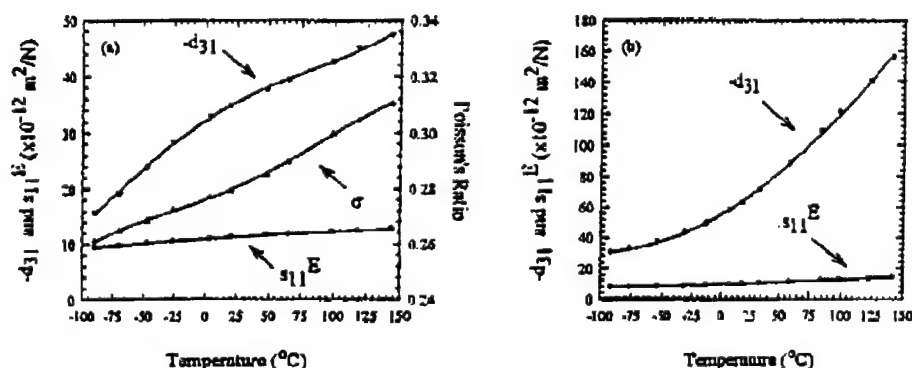


Figure 4. Variation of  $d_{31}$ ,  $s_{11}^E$ , and Poisson's ratio with temperature for: (a) BPNT-40 and (b) BPNT-50 ceramics.

The temperature dependence of various piezoelectric characteristics of BPNT-50 is shown in figures 3(a), 4(a), and 5(a). All of the property coefficients increase with temperature, with the exception of the mechanical quality factor,  $Q_m$ . All of the plots show some change in slope near  $-25^\circ\text{C}$ . This could probably be due to a slight curvature in the morphotropic phase boundary (which is located at  $x = 0.445$ ). During heating cycles the three coupling factors,  $k_p$ ,  $k_{31}$ , and  $k_t$ , attain nearly constant values (21.7 %, 12.8 %, and 51.3 %, respectively) at  $-125^\circ\text{C}$ . The elastic compliance  $s_{11}^E$  is less dependent on temperature and reaches a maximum value of  $12.71 \times 10^{-12} \text{ m}^2/\text{N}$  at  $150^\circ\text{C}$ , the upper temperature at which the measurements were made. The piezoelectric constant,  $d_{31}$ , approaches  $-47.6 \text{ pC/N}$  at  $150^\circ\text{C}$ .

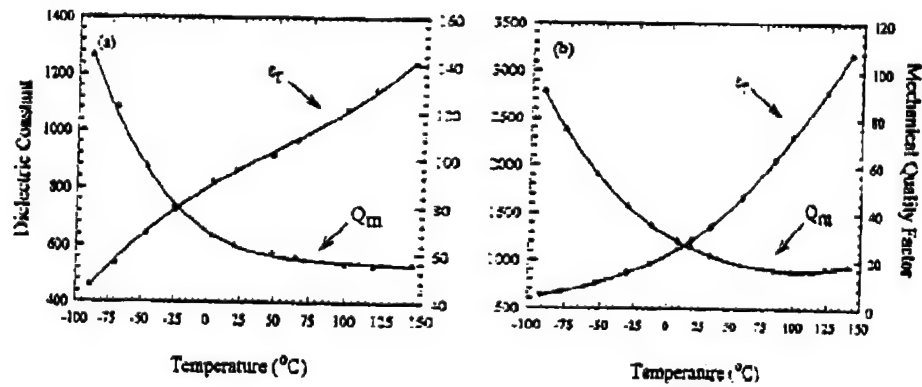


Figure 5. Variation of the dielectric constant and mechanical quality factor with temperature for: (a) BPNT-40 and (b) BPNT-50 ceramics.

The temperature dependence of the piezoelectric coefficients for BPNT-40 is shown in figures 3(b), 4(b) and 5(b). Unlike the case of BPNT-50, the effect of the morphotropic phase boundary cannot be detected, as the temperature of the second dielectric anomaly shifts from  $25^\circ\text{C}$  to  $230^\circ\text{C}$  in this composition. The coefficients  $k_{31}$ ,  $d_{31}$  and  $s_{11}^E$  and the dielectric constant all increase with temperature to maximum values of:  $k_{31} = 25.8 \%$ ,  $d_{31} = 156.6 \text{ pC/N}$ ,  $s_{11}^E = 14.2 \times 10^{-12} \text{ m}^2/\text{N}$ , and  $\epsilon_r = 3179$ . The mechanical quality factor,  $Q_m$ , decreases to a value of 18. After the temperature cycling, between  $-100^\circ\text{C}$  and  $150^\circ\text{C}$ , the room temperature piezoelectric coefficients return to their original values.

Table 1. Property coefficients for BPNT-40 and BPNT-50 ceramics.

$\text{Bi}(\text{NiTi})_{0.5}\text{O}_3$ / $\text{PbTiO}_3$	(40/60)	(50/50)
<b>Dielectric:</b>		
K at 1 kHz	1289	856
D at 1 kHz (%)	8.40	4.70
<b>Transition temperatures:</b>		
$T_c$ ( $^{\circ}\text{C}$ )	340	375
$T_c'$ ( $^{\circ}\text{C}$ )	230	-25
<b>Dielectric Hysteresis:</b>		
$P_r$ ( $\mu\text{C}/\text{cm}^2$ )	37.86	37.17
$E_s$ (kV/cm)	25.75	41.14
$P_{\text{max}}$ ( $\mu\text{C}/\text{cm}^2$ )	50.35	46.73
<b>Coupling factors:</b>		
$k_p$ (%)	32.50	20.08
$k_{31}$ (%)	19.68	12.05
$k_t$ (%)	57.05	46.55
<b>Piezoelectric constants:</b>		
$d_{33}$ (pC/N)	250	105
$d_{31}$ (pC/N)	-67	-35
$d_h$ (pC/N) (calc.)	116	35
$d_h$ (pC/N) (meas.)	111	34
$d_{hg}$ ( $\times 10^{-12}$ m <sup>2</sup> /N)	1055	150
<b>Frequency constants:</b>		
$N_p$ (Hz m)	2526	2351
$N_t$ (Hz m)	2077	1924
<b>Elastic compliance:</b>		
$s_{11}^E$ ( $\times 10^{-12}$ m <sup>2</sup> /N)	10.18	11.34
<b>Mechanical quality factor:</b>		
$Q_m$	24	64
<b>Poisson's ratio:</b>		
$\sigma$	0.2669	0.2796

### CONCLUSIONS

Table 1 summarizes all the property coefficients measured on the Mn doped BPNT-40 and BPNT-50 compositions. The high transition temperatures (400°C) and large remanent polarizations (37  $\mu\text{C}/\text{cm}^2$ ), look promising for high temperature piezoelectric applications. BPNT ceramics have also shown a high mechanical strength and a nominal temperature dependence in the range of experimental measurement. Large and attractive  $d_{33} \sim 111$  pC/N and  $d_{31} \sim 1055 \times 10^{-12}$  m<sup>2</sup>/N in BPNT-40 are also promising for hydrostatic sensor applications. Further studies are underway to improve upon  $d_{33}$  values on these compositions.

### REFERENCES

1. T. Takenaka and M. Yamada, *Jpn. J. Appl. Phys.*, Vol. 32, pp. L928-L931 (1993).
2. T. Takenaka and M. Yamada, *Jpn. J. Appl. Phys.*, Vol. 32, pp. 4218-4222 (1993).
3. T. Takenaka, M. Yamada, and T. Okuda, *Ferroelectrics*, Vol. 154, pp. 259-264 (1994).
4. T. Okuda, M. Yamada, and T. Takenaka, *Jpn. J. Appl. Phys.*, Vol. 33, pp. 5356-5360 (1994).
5. A.S. Bhalla, et al., Office of Naval Research review meeting, September 1995, Naval Research Laboratory, Washington DC.
6. "IRE Standards on Piezoelectric Crystals: Measurement of Piezoelectric Ceramics", *Proceedings of the IRE*, Vol. 49, p 1161 (1961).
7. A.S. Bhalla and R.Y. Ting, *Sensors and Materials*, Vol. 4, pp. 181-185 (1988).



# **APPENDIX 12**

Electromechanical Properties of Lead Zirconate Titanate Piezoceramics  
Under the Influence of Mechanical Stresses

Q. M. Zhang and Jianzhong Zhao

Materials Research Laboratory and Department of Electrical Engineering  
The Pennsylvania State University, University Park, Pa 16802

Abstract:

In lead zirconate titanate (PZT) piezoceramics, external stresses can cause substantial changes in the piezoelectric coefficient, dielectric constant, and elastic compliance due to nonlinear effects and stress depoling effect. In both soft and hard PZT piezoceramics, the aging can produce memory effect which will facilitate the recovery of the poled state in the ceramics from momentary electric or stress depoling. In hard PZT ceramics, the local defect fields built up during the aging process can stabilize the ceramic against external stress depoling which results in a marked increase in the piezoelectric coefficient and electromechanical coupling factor in the ceramic under the stress. While soft PZT ceramics can be easily stress depoled (losing piezoelectricity), a DC bias electric field, parallel to the original poling direction, can be employed to maintain the ceramic poling state so that the ceramic can be used to high stresses without depoling.

## I. Introduction

Piezoelectric ceramic, especially lead zirconate titanate ceramics (PZT), is widely used in electromechanical actuators, sensors, and transducers.<sup>1,2</sup> In these applications, piezoceramics are often subject to high mechanical stress. For instance, in high power underwater transducers, a high compressive stress is used to prestress the piezoceramic so that even at high electric driving fields, the ceramic is still at compressive states. Since ceramics inherently have a much higher mechanical strength to compressive stresses compared with extensive stresses, prestress can improve the reliability of a ceramic transducer or actuator significantly.<sup>1</sup> Due to nonlinear effects, one of the direct consequences of the high mechanical stress is the change of material properties from their stress free values.<sup>3-5</sup> In addition, the piezoelectric state in PZT ceramics is a result of poling of the ceramic. When a high mechanical stress is applied to the ceramic, it will reorient the polarization directions at each grain and may cause depoling of the piezoceramic.<sup>6,7</sup> This will certainly impose a limit on the maximum stress level which can be applied to a piezoceramic. Therefore, in order to properly utilize these piezoceramics in various actuator and transducer applications the nonlinear behavior under stress and limiting stress field should be studied in these ceramics.

In studying the effect of mechanical stresses on the responses of PZT piezoceramics, it is also important to realize that aging and deaging processes may play a significant role in modifying the material properties.<sup>8,9</sup> Aging in PZT ceramics is a process of slow evolution of the material properties with time after it is forced to a new state due to poling, large change of temperature, or subject to a high mechanical stress. For instance, after the poling, there exist mechanical stresses and charge imbalance at grain boundaries due to the redirection of the polarization at each domain to be close to the poling direction in the poling process. A slow reorientation of domains after the poling will reduce the mechanical stress at grain boundaries and

this plus drafting of space charges will compensate for the charge imbalance (to minimize the elastic and electric free energy in the ceramics).<sup>8,10</sup> Correspondingly, there is a reduction of the piezoelectric, dielectric, and elastic compliance due to the stabilization of the domain configuration through the aging, a well known phenomenon which occurs in both soft and hard PZT ceramics. In addition, the commercial PZT piezoceramic is either acceptor (such as Fe, Co, Mn, Cr, etc.) or donor (such as La, Nb, Sb, etc.) doped to improve the material performance. The dopants will induce either oxygen or lead vacancies in the lattice, forming mobile or immobile charged defects such as dipoles as well as local stress fields.<sup>2,11</sup> The mobile charged defects will align themselves to the polar direction of the domain they reside to build local fields which in turn stabilize a domain configuration to form so called hard PZT. While immobile defects cause frustration in the domains to form soft PZT.<sup>7,11</sup> Hence, in hard PZT ceramics, there is a second aging process associated with the reorientation of the mobile charged defects. If an aged PZT ceramic is forced to change to another state, a new domain configuration will form which may not be compatible with the established grain boundary conditions and local defect fields (in hard PZT). Correspondingly, the material is in a metastable state, yielding higher dielectric constant, piezoelectric coefficients, and elastic compliance.

In this paper, we report the results on the effect of uniaxial compressive stress, applied parallel to the initial poling direction, on the piezoelectric coefficient, dielectric constant, and elastic compliance of PZT piezoceramics. For soft PZT ceramics, the effect of limiting stress level on the piezoelectric coefficients and the DC electric bias field to stabilize the polarization against the stress depoling were also evaluated. For hard PZT ceramics, the aging of the piezoelectric coefficient under a constant stress was measured. In addition, we also compared the polarization hysteresis loops of PZT ceramics investigated here in both aged and fresh (deaged) specimens to quantify the effect of aging on these ceramics.

## II. Experimental

The PZT ceramic samples selected for the study are PZT-5H, PZT-5A, PZT-4, and PZT-8 purchased from Morgan Matroc, Inc.<sup>12</sup> PZT-5H and PZT-5A are donor doped (La in PZT-5H and Nb in PZT-5A). PZT-4 and PZT-8 are acceptor doped (Cr in PZT-4 and Fe and Mn in PZT-8). PZT-5H and PZT-5A are soft type PZT which have high piezoelectric, dielectric, and elastic compliance. While PZT-4 and PZT-8 are hard type PZT which have relatively low piezoelectric, dielectric, and elastic compliance. For the convenience of the presentation, the relevant parameters for these materials (aged) at stress free conditions are listed in Table I.<sup>12</sup> Apparently, the responses of the materials evolve from the soft to the hard following the sequence of PZT-5H, PZT-5A, PZT-4, and PZT-8.

For a piezoelectric ceramic material, the relevant parameters are defined by the constitutive equations:<sup>13</sup>

$$D_i = \epsilon_{ij}^T E_j + d_{im}^d T_m \quad (1a)$$

$$S_k = d_{jk}^c E_j + s_{km}^E T_m \quad (1b)$$

where  $D_i$  is the electric displacement.  $E_j$  is the applied electric field,  $S_k$  is the strain component,

and  $T_m$  is the stress component ( $i, j = 1 - 3$ , and  $m, k = 1 - 6$ ). The proportional coefficients  $\epsilon_{ij}^T$ ,

$d_{im}^d$ ,  $d_{jk}^c$ , and  $s_{km}^E$  are the dielectric permittivity, the piezoelectric coefficients of the direct and

converse effects, and the elastic compliance, respectively. In PZT piezoceramics, it has been

shown that the direct and converse piezoelectric coefficients are equal to each other approximately

and therefore, they will not be distinguished here.<sup>7</sup> As mentioned in the introduction, these

parameters will change with applied mechanical stress which will be investigated.

The experimental set-up which provides required uniaxial stress has been described in another publication.<sup>7</sup> The dimensions of the test specimen in the mechanical stress experiment were  $4.8 \times 4.8 \times 5 \text{ mm}^3$ . In order to satisfy the requirement that the length of the sample should be at least three times longer than the lateral dimension to ensure a uniaxial stress, three ceramic samples were stacked together to form a test sample assembly of dimensions  $4.8 \times 4.8 \times 15 \text{ mm}^3$ . To further reduce the end clamping effect in the lateral directions, the data was taken from the sample at the middle when all three sections were subjected to the same driving conditions. For example, for  $d_{33}$  and  $d_{31}$  measurement, the same voltage was applied to the three sections and only the strain response at the middle section was taken.

The polarization hysteresis loop was measured by a standard Sawyer-Tower circuit at 10 Hz. The dielectric constant was measured using a multi-frequency LCR meter (HP model 4192A). The strain response of the samples was measured by a strain gauge (KYOWA KFR-02-120-C1-11). To improve the signal to noise ratio the voltage signal from the strain gauge amplifier was measured by a Lock-in amplifier.

For the dielectric constant and  $d_{ij}$  measurement, it was found that the results did not crucially depend on the alignment of the specimen. However, for  $s_{ij}^E$  measurement, large error may occur even for a very small misalignment of the sample (the stress was not uniformly applied to the test sample) or if the sample was not prepared properly so that the two faces which were subjected to the stress were not exactly parallel to each other. A special sample holder was designed to ensure a proper alignment of the test samples and two strain gauges were attached to the opposite faces of the specimen to monitor the strain responses.

The results on the dielectric constant, piezoelectric coefficient, and elastic compliance were acquired at room temperature and a frequency of 10 Hz. It is expected that upon change of the stress level, there is a finite time period for the material to reach a new equilibrium state (aging). It

was found that most of the changes of the data occurred during the first 5 minutes after the change of the DC stress level. We also examined several samples under a longer waiting period and found that there was not marked change in the weak signal properties between the data taken after 10 minutes and after one day. This relatively fast aging is associated with the change due to the grain boundary stress and charge imbalance and occurs in both soft and hard PZT ceramics. For hard PZT, there is an additional aging process which takes a much longer time associated with the reorientation of local defect dipoles (several weeks or longer). Hence, in order to carry out a meaningful measurement within a reasonable time frame, all the data were taken 10-15 minutes after the change of the stress level. The results reported here on the dielectric constant, piezoelectric coefficient, and elastic compliance were taken from the first stress cycle.

### III. Results and Discussion

#### (3.1) The Polarization Hysteresis Loops in Soft and Hard PZT Ceramics

To a large extent, the properties of PZT piezoceramics are determined by the state of ceramic after poling. Aging results in a change in electromechanical properties of PZT ceramics after poling.<sup>8</sup> Thus, poled states of aged and fresh (deaged or rejuvenated) specimens were first investigated in terms of their polarization hysteresis loops.

Figure 1 presents the polarization hysteresis loops for aged PZT ceramics recorded from the first few cycles. These are the samples obtained from the manufacturer and are aged for more than 6 months. One interesting feature common to all the specimens, both soft and hard PZT, is that the switching field back to the original poling direction in aged samples after field depoling is zero, indicating a memory effect in these ceramics. For soft PZT ceramics, it took several hundred cycles to remove this memory effect, while for hard PZT, it took many more cycles due to the long aging time.<sup>14</sup> We did not pursue this beyond a thousand cycles for hard PZT and after that the ceramic remained in a strongly internal biased state. In addition, the depoling field for these aged hard PZT ceramics is much higher than that of soft PZT, a manifestation of the

existence of local bias fields to stabilize the domain orientation against external fields to depole the ceramic.

In contrast, the polarization hysteresis loops for the same PZT ceramics but deaged exhibit a symmetric loop as shown in figure 2. The deaged (fresh) samples were prepared by heating the aged PZT ceramic to above 400 °C, which is above the Curie point of all the ceramics, for more than 1 day. It is also interesting to note that as shown in table II, the coercive field  $E_c$  of hard PZT in these deaged specimens is not higher than that in soft PZT.

Compared with the data in figures 1 and 2, the depoling field in aged soft PZT ceramics is nearly equal to the coercive field in deaged samples which results in a much narrower hysteresis loop in aged samples compared with deaged samples. While for aged hard PZT ceramics, the depoling field is not well defined and there exists no sharp switching field, indicating a broad distribution of the local defect field strength.

These observations indicate that in both soft and hard PZT ceramics, the space charge accumulated at the grain boundaries will facilitate the recovering of a depoled ceramic to nearly the original poled state. Therefore, aged PZT piezoceramic can be depoled electrically or mechanically momentarily without losing substantially the polarization and piezoelectric activity. The observed "hard" PZT behavior in aged samples is mainly due to the alignment of local charged defects within grains which apparently have a much stronger effect on the material responses than that caused by the space charge accumulated and stress compatibility established at the grain boundaries through the aging.

### (3.2) The Compressive Stress $T_3$ on the Electromechanical Properties of Soft PZT Ceramics

Shown in figures 3 and 4 are the stress dependence of  $d_{33}$  and  $d_{31}$ ,  $K_{33}$  (dielectric constant =  $\epsilon_{33}^T / \epsilon_0$ , where  $\epsilon_0$  is the vacuum permittivity), and  $s_{33}^E$  and  $s_{31}^E$  for PZT-5H and PZT-5A (the data were acquired when the stress was maintained). A one stress cycle (from 0 to 150 MPa and back to 0) took about 8 to 10 hours. Apparently, for soft PZT there is a large drop of the piezoelectric



coefficients with stress at a stress level above about 50 MPa. As the field is reduced to zero after reaching 150 MPa, the piezoelectric coefficients become much smaller than those in the originally aged samples, indicating a partial depoling in these ceramics.<sup>6</sup> Similarly, in these partially depoled samples, the elastic compliance also becomes smaller, while the dielectric constant does not show much change.

The experimental results reveal that soft PZT ceramics can be easily depoled by the compressive mechanical stress  $T_3$ . However, soft PZT ceramics are important piezoelectric materials for actuator and transducer applications. Therefore, the question is what is the limiting stress level which can be applied to a soft PZT without causing a substantial depoling of the ceramic. To answer this question, the piezoelectric coefficient  $d_{33}$  was measured on PZT-5H and PZT-5A at stress free state after the specimens were subject to a  $T_3$  (peak stress, denoted as  $T_{3M}$ ) stress for 10 minutes. Data presented in figure 5 are  $d_{33}$  thus obtained (after the stress was removed) versus the applied maximum stress  $T_{3M}$ . To show the depoling effect due to the stress, the data is presented in the reduced unit, i.e.,  $d_{33}(\text{after the stress } T_{3M})/d_{33}(\text{sample from manufacturer})$ . In this experiment, each data point was obtained from a specimen having not been subjected to a stress prior to the measurement to insure the same initial condition for each data point. To quantify the result, the stress  $T_{3M}$  which results in a reduction of  $d_{33}$  by 10% is defined as the limiting stress. For PZT-5H,  $T_{3M}$  is at about 50 MPa, and for PZT-5A, it is higher and is near 60 MPa. In addition, the data also reveals that for PZT-5A, it can retain more than 70% of  $d_{33}$  even after subjected to more than 100 MPa stress. This is consistent with the fact that PZT-5A has a higher coercive field than that of PZT-5H and hence, is more difficult to be stress depoled.

Although soft PZT can be easily stress depoled, these ceramics can be used to high stress levels without been depoled by applying a DC bias electric field. Shown in figure 6 is the change of  $d_{33}$  of PZT-5H with stress up to 150 MPa. The difference between the data in figure 6 and in figure 3 is that here a DC electric field of 5 kV/cm, which is parallel to the original poling direction, is applied to the ceramic. Apparently, after a 150 MPa stress cycle, the ceramic can still

retain 90% of the original piezoelectricity. Since the coercive field  $E_c$  for deaged PZT-5H ceramic is at 9 kV/cm, the result in figure 5 indicates that a field at below  $E_c$  can be used to stabilize a ceramic from the stress depoling. On the other hand, applying a field of 5 kV/cm in the direction opposite to the original poling direction results in a much smaller value of  $d_{33}$  after 150 MPa stress cycle. The results here are consistent with those in figure 1 where in aged soft PZT ceramics, there is a memory of the original poling direction and hence, a small electric field parallel to the original poling direction can re-pole the ceramic back to a high polarization level.

### (3.3) The Compressive Stress $T_3$ on the Electromechanical Properties of Hard PZT Ceramics

Shown in figures 7 and 8 are the stress dependence of  $d_{33}$  and  $d_{31}$ ,  $K_{33}$ , and  $s_{33}$  and  $s_{31}$  for PZT-4 and PZT-8. Quite different from soft PZT ceramics, hard PZTs exhibit a large increase of piezoelectric coefficients and dielectric constant with stress. For both PZT-4 and PZT-8, the piezoelectric coefficients reach more than 40% higher than those of the aged samples measured before the stress. After a stress cycle of 150 MPa, the piezoelectric coefficients and dielectric constant return to the zero stress state with higher values. For PZT-8, even after a stress cycle to 280 MPa, the ceramic can still retain a  $d_{33}$  equal to the value of the aged sample before stress. This large increase in the piezoelectric coefficients also results in an increase of the electromechanical coupling factor with stress as shown in figure 9. And apparently, a longitudinal electromechanical coupling factor  $k_{33}$  higher than 0.85 can be obtained in hard PZT which is far above the value even in soft PZT. This observation clearly raises an issue that there is a potential that by proper microstructure engineering, a high coupling factor may be reached in PZT piezoceramics.

Undoubtedly, the increase in the electromechanical responses in hard PZT ceramics is caused partially by the deaging effect. The high applied stress changes the domain orientation with respect to the local field built up by oxygen vacancies and dopants through the aging process which transforms the material towards soft PZT. However, under a stress of 100 MPa or more, as

been shown by Cao and Evans, there is a change in strain of more than 0.4% and loss of remanent polarization level of more than  $10 \mu\text{C}/\text{cm}^2$  in hard PZT ceramics.<sup>6</sup> Compared with the polarization hysteresis loops for hard PZT ceramics (figures 1 and 2), it is clear that the material at this stress level is substantially depoled through non-180° domain reorientation process. Clearly, the ceramic is deaged. But, the interesting issue here is that even at such a low polarization level, the ceramic can still exhibit such a high piezoelectric activity and coupling factor compared with the values obtained at fully poled state without stress. This certainly cannot be explained based on deaging alone. Since the response from the intrinsic contribution is electrostrictive, at such a low polarization level, its contribution to the piezoelectric activity is very small.<sup>15</sup> Therefore, the polarization response here should be mainly through non-180° domain wall motions which have a high electromechanical coupling factor and are not electrostrictive in nature (not depends on the poling level). That is, in these partially stress depoled hard PZT, the piezoelectric and dielectric responses are mainly through non-180° domain wall motions, resulting in a high piezoelectric coefficient and coupling factor. This behavior is also in sharp contrast with that observed in soft PZT where the depoling destroys the piezoelectric activity. The difference here is presumably caused by the local defect fields which are different in the two types of ceramics. Further more, as shown in figure 10, even after a long time aging, the piezoelectric coefficient  $d_{31}$  of PZT-8 under a 90 MPa stress is still far above the value obtained under the stress free condition taken before the application of stress, which is consistent with an early experimental result.<sup>3</sup> In viewing of these findings, the detailed functions of the local defect fields in both soft and hard PZT ceramics in partially stress depoled states should be further studied. And clearly, the large increase of the piezoelectric activity observed in hard PZT ceramics is more than a deaging effect.

In fact, an increase of the piezoelectric coefficients and coupling factor with  $T_r$  stress was also observed in soft PZT as shown in figures 3 and 4. Careful inspection of the figures reveals that at stress level before depoling occurs (50 MPa), there is a slight increase of piezoelectric coefficients

and coupling factor (becomes larger than 0.8). These results indicate that by moving the polarization direction of the domains locally away from the averaged poling direction, increased non-180° domain wall motions in PZT ceramics (under  $T_3$  stress) can result in an increase in piezoelectric activity and coupling factor. This observation may resemble the experimental results on  $\text{Pb}(\text{Zn}_{1/3}\text{Nb}_{2/3})\text{O}_3$ - $\text{PbTiO}_3$  relaxor single crystals where a high piezoelectric response and coupling factor were observed when the crystal was poled along [001] direction which is not the direction of the spontaneous polarization.<sup>16,17</sup>

#### (3.4) Load Curves for PZT Piezoceramics

The load curves for PZT-5H, a soft PZT, and PZT-8, a hard PZT were measured under different DC electric bias fields and the results are presented in figure 11. Several features are revealed from the figure. In PZT-5H, there is a large non-linearity in both the strain-DC applied electric field relationship and in the strain-stress relationship. In PZT-8, the non-linear effect is much smaller. These are consistent with the results of an early publication.<sup>5</sup> The compliance  $s_{33}^E$  measured here (under near DC condition) is more than twice of that measured at 10 Hz (from the load curves under a small DC field,  $1 \text{ kV/cm}$ ,  $s_{33}^E = \Delta S_3 / \Delta T_3$  is about  $40 \times 10^{-12} \text{ m}^2/\text{N}$  for PZT-5H and  $30 \times 10^{-12} \text{ m}^2/\text{N}$  for PZT-8), indicating a strong frequency dependence at very low frequency region. For hard PZT, for the DC bias fields studied, there is no large change of compliance with DC bias field. For PZT-5H, at low stress region (stress near zero), there is a slight increase of the compliance with DC electric bias field. On the other hand, the slope for the load curve under  $6 \text{ kV/cm}$  at near  $20 \text{ MPa}$  stress level becomes near half of that at low stress level (from  $47 \times 10^{-12}$  to  $23 \times 10^{-12} \text{ m}^2/\text{N}$ ). It is expected that DC bias field will stabilize the poling and smear out the stress depoling region, and hence DC bias fields will affect load curves, especially for soft PZT ceramics.

#### IV. Summary and Acknowledgement

The results presented here indicate:

(1) There is a large difference in the polarization hysteresis loops and other material properties in aged and fresh samples. In fresh samples, the coercive field for hard PZT may not be higher than those in soft PZT. In aged PZT ceramics, there is no well defined coercive field. For hard PZT ceramics, local fields stabilize the poling state against electric field and stress depoling. While there is a near zero coercive field in returning to the original poling direction of the hysteresis loop for both hard and soft PZT ceramics.

(2) There is a large change of the material properties with stress due to nonlinear effects and the stress depoling. The material properties at stress free state cannot reflect the properties under stress. Further more, it can also be inferred that the nonlinear effects due to stress alone, due to applied electric field alone, and due to combined stress and electric field, will produce quite different material responses.

(3) Soft PZT ceramics can be easily stress depoled and the limiting stress  $T_j$  for PZT-5H and PZT-5A is at about 50 MPa level. A DC electric field can be used to stabilize soft PZT to against the stress depoling. The DC bias field used to stabilize the polarization in an aged sample can be smaller than the coercive field measured from deaged samples.

(4) Compressive stress  $T_j$  can significantly increase the piezoelectric activity and coupling factor in hard PZT ceramics. This increase is not an effect of deaging alone, but rather involves a change of domain orientations with respect to the external field and applied stress and the coupling of the local polarization to the local defect fields.

The authors thank Dr. Z.-Y. Cheng for valuable discussions. This work was supported by the Office of Naval Research.

Table I. The properties of PZT piezoceramics under stress free condition

Material	PZT-5H	PZT-5A	PZT-4	PZT-8
$d_{33}$	593	374	296	225
$d_{31}$	-274	-171	-123	-97
$K_{33}$	3400	1700	1300	1000
$s_{33}$	20.7	18.8	15.5	13.9
$s_{13}$	-8.45	-7.22	-5.31	-4.6
$s_{11}$	16.5	16.4	12.3	11.1
$k_{33}$	0.75	0.7	0.7	0.64
$k_{31}$	0.39	0.34	0.33	0.3

(d: pC/N, s:  $10^{-12}$  m<sup>2</sup>/N)

Table II. Coercive field of thermally deaged PZT ceramics

Material	PZT-5H	PZT-5A	PZT-4	PZT-8
$E_c$ (kV/cm)	9	14	12	15

## References:

1. J. M. Herbert, "Ferroelectric Transducers and Sensors" (Gordon and Breach, NY 1982).
2. B. Jaffe, W. R. Cook, and H. Jaffe, "Piezoelectric Ceramics" (Academic Press, London and New York, 1971).
3. H. Krueger and D. Berlincourt, "Effects of high static stress on the piezoelectric properties of transducer materials," J. Acoust. Soc. Am., 33, pp. 1339-1344 (1961).
4. H. Krueger, "Stress sensitivity of piezoelectric ceramics: part 1. Sensitivity to compressive stress parallel to the polar axis," J. Acoust. Soc. Am., 42, pp. 636-646 (1967).
5. V. Mueller and Q. M. Zhang, "Shear response of lead zirconate titanate piezoceramics," J. Appl. Phys. 83, pp. 3754-3760 (1998).
6. H. Cao and A. Evans, "Nonlinear deformation of ferroelectric ceramics," J. Amerm. Soc. 76, pp. 890-896 (1993).
7. Q. M. Zhang, J. Zhao, K. Uchino, and J. Zheng, "Change of weak field properties of Pb(ZrTi)O<sub>3</sub> piezoceramics with compressive uniaxial stress and its links to the effect of dopants on the stability of the polarization in the materials," J. Mater. Res. 12, pp. 226-234 (1997).
8. W. A. schulze and K. Ogino, "Review of literature on aging of dielectric." Ferro. 87, pp. 361-377 (1988).
9. R. Y. Nishi, "Effects of one-dimensional pressure on the properties of several transducer ceramics," J. Acoust. Soc. Am., 40, pp. 486-495 (1966).
10. W. Wersing, "On the stabilization field of lead-titanate-zirconate ceramics doped with transition metal ions." Ferroelectrics, 12, pp. 143-145 (1976).
11. M. E. Lines and A. M. Glass, "Principles and Applications of Ferroelectrics and Related Materials" (Clarendon Press, Oxford, 1977).

12. PZT-5H, PZT-5A, PZT-4, and PZT-8 are the trade marks of Morgan Matroc, Inc. (Bedford, OH) for its PZT piezoceramics.
13. IEEE Standard on Piezoelectricity, ANSI/IEEE, Std 176 (1988).
14. M. Takahashi, "Space charge effect in lead zirconate titanate ceramics caused by the addition of impurities," Jpn. J. Appl. Phys. 9, pp. 1236-1246 (1970).
15. A. F. Devonshire, "Theory of ferroelectricity," Phil. Mag. 3, pp. 85-130 (1954).
16. S. E. Park and T. R. Shrout, "Ultrahigh strain and piezoelectric behavior in relaxor based ferroelectric single crystals," J. Appl. Phys. 82, pp. 1804-1811 (1997).
17. J. Kawata, K. Uchino, and S. Nomura, "Dielectric and piezoelectric properties of  $0.9\text{Pb}(\text{Zn}_{1/3}\text{Nb}_{2/3})\text{O}_3$ - $0.09\text{PbTiO}_3$  single crystals," Jpn. J. Appl. Phys., 21, pp. 1298-1302 (1982).



Figure captions:

Figure 1. The polarization hysteresis loops of aged PZT piezoceramics.

Figure 2. The polarization hysteresis loops of thermally deaged (fresh) PZT ceramics.

Figure 3. The dependence of the weak signal piezoelectric coefficients ( $d_{33}$  and  $d_{31}$ ), dielectric constant  $K_{33}$ , and elastic compliance ( $s_{33}$  and  $s_{13}$ ) of PZT-5H on the compressive uniaxial stress  $T_3$ . Solid and dashed lines are drawn to guide eyes.

Figure 4. The dependence of the weak signal piezoelectric coefficients ( $d_{33}$  and  $d_{31}$ ), dielectric constant  $K_{33}$ , and elastic compliance ( $s_{33}$  and  $s_{13}$ ) of PZT-5A on the compressive uniaxial stress  $T_3$ . Solid and dashed lines are drawn to guide eyes.

Figure 5. The piezoelectric coefficient  $d_{31}$  retained (compared with the initial value in aged sample) after the specimen is subjected to a  $T_3$  stress and then back to stress free state for PZT-5H. Solid and dashed lines are drawn to guide eyes.

Figure 6. The dependence of  $d_{31}$  on the compressive  $T_3$  stress while under a 5 kV/cm DC electric bias field which is parallel to the original poling direction for PZT-5H. Solid line is drawn to guide eyes.

Figure 7. The dependence of the weak signal piezoelectric coefficients ( $d_{33}$  and  $d_{31}$ ), dielectric constant  $K_{33}$ , and elastic compliance ( $s_{33}$  and  $s_{13}$ ) of PZT-4 on the compressive uniaxial stress  $T_3$ . Solid and dashed lines are drawn to guide eyes.

Figure 8. The dependence of the weak signal piezoelectric coefficients ( $d_{33}$  and  $d_{31}$ ), dielectric constant  $K_{33}$ , and elastic compliance ( $s_{33}$  and  $s_{13}$ ) of PZT-8 on the compressive uniaxial stress  $T_3$ . Solid and dashed lines are drawn to guide eyes.

Figure 9. The dependence of the longitudinal electromechanical coupling factor  $k_{33}$  on the compressive uniaxial stress  $T_3$  for PZT-4 and PZT-8 piezoceramics. Solid and dashed lines are drawn to guide eyes.

Figure 10. Aging of  $d_{31}$  of PZT-8 over one month time under a constant stress of 90 MPa.  $d_{31}$

aged after one month aging under stress is still higher than that under stress free condition. Dashed line is drawn to guide eyes.

Figure 11. Load curves of longitudinal strain versus  $T_c$  for PZT-5H and PZT-8 piezoceramics. The applied DC electric fields are indicated.

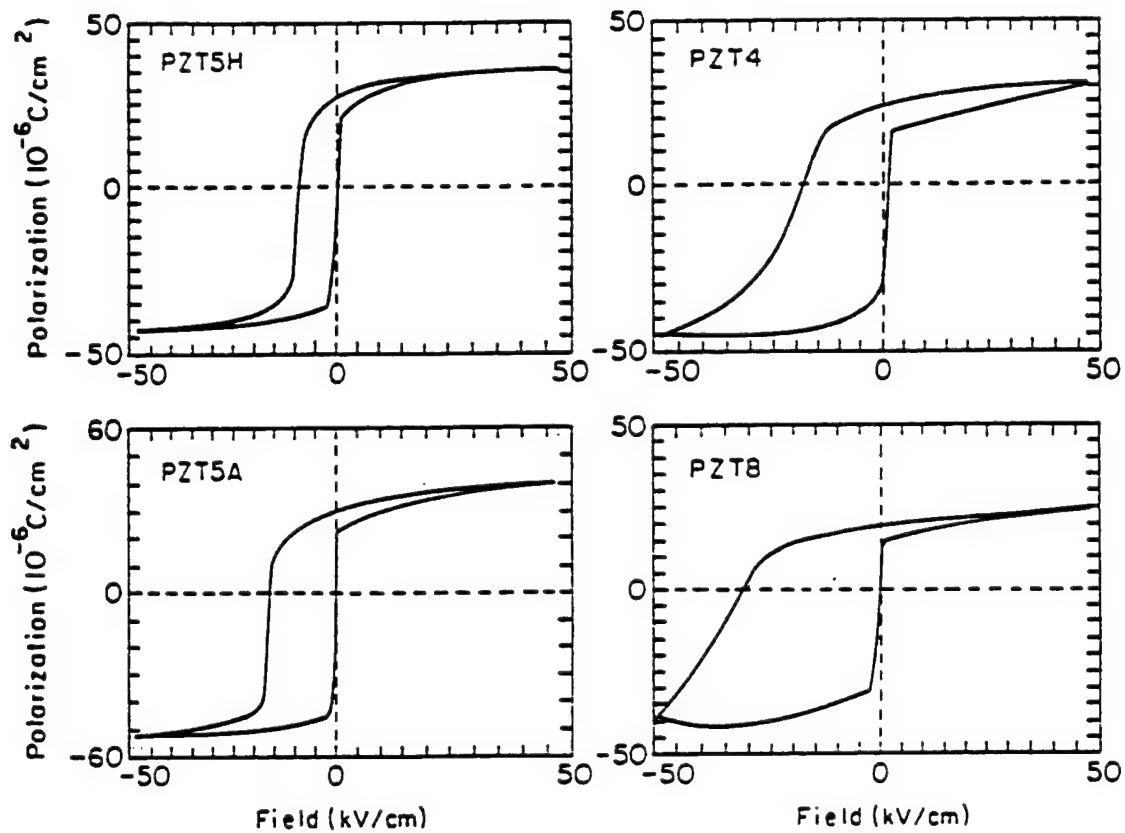


Fig. 1

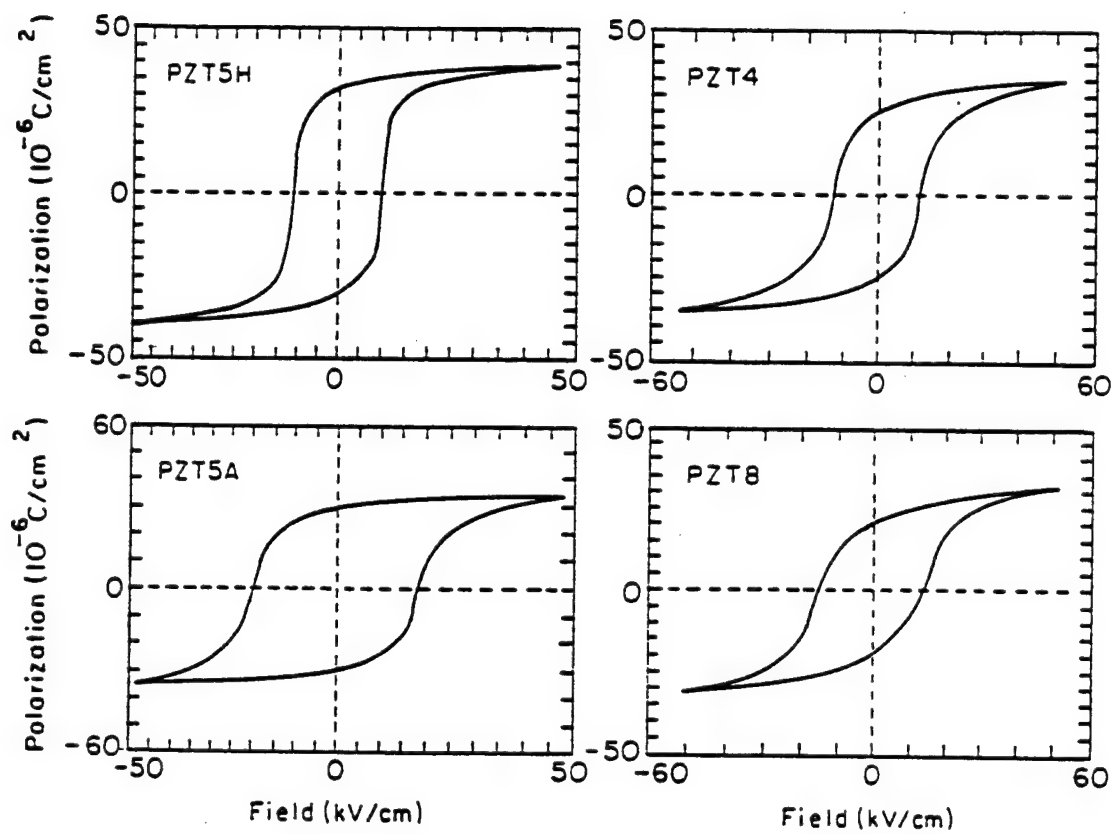


Fig.2

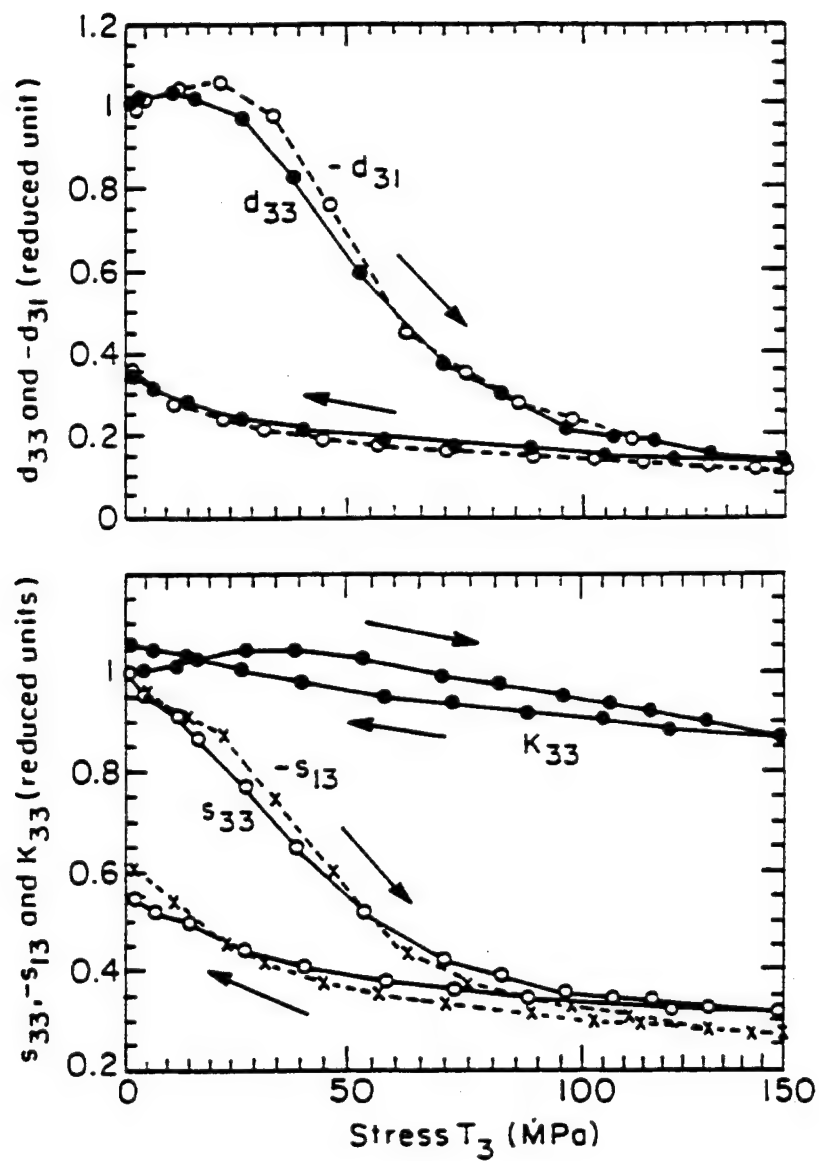


FIG. 3

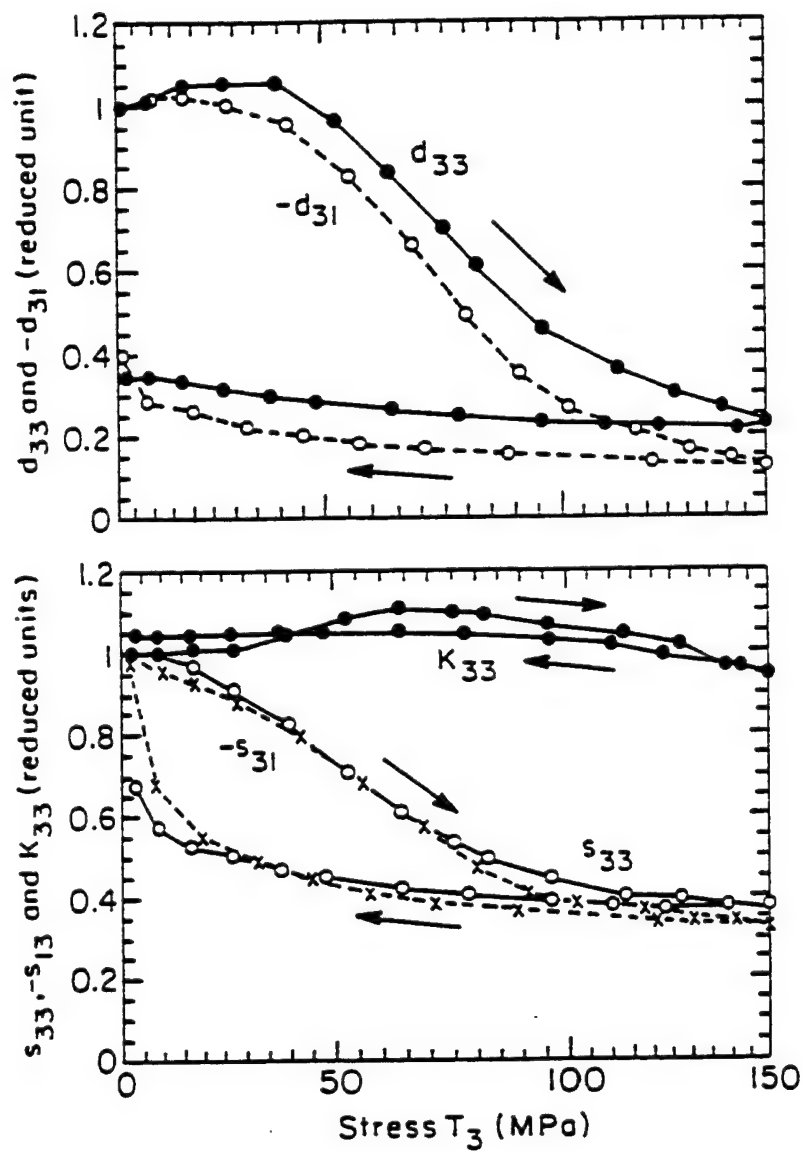


Fig.4

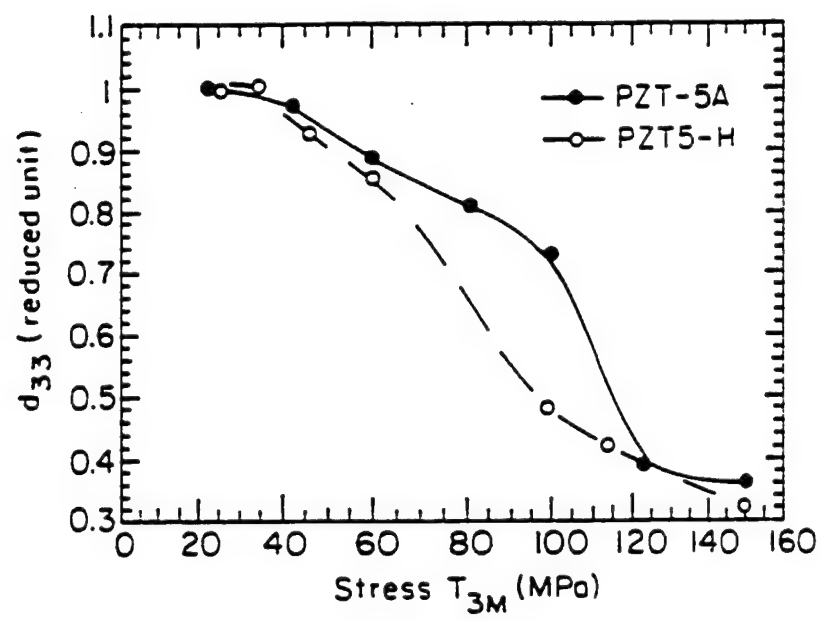


Fig. 5

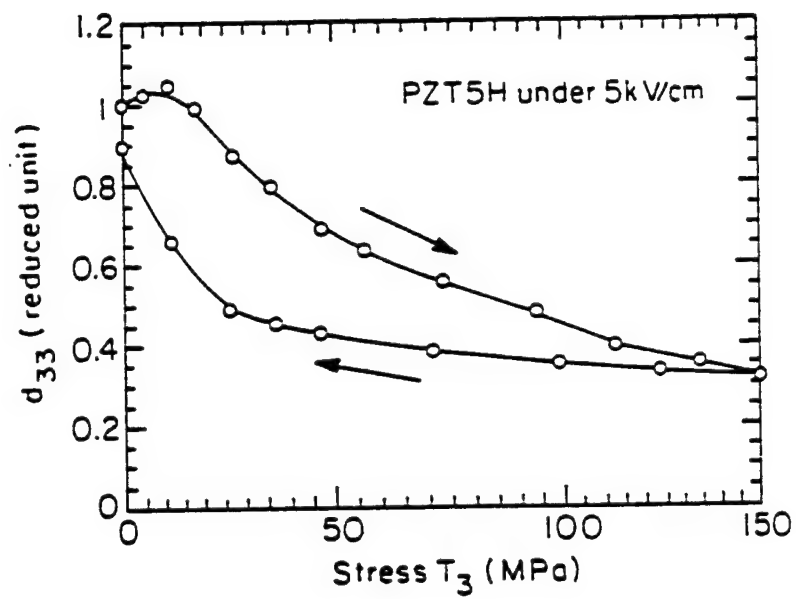


Fig. 6



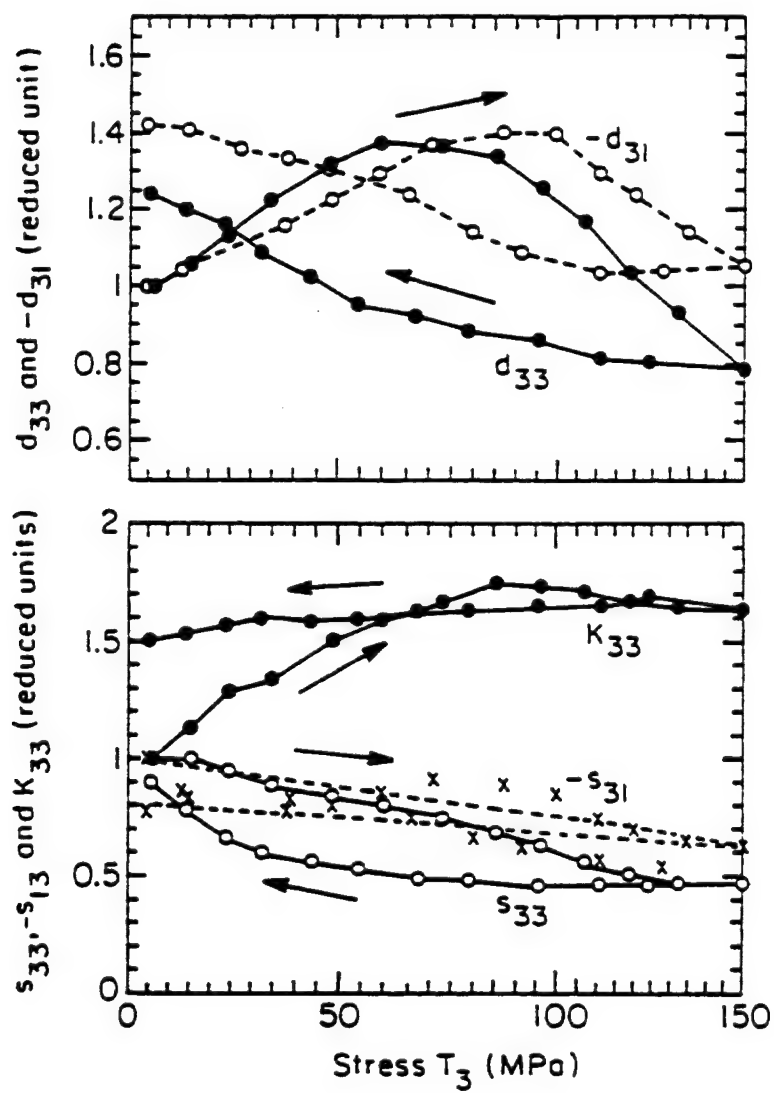


FIG. 7

Fig

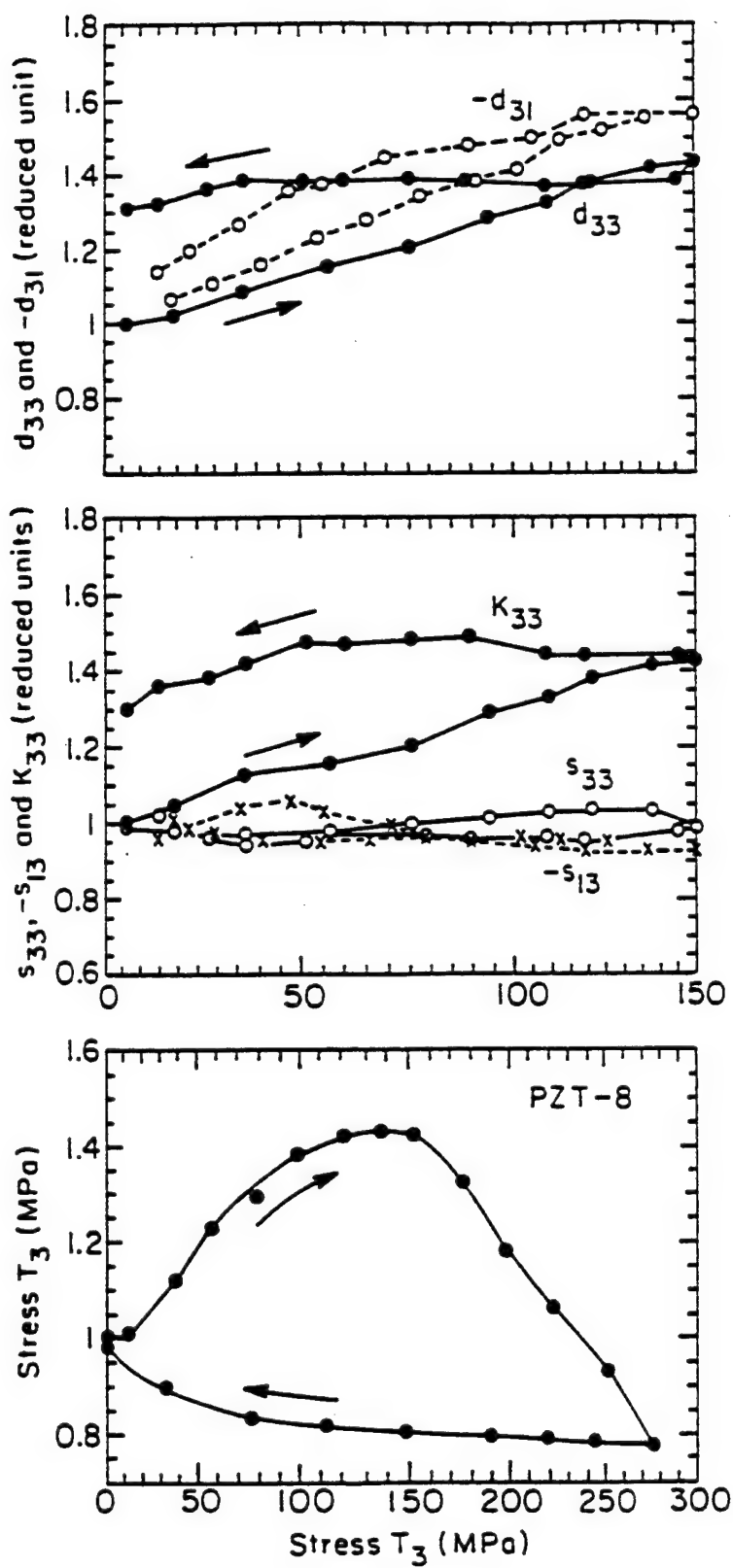


Fig. 8

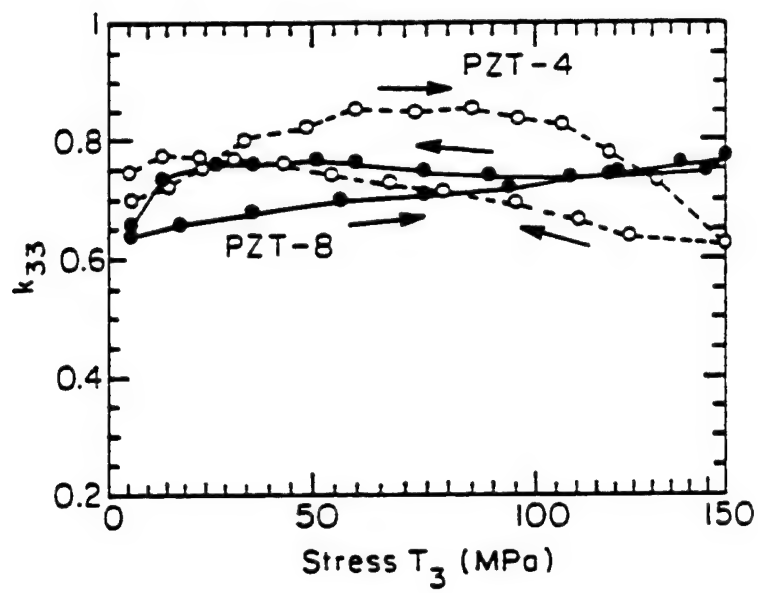


Fig. 9

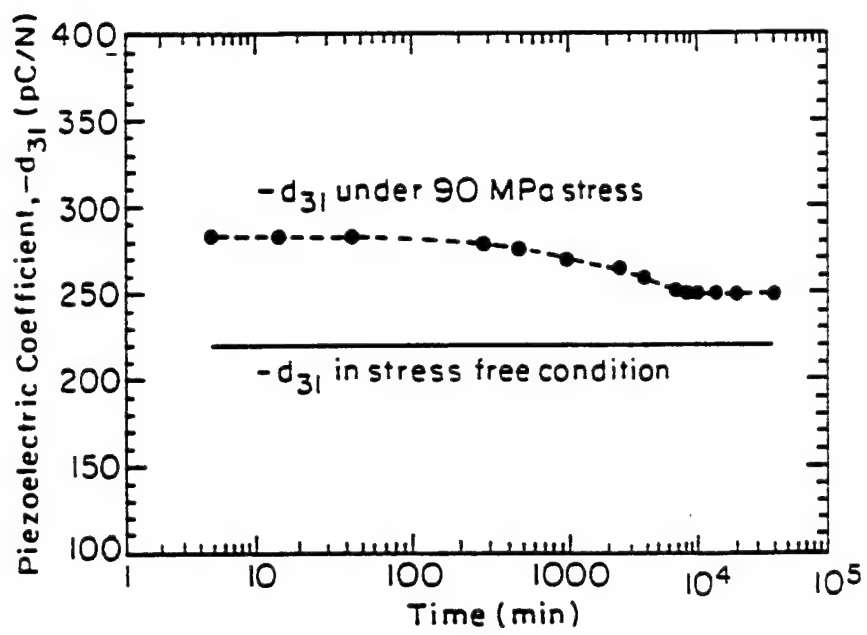


Fig. 10

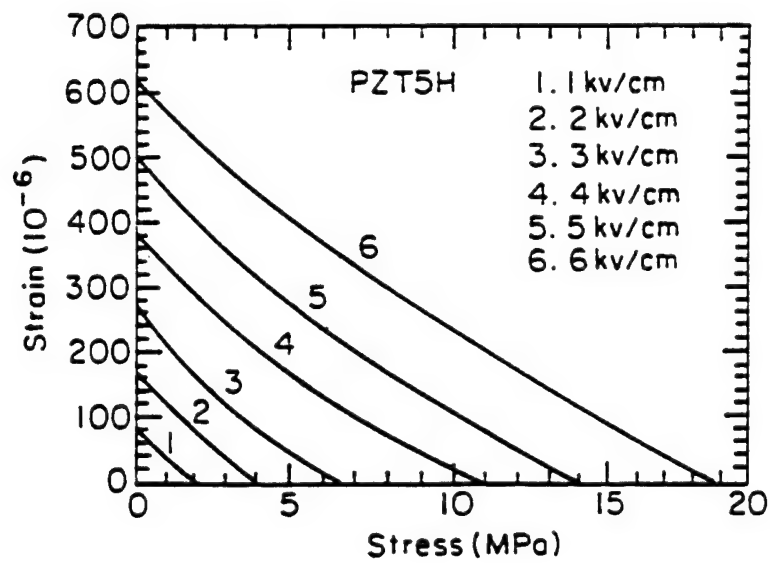
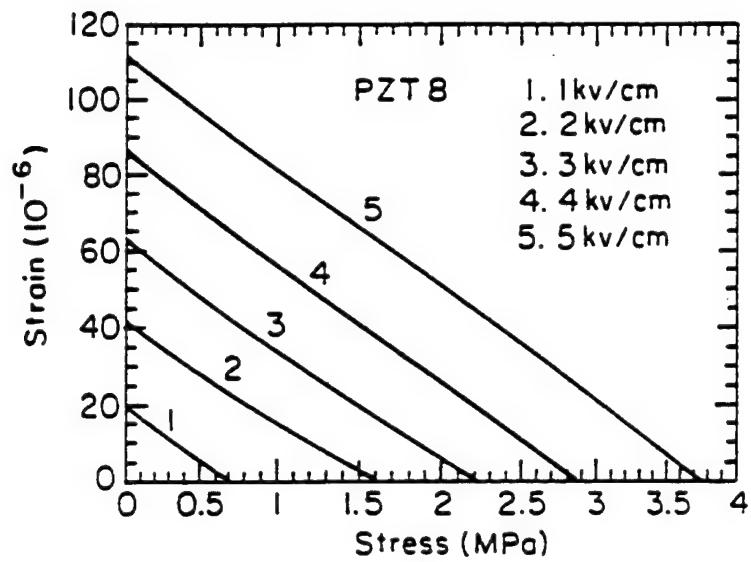


Fig. 11

# **APPENDIX 13**

# Behavior of soft piezoelectric ceramics under high sinusoidal electric fields

V. D. Kugel<sup>(a)</sup> and L. E. Cross

*The Materials Research Laboratory, The Pennsylvania State University, University Park, Pennsylvania 16802*

(Received 8 July 1997; accepted for publication 2 June 1998)

The behavior of piezoelectric, dielectric, and elastic characteristics of soft piezoelectric lead zirconate titanate (PZT) ceramics was investigated under sinusoidal electric field  $E$  applied along the poling direction and under mechanical stress-free conditions for a frequency range 10 Hz–10 kHz. Electrical displacement  $D_3$  along the poling direction, mechanical strain  $S_1$  in the direction perpendicular to the poling direction, and the resonant frequency  $\nu_r$  of electromechanically uncoupled bending vibrations of polarized plates were measured. Commercial ceramics PZT5H, 3203HD, and PK1550 with chemical composition near the morphotropic phase boundary were used in the study. It was found that the amplitude and phase of the first harmonic of the relative strain  $S_1^{(1)}/E_m$  and of the relative electrical displacement  $D_3^{(1)}/E_m$  increase similarly with increasing amplitude  $E_m$  of the electric field if the amplitude is less than coercive field. The corresponding increase in the square of the resonant frequency is more moderate. The dependencies are described well by linear functions except for low electric fields. The functions  $S_1^{(1)}/E_m$  and  $D_3^{(1)}/E_m$  demonstrate frequency dispersion as well. Relative amplitude of the second harmonic of the electrical displacement,  $D_3^{(2)}/D_3^{(1)}$ , which is polar, also increases almost linearly with increasing  $E_m$ . The relative third harmonic  $D_3^{(3)}/D_3^{(1)}$  demonstrates saturationlike behavior. By means of the electric pulse technique, it was found that irreversible changes in the remnant polarization take place even at electric fields much smaller than the coercive field. A mathematical model of a hysteretic transducer, describing the electric field dependence of electromechanical properties of soft piezoelectric PZT ceramics, was suggested. According to this approach, the response depends not only on the instantaneous magnitude of the input signal (e.g., electric field) but also on its past extreme values. It was shown that the experimental Rayleigh law is a particular case of the suggested approach. The model relates directly electric field dependencies of complex piezoelectric coefficient  $d_{31}(E_m)$  and  $S_1^{(1)}/E_m$ , of complex dielectric permittivity  $\epsilon_{33}^*(E_m)$  and  $D_3^{(1)}/E_m$ , and of the amplitude of elastic compliance  $s_{11}^E(E_m)$  and  $\nu_r^2$ . Application of the model to experimental data showed that the model describes well the first three complex harmonics of  $D_3$  and the irreversible change in the remnant polarization. Physical causes of the observed behavior were analyzed. As an alternative to the model based on the 90° polarization reorientation and tetragonal/rhombohedral phase boundary motion, a new approach was suggested. In this model, the observed hysteretic changes in the electromechanical properties are assumed to be caused by the electric field dependency of the mechanical stress acting at interdomain boundaries in the partly constrained crystallites of these ceramics. © 1998 American Institute of Physics. [S0021-8979(98)08217-6]

## INTRODUCTION

Piezoelectric ceramics possess excellent electromechanical properties that make them very attractive for application in electromechanical and electroacoustical transducers. One important class of these transducers is high power sound and ultrasound transducers, which are operated under high electric field. A new type of such a high-power sound transducer or active noise control has been developed recently.<sup>1</sup> Principal elements of the transducer are piezoelectric ceramic bimorph cantilevers that are driven by high electric field (Fig. 1). Small-signal electromechanical properties of the piezoelectric bimorph structures can be characterized using piezoelectric  $d_{31}$ , dielectric  $\epsilon_{33}^T$ , and elastic  $s_{11}^E$  constants,

while corresponding high-signal coefficients are highly dependent on the electric field.<sup>2</sup> Study of the high-signal coefficients is technically important. It has been widely acknowledged that electromechanical properties of piezoelectric ceramics depend on the applied electric field.<sup>3–10</sup> Nevertheless, because of extremely complicated domain structure of piezoelectric ceramics, our knowledge in this is far from complete. Most of the data available are related to the amplitude and phase of  $\epsilon_{33}^T(E)^{2-6,8,10}$  and amplitude of  $d_{31}(E)^{2,6,8,10}$  almost no data concerning complex  $d_{31}(E)$  and  $s_{11}^E/(E)$  have been published. No comprehensive theoretical model capable of explaining the behavior electromechanical characteristics under high electric field was suggested. In one approach,<sup>7–11</sup> the Taylor series expansion of thermodynamic potentials leads to the following relations between components of the instantaneous mechanical stress  $T$  and strain  $S$ , electrical displacement  $D$  and field  $E$ :<sup>7</sup>

<sup>(a)</sup>Present address: INTEL Israel (74), Mail Stop IDC-3C, MTM, P.O.B. 659, Haifa 31015, Israel; electronic mail: vkugel@il.intel.com

$$\begin{aligned}
S_i &= s_{ij}^E T_j + d_{mi} E_m + s_{ijk}^E T_j T_k + 2d_{mik} T_k E_m + R_{mni} E_m E_n \\
&\quad + R_{mnp} E_m E_n E_p + s_{ijkl}^E T_j T_k T_l + \dots, \\
D_m &= d_{mi} T_i + \epsilon_{mn}^T E_n + d_{mij} T_i T_j + 2R_{mni} T_i E_n \\
&\quad + \epsilon_{mnp}^T E_n E_p + \epsilon_{mnpq}^T E_n E_p E_q + \dots,
\end{aligned} \quad (1)$$

where  $s$ ,  $d$ ,  $R$ , and  $\epsilon$  are electromechanical characteristics (constants) of a piezoelectric media. Superscripts  $E$  and  $T$  denotes boundary conditions  $E = \text{const}$  and  $T = \text{const}$ , respectively. It is assumed in Eq. (1) that the piezoelectric media does not exhibit losses. The principal drawback of this approach is that the model (1) does not take into account hysteretic relations between  $T$ ,  $S$ ,  $D$ , and  $E$  for macroscopically controlled boundary conditions like  $T=0$ . Experimental data for PZT ceramics<sup>4,8-10</sup> suggest that the hysteresis contributes significantly to the electromechanical response of the piezoelectric ceramics at high electric fields. Recently, the experimental Rayleigh law,<sup>12</sup> describing the hysteresis dependence between the magnetization and magnetic field, has been ap-

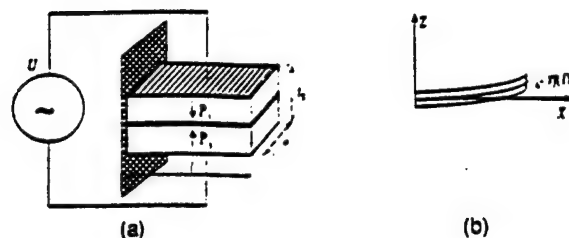


FIG. 1. (a) A schematic view of the piezoelectric  $d_{31}$  bimorph cantilever with series connection.  $P$ , denotes the vector of the spontaneous polarization. (b) Flexural displacement of the transducer in the  $ZX$  plane under applied voltage.

plied to the mechanical stress dependence of piezoelectrically induced charge on polar surfaces of piezoelectric ceramics.<sup>13,14</sup> According to Lord Rayleigh,<sup>12</sup> the hysteresis dependencies between  $Y$  (the change in the magnetization) and  $X$  (the magnetic field) when  $X$  varies in the range from  $-X_m$  to  $+X_m$  can be written as

$$Y = \alpha_R X + \beta_R X_m^2 \begin{cases} -1 - \frac{1}{2} \left( 1 - \frac{X}{X_m} \right)^2 & \text{when } X \text{ is increasing from } -X_m \text{ to } +X_m, \\ +1 - \frac{1}{2} \left( 1 - \frac{X}{X_m} \right)^2 & \text{when } X \text{ is diminishing from } +X_m \text{ to } -X_m. \end{cases}$$

where  $\alpha_R$  and  $\beta_R$  are constants describing reversible and irreversible components, respectively. According to experimental data,<sup>13,14</sup> function (2) describes very well the stress dependence of the amplitude of the piezoelectrically induced charge. Nevertheless, as follows from the expansion of Eq. (2) in Fourier's series,<sup>12</sup> function  $Y$  does not have the second harmonic while experimental data<sup>3</sup> show that the second harmonic of electrical displacement  $D_2$  increases significantly with increasing electric field. The suggested functional dependence cannot also explain peculiarities of a gradual increase of the dielectric permittivity in the region where the permittivity begins to grow upon increasing amplitude of the electric field.<sup>8</sup> It should be noted that Eq. (2) is purely intuitive and it is not a result of the Taylor series expansion.

This work was undertaken in an attempt to investigate experimentally and theoretically the behavior of complex piezoelectric  $d_{31}(E_m)$  and dielectric  $\epsilon_{33}^T(E_m)$  coefficients, and the amplitude of elastic  $s_{11}^E(E_m)$  coefficient of soft PZT under high sinusoidal electric fields and stress-free conditions ( $T=0$ ) in the frequency range of 10 Hz–10 kHz. The approach adopted is described in Sec. II. Experimental techniques are presented in Sec. III. Experimental results are analyzed in Sec. IV. Mathematical and physical models and their comparison with experimental data are considered in Sec. V. Summary and conclusions are given in Sec. VI.

## II. METHODOLOGY OF CHARACTERIZING ELECTROMECHANICAL PROPERTIES UNDER HIGH ELECTRIC FIELD

Because of extremely complicated coupling between electric and mechanical properties in piezoelectric ceramics, the electromechanical response in these materials is highly dependent on electrical and mechanical boundary conditions. Equation (1) may be used as an illustration although it may not be a valid mathematical description of the complex behavior. As is seen from the equation, the behavior of both  $S$  and  $D$  is described by a different set of coefficients for free ( $E=0$ ) and stress-free ( $T=0$ ) boundary conditions. Therefore, all electromechanical coefficients describing electric, mechanical, and interaction nonlinearities should be known for finding values of  $S$  and  $D$  for arbitrary boundary conditions. In addition, frequency dependencies of these coefficients should be determined because of the frequency dependence in the nonlinear behavior.<sup>3</sup> This is a very complicated task lying far beyond the scope of this work.

In this work, dielectric properties along the poling direction (the  $Z$  axis; subscript 3) and piezoelectric and elastic properties in the perpendicular direction (the  $X$  axis; subscript 1) are studied. Equation (1) can be used as a starting point for finding the appropriate experimental technique for measuring corresponding functional dependencies between



$D_3$ ,  $T_1$ ,  $S_1$ . In the final part of this section, limitations of the suggested measuring procedure related to possible inaccuracy of Eq. (1) for describing hysteretic behavior will be considered.

As follows from Eq. (1) for a particular case when the electric field is applied along the polar  $Z$  axis ( $E_1 = E_2 = 0$ ,  $E_3 = E$ ), and the mechanical stress acts only along the  $X$  axis (only  $T_1 = 0$ ), the relations between  $S_1$ ,  $T_1$ ,  $D_3$ , and  $E$  are written as

$$S_1 = s_{11}^E T_1 + d_{31} E + s_{111}^E T_1^2 + 2d_{311} T_1 E + R_{331} E^2 + R_{333} E^3 + s_{1111}^E T_1^3 + \dots, \quad (3)$$

$$D_3 = d_{31} T_1 + \epsilon_{33}^T E + d_{311} T_1^2 + 2R_{331} T_1 E + \epsilon_{333}^T E^2 + \epsilon_{3333}^T E^3 + \dots$$

By grouping all terms, which depend only on the electric field, and introducing

$$d_{31}(E) = d_{31} + R_{331} E + R_{333} E^2 + \dots, \quad (4)$$

$$\epsilon_{33}^T(E) = \epsilon_{33}^T + \epsilon_{333}^T E + \epsilon_{3333}^T E^2 + \dots$$

and

$$s_{11}^E(E, T_1) = s_{11}^E + s_{111}^E T_1 + 2d_{311} E + s_{1111}^E T_1^2 + \dots, \quad (5)$$

$$d'_{31}(E, T_1) = d_{31} - d_{311} T_1 + 2R_{331} E + \dots,$$

Eq. (3) can be written as

$$S_1 = s_{11}^E(E, T_1) T_1 + d_{31}(E) E, \quad (6)$$

$$D_3 = d'_{31}(E, T_1) T_1 + \epsilon_{33}^T(E) E.$$

Thus, electromechanical coefficients  $s_{11}^E(E, T_1)$ ,  $d_{31}(E)$ ,  $d'_{31}(E, T_1)$ , and  $\epsilon_{33}^T(E)$  are functions of the electric field and mechanical stress in a nonlinear piezoelectric media. In Eq. (6), terms describing the interaction between  $E$  and  $T_1$  (e.g.,  $d_{311}$  and  $R_{331}$ ) are included in  $s_{11}^E(E, T_1)$  and  $d'_{31}(E, T_1)$ ; instead of this they can be introduced in  $d_{31}(E)$  and  $\epsilon_{33}^T(E)$ , respectively.

As follows from Eq. (6), strain  $S_1$  and electrical displacement  $D_3$  are directly related to  $d_{31}(E)$  and  $\epsilon_{33}^T(E)$  under stress-free conditions ( $T=0$ ),

$$S_1 = d_{31}(E) E, \quad T=0, \quad (7)$$

$$D_3 = \epsilon_{33}^T(E) E.$$

Thus, coefficients  $d_{31}(E)$  and  $\epsilon_{33}^T(E)$  can be determined by measuring the mechanical strain in the transverse direction and electrical displacement in the polar direction under stress-free conditions. If the sinusoidal electric field is used, the amplitude and phase characteristics of harmonics of  $S_1$  and  $D_3$  can be gauged.

Measuring  $s_{11}^E(E, T_1)$  and  $d'_{31}(E, T_1)$  is a significantly more complicated problem since coefficients describing interaction between  $E$  and  $T_1$  should be determined. Therefore, the experimental technique, which gives only information about  $s_{11}^E(E, 0) = s_{11}^E(E)$  (stress-free conditions), was adopted in the present study: measuring the fundamental resonant frequency  $\nu_r$  of bending vibrations of a poled piezoelectric ceramic plate in the cantilever configuration (Fig. 2).

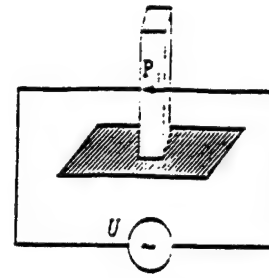


FIG. 2. Schematic view of the polarized piezoelectric plate in the cantilever configuration.  $P_s$  denotes the vector of spontaneous polarization directed along the polar  $Z$  axis. Voltage  $U$  is applied to polar surfaces of the plate.

Measuring resonant frequency of longitudinal mechanical vibrations excited by the electric field through the primary piezoelectric effect has been used by several authors.<sup>7,15</sup> Since the resonant frequency is a function of the corresponding mechanical compliance, the dependence of the frequency on the electric field gives information about nonlinearities in the mechanical compliance.<sup>7,15</sup> If the mechanical quality factor is high enough, mechanical nonlinearities are dominant because of a very high level of vibrations. Therefore this method is not applicable for finding  $s_{11}^E(E)$ . Moreover, the frequency range of primary interest in this study was 100 Hz–1 kHz while the frequency range of longitudinal vibrations is usually far above 10 kHz. Thus, another type of vibration should be considered. The bending mode, which is excited by the electric field in bimorph cantilevers (Fig. 1) may be a possible alternative. The fundamental resonant frequency of bending vibrations is<sup>2</sup>

$$\nu_r = \frac{1.875^2}{4\pi} \frac{r_c}{l^2} \frac{1}{\sqrt{3s_{11}^E \rho}}, \quad (8)$$

where  $r_c$  is the thickness,  $l$  is the length of the bimorph cantilever (Fig. 1), and  $\rho$  is the density of the material. Nevertheless, it is quite difficult to analyze the dependence of  $\nu_r$  on  $E$  in piezoelectric bimorphs since the mechanical stress can reach a very high level, and in addition, the stress is nonuniform. Preliminary experimental studies showed that bending resonant vibrations can be excited in piezoelectric plates poled along their thickness (Fig. 2). These bending vibrations arise due to nonuniform distribution of spontaneous polarization of domains. Because of a relatively low level of the bending vibrations in the piezoelectric plate (Fig. 2) it can be assumed that the mechanical compliance depends only on the electric field,  $s_{11}^E(E, 0) \equiv s_{11}^E(E)$  i.e., the dependence of  $\nu_r$  on  $E$  is caused mainly by interaction nonlinearities, e.g.,  $d_{311}$  in Eq. (5). The corresponding wave equation coincides with the same one describing bending vibrations along the  $X$  axis in a linear piezoelectric beam<sup>2</sup>

$$\frac{\partial^2 \eta}{\partial x^2} - \frac{12\rho s_{11}^E(E)}{r_c^2} \frac{\partial^2 \eta}{\partial t^2} = 0. \quad (9)$$

where  $\eta$  is the neutral surface displacement of a bent cantilever (Fig. 1).<sup>2</sup> Assuming that the plate is driven at the resonant frequency  $\nu_r$ ,  $E = E_m \sin(\omega t)$  and all other harmonics of the displacement have a much smaller amplitude, the displacement is written as  $\eta \approx \eta_m^{(1)} \sin(\omega t)$ . Expansion of the mechanical compliance in the Fourier's series yields

$$\frac{\partial^2 \eta_m^{(1)}}{\partial y^2} \sin(\omega t + \varphi_r) - \omega_r^2 \frac{12\rho [s_{11}^E(E)]^{(0)} \sin(\omega t + \varphi_r) + \frac{1}{2} [s_{11}^E(E)]^{(2)} \sin(\omega t - \varphi_r)}{t_c^2} \eta_m^{(1)} = 0. \quad (11)$$

Since for a low level of losses,  $\varphi_r \approx -\pi/2$ , Eq. (11) reduces to a similar one describing the amplitude of vibrations of a linear piezoelectric beam.<sup>2</sup> The fundamental resonant frequency of bending vibrations of the cantilever is written as

$$\nu_r = \frac{1.875^2}{4\pi} \frac{t_c}{l^2} \frac{1}{\sqrt{3\{[s_{11}^E(E_m)]^{(0)} + \frac{1}{2}[s_{11}^E(E_m)]^{(2)}\}} \rho}. \quad (12)$$

Thus, measurement of the resonant frequency as a function of the electric field gives an idea of the field dependence of the amplitude of the first and third harmonics of the mechanical compliance. It must be noted that through all derivations it was tacitly assumed that Eq. (6) is a proper description of the high-field behavior and losses in the media were neglected.

As was noted above, Eq. (6) may not be valid for a system with hysteresis and losses. For a hysteretic piezoelectric media with the given boundary conditions the corresponding piezoelectric relations can be written as

$$S_1 = f_1(T_1) + f_2(E)f_3(T_1) - f_4(E), \quad (13)$$

$$D_3 = g_1(T_1) + g_2(E)g_3(T_1) - g_4(E),$$

where  $f_j(T_1)$ ,  $f_i(E)$ ,  $g_j(T_1)$ , and  $g_i(E)$  are multiple-valued functions since multivaluedness is inherent property of hysteresis [see, for example, Eq. (2)]. For  $T_1 = 0$ , Eq. (13) reduces to

$$S_1 = f_4(E), \quad (14)$$

$$D_3 = g_4(E).$$

Thus, measurements of  $S_1$  and  $D_3$  as a function of  $E$  under  $T_1 = 0$  can provide information about which of Eqs. (4) and (7), or (14) is a correct description of piezoelectric and dielectric properties under high electric field. In contrast, the suggested procedure of measuring mechanical properties by means of Eq. (12) is a limited one since it is based on the assumption that Eqs. (6) and (10) are valid. Nevertheless, it is reasonable to assume that these equations are correct if the electric field and losses are not too high. Moreover, the validity of Eq. (6) is not restricted to the validity of Eqs. (4) and (5), therefore function  $[s_{11}^E(E_m)]^{(0)} \pm \frac{1}{2}[s_{11}^E(E_m)]^{(2)}$  obtained from measuring  $\nu_r$  can provide information about nonlinear or hysteresis origin of these dependencies.

Thus, the mechanical strain  $S_1$  and dielectric displacement  $D_3$  of unconstrained piezoelectric ceramic plates and

$$s_{11}^E = [s_{11}^E(E_m)]^{(0)} + \sum_{i=1}^{\infty} [s_{11}^E(E_m)]^{(i)} \cos(i\omega t), \quad (10)$$

where  $[s_{11}^E(E_m)]^{(i)}$  is the amplitude of the  $i$ th harmonic. Substituting Eq. (10) into Eq. (9) and taking into account only terms contributing to the fundamental vibrations, one obtains

the fundamental resonant frequency of bending vibrations  $\nu_r$  of piezoelectric ceramic plates in the cantilever configuration were chosen for characterizing the behavior of piezoelectric ceramics under high electric fields.  $S_1$  and  $D_3$  were determined by measuring harmonics of strain  $S_1$  along the  $X$  axis and of the electric current density  $J$  along the polar  $Z$  axis under the sinusoidal electric field and stress-free conditions. In ceramics with low electric conductivity the harmonics of the electric current density  $J^{(i)}$  are directly related to the harmonics of the electrical displacement  $D_3^{(i)}$ ,

$$D_3^{(i)} = \int J_m^{(i)} \sin(i\omega t - \varphi_i^{(i)}) dt = \frac{J_m^{(i)}}{i\omega} \sin\left(i\omega t - \varphi_i^{(i)} - \frac{\pi}{2}\right), \quad \geq 1, \quad (15)$$

where  $\omega$  is the angular frequency of the applied electric field  $E = E_m \sin(\omega t)$ ,  $J_m^{(i)}$  and  $\varphi_i^{(i)}$  are the amplitude and phase of the  $i$ th harmonic, respectively. In addition to  $S_1$ ,  $D_3$  and  $\nu_r$ , irreversible change  $\Delta P_i$  in the remnant polarization in the polar direction under pulsed electric field was measured since this method also provides information regarding hysteretic properties of piezoelectric ceramics. It should be stressed that this irreversible change  $\Delta P_i$  can be caused by both the spontaneous polarization reorientation and hysteresis in the mechanical boundary conditions for ferroelectric domains under applied electric field.

### III. EXPERIMENTAL TECHNIQUES

Soft piezoelectric lead zirconate titanate ceramics PZT5H (Morgan Matroc, Inc.), 3203HD (Motorola, Inc.), and PK1550 (Piezo Kinetic, Inc.) were used in the experiments. The ceramics are donor-doped PZT and have a chemical composition near the morphotropic phase boundary. Prepared samples had a shape of parallelepipeds with rectangular cross section. The thickness of the samples was 0.5–3 mm, the width was 3–10 mm, and the length was 10–30 mm. Surfaces having the largest area were electrodeposited with electroless nickel or sputtered gold and the samples were poled along their thickness at 90–120 °C with  $E = 15$ –20 kV/cm in the silicon oil bath. All measurements were conducted on samples aged for at least 24 h.

The harmonic spectrum of the electric current density through samples under the applied sinusoidal voltage  $U$  was

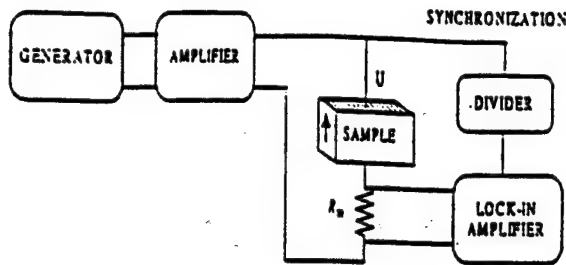


FIG. 3. Experimental setup for measuring  $D_3(E)$ .  $\uparrow$  denotes the direction of polarization.

measured by means of the experimental setup shown in Fig. 3. Resistor  $R_m = 3\text{--}50\ \Omega$  was chosen such that  $100R_m \ll 1/\omega C_s$ , where  $C_s$  is the capacitance of the sample. Voltage across the sample was delivered from the power amplifier (790 Series, PCB Piezotronics, Inc., or PA-250H, Julie Research Laboratories, Inc.). The input ac signal to the power amplifier was supplied by a generator DS345 (Stanford Research Systems, Inc.). Voltage across resistor  $R_m$  was gauged by a lock-in amplifier SR830 DSP (Stanford Research Systems, Inc.), which was synchronized with the output voltage of the amplifier by means of the voltage divider. For measuring the harmonic spectrum of  $D_3$  at small electric fields, a low-distortion generator DS360 (Stanford Research Systems, Inc.) was used without the amplifier. Voltage and frequency ranges of the experimental setup were 0–300 V rms and 0–20 kHz, respectively. Harmonic spectrum of  $J$  was calculated from the following equation:

$$J_m^{(i)} \sin(i\omega t + \varphi_J^{(i)}) = \frac{U_{mR}^{(i)}}{R_m A} \sin(i\omega t + \varphi_U^{(i)}), \quad (16)$$

where  $U_{mR}^{(i)}$  is the measured amplitude of the  $i$ th harmonic of the voltage across resistor  $R_m$ ,  $A$  is the electrode area, and  $\varphi_U^{(i)}$  is the measured phase of the  $i$ th harmonic of the voltage. Equations (15) and (16) were used for finding amplitude  $D_{3m}^{(i)}$  and phase  $\varphi_D^{(i)}$  of the  $i$ th harmonic of the electrical displacement.

Amplitudes  $S_{1m}^{(i)}$  and phases  $\varphi_S^{(i)}$  of the harmonics of strain  $S_1$  were measured by means of the double-beam laser interferometer<sup>16</sup> and strain gauges. The interferometer is described elsewhere.<sup>16</sup> An experimental setup for measuring strain with strain gauges is shown in Fig. 4. Since poled piezoelectric ceramics have symmetry point group  $\approx mm$  there was no need to align the strain gauge along a certain direction at the polar surface. Strain gauges KFR-02-12-C-11 and

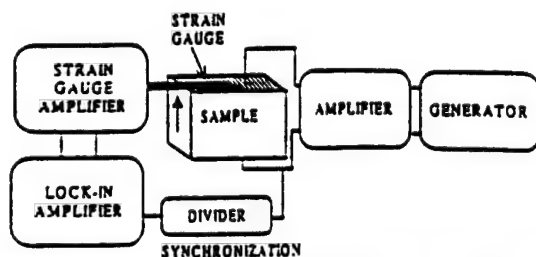


FIG. 4. An experimental setup for measuring strain  $S_1$  by means of strain gauges.

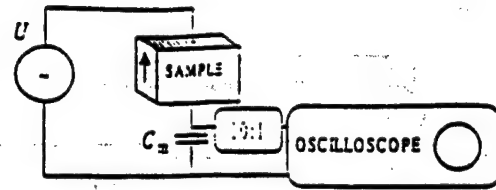


FIG. 5. An experimental setup for measuring reversible and irreversibly changed polarization.

a strain gauge amplifier DPM-612B (KYOWA Electronic Instruments) were used. Frequency response of the strain in the range 10 Hz–10 kHz at low electric fields was measured by means of the laser interferometer. The electric field dependence of the strain in the frequency range 10–500 Hz was gauged by the strain gauge setup. Phase delay introduced by the strain gauges was calculated using phase characteristics of  $S_1$  obtained for the same sample with the laser interferometer.

The electric field dependence of the fundamental resonant frequency of bending vibrations of the piezoelectric cantilever (Fig. 2) was determined by measuring the frequency of the maximum tip displacement along the  $Z$  axis (Fig. 1). A photonic sensor MTI 2000 (MTI Instruments Division) with a corresponding set of electronic equipment were used. A complete description of the experimental setup is given elsewhere.<sup>17</sup>

To measure the irreversible change in the remnant polarization under high electric field the electric pulse technique was used (Fig. 5). A pair of single rectangular pulses having opposite polarities or single sinusoidal pulse consisting of one period of sinusoidal voltage were delivered to the sample by means of the generator DS345 and the amplifier 790. A digital oscilloscope LeCroy 9310A (LeCroy Corporation) with probe 10:1 (10 M $\Omega$  the input resistance) were used to measure the induced on capacitor  $C_m = 1.015\ \mu\text{F}$  electric charge. The amount of the irreversible change in the remnant polarization,  $\Delta P_i$ , is equal to

$$\Delta P_i = \frac{\Delta U_c C_m}{A}, \quad (17)$$

where  $\Delta U_c$  is residual voltage remaining on the capacitor  $C_m$  after the second of two consecutive rectangular pulses with opposite polarities applied to the sample. The capacitor was short-circuited after the first pulse. Presumably, the second voltage pulse is the one causing the irreversible change in the polarization. The duration of each rectangular pulse was 50 ms. Equation (17) is also valid for the sinusoidal pulse if the irreversible change  $\Delta P_i$  takes place during the second part of the pulse only. The duration of the sinusoidal pulse was 100 ms.

To characterize  $D_3(E)$ ,  $S_1(E)$ , and  $S_1(D_3)$  hysteric loops, a modified Sawyer-Tower circuit with  $C_m = 9.64\ \mu\text{F}$  was used (Fig. 6). Generator DS345 and an amplifier BOP 1000M (KEPCO Inc.) with an output voltage up to 1 kV delivered high sinusoidal voltage to the sample under test.

Crystallographic structure of the ceramics used was determined by the x-ray diffraction (XRD) method (Cu  $K\alpha$

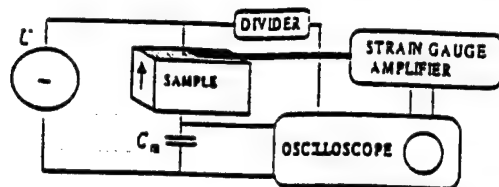


FIG. 6. A modified Sawyer-Tower circuit for measuring hysteresis loops.

characteristic line) using powder diffractometer SCINTAG VAX 3100 system. A spectrum produced by the  $K\alpha_2$  line of a Cu source was stripped off.

All measurements were carried out at room temperature. A small-signal complex dielectric constant  $\epsilon_{33}^T$  at frequencies far from resonances was calculated by neglecting nonlinearities and using Eqs. (7), (15), and (16).

$$\epsilon_{33}^T = \frac{D_{3m}^{(1)} e^{j\phi_D^{(1)}}}{E_m} = \frac{U_m^{(1)}}{R_m A \omega E_m} e^{j(\phi_U^{(1)} - \pi/2)}, \quad (18)$$

$$E_m = \frac{U_m}{t_c},$$

where  $U_m$  is the amplitude of the applied voltage and  $t_c$  is the thickness of the ceramic sample. Since  $\epsilon_{33}^T$  is complex, it also contains information about losses: dissipation factor (DF) is written as

$$DF = \tan(\phi_D^{(1)}). \quad (19)$$

It was assumed in the  $\epsilon_{33}^T$  calculations that the parallel resistance-capacitance ( $R_p C_p$ ) circuit describes electrical characteristics of the ceramics. Small-signal complex piezoelectric constant  $d_{31}$  was calculated from Eq. (7) using the magnitude of the first harmonic of the strain  $S_1$ .

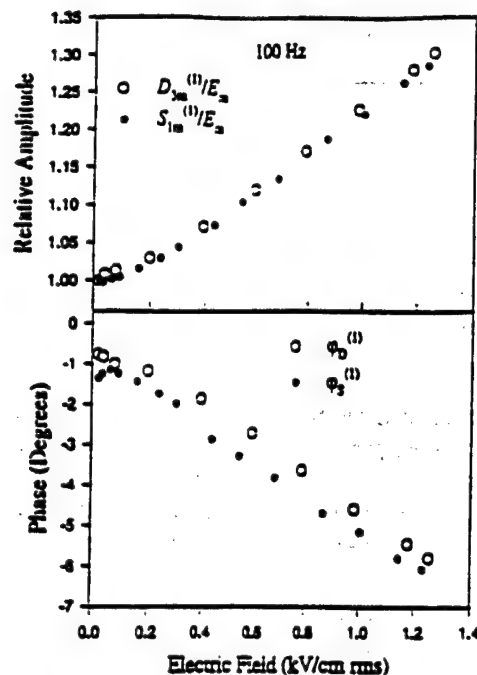
$$d_{31} = \frac{S_{1m}^{(1)} e^{j\phi_S^{(1)}}}{E_m}. \quad (20)$$

#### IV. EXPERIMENTAL RESULTS

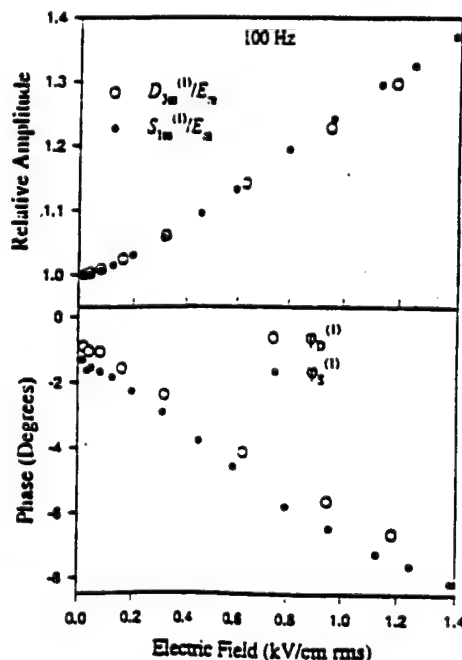
All measured values, except for those characterizing hysteresis loops (e.g., coercive field  $E_c$  and remnant polarization  $P_r$ ) were root-mean-square (rms) magnitudes. The results presented here were obtained under alternating electric field without dc bias. Measured small-signal dielectric and piezoelectric characteristics of PZT5H, 3203HD, and PK1550 ceramics are shown in Table I. Since  $D_{3m}^{(1)} e^{j\phi_D^{(1)}}/E_m$  and  $S_{1m}^{(1)} e^{j\phi_S^{(1)}}/E_m$  at a low level of  $E_m$  are equal to  $\epsilon_{33}^T$  and  $d_{31}$ , respectively, it is convenient to analyze ratios

TABLE I. Small-signal parameters of investigated commercial ceramics.

Material	$E_c$ , kV/cm (20 Hz)	$P_r$ , $\mu\text{C}/\text{cm}^2$ (20 Hz)	Small-signal properties		
			$d_{31}$ , pm/V (100 Hz)	Relative $\epsilon_{33}^T$ , (100 Hz)	DF, (100 Hz)
PK1550	8.2	20.0	-236	3285	0.012
PZT5H	8.4	29.7	-288	3294	0.017

FIG. 7. Field dependencies of the relative amplitudes of  $D_{3m}^{(1)} e^{j\phi_D^{(1)}}/E_m$  and  $S_{1m}^{(1)} e^{j\phi_S^{(1)}}/E_m$  and of their phases for PK1550 at 100 Hz.

$D_{3m}^{(1)} e^{j\phi_D^{(1)}}/E_m$  and  $S_{1m}^{(1)} e^{j\phi_S^{(1)}}/E_m$  as a function of  $E_m$ . Relative change in the amplitudes of these ratios and their phase characteristics as a function of  $E_m$  for the ceramics studied are shown in Figs. 7-9.  $D_{3m}^{(1)} e^{j\phi_D^{(1)}}/E_m$  and  $S_{1m}^{(1)} e^{j\phi_S^{(1)}}/E_m$  were normalized with respect to their value at low electric field,  $E_m < 20$  V/cm. As is seen from these graphs, for all studied polarized ceramics, the field dependencies of the amplitudes and phases of  $D_{3m}^{(1)}$  and  $S_{1m}^{(1)}$  for each type of ceramic



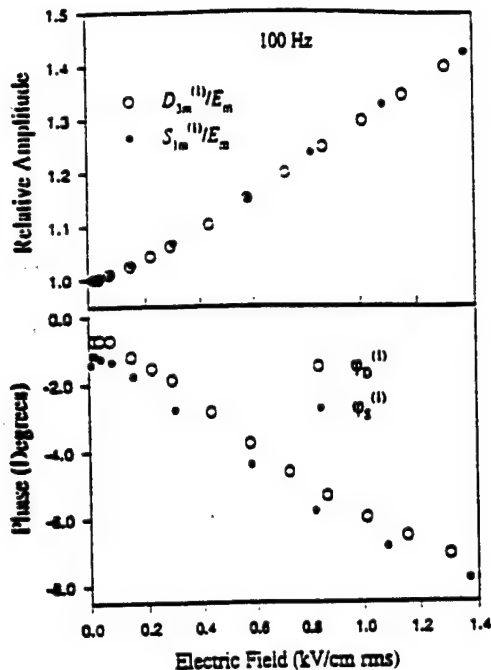


FIG. 9. Field dependencies of the relative amplitudes of  $D_{3m}^{(1)}/E_m$  and  $S_{1m}^{(1)}/E_m$  and of their phases for 3203HD at 100 Hz.

was very similar in the range of 0–1.4 kV/cm. Additional experiments showed that this is also valid for electric fields at least up to 2.1 kV/cm. A small phase shift between  $D_{3m}^{(1)}$  and  $S_{1m}^{(1)}$  can be attributed to the experimental limitations in determining the strain phase by means of the strain gauges. Amplitudes  $D_{3m}^{(1)}$  and  $S_{1m}^{(1)}$  increased almost linearly with increasing  $E_m$  except for the initial part ( $E_m < 0.1$  kV/cm rms) where the dependencies were more complicated. It was found that there was small hysteresis in  $D_{3m}^{(1)}(E_m)$  and  $S_{1m}^{(1)}(E_m)$  dependencies: upon decreasing the amplitude of the applied electric field from the maximum to a small value (less than 10 V/cm) the value of  $D_{3m}^{(1)}(E_m)/E_m$  and  $S_{1m}^{(1)}(E_m)/E_m$  ( $E_m \rightarrow 0$ ) exceeded their initial amplitudes by several percent. The relaxation time was on the order of dozens of minutes.

A study of the effect of dc bias was also conducted. It was found that the shape of functions  $D_{3m}^{(1)}(E_m)/E_m$  and  $S_{1m}^{(1)}(E_m)/E_m$  depended significantly on biasing dc electric field. If the biasing electric field was high enough, functions  $D_{3m}^{(1)}(E_m)/E_m$  and  $S_{1m}^{(1)}(E_m)/E_m$  had a bell shape, i.e., they even decreased at a certain amplitude of the electric field that was not the case for zero dc bias.

The field dependencies of the ratio  $[\nu_r(0)/\nu_r(E_m)]^2$  and of the tip displacement of the piezoelectric cantilever (Fig. 2) at the fundamental resonant frequency of bending vibrations are shown in Fig. 10. The measured phase shift between the applied electric field and tip displacement was  $\phi_r \approx -75^\circ \approx 15^\circ$ . As is seen from the figure,  $[\nu_r(0)/\nu_r(E_m)]^2$  increased almost linearly with increasing electric field except for low electric field. From a comparison of Figs. 7–9 and 10, the field dependence of  $[\nu_r(0)/\nu_r(E_m)]^2$  was more moderate than that of functions  $D_{3m}^{(1)}(E_m)/E_m$  and  $S_{1m}^{(1)}(E_m)/E_m$ .

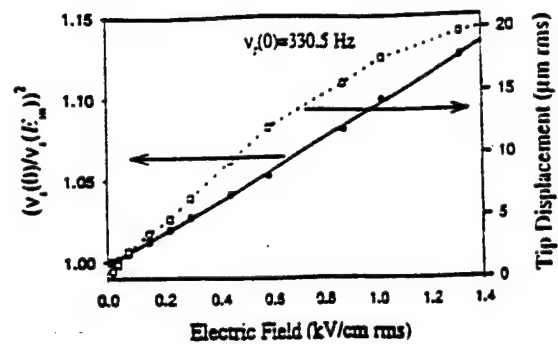


FIG. 10. Field dependencies of  $[\nu_r(0)/\nu_r(E_m)]^2$  and of the tip displacement at resonance for PK1550 ceramic plate in the cantilever configuration. The length of cantilever is 27 mm, the width is 11 mm, and thickness is 0.55 mm.

Frequency dependencies of functions  $D_{3m}^{(1)}/E_m$  and  $S_{1m}^{(1)}/E_m$  in the range of 10 Hz–10 kHz in small electric fields (less than 10 V/cm rms) are presented in Fig. 11. The functions were normalized with respect to their value at 100 Hz. As is seen in the figure, the functional dependencies of the electrical displacement and strain had the same tendency of a slow decrease with increasing frequency. Scattering in the magnitude of the strain measured by means of the laser interferometer was probably caused by instrumental limitations and spurious vibrations due to the sample clamping in the holder. Despite a good stability of results obtained with the strain gauge, it was found that the strain gauge cannot be

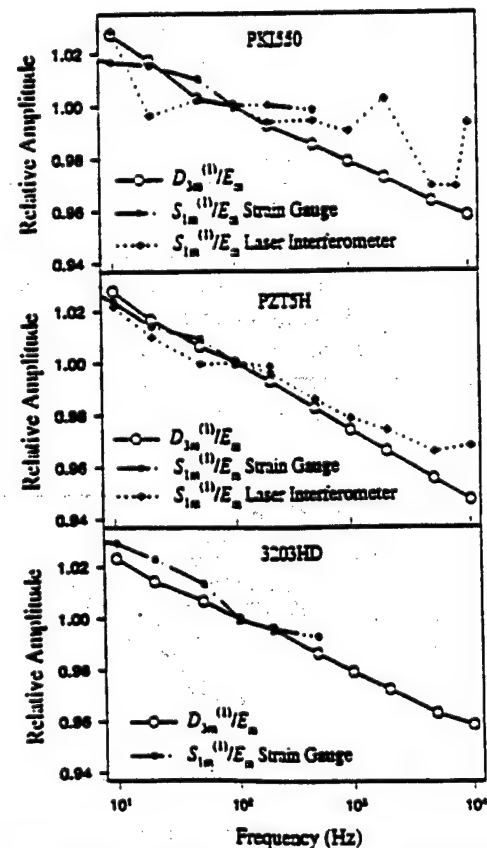


FIG. 11. Frequency dispersion of the amplitude of the first harmonics of the electrical displacement  $D_3$  and strain  $S_1$  at low electric field.



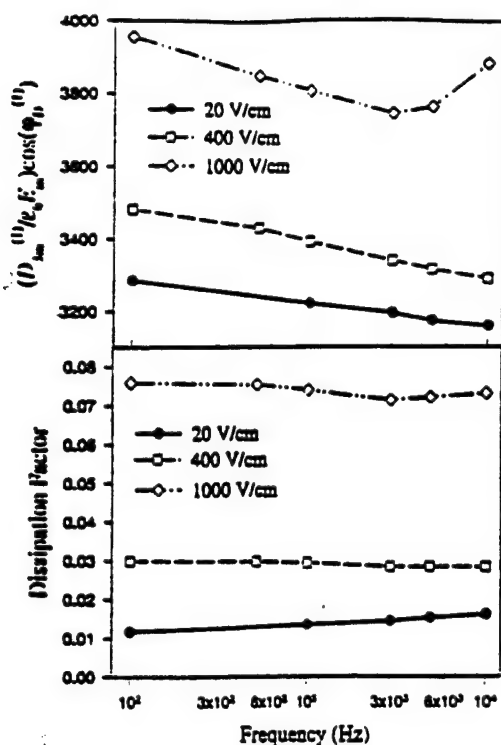


FIG. 12. Frequency dispersion of  $(D_{3m}^{(1)}/\epsilon_0 E_m) \cos(\varphi_D^{(1)})$  and  $DF$  at different electric fields (rms) for PK1550.

used at frequencies above 500 Hz. This was caused by increasing phase delay introduced by the strain gauge.

Frequency dispersion of the amplitudes of the real and imaginary parts of  $D_{3m}^{(1)}/E_m$  for PK1550 was also studied under various levels of the applied sinusoidal field. Since at small electric fields the real part of the relative dielectric permittivity is equal to  $(D_{3m}^{(1)}/\epsilon_0 E_m) \cos(\varphi_D^{(1)})$  and the dielectric losses are expressed by Eq. (19), the electric field dependencies of these quantities were calculated and plotted in Fig. 12. As is seen in the figure, the shape of the frequency dispersion curves depended on the amplitude of the applied field. Field dependencies of the normalized amplitudes of  $D_{3m}^{(1)}/E_m$  at 100 Hz and 1 kHz for the ceramics studied are given in Fig. 13. As shown in the graph, a nonlinear increase in the first harmonic  $D_{3m}$  at 100 Hz was large than at 1 kHz.

The initial part of the electric field dependence of  $D_{3m}^{(1)}/E_m$  at several frequencies and the corresponding graph

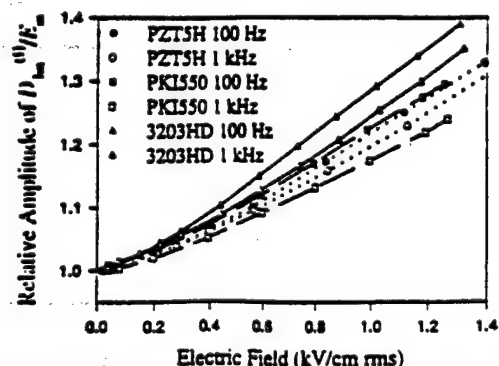


FIG. 13. Field dependencies of normalized amplitudes of  $D_{3m}^{(1)}/E_m$  at 100 Hz and 1 kHz for the ceramics studied.

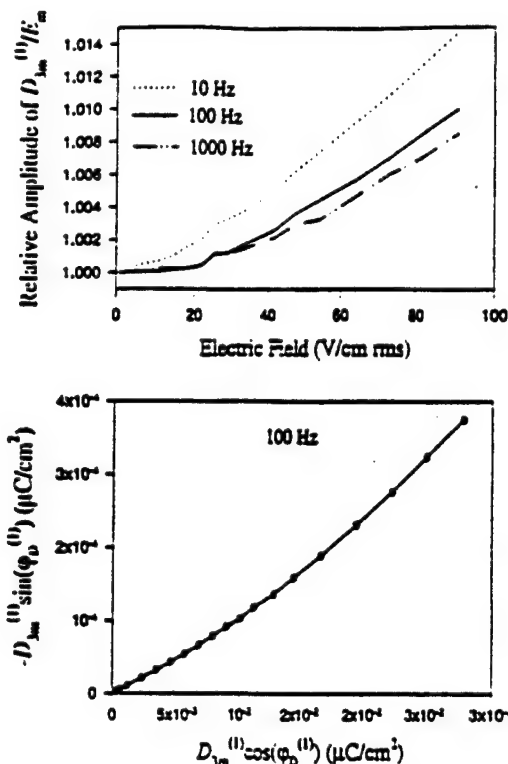


FIG. 14. Initial part of the electric field dependence of  $D_{3m}^{(1)}/E_m$  at several frequencies and the corresponding graph of  $-D_{3m}^{(1)} \sin(\varphi_D^{(1)})$  vs  $D_{3m}^{(1)} \cos(\varphi_D^{(1)})$  at 100 Hz for 3203HD sample.

of  $-D_{3m}^{(1)} \sin(\varphi_D^{(1)})$  vs  $D_{3m}^{(1)} \cos(\varphi_D^{(1)})$  at 100 Hz for the 3203HD sample are shown in Fig. 14. As can be seen in the first graph, the dependence of  $D_{3m}^{(1)}/E_m$  on  $E_m$  at an electric field smaller than 0.1 kV/cm had significant nonlinearity and frequency dispersion. It was also found that there was a significant time instability in the absolute value of the dielectric response at this very fine scale. Moreover, hysteresis was observed: even if the amplitude of the electric field increased from zero to a relatively low level of 50–100 mV/cm, the initial values of  $D_{3m}^{(1)}$  and of the slope of  $D_{3m}^{(1)}/E_m$  changed during immediate consecutive measurements. Nevertheless, if second measurements were repeated for several hours, the slope of  $D_{3m}^{(1)}/E_m$  was almost consistent with that in the initial measurements. The second graph of Fig. 14 shows that the ratio between the amplitudes of imaginary and real parts of  $D_{3m}^{(1)}$  was nonlinear.

Field dependencies of amplitudes and phases of the first three harmonics of the electrical displacement for a 3203HD sample are shown in Fig. 15. Field dependencies of amplitudes and phases of the first and second harmonics of the electrical displacement for another 3203HD sample are shown in Fig. 16. It should be noted that the level of the second and third harmonics of the electrical displacement caused by the instrumental nonlinearities was at least three times smaller than the measured values of  $D_{3m}^{(2)}$  and  $D_{3m}^{(3)}$  for the ceramics studied. The experimental data of Figs. 15 and 16 demonstrate that despite an increase of  $D_{3m}^{(1)}/E_m$  1.5–1.6 times at 2 kV/cm rms, the relative level of the second and third harmonics was less than several percent. As shown in Figs. 15 and 16, the second harmonic was polar and it phas

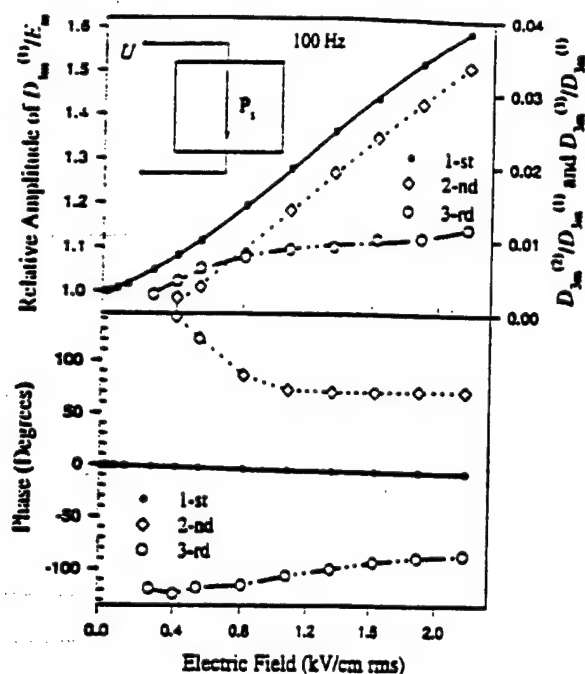


FIG. 15. Field dependencies of amplitudes and phases of the first three harmonics of the electrical displacement for 3203HD sample.

was close to  $-90^\circ$  or  $-90^\circ$  depending on the mutual direction of the spontaneous polarization and electric field. It is also follows that the field dependence of the amplitude of the second harmonic varied from sample to sample. Moreover, experimental results also showed that the harmonic was unstable in time. Surprisingly, the third harmonic demonstrated saturationlike behavior (Fig. 15). The phase of the harmonic was close to  $-90^\circ$ .

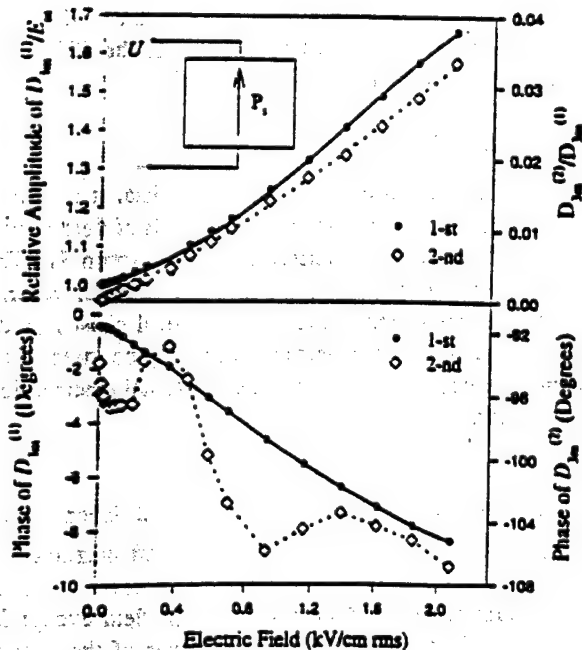


FIG. 16. Field dependencies of amplitudes and phases of the first and second harmonics of the electrical displacement for another 3203HD sample.

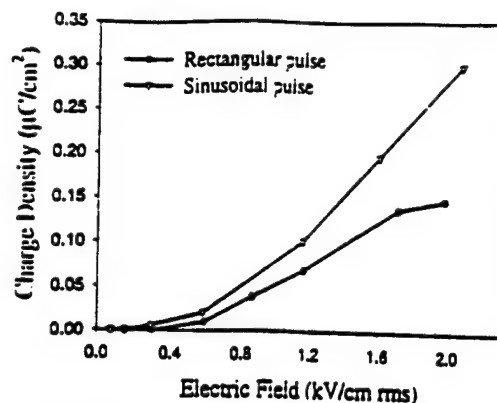


FIG. 17. Dependencies of the irreversible change in the remnant polarization on the electric field for 3203HD sample.

Dependencies of the irreversible change  $\Delta P_r$  in the remnant polarization on the electric field for a 3203HD sample are shown in Fig. 17. As shown, the change in the polarization took place even at electric fields much smaller than the coercive equal to 8.6 kV/cm. From a comparison of the amount of the changed polarization for sinusoidal and rectangular pulses, the change in the polarization depended on the amplitude and not on the rms value of the applied electric field (for pulses with the same duration).

$D_3(E)$ ,  $S_1(E)$ , and  $S_1(D_3)$  hysteresis loops in 1 and 13 kV/cm rms for a 3203HD sample are shown in Figs. 18 and 19, respectively. The frequency of the electric field was 10 Hz. As shown in Fig. 18,  $S_1$  vs  $D_3$  was a linear function and there was no phase shift between  $S_1$  and  $D_3$  while there was a phase shift between  $D_3$  and  $E$  and  $S_1$  and  $E$  at 1 kV/cm rms. This is consistent with phase characteristics of the first

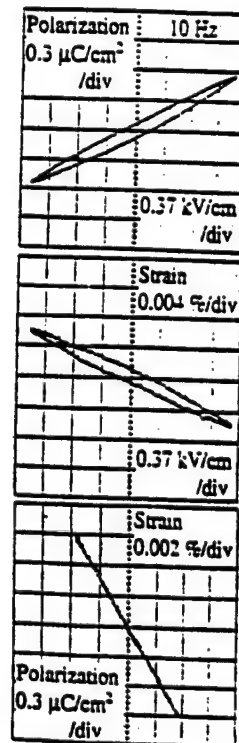


FIG. 18.  $D_3(E)$ ,  $S_1(E)$ , and  $S_1(D_3)$  hysteresis loops for 3203HD sample in electric field 1 kV/cm rms.

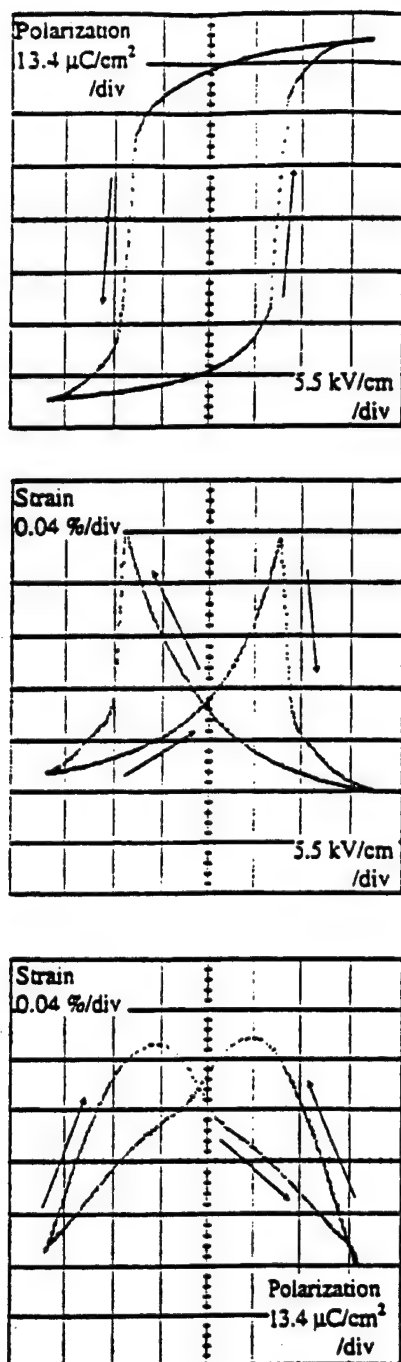


FIG. 19.  $D_3(E)$ ,  $S_1(E)$ , and  $S_1(D_3)$  hysteresis loops for 3203HD sample in electric field 13 kV/cm rms. The frequency of the field is 10 Hz.

harmonics of  $D_3$  and  $S_1$  (Fig. 9), which demonstrated the same behavior. This simple relation between  $S_1$  and  $D_3$  broke under an electric field that was higher than the coercive field (Fig. 19): the behavior became hysteretic. It was also found that under this level of the field, hysteretic loops decreased in time but they could be restored by holding the sample under zero field for a time depending on the sample.

Part of XRD spectra ( $2\theta$  scan, Cu  $K\alpha_1$  line) and their deconvolutions for poled and depoled 3203HD ceramics are shown in Fig. 20. This range of  $2\theta$  was chosen since the tetragonal (T) and rhombohedral (R) phases are distinguishable on x-ray powder diffractograms at a 200/020/002 set of lines.<sup>18</sup> The 200 reflections form a doublet in the tetragonal

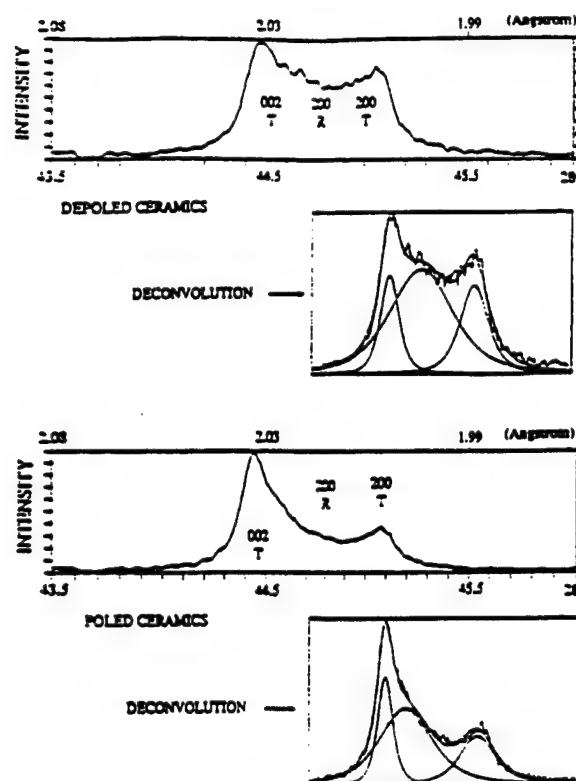


FIG. 20. Part of XRD spectra ( $2\theta$  scan) and their deconvolutions for poled and depoled 3203HD ceramics.

phase while 200 is a singlet in the rhombohedral phase. As is seen from the results of the deconvolution, there was a triplet at the 200/020/002 set. Therefore, 3203HD ceramics had the chemical composition at the morphotropic phase boundary (MPB) since both tetragonal and rhombohedral phases were presented in the ceramics. Calculated from the data the  $c/a$  ratio for the tetragonal cell was equal to 1.0133. Comparison of XRD spectra for depoled and poled ceramics showed that there was a significant amount of  $90^\circ$  domain walls in the tetragonal phase of the poled ceramics since the 200 T line did not disappear upon poling the sample.

## V. DISCUSSION

In the discussion of the experimental data, it is convenient to begin from the mathematical analysis of field dependencies of the electrical displacement  $D_3$  and strain  $S_1$ . This makes it possible to find an adequate mathematical description of the experimental data. Then, physical causes of the observed behavior of the electromechanical properties of the soft piezoelectric ceramics under the sinusoidal electric field are analyzed.

### A. Nonlinear model

As seen from Figs. 7–9 and 13–16, field dependencies of  $D_{3m}^{(1)} e^{j\psi_D^{(1)}}/E_m$  and  $S_{1m}^{(1)} e^{j\psi_S^{(1)}}/E_m$  for all soft piezoelectric ceramics studied show an almost linear increase with increasing amplitude of the sinusoidal electric field except for low electric fields (Fig. 14). Relative values of the second harmonic of the electrical displacement  $D_3$  also demonstrate almost linear dependence, while the third harmonic of the electrical displacement  $D_3$  shows a saturationlike behavior



(Figs. 15 and 16). Mathematical analysis of these dependencies can provide information as to whether nonlinear or hysteretic models are adequate for describing the electromechanical properties. As follows from the nonlinear model of the field dependence of  $S_1$  and  $D_3$  under stress-free conditions. [Eqs. (4) and (7)], corresponding dependencies can be written as

$$\begin{aligned} S_1 &= d_{31}E + R_{331}E^2 + R_{333}E^3 + \dots, \\ D_3 &= \epsilon_{33}^T E + \epsilon_{333}^T E^2 + \epsilon_{3333}^T E^3 + \dots \end{aligned} \quad (21)$$

As follows from the spectral analysis of Eq. (21) for sinusoidal applied electric field  $E = E_m \sin(\omega t)$ , the first three harmonics of  $S_1$  and  $D_3$  (not including the dc component) can be written as

$$S_1^{(1)} = \left( d_{31} + \frac{3}{4} R_{331} E_m^2 + \dots \right) E_m \sin(\omega t), \quad (22)$$

$$S_1^{(2)} = \left( \frac{1}{2} R_{331} E_m + \dots \right) E_m \sin\left(2\omega t - \frac{\pi}{2}\right),$$

$$S_1^{(3)} = \left( \frac{1}{2} R_{333} E_m^2 + \dots \right) E_m \sin(3\omega t - \pi),$$

$$D_3^{(1)} = \left( \epsilon_{33}^T + \frac{3}{4} \epsilon_{333}^T E_m^2 + \dots \right) E_m \sin(\omega t) \quad (23)$$

$$D_3^{(2)} = \left( \frac{1}{2} \epsilon_{333}^T E_m + \dots \right) E_m \sin\left(2\omega t - \frac{\pi}{2}\right),$$

$$D_3^{(3)} = \left( \frac{1}{2} \epsilon_{3333}^T E_m^2 + \dots \right) E_m \sin(3\omega t - \pi).$$

As seen from Eqs. (22) and (23), the series in brackets consists of odd powers of  $E_m$  for even harmonics and of even powers of  $E_m$  for odd harmonics of  $S_1$  and  $D_3$ . Keeping only two first terms in the series expansion of the harmonics of  $D_3$ , corresponding approximating functions can be written as

$$\begin{aligned} \frac{D_{3m}^{(1)}}{E_m} &\approx \alpha_0 + \alpha_2 E_m^2, \\ \frac{D_{3m}^{(2)}}{D_{3m}^{(1)}} &\approx \frac{\alpha_1 E_m + \alpha_3 E_m^3}{\alpha_0 + \alpha_2 E_m^2}, \\ \frac{D_{3m}^{(3)}}{D_{3m}^{(1)}} &\approx \frac{\frac{1}{3} \alpha_2 E_m + \alpha_4 E_m^4}{\alpha_0 + \alpha_2 E_m^2}, \end{aligned} \quad (24)$$

where  $\alpha_i$  are fitting parameters. Thus, five constant parameters are used for approximation of the amplitudes of the first three harmonics of  $D_3$  with polynomials. Fitting experimental data of Fig. 15 for the first three harmonics of  $D_3$  according to Eq. (24) is shown in Fig. 21. Clearly, the functional dependencies of the first and third harmonics do not describe satisfactorily the experimental data. The first equation in set (24) corresponds to a quadratic dependency while experimental data for  $D_{3m}^{(1)}/E_m$  demonstrate an approximately linear dependence of the amplitude on the applied electric

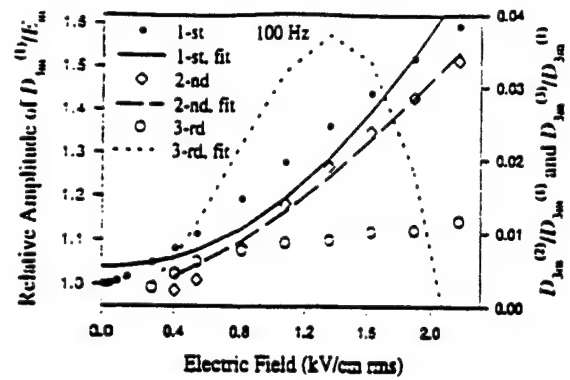


FIG. 21. Fitting nonlinear model to experimental amplitudes of the first three harmonics of  $D_3$  for 3203HD sample (Fig. 15).

field except for low electric fields. Moreover, as seen from Eqs. (22) and (23), the fact that there are no losses in the nonlinear model of  $D_{3m}^{(1)}/E_m$  and  $S_{1m}^{(1)}/E_m$  contradicts experimental results, which showed a steady increase in the phase shift with increasing amplitude of the electric field (Figs. 7–9, and 14–16). The nonlinear function for approximating the third harmonic [last equation in set (24)] departs significantly from the experimental data. In addition, the phase of the third harmonic according to the model should be  $-\pi$  [Eq. (23)] while the experimental values are close to  $-\pi/2$  (Fig. 15). Using Eqs. (5), (11), and (12), it can be also shown that for the nonlinear model the relative change in the resonant frequency squared,  $[\nu_r(0)/\nu_r(E_m)]^2$ , is described by a quadratic law similar to one for  $D_{3m}^{(1)}/E_m$  and  $S_{1m}^{(1)}/E_m$ . Nevertheless, corresponding experimental data (Fig. 10) demonstrate approximately linear dependence. Thus, as follows from the analysis conducted above, the nonlinear model does not provide an adequate description of the electric field dependencies of the studied electromechanical properties of the soft piezoelectric ceramics under stress-free conditions.

## B. Hysteretic model

As was discussed in Sec. I, a hysteretic model can be suggested as an alternative for describing the behavior of the soft piezoelectric ceramics under applied electric field. The main peculiarity of hysteresis is multivaluedness in functional dependencies. It should be noted that from the mathematical viewpoint the nonlinear model is a partial case of the hysteretic model.

As was shown in Sec. II, Eq. (14) is the most general hysteretic function which can characterize electric field dependencies of  $D_3$  and  $S_1$  under stress-free conditions. There is an experimental confirmation that soft piezoelectric ceramics demonstrate hysteretic behavior in the electric field. As follows from Fig. 17, an irreversible change  $\Delta P_i$  in the remnant polarization takes place in the periodic electric field that is much smaller than the coercive one (Fig. 17). This irreversible change, i.e., hysteretic process, contributes to the observed increase in the amplitude and phase delay of harmonics of  $D_3$  with increasing electric field. A qualitative analysis regarding the correlation in the behavior of  $D_3$  and  $\Delta P_i$  will be given later.

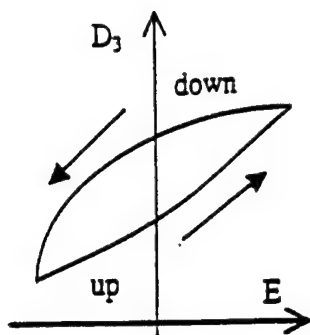


FIG. 22. Schematic view of minor hysteresis loop.

We begin from the analysis of the second equation in set (14). Assuming that the dependence  $D_3(E)$  is hysteretic, and neglected by frequency-related hysteresis, one arrives at the model of the static hysteretic transducer.<sup>19</sup> According to Mayergoyz,<sup>19</sup> there are two types of static hysteretic transducers: one with local memory in which the past exerts its influence upon the future through the current value of output (e.g.,  $D_3$ ), and one with nonlocal memories in which future output values depend not only on its current value but on past extreme values of input (e.g.,  $E$ ) as well. Experimental data for piezoelectric ceramics<sup>3,5</sup> demonstrate the existence of crossing and partially coincident minor  $D_3(E)$  loops. This suggests that the future  $D_3$  value is not uniquely specified by current values of  $D_3$  and  $E$ . Thus, it is reasonable to consider piezoelectric ceramics as hysteretic transducers with nonlocal memory.

Since experimental hysteresis loops  $D_3(E)$  and  $S_1(E)$  at electric fields much smaller than the coercive field have rather simple geometrical shapes (Fig. 18), truncated Taylor's series can be used for describing ascending and descending branches of the loops (Fig. 22):

$$D_3^u(E) = D_3^u(0) + \alpha^u E + \beta^u E^2 + \gamma^u E^3, \quad (25)$$

$$D_3^d(E) = D_3^d(0) + \alpha^d E + \beta^d E^2 + \gamma^d E^3,$$

where  $\alpha$ ,  $\beta$ , and  $\gamma$  are functions depending on the corresponding sequence of past extremum values of the electric field: superscripts "u" and "d" describe ascending and descending branches of  $D_3$ , respectively (Fig. 22). Clearly, strain  $S_1$  can be described by the equations analogous to Eq. (25).

In the periodical electric field with two extreme values  $-E_m$  and  $+E_m$ , the following initial conditions are fulfilled for steady-state hysteresis loops:

$$D_3^u(E_m) = D_3^d(E_m), \quad (26)$$

$$D_3^u(-E_m) = D_3^d(-E_m).$$

In addition, in this case  $\alpha$ ,  $\beta$ , and  $\gamma$  are functions of  $E_m$  only. Using Eq. (26), Eq. (25) reduces to

$$D_3(E) = D_3^d(0) + \alpha(E_m)E + \gamma(E_m)E^3 + \begin{cases} \beta^u(E_m)E^2, & \text{up,} \\ [\beta^u(E_m) - \beta^d(E_m)]E_m^2 + \beta^d(E_m)E^2, & \text{down,} \end{cases} \quad (27)$$

where

$$\alpha(E_m) = \alpha^u = \alpha^d, \quad (28)$$

$$\gamma(E_m) = \gamma^u = \gamma^d.$$

Thus, as seen from a comparison of Eqs. (21) and (27), the Taylor's expansion coefficients in the hysteretic model become a function of  $E_m$  and the relation between  $D_3$  and  $E$  becomes a multiple valued function. Fourier's analysis of harmonics of  $D_3$  for the hysteretic model (27) with  $E = E_m \sin(\omega t)$  gives

$$D_3^{(0)} = D_3^d(0) - \frac{\beta^d(E_m) - \beta^u(E_m)}{4} E_m^2, \\ D_3^{(1)} = [\alpha(E_m) + \frac{1}{2} \gamma(E_m)] E_m \sin(\omega t) - \frac{4}{3\pi} [-\beta^d(E_m) + \beta^u(E_m)] E_m^2 \cos(\omega t), \quad (29)$$

$$D_3^{(2)} = \frac{1}{2} [\beta^d(E_m) + \beta^u(E_m)] E_m^2 \sin\left(2\omega t - \frac{\pi}{2}\right),$$

$$D_3^{(3)} = -\frac{1}{2} \gamma(E_m) E_m^3 \sin(3\omega t) - \frac{4}{15\pi} [-\beta^d(E_m) + \beta^u(E_m)] E_m^2 \cos(3\omega t).$$

In ferroelectrics such as soft piezoelectric ceramics, which have a significant amount of domain walls and very complex elastic boundary conditions, it is reasonable to assume that functions  $\alpha(E_m)$ ,  $\beta(E_m)$ , and  $\gamma(E_m)$  are rather smooth and are well described by truncated Taylor's series at amplitudes of the electric field much smaller than the coercive one. Assuming that  $\gamma(E_m) \approx 0$  and expanding  $\alpha(E_m)$  and  $\beta(E_m)$  in Taylor's series and using only the first two terms in these series, Eq. (27) reduces to

$$D_3(E) = D_3^d(0) + (\alpha_0 + \alpha_1 E_m)E + \begin{cases} (\beta_0^u + \beta_1^u E_m)E^2, & \text{up,} \\ (\beta_0^u + \beta_1^u E_m - \beta_0^d - \beta_1^d E_m)E_m^2 + (\beta_0^d + \beta_1^d E_m)E^2, & \text{down.} \end{cases} \quad (30)$$

where  $\alpha_0$ ,  $\alpha_1$ ,  $\beta_0$ , and  $\beta_1$  are the expansion constants. It can be shown that Eq. (2) introduced by Lord Rayleigh for describing the hysteresis in magnetic media is a partial case of Eq. (30) when the reference level and its change in the electric field are neglected in both equations and  $\alpha_0 = \alpha_R$ ,  $\alpha_1 = 2\beta_0^u = -2\beta_0^d = \beta_R$ , and  $\beta_1^u = \beta_1^d = 0$ .

Corresponding to Eq. (30) the first four harmonics (including the dc component) are

$$D_3^{(0)} = D_3^u(0) - \frac{2(\beta_0^{(1)} + \beta_1^{(1)} E_m) - \beta_0^{(2)} + \beta_1^{(2)} E_m}{4} E_m^2,$$

$$D_3^{(1)} = (\alpha_0 + \alpha_1 E_m) E_m \sin(\omega t)$$

$$- \frac{4}{3\pi} (\beta_0^{(1)} + \beta_1^{(1)} E_m) E_m^2 \cos(\omega t),$$

$$D_3^{(2)} = \frac{1}{2} (\beta_0^{(2)} + \beta_1^{(2)} E_m) E_m^2 \sin\left(2\omega t - \frac{\pi}{2}\right),$$

$$D_3^{(3)} = \frac{4}{15\pi} (\beta_0^{(1)} + \beta_1^{(1)} E_m) E_m^2 \sin\left(3\omega t - \frac{\pi}{2}\right),$$
(31)

where

$$\beta_0^{(1)} - \beta_1^{(1)} E_m = \beta_0^u + \beta_1^u E_m - \beta_0^d - \beta_1^d E_m,$$

$$\beta_0^{(2)} - \beta_1^{(2)} E_m = \beta_0^u + \beta_1^u E_m - \beta_0^d - \beta_1^d E_m.$$
(32)

Thus, Eq. (31) can be considered as a first order approximation for describing harmonics of the hysteresis dependence of  $D_3$  on the sinusoidal electric field  $E = E_m \sin(\omega t)$ . A set of equations analogous to Eq. (31) can be also written for  $S_1(E)$ . As is seen in Eqs. (29) and (31), there is a phase delay  $\varphi_D^{(1)}$  in the first harmonic  $D_3^{(1)}$ , which appears, owing to the hysteresis. It should be noted that in the type of hysteresis loop schematically presented in Fig. 22,  $\beta^u(E_m) > 0$  and  $\beta^d(E_m) < 0$ . Therefore, the phase of the first harmonic is always negative. The sign of the phase of the second harmonic depends on the sign of the sum  $\beta^u(E_m) + \beta^d(E_m)$ . Depending on the mutual direction of the remnant polarization and the applied electric field, the sum can be positive or negative. The sign of the third harmonic phase can be negative or positive, but for the dependence represented by Eq. (30) it should be  $-\pi/2$ . Thus, in the first approximation the phase shift of the second harmonic is  $-\pi/2$  and of the third one is  $-\pi/2$  [Eq. (31)]. This qualitative analysis of phase characteristics of the first three harmonics of  $D_3$  is in agreement with the experimental data of Figs. 15 and 16. It should be noted that the nonlinear model [Eqs. (21)–(23)] fails to explain the phase shift in the first harmonic and gives a wrong phase of the third harmonic.

As follows from Eq. (29),  $D_3^{(1)} \sin(\varphi_D^{(1)}) / D_3^{(3)} \sin(\varphi_D^{(3)}) = 5$  and corresponding values calculated from the experimental data of Fig. 15 are given in Fig. 23. The theoretical value is smaller than the experimental ratio, which equals approximately 13. We assume that the discrepancy is related to the limited accuracy of the presentation of the hysteresis by the cubic polynomials in  $E$  [Eq. (25)], which gives the hysteretic part represented by quadratic terms in Eq. (27). Analysis shows that if the hysteretic part of the dependence  $D_3(E)$  is described by the term including  $E^4$  only, the ratio

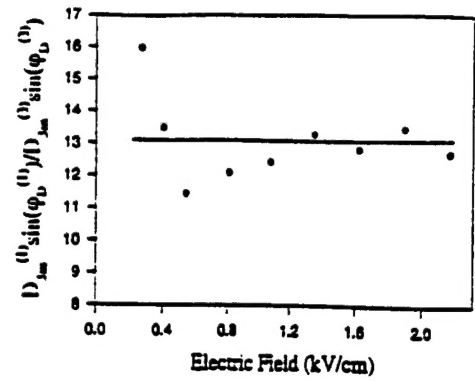


FIG. 23. Experimental values of  $D_3^{(1)} \sin(\varphi_D^{(1)}) / D_3^{(3)} \sin(\varphi_D^{(3)})$  from data of Fig. 15.

$D_3^{(1)} \sin(\varphi_D^{(1)}) / D_3^{(3)} \sin(\varphi_D^{(3)})$  is equal to 21, which is larger than the experimental value. Therefore, polynomial  $D_3(E)$ , which includes terms up to the fourth power of  $E$ , should give a much better approximation for the third harmonic, since, in this case, the hysteretic part of the dependence is a combination of terms containing  $E^2$  and  $E^4$ . To overcome the discrepancy in the presentation of the third harmonic  $D_3^{(3)}$ , the harmonic can be approximated by the function proportional to the corresponding part in the first harmonic. Therefore the last equation in the set (31) transforms to

$$D_3^{(3)} = \beta_0^{(3)} (\beta_0^{(1)} + \beta_1^{(1)} E_m) E_m^2 \sin\left(3\omega t - \frac{\pi}{2}\right). \quad (33)$$

Finally, taking into account the fact that the phase of the first harmonic is relatively small, the following set of approximation functions can be written for the hysteretic model [for see comparison Eq. (24)];

$$\frac{D_3^{(1)}}{E_m} \approx \alpha_0 + \alpha_1 E_m,$$

$$\varphi_D^{(1)} = -\arctan\left(\frac{\frac{3}{4\pi} (\beta_0^{(1)} + \beta_1^{(1)} E_m) E_m}{\alpha_0 + \alpha_1 E_m}\right),$$
(34)

$$\frac{D_3^{(2)}}{D_3^{(1)}} \approx \frac{\frac{1}{2} (\beta_0^{(2)} + \beta_1^{(2)} E_m) E_m}{\alpha_0 + \alpha_1 E_m},$$

$$\frac{D_3^{(3)}}{D_3^{(1)}} \approx \frac{\beta_0^{(3)} (\beta_0^{(1)} + \beta_1^{(1)} E_m) E_m}{\alpha_0 + \alpha_1 E_m}.$$

Thus, seven parameters describe first three harmonics of  $D_3$  (including the phase of  $D_3^{(1)}$ ) in the model of the hysteresis transducer. It should be noted that Eq. (33) for the third harmonic does not follow from Eq. (30). Fitting Eq. (34) to the experimental data of Fig. 15 is shown in Fig. 24. As is seen from the graph, there is a good agreement between the hysteretic model and the experiment except for low electric fields. Using results of the fit parameters, the hysteresis loop [Eq. (30)] can be restored. From the loop, the irreversible change in the remnant polarization  $\Delta P_i$  during one cycle, which is equal to  $(\beta_0^u + \beta_1^u E_m - \beta_0^d - \beta_1^d E_m) E_m^2$  [see Eq. (30)] can be found. Calculated  $\Delta P_i$  is in good agreement with the

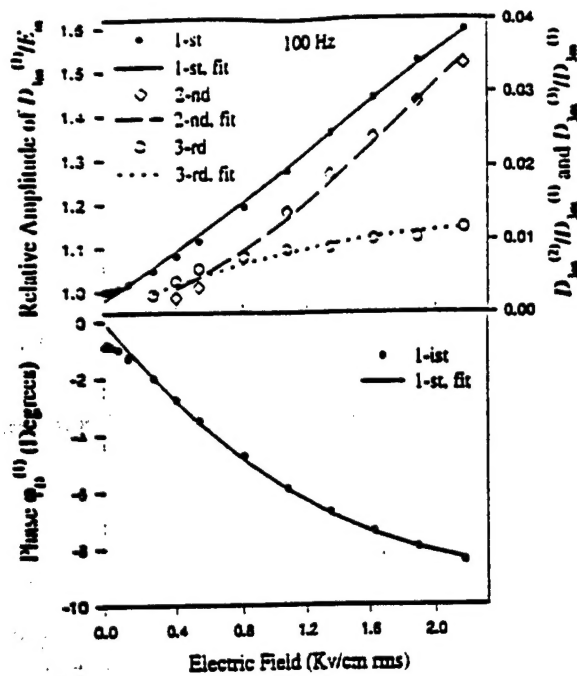


FIG. 24. Fitting hysteretic model to experimental amplitudes of the first three harmonics of  $D_3$  for 3203HD sample (Fig. 15).

measured results using the sinusoidal-pulse technique (Fig. 17): the discrepancy does not exceed 20%–25%.

Thus, analysis of the hysteretic model of  $D_3(E)$  conducted above demonstrates that the model is a very good approximation for describing the behavior of the electrical displacement  $D_3$  under the high electric field and stress-free conditions. A simplification of the hysteresis loop  $D_3(E)$  can be made since despite a significant change in the dc component and first harmonic with increasing electric field, the relative level of the second and third harmonics does not exceed several percent (see Figs. 15–17). Therefore, Eq. (30) reduces to

$$D_3(E) = D_3^{(0)}(E_m) + D_3^{(1)}(E_m), \quad E = E_m \sin(\omega t). \quad (35)$$

Thus, the dielectric response of the soft piezoelectric PZT ceramics to the applied sinusoidal electric field, which is smaller than the coercive one, basically consists of two components: the dc part and ac part at the same frequency  $\omega$ . Usually since only the first harmonic is of importance, changes in the remnant polarization level can be omitted and complex-function formalism can be used for describing the dielectric response:

$$D_3^* = \epsilon_{33}^T(E_m) E_m. \quad (36)$$

where  $D_3^*$  is the complex amplitude of the ac component of the electrical displacement along the polar axis, and  $\epsilon_{33}^T(E_m)$  is the complex dielectric permittivity in the sinusoidal electric field, which is approximately given by [see Eq. (34)]

$$\epsilon_{33}^T(E_m) = (\alpha_0 + \alpha_1 E_m) e^{-j \arctan(3/4 \pi \beta_0^{(1)} + \beta_1^{(1)} E_m) E_m / (\alpha_0 + \alpha_1 E_m)}, \quad (37)$$

where  $\alpha_0$  practically coincides with small-signal dielectric permittivity,  $\alpha_0 \approx \epsilon_{33}$ . It should be noted that Eq. (37) is valid only for the case when no dc bias is applied (The elec-

tric field changes from  $-E_m$  to  $-E_m$ ). With the dc bias applied, function  $\epsilon_{33}^T(E_m)$  can differ from that described by Eq. (37).

As seen from Figs. 7–9 there is a strong correlation between pairs  $D_{3m}^{(1)} e^{j\phi_0^{(1)}} / E_m$  and  $S_{1m}^{(1)} e^{j\phi_1^{(1)}} / E_m$  for all ceramic studied in electric fields 0–1.4 kV/cm rms. Therefore, the suggested hysteretic model should be also valid for function  $S_1(E)$  in this range. Corresponding to Eq. (36) the strain field relation under stress-free conditions is

$$S_{1m}^* = d_{31}(E_m) E_m, \quad (38)$$

where  $S_{1m}^*$  is the complex amplitude of the ac component of the mechanical strain in the direction perpendicular to the polar axis and  $d_{31}(E_m)$  is the complex piezoelectric coefficient in the sinusoidal electric field; the coefficient is approximately described by the function directly proportional to the right part of Eq. (37). Thus, as follows from Eqs. (36) and (38), experimentally measured complex function  $D_{3m}^{(1)} e^{j\phi_0^{(1)}} / E_m$  and  $S_{1m}^{(1)} e^{j\phi_1^{(1)}} / E_m$  (see Figs. 7–9 and 11–14) are equal to complex dielectric  $\epsilon_{33}^T(E_m)$  and piezoelectric  $d_{31}(E_m)$  coefficients, respectively.

It is also reasonable to assume that the behavior of elastic properties of soft piezoelectric ceramics is of the hysteretic type and mechanical compliance  $s_{11}^E(E_m)$  is described by a formula similar to Eq. (37). Therefore, the first harmonic should be dominant in the ac component of the mechanical response and should increase linearly with increasing amplitude of the electric field. Therefore, the fundamental resonant frequency of bending vibrations under stress-free condition instead of Eq. (12) is described by

$$\nu_r = \frac{1.875^2}{4\pi} \frac{t_c}{l^2} \frac{1}{\sqrt{3|s_{11}^E(E_m)|\rho}}, \quad (39)$$

where  $|s_{11}^E(E_m)|$  is the amplitude of the elastic coefficient. As follows from Fig. 10,  $|s_{11}^E(E_m)|$  increases almost linearly with increasing electric field that is consistent with the suggested hysteretic model. The field dependence of the amplitude of  $s_{11}^E(E_m)$  is more gradual than that of  $\epsilon_{33}^T(E_m)$  and  $d_{31}(E_m)$ . For example, for PK1550 ceramics, as follows from Fig. 7 and Eq. (37),  $|\epsilon_{33}^T(E_m)| / |\epsilon_{33}^T(0)| \approx 0.981 + 0.251 E_m$  and as follows from Fig. 10 and Eq. (39),  $|s_{11}^E(E_m)| / |s_{11}^E(0)| \approx 0.998 + 0.097 E_m$ , where  $E_m$  is in kV/cm rms. Therefore the slope of the function  $s_{11}^E(E_m)$  is about 40% of that of  $\epsilon_{33}^T(E_m)$  for these ceramics.

Thus, the analysis conducted above strongly supports the hypothesis that hysteresis is the cause of the high field behavior of the soft piezoelectric ceramics. Previous works<sup>13,14</sup> suggested that the dependence of piezoelectric coefficient on applied mechanical stress is also of hysteretic type. As logical sequel to this, it can be assumed that under simultaneous action of the electric field and mechanical stress, the electromechanical response of the ceramics will be essentially of the hysteretic type. If sinusoidal electric field is applied along the Z axis, and sinusoidal mechanical stress acts along the X axis, the following set of equations may approximately describe the electromechanical response:



$$S_{1m}^* = s_{11}^E(E_m, T_{1m})T_{1m} - d_{31}(E_m, T_{1m})E_m, \quad (40)$$

$$D_{3m}^* = d_{31}^*(E_m, T_{1m})T_{1m} - \epsilon_{33}^T(E_m, T_{1m})E_m,$$

where  $T_{1m}$  is the amplitude of the mechanical stress, dc components are not included in set (40). It should be noted that there is a principal difference between Eqs. (5) and (6) corresponding to the nonlinear model and Eq. (40) describing the hysteretic model. First, Eq. (40) describes relations between complex amplitudes while Eqs. (5) and (6) are related to instant values. Second, in the nonlinear model, a significant increase in the first harmonic of the electromechanical response implies a corresponding significant increase in the amplitude of higher odd harmonics [see, for example, Eq. (24)]. This is not true for the hysteretic model (40) in which only first harmonics are taken into account since experiments show that higher harmonics are not significant at electric fields lower than the coercive one.

Before proceeding with the analysis of the physical reasons for the observed hysteretic behavior of soft piezoelectric ceramics, several important remarks regarding limitations of the developed hysteretic model should be made. The suggested hysteretic model is of a static type, i.e., it does not take into account the frequency dispersion of electromechanical characteristics of the ceramics. Experimental data (Figs. 11–14) demonstrate that there is a small frequency dependence in the measured electrical displacement  $D_3$  and mechanical strain  $S_1$ ; the frequency dispersion is also a function of the electric field. Experimental data also show (Fig. 14) that there are peculiarities in the behavior of  $\epsilon_{33}^T(E_m)$  at low electric fields that are not described by Eqs. (37) and (40). Finally, according to Eq. (37) the phase of the dielectric permittivity  $\epsilon_{33}^T(E_m)$  approaches zero at low electric fields, while corresponding experimental values fall within the range  $(-0.2^\circ - 1.0^\circ)$  (see Fig. 24). Thus, there are dielectric losses having nonhysteretic origin that are not included in the suggested hysteretic model. Nevertheless, the hysteretic model describes the main peculiarities of studied electromechanical properties of soft piezoelectric ceramics at high electric fields.

## 2. Physical models

In this section, possible physical mechanisms of the observed behavior of soft piezoelectric ceramics under the electric field will be analyzed. As is seen from Figs. 7–9 and the corresponding hysteretic model [Eqs. (36) and (38)] there is strong correlation between complex dielectric  $\epsilon_{33}^T(E_m)$  and piezoelectric  $d_{31}(E_m)$  coefficients for all ceramics studied in the electric field of 0–1.4 kV/cm rms. The data of Fig. 11 demonstrate that frequency dependencies of  $\epsilon_{33}^T(E_m)$  and  $d_{31}(E_m)$  are also similar. As is seen from a comparison of Figs. 7 and 10 and Eqs. (36), (38), and (39), the field dependence of the amplitude of  $s_{11}^E(E_m)$  is more gradual than that of  $\epsilon_{33}^T(E_m)$  and  $d_{31}(E_m)$ . Comparison of  $D_3(E)$ ,  $S_1(E)$ , and  $(D_3)$  hysteresis loops (Figs. 18 and 19) also shows that there is a linear relation, without phase shift, between  $D_3$  and  $S_1$  in the electric field of 1 kV/cm rms. In electric fields higher than the coercive one the correlation breaks up: the electrical displacement  $D_3$  and strain  $S_1$  behave in a very different manner (Fig. 19).

One possible explanation of the observed behavior of the electromechanical properties of the ceramics is based on the model of the domain wall and interphase boundary motion. According to this approach, the reorientation of the spontaneous polarization of microscopic domains under applied electric field contributes to the dielectric, piezoelectric, and elastic response of the media.<sup>3,32,21</sup> This extrinsic contribution to the electromechanical properties was estimated to be especially significant for soft piezoelectric ceramics.<sup>21</sup> XRD data (Fig. 20) show that the ceramics studied consist of a mixture of tetragonal and rhombohedral phases. 180° polarization switching in both phases does not produce a change in the three-dimensional strain. The angle characterizing the rhombohedral cell is very close to 90° in PZT ceramics at MPB,<sup>22</sup> therefore 71° or 109° polarization reorientation in this phase also does not produce a significant change in the space position of the domain. Thus, the above discussed domain processes can contribute mainly to the dielectric response in PZT. 90° polarization reorientation in the tetragonal state and the tetragonal/rhombohedral phase boundary motion can contribute significantly to both dielectric and piezoelectric responses since the polarization change is accompanied by a significant (up to several percent) change in the domain dimensions along certain directions. This domain reorientation also causes mechanical stress in the media that finally produces an apparent change in the elastic properties. Therefore, according to the model based on the polarization reorientation, an increase in the 90° and tetragonal/rhombohedral polarization reorientation should be responsible for an observed increase in  $\epsilon_{33}^T(E_m)$ ,  $d_{31}(E_m)$ , and  $s_{11}^E(E_m)$  with increasing electric field. Clearly, hysteretic behavior of the electromechanical characteristics is also a result of the polarization reorientation. When the electric field is sufficiently high, 180°, 71°, and 109° polarization switching probably becomes dominant. Therefore,  $D_3(E)$  and  $S_1(E)$ , unlike for fields smaller than the coercive one (Fig. 18), behave in a different manner (Fig. 19). It is rather difficult to develop a corresponding qualitative mathematical model since it should take into account the polarization reorientation in numerous domains with corresponding complex microscopic boundary conditions. It should be noted that it is unclear from the model of the domain wall motion, why functions  $\epsilon_{33}^T(E_m)$  and  $d_{31}(E_m)$  under zero bias behave in a similar manner as follows from the experimental data. In general, 90° and tetragonal/rhombohedral polarization reorientation should not necessarily contribute equally to the change in the dielectric and piezoelectric functions.

Soft piezoelectric PZT ceramics consist of numerous grains with extremely complicated domain structure and possess very high electromechanical coupling. Thus, the application of electric field to the ceramics can cause a change in the internal mechanical stress acting on a microdomain since this microdomain and its surrounding matrix may have a different orientation of their polar axes. This change in the mechanical stress, in turn, can affect macroscopic electromechanical characteristics of the ceramics. Therefore, a model can be suggested in which the observed changes in the electromechanical properties of the ceramics are attributed to the change in the microscopic mechanical stress acting on tetragonal

onal and rhombohedral microdomains because of the applied electric field. The stress is a result of the interaction of a microdomain with surrounding grains and domains. Hysteretic behavior of the electromechanical characteristics is probably caused by the hysteretic nature of this interaction since mechanical properties of the surface of grains differ from those of the microdomains. Calculations based on the thermodynamic theory<sup>23,24</sup> of the ferroelectric state of PZT ceramics with composition on the morphotropic phase boundary show that compressive and tensile stress on the order of 10–20 MPa can cause a corresponding change in electromechanical properties of ceramics on the order of 10%–40%. This value of the mechanical stress as well as corresponding changes in piezoelectric, dielectric, and elastic properties are quite reasonable for the soft PZT ceramics. This model is applicable only if the amplitude of the electric field is smaller than the coercive field. For fields greater than the coercive field, polarization switching should dominate (Fig. 19). It should be noted that the effect of the internal static mechanical stress was suggested<sup>22,25</sup> as being responsible for the high dielectric permittivity of fine-grained BaTiO<sub>3</sub> ceramics and the theory was proved correct experimentally.<sup>27</sup> Nevertheless, at the present level of knowledge of the physical properties of soft PZT ceramics, it is impossible to determine which model—that of the domain wall motion, that of the internal stress, or that of their combination—is valid.

## VI. SUMMARY AND CONCLUSIONS

In this work, experimental and theoretical studies of the behavior of dielectric, piezoelectric, and elastic characteristics of commercial soft piezoelectric PZT ceramics in the sinusoidal electric field applied along the poling direction under mechanical stress-free conditions in the frequency range 10 Hz–10 kHz were conducted. Experimental results demonstrate that amplitudes and phases of the harmonics of relative strain  $S_1^{(1)}/E_m$  and of relative electrical displacement  $D_3^{(1)}/E_m$  increase similarly with increasing amplitude  $E_m$ , if the amplitude is less than coercive field. An increase in the square of resonant frequency  $\nu_0^2$  of electromechanically decoupled bending vibrations is more moderate. These amplitude dependencies are very well described by linear functions except for small electric fields. Relative amplitude of the second harmonic of the electrical displacement,  $D_3^{(2)}/D_3^{(1)}$ , which is polar, also increases almost linearly with increasing  $E_m$ . The relative third harmonic  $D_3^{(3)}/D_3^{(1)}$  demonstrates saturationlike behavior. Based on these experimental data a novel model, in which the ceramics are considered to behave like a hysteretic transducer, is developed. This approach makes it possible to model hysteretic dependencies of the electromechanical characteristics and to relate directly electric field dependencies of complex piezoelectric coefficient  $d_{31}(E_m)$  and  $S_1^{(1)}/E_m$ , of complex dielectric permittivity  $\epsilon_{33}^*(E_m)$  and  $D_3^{(1)}/E_m$ , and of the amplitude of elastic compliance  $s_{11}^E(E_m)$  and  $\nu_0^2$ . The model effectively describes field dependencies of the first three harmonics of

$D_3(E_m)$ , as well as the irreversible change in the remnant polarization under pulsed electric field. Several physical models for the observed behavior were analyzed. In one approach, the explanation is based on the 90° ferroelectric domain and tetragonal/rhombohedral phase boundary motion. In order to better explain the experimental results, a new physical model was developed. According to the model, the observed change in electromechanical properties under the electric field is caused by the field dependence of the mechanical stress acting at interdomain boundaries. It is assumed that this stress is caused by the electromechanical interaction of a microdomain with surrounding microdomains and grains. This surrounding media acts as a viscoelastic structure that causes hysteretic behavior in the electromechanical properties.

## ACKNOWLEDGMENT

This work was supported by the Office of Naval Research under Contract No. N00014-94-1-1140.

- <sup>1</sup> B. Xu, Q. Zhang, V. D. Kugel, and L. E. Cross, *Proc. SPIE* 3717, 38 (1996).
- <sup>2</sup> V. D. Kugel, Baomin Xu, Q. M. Zhang, and L. E. Cross, *Sensors and Actuators A* (accepted).
- <sup>3</sup> H. G. Baerwald and D. A. Berlincourt, *J. Acoust. Soc. Am.* 25, 70 (1953).
- <sup>4</sup> D. A. Berlincourt and H. H. A. Krueger, *J. Appl. Phys.* 30, 1804 (1959).
- <sup>5</sup> J. H. Belding and M. G. McLaren, *Ceram. Bull.* 49, 1025 (1970).
- <sup>6</sup> R. S. Woollett and C. L. LeBlanc, *IEEE Trans. Sonics Ultrason.* 20, 2 (1973).
- <sup>7</sup> H. Beige and G. Schmidt, *Ferroelectrics* 41, 39 (1982).
- <sup>8</sup> S. Li, W. Cao, and L. E. Cross, *J. Appl. Phys.* 69, 7219 (1991).
- <sup>9</sup> Y. Saito, *Jpn. J. Appl. Phys., Part 1* 34, 5313 (1995).
- <sup>10</sup> Q. M. Zhang, H. Wang, and J. Zhao, *J. Intell. Mater. Syst. Struct.* 6, 8 (1995).
- <sup>11</sup> D. F. Nelson, *J. Acoust. Soc. Am.* 63, 1739 (1978).
- <sup>12</sup> Lord Rayleigh, *Philos. Mag. Suppl.* 23, 225 (1887).
- <sup>13</sup> D. Damjanovic and M. Demarin, *J. Phys. D* 29, 2057 (1996).
- <sup>14</sup> D. Damjanovic, M. Demarin, F. Chu, and N. Setter, *Proceedings of 10th IEEE International Symposium on Applications of Ferroelectric Catalog Number 1996, 96CH35948*, p. 251.
- <sup>15</sup> H. Beige, *Ferroelectrics* 51, 113 (1983).
- <sup>16</sup> Q. M. Zhang, S. J. Jang, and L. E. Cross, *J. Appl. Phys.* 65, 2807 (1988).
- <sup>17</sup> V. D. Kugel, Q. M. Zhang, B. Xu, Q. M. Wang, S. Chandran, and L. E. Cross, *Proceedings of 10th IEEE International Symposium on Applications of Ferroelectric Catalog Number 1996, 96CH35948*, p. 65.
- <sup>18</sup> K. Mishra, D. Pandey, and A. P. Singh, *Appl. Phys. Lett.* 69, 1707 (1996).
- <sup>19</sup> I. D. Mayergoyz, *Mathematical Models of Hysteresis* (Springer, New York, 1991), Introduction, Chap. 1.
- <sup>20</sup> Q. M. Zhang, W. Y. Pan, S. J. Jang, and L. E. Cross, *J. Appl. Phys.* 64, 45 (1988).
- <sup>21</sup> Q. M. Zhang, H. Wang, N. Kim, and L. E. Cross, *J. Appl. Phys.* 75, 4 (1994).
- <sup>22</sup> B. Jaffer, R. S. Roth, and S. Marzullo, *J. Res. Natl. Bur. Stand.* 55, 2 (1955).
- <sup>23</sup> A. F. Devonshire, *Philos. Mag.* 42, 1065 (1951).
- <sup>24</sup> A. Amin, M. J. Haun, B. Badger, H. McKinsry, and L. E. Cross, *Ferroelectrics* 65, 107 (1985).
- <sup>25</sup> W. R. Buessem, L. E. Cross, and A. K. Goswami, *J. Am. Ceram. Soc.* 33 (1966).
- <sup>26</sup> W. R. Buessem, L. E. Cross, and A. K. Goswami, *J. Am. Ceram. Soc.* 36 (1966).
- <sup>27</sup> R. C. Pohanka, R. W. Rice, and B. E. Walker, Jr., *J. Am. Ceram. Soc.* 71 (1976).